

Dissertation

Submitted to the

Combined Faculty of Natural Sciences and Mathematics

Heidelberg University, Germany

for the degree of

Doctor of Natural Sciences (Dr. rer. nat.)

Presented by

M. Sc. Friedrich Maaß

Born in: Weimar, Germany

Oral Examination: November 6th, 2018

Für Emil und Smilla.

The Metal/Organic Interface

-

**Binding, Adsorption Geometry,
and Electronic Structure**

Referees

Prof. Dr. Petra Tegeder

Prof. Dr. Annemarie Pucci

Abstract

Metal/organic interfaces as they appear between electrodes and organic semiconductors in organic electronics decisively determine device properties of transistors, light emitting diodes, or photovoltaic cells. The interactions within the organic semiconductor and between organic adsorbate and metallic substrate lead to characteristic properties of the particular interface. These properties, namely the binding strength, the adsorption geometry, and the electronic structure, have been studied with comprehensive surface sensitive experimental methods like high-resolution electron energy-loss spectroscopy (HREELS) and temperature-programmed desorption (TPD). The use of single crystal metal surfaces as substrates and self-assembling small organic molecules as adsorbates lead to insights into structure-property relationships that will contribute to the further development of materials and devices.

The first part of this work investigates the bonding strength between metal substrates and organic adsorbates. With the quantification of binding energies of simple aromatic molecules on coinage metal surfaces by means of TPD, this part enters questions of basic surface science. Besides the delivery of benchmarks of unrivalled accuracy for the further development of computational methods to model binding properties of adsorbate-covered surfaces the focus of this part also lays on the first investigation of the extraordinary coverage dependency of the binding energy of such systems. The second part is about the self-assembly of small-molecule organic semiconductors on metal surfaces, and how this arrangement is influenced by the molecular structure. This part covers the elucidation of adsorption geometries of N-heteropolycyclic aromatic molecules on the Au(111) surface by means of vibrational HREELS. Moreover, electronic HREELS enabled us to get insight into the electronic structure of these interfaces. To maximize the interaction between metal bands and the π -system of the adsorbate the planar molecules prefer a planar adsorption geometry. This presetting of a flat geometry works subsequently as a template for further layers which leads to a growth mechanism and therefore film structure significantly different from that of the bulk crystal. The last part of this work studies the influence of organic adsorbate films on collective electronic properties of the metal surface with angle-resolved HREELS. Characteristic collective excitations of a two-dimensional electron gas present on the pristine gold surface are strongly influenced in their properties by adsorbate layers, e.g., they show a strongly enhanced intensity and a varied dispersion relation.

Kurzzusammenfassung in deutscher Sprache

Metall/Organik-Grenzflächen, wie sie in der organischen Elektronik zwischen Elektroden und organischen Halbleitern auftreten, beeinflussen maßgeblich die Eigenschaften von Bauteilen wie Transistoren, Leuchtdioden oder photovoltaischen Zellen. Die Wechselwirkungen innerhalb der organischen Schicht und zwischen organischem Halbleiter und metallischem Substrat führen zu charakteristischen Eigenschaften dieser Grenzflächen. Diese Eigenschaften, namentlich Bindungsstärke, Adsorptionsgeometrie und elektronische Struktur, wurden mit Hilfe oberflächensensitiver Methoden wie hochauflösender Elektronenenergieverlustspektroskopie (HREELS) und temperatur-programmierter Desorption (TPD) untersucht. Als Substrat dienten jeweils Metall-Einkristallobertflächen, als Adsorbat molekulare organische Halbleiter. Dies führte zu Einblicken in Struktur-Eigenschaften-Beziehungen die zur weiteren Entwicklung von Materialien und Bauteilen beitragen werden.

Der erste Teil dieser Arbeit behandelt mit der quantitativen Bestimmung der Bindungsenergien von einfachen aromatischen Molekülen auf verschiedenen Münzmetalloberflächen mittels TPD grundlegende Fragen der Oberflächenphysik. Neben der Etablierung neuer Richtwerte zur Weiterentwicklung von rechnergestützten Verfahren zur Modellierung von adsorbatbedeckten Oberflächen, lag ein weiterer Fokus auf der erstmals eingehend untersuchten starken Abhängigkeit dieser Bindungsenergien vom Bedeckungsgrad. Der zweite Teil behandelt die Anordnung von molekularen organischen Halbleitern auf Metalloberflächen und wie diese Anordnung von der Struktur der Moleküle beeinflusst wird. Mit HREELS wurden die elektronische Struktur und die Adsorptionsgeometrie neuartiger N-heteropolyzyklischer aromatischer Halbleiter auf der Au(111)-Oberfläche aufgeklärt. Zur Maximierung der Wechselwirkung zwischen Metallbändern und π -System des Adsorbats bevorzugten flache organische Halbleiter planare Adsorptionsgeometrien. Diese Vorgabe einer flachen Geometrie dient anschließend als Templat für viele weitere Schichten, mit der Folge, dass sich das Wachstum in dünnen Filmen erheblich von dem im Kristall unterscheidet. Der letzte Teil dieser Arbeit untersucht den Einfluss von organischen Adsorbaten auf kollektive elektronische Eigenschaften der Metalloberfläche mittels winkelaufgelöster HREELS. Charakteristische kollektive Anregungen eines zweidimensionalen Elektronengases, die auf der reinen Metalloberfläche existieren, werden z.B. in ihrer Intensität oder Dispersionsrelation von Adsorbatschichten wesentlich beeinflusst.

Contents

Abstract	5
Kurzzusammenfassung in deutscher Sprache	7
1. Introduction	21
2. Experimental Methods and Setup	27
2.1. Temperature-Programmed Desorption (TPD)	27
2.2. High-Resolution Electron Energy-Loss Spectroscopy (HREELS)	34
2.3. Density Functional Theory (DFT)	39
2.4. Experimental Setup	42
2.4.1. Ultra-high Vacuum System	42
2.4.2. Au(111) Surface and Sample Preparation	45
3. Binding of Aromatic Molecules on Coinage Metal Surfaces	49
3.1. Background: The Metal/Organic Interface	50
3.1.1. Adsorbate-Substrate Interactions	50
3.1.2. Adsorbate-Adsorbate Interactions	53
3.2. Benzene on Coinage Metals	55
3.3. Discussion: Equal Stability on Different Metals	61
3.4. Acenes on Au(111)	63
3.5. Discussion: Binding Energy and the Size of the Aromatic System	67
4. Adsorption and Growth of Functional Molecules on Au(111)	69
4.1. Background: N-Heteropolycyclic Aromatic Molecules	69
4.2. TIPS-Pentacene	73
4.3. Quinoxalinophenanthrophenazine (QPP) and tBu-QPP	81
4.4. Tetraazaperopyrene (TAPP) and its Halogenated Derivatives	87
4.5. Discussion: Substrate-Directed Growth and the Influence of Substituents	95
5. Collective Excitations at Metal/Organic Interfaces	99

Contents

5.1. Background: Plasmons at Metal Surfaces	100
5.2. Angle-Resolved electronic HREELS measurements	105
5.2.1. Au(111)	106
5.2.2. TCNQ and F ₄ TCNQ on Au(111)	108
5.2.3. Analogous Excitations in other Systems	114
5.2.4. Discussion: Adsorbate Influenced Surface Plasmon Ex- citations	117
5.3. Vibrational Measurements	121
5.3.1. Background: IDCT and Fano-resonances	122
5.3.2. TCNQ and its Fluorinated Derivatives on Au(111) . . .	124
5.3.3. Discussion: Interactive Vibrational and Electronic Exci- tations	127
6. Conclusion and Outlook	129
A. List of Acronyms	133
B. Dosing and Experimental Parameters	137
C. DFT Parameters and Commented Gaussian09 Input	141
D. Benzene on Cu(111): TPD and HREELS	143
E. Prefactors for Benzene on Coinage Metal Surfaces	147
F. TIPS-Pn and TIPS-TAP: Further Studies and Vibrational Assign- ments	149
F.1. TIPS-Pn and TIPS-TAP: TPD and Mass Spectrometry	152
F.2. TIPS-Pn: Electronic HREELS	154
F.3. TIPS-TAP: HREELS	154
G. QPP and tBu-QPP: Further Studies and Vibrational Assignments	157
G.1. QPP and tBu-QPP: TPD	159
G.2. QPP and tBu-QPP: Electronic HREELS	160
H. TAPP and its Derivatives: Further Studies and Vibrational Assign- ments	161
H.1. TAPP and its Derivatives: TPD	166
H.2. TAPP and its Derivatives: Electronic HREELS	167

I. Angle-Resolved HREELS: Further Measurements	169
I.1. Explanation and Exemplary Arduino Input for Automated Measurements	169
I.2. Influence of the Preparation	172
I.3. Influence of the Crystal Orientation	173
I.4. Influence of the Primary Electron Energy	174
I.5. Influence of the Coverage	175
I.6. Analogous Excitations	176
I.7. Vibrational Assignments for F ₄ TCNQ	183
J. Calculated Optimized Structures	185
List of Publications	233
Acknowledgments	237

Contents

List of Figures

2.1.	TPD scheme: On-surface processes and the TPD measurement .	28
2.2.	Desorption spectra for different desorption orders	30
2.3.	Calculated spectra illustrating the <i>complete analysis</i>	33
2.4.	The Delta 0.5 HREEL spectrometer	35
2.5.	Dipole scattering and surface selection rule	37
2.6.	Ultrahigh vacuum chamber and experimental setup	44
2.7.	The Au(111) surface	46
2.8.	Exemplary dosing and TPD spectra	47
3.1.	Structural formulas of acenes from benzene to pentacene	49
3.2.	The metal-semiconductor interface	52
3.3.	Lateral interactions: PTCDA and pentacene	53
3.4.	Substrate-mediated interactions	55
3.5.	<i>Complete analysis</i> for Bz on Au(111)	57
3.6.	Bz on Au(111), Ag(111), and Cu(111)	59
3.7.	Acene TPD measurements on Au(111)	63
3.8.	Pentacene and tetracene on Au(111)	65
3.9.	Pentacene monolayer and Acenes' desorption energies	67
4.1.	Structural variability of N-heteropolycyclic molecules	70
4.2.	TAPP-Br, structural formula, and frontier orbitals	72
4.3.	TPD spectra of TIPS-Pn	74
4.4.	Vibrational HREELS of TIPS-Pn	76
4.5.	Characteristic vibrational modes of TIPS-Pentacene	78
4.6.	Electronic HREELS of TIPS-Pn	79
4.7.	Vibrational HREELS of QPP and tBu-QPP	82
4.8.	Characteristic vibrational modes of QPP	84
4.9.	Electronic HREELS of QPP and tBu-QPP	85
4.10.	Vibrational HREELS of TAPP	88
4.11.	Characteristic vibrational modes of TAPP	89
4.12.	Vibrational HREELS of TAPP derivatives	91

List of Figures

4.13. Electronic HREELS of TAPP derivatives	93
4.14. Adsorption model for different N-heteropolycycles and TIPS-Pn	96
4.15. Calculated HOMO and LUMO energies	97
5.1. Dimension dependent plasmon dispersion	102
5.2. Surface plasmon and surface state	103
5.3. Au(111) surface state and surface plasmons	104
5.4. Angle-resolved electronic HREELS of Au(111)	107
5.5. STM images of F ₄ TCNQ and TCNQ on Au(111)	108
5.6. Electronic HREELS of F ₄ TCNQ and TCNQ	109
5.7. Angle-resolved HREELS of F ₄ TCNQ and TCNQ	113
5.8. Structural formula of the investigated organic molecules	115
5.9. The plasmonic excitation in other systems	116
5.10. Electron affinity and developed interaction model	120
5.11. Fano resonance and IDCT	122
5.12. Vibrational HREELS of TCNQ, F ₂ TCNQ, and F ₄ TCNQ	126
C.1. DFT parameters and commented input file	141
D.1. Bz on Cu(111): TPD and HREELS measurements	144
E.1. Prefactors for Bz on Au(111), Ag(111), and Cu(111)	148
F.1. Visualized Vibrations for TIPS-Pn	151
F.2. Mass spectrometry and TPD for TIPS-Pn and TIPS-TAP	153
F.3. Electronic HREELS data of 1 ML TIPS-Pn on Au(111)	154
F.4. Vibrational and electronic HREELS of TIPS-TAP	155
G.1. Visualized Vibrations for QPP	157
G.2. TPD measurements for QPP and <i>t</i> Bu-QPP	159
G.3. Electronic HREELS data of QPP and <i>t</i> Bu-QPP monolayers on Au(111)	160
H.1. Visualized Vibrations for TAPP	163
H.2. Visualized Vibrations for TAPP-H	165
H.3. TPD measurements for all TAPP derivatives	166
H.4. Electronic HREELS data for monolayers of all TAPP derivatives on Au(111)	167
I.1. Commented Arduino program code	171

I.2.	Electronic HREELS of F ₄ TCNQ multilayers: Influence of Preparation	172
I.3.	Crystal orientation and dispersion	173
I.4.	F ₄ TCNQ and TCNQ: Varied primary electron energies	174
I.5.	F ₄ TCNQ and TCNQ: Varied coverages	175
I.6.	TPD and HREELS measurements for TCNQ ⁻ TTF ⁺	177
I.7.	TPD and HREELS measurements for F ₂ TCNQ	178
I.8.	TPD and HREELS measurements for pentacene	179
I.9.	TPD and HREELS measurements for tetracene	180
I.10.	TPD and HREELS measurements for TTF	181
I.11.	TPD and HREELS measurements for anthracene	182
I.12.	Visualized vibrations of F ₄ TCNQ	184
J.1.	Calculated structure of TIPS-Pn	186
J.2.	Calculated structure of QPP	187
J.3.	Calculated structure of <i>t</i> Bu-QPP	188
J.4.	Calculated structure of TAPP	189
J.5.	Calculated structure of TAPP-H	190
J.6.	Calculated structure of TAPP-Cl	191
J.7.	Calculated structure of TAPP-Br	192
J.8.	Calculated structure of TAPP-I	193
J.9.	Calculated structure of TCNQ	194
J.10.	Calculated structure of F ₂ TCNQ	195
J.11.	Calculated structure of F ₄ TCNQ	196
J.12.	Calculated structure of TTF	197

List of Figures

List of Tables

3.1. Desorption energies of Bz on Au(111), Ag(111), and Cu(111) . .	61
3.2. Obtained prefactors for Bz on Au(111), Ag(111), and Cu(111) .	62
4.1. Investigated polycyclic molecules	71
5.1. Energetic position of feature P for different organic adsorbates .	117
B.1. Dosing parameters for all measurements	138
F.1. TIPS-Pn: Vibrational assignments	150
G.1. QPP and <i>t</i> Bu-QPP: Vibrational assignments	158
H.1. TAPP: Vibrational assignments	162
H.2. TAPP-H: Vibrational assignments	164
I.1. F ₄ TCNQ: Vibrational assignments	183

List of Tables

1. Introduction

With the invention of the transistor by Shockley, Bardeen, and Brattain [1] the control of small currents became cheap and energy efficient. It is obvious that these first germanium [2], then silicon based [3] electronics changed the world completely [4]. And silicon is the perfect material for applications like central processing units (CPU) or conventional photovoltaic cells where it is used today. But with ongoing developments new applications are within reach where organic (molecule based) materials have advantages compared to silicon or other inorganic materials [5–7]. Such advantages are e.g. transparency, flexibility, and low-weight if a suitable substrate is used [8–12]. This allows the development of new kinds of displays [13, 14], solar cells [15–17], or light emitting diodes [18–22] which then can be used in new ways we cannot even predict. As for the use in organic electronic devices only small amounts of organic molecules are needed, such devices can be cheap [23], even more, if the organic semiconductors are produced on an industrial scale. Organic semiconductors are easy to process as many of them are soluble in water, processable *via* printing [13, 24], and do not necessarily need vacuum conditions. Furthermore, they help to save resources as they are easier to recycle and the production process works at ambient temperatures and therefore needs less energy. Organic electronics will not replace silicon-based devices, but they will expand existing and open up completely new fields for application [25–28]. Probably the most important advantage has not been mentioned yet. Compared to the rigid structure of crystalline silicon with its inherent electronic structure and given band gap the use of organic molecules allows the tailoring of a perfect semiconductor material for any intended use [29]. This led to the new multi-billion-dollar market for organic light emitting diodes (OLED) which are used in displays for TVs and smartphones today [30, 31]. But efficient tailoring is only possible if there is a certain understanding of the underlying structure/function relationship [32], otherwise, it is more of a trial-and-error approach. To find a rational way to new organic semiconductors that help to improve device performance, knowledge about critical elementary processes is

1. Introduction

necessary. Many of these processes like charge separation or charge injection are related to interfaces [33–39]. And properties of metal/organic interfaces are determined by, e.g., adsorption of molecules on and binding to a substrate, molecular aggregation and composition of self-assembled films [40–44]. Due to the vast amount of possible structure/property relationships, the aim of this work is to deliver reliable contributions to particular topics. By studying the binding strength between adsorbate and substrate, the adsorption geometry, and the electronic structure of a variety of metal/organic interfaces this work helps to establish guidelines for tailored organic semiconductors.

The binding between an organic molecule and a metallic surface, e.g., between an organic semiconductor film and an electrode, influences interfacial properties [33, 34, 44, 45]. Despite long research, there is only little quantitative knowledge about the underlying physical processes [46, 47]. As the study in devices always contains lots of unknowns, the focus in this work is on well-defined systems, consisting of simple aromatic molecules as organic adsorbates and the (111)-surfaces of the coinage metals Au, Ag, and Cu, with their different electronic structures, as substrates. This work investigates the dependency of the binding energy on the size of the aromatic systems as well as on the substrate material. First, benzene is studied on Au, Ag, and Cu with temperature-programmed desorption (TPD) [48], where adsorbate-covered surfaces are heated with a specific heating-rate in front of a mass spectrometer. The (coverage dependent) binding energy is then extracted from the resulting desorption data with analytical methods [49]. The influence of the size of the aromatic system is studied on the Au(111)-surface, where the same technique as above is applied to the acene series from benzene *via* naphthalene, anthracene, and tetracene to pentacene. The resulting TPD-data gives hints on adsorbate-adsorbate and substrate-mediated interactions.

The adsorption and growth of organic semiconductor layers on metal surfaces and the resulting film morphology are further crucial research fields, as parameters like binding strength, charge injection, or charge separation depend strongly on the orientation of the adsorbate molecules relative to the substrate [40, 41, 50–52]. The thin-film properties can vary extremely from the corresponding bulk properties and therefore the prediction of device performance demands a knowledge of the behavior at the interface. This work aims to find structural guidelines to predict film growth behavior from the molecular shape. Therefore vibrational spectroscopy, namely high-resolution electron

energy-loss spectroscopy (HREELS) is applied to a new class of organic semiconductors, namely N-heteropolycycles [53], on Au(111) [54,55]. HREELS has been widely used to study adsorbate-covered surfaces before, e.g. to investigate planar aromatic molecules [56–58], graphene nanoribbons [59], or isomerization processes in molecular switches [60–62]. Here, monochromatized low-energy electrons are accelerated to a sample and analyzed angle- and energy-resolved after scattering [63]. The use of low-energy electrons deserves the surface sensitivity, the measurement of loss-energies gives the vibrational spectrum and the angular dependent measurements lead to conclusions about the orientation of the molecules on the surface. Comprehensive density functional theory (DFT) calculations allow precise vibrational mode assignments. Significant progress in organic chemistry in synthesizing N-heteroaromatic molecules in recent years [64–66] now offers the opportunity to obtain aza-substituted isoelectronic analogues of well-known purely hydrocarbon organic semiconductors. N-Heteropolycyclic aromatic molecules are promising candidates for air-stable and soluble n-type semiconductors [64,67–72]. The aza-substitution itself and further particular variations in the molecular structure by the introduction of sidechains offer the opportunity to study their impact on adsorption and electronic properties. This will help to find general structure/property relations to find ways to tailored organic semiconductors. Therefore several systems with different substituents have been studied. The adsorption behavior of the planar quinoxalinophenanthrophenazine (QPP) [55] is compared with *t*Bu-QPP, an analogue with bulky tert-butyl sidechains. 6,13-Bis(triisopropylsilylethynyl)pentacene (TIPS-Pn) [52,73] is investigated as well as tetraazaperopyrenes (TAPP) derivatives [54]. Substituents cannot only influence the adsorption behavior. At particular positions, there is also a major influence on the electronic structure. Thus, TAPP is investigated not only with bulky groups at the tip-positions of the molecule but also with electron withdrawing halogens at side positions. The performance of organic electronic devices depends critically on the electronic structure of metal/organic interfaces. And interfaces usually demonstrate properties which cannot be explained by the separate components, or a property of one component changes drastically if it is part of an interface.

With HREELS it is also possible to obtain electronic excitation spectra which show, e.g., the optical gap and if it is influenced by the interface. Beside these single-particle excitations, well-ordered interfaces can also exhibit

1. Introduction

collective excitations of electrons (surface plasmons) or the lattice (surface phonons) [74]. Surface plasmons can give new ways to transport or adsorb energy but can also deliver decay channels for former excitations and therefore critically influence device performance [75, 76]. Surface plasmons can be divided into two regimes. A “conventional” surface plasmon of the electrons close to the surface which are strongly influenced by the bulk electron gas and a two-dimensional plasmon of electrons associated to the metal surface state. Due to its acoustic like dispersion in the long-wavelength limit, the latter is named “acoustic” surface plasmon (ASP) [76, 77]. So far this phenomenon has been studied only on single-crystal metal surfaces [76, 78–81] but older data for adsorbate-covered surfaces suggest that it is still present when molecules are attached to the surface [82]. Nevertheless, the influence of adsorbates on the ASP is rather unknown and therefore investigated here with angle-resolved electronic HREELS as this method provides the opportunity to study the dependency of excitation energies on the transferred wave vector component parallel to the surface. The collective behavior is studied at various systems ranging from tetracyanoquinodimethane (TCNQ) and its fluorinated derivatives *via* tetrathiafulvalene (TTF) to the acenes anthracene, tetracene, and pentacene on Au(111). With TCNQ and its di- (F_2 TCNQ) and tetrafluorinated (F_4 TCNQ) derivative the influence of a charge transfer can be studied as the increasing fluorination leads to increased electron affinity and thus to a substrate-to-adsorbate electron transfer in the case of F_4 TCNQ/Au(111) while TCNQ/Au(111) shows none. Earlier studies [82–84] also revealed a connection between electronic and particular vibrational excitations. Such a Fano-like coupling has been described for adsorbate-covered surfaces as an interfacial dynamical charge-transfer but was not connected to plasmonic excitations. Investigating systems that show a broad plasmonic excitation with vibrational HREELS leads to insights into the nature of this coupling.

Outline

As with TPD, HREELS, and DFT, several methods are applied to many different adsorbate/substrate systems in this work, a short explanation of the chosen structure is helpful. After a brief introduction into the used methods and the experimental setup (Chapter 2), the three main result chapters follow. As these three chapters cover rather different topics there is no general

theoretical background given. Instead, each chapter begins with an individual background section to give the information necessary to understand and rank the related results. Chapter 3 first gives background information about the metal/organic interface itself and adsorbate-substrate as well as adsorbate-adsorbate interactions. Then, TPD-studies of benzene on Au(111), Ag(111), and Cu(111) are presented, followed by the investigation of the acene series on the Au(111)-surface from benzene *via* naphthalene, anthracene, and tetracene to pentacene. In Chapter 4 the introductory part presents the class of N-heteropolycyclic organic semiconductors and its possible positions for substitutions. The results about adsorbate geometry and electronic structure follow in the order QPP, *t*Bu-QPP, TIPS-Pn, and TAPP with its derivatives TAPP-H, TAPP-Cl, TAPP-Br, and TAPP-I. Chapter 5 completes the results part with an introduction to surface plasmons and the investigations of TCNQ, F₂TCNQ, F₄TCNQ, [TTF]⁺[TCNQ]⁻, TTF, pentacene, tetracene, and anthracene on Au(111) with angle-resolved electronic HREELS. The related vibrational properties of TCNQ and its fluorinated derivatives follows in the last section.

1. *Introduction*

2. Experimental Methods and Setup

This chapter briefly explains the used experimental techniques followed by a presentation of the ultra-high vacuum system and an introduction to the mainly used gold surface and the preparation process. The order of the explained techniques is loosely oriented at a real experiment which starts with temperature-programmed desorption (TPD) measurements to get information about the dosing parameters, the preparation of a certain coverage and furthermore on important properties like the coverage dependent binding energies. With a well-defined coverage, the different kinds of high-resolution electron energy-loss spectroscopy (HREELS) measurements are performed and the corresponding vibrational modes are then assigned with the help of density functional theory (DFT) calculations. For detailed and comprehensive information the relevant literature is referenced.

2.1. Temperature-Programmed Desorption (TPD)

TPD goes back to the 1960s when adsorbate-covered surfaces were heated and the pressure rise due to desorbing species delivered rudimentary information about surface related phenomena [85]. The technique was named thermal desorption spectroscopy (TDS) and sometimes is today, but as it is no “spectroscopic” method in the literal sense, it is better called temperature-programmed desorption. With the today’s temperature control electronics, the heating of the sample with a specific heating rate and desorbing species can be precisely quantified with quadrupole mass spectrometers (QMS) (detailed descriptions in refs. [86–88]).

2. Experimental Methods and Setup

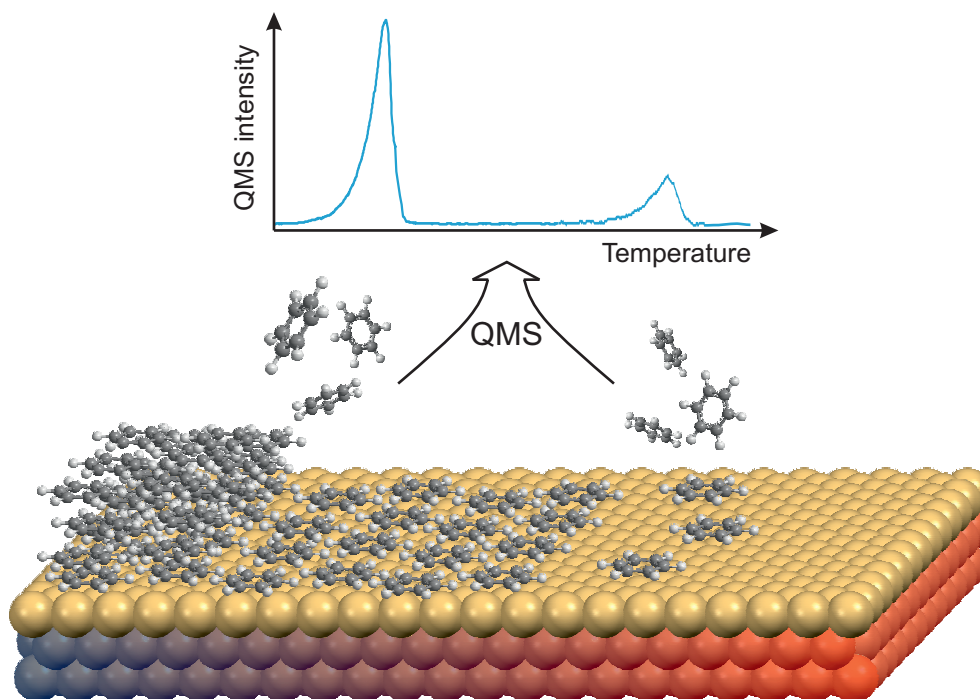


Figure 2.1.: TPD scheme showing on-surface processes and resulting TPD measurement. Bottom: Substrate with increasing temperature and decreasing coverage from left (blue, multilayer) to right (red, pristine surface). Top: Desorbing species measured with a QMS give the intensity *vs.* temperature curve.

Figure 2.1 illustrates the technique from the conditions on the surface (bottom) to the obtained spectrum (top). The metal surface is colour coded from blue (left, cold) to red (right, hot) and symbolizes the heating of the substrate with a constant heating rate. The substrate was previously covered with several layers of adsorbate molecules and as long the attractive intermolecular forces exceed the thermal energy no desorption occurs and therefore the QMS positioned above the surface does not detect any signal (left edge). When thermal energy equals the intermolecular forces all layers above the monolayer desorb one after the other and lead to an intense and sharp peak in the spectrum. Due to the stronger attractive substrate-adsorbate interactions the monolayer sticks to the surface up to often much higher temperatures and desorbs giving a characteristic peak shape depending on the desorption order and the predominate intermolecular interactions. Theoretically, TPD is a spectroscopy of the desorption energy (E_{des}) which is needed to let adsorbed molecules desorb. If an activation barrier has to be overcome during this process, this barrier would be measured. But for many cases, it is allowed to put

2.1. Temperature-Programmed Desorption (TPD)

the measured energy on a level with the binding energy E_B which is released when a molecule sticks to the surface. Following a simple kinetic ansatz with the coverage θ as

$$\theta = \frac{N_{ads}}{N} \quad (2.1)$$

where N_{ads} and N are the number of occupied and all adsorption sites, respectively, the rate of desorption r_{des} in monolayers per second is given by

$$r_{des} = -\frac{\delta\theta}{\delta t} = k_{des}\theta^n \quad (2.2)$$

with rate constant k_{des} and desorption order n . The rate constant can be expressed by an Arrhenius term and equation 2.2 becomes the so-called Polanyi-Wigner equation with prefactor ν_0 and surface temperature T_S :

$$r_{des} = \nu_0\theta^n \exp\left(-\frac{E_{des}}{k_B T_S}\right). \quad (2.3)$$

With today's control electronics, a precise heating rate $\beta = \delta T_S / \delta t$ is experimentally feasible and eq. 2.3 can be rewritten as

$$-\frac{\delta\theta}{\delta T_S} = \frac{\nu_0}{\beta}\theta^n \exp\left(-\frac{E_{des}}{k_B T_S}\right). \quad (2.4)$$

Written logarithmically eq. 2.4 has the form of an Arrhenius term and E_{des} , n , and ν_0 can be obtained from slope and intercept of the $\ln\delta\theta/\delta T_S$ vs. $1/T_S$ graph.

$$\ln\frac{\delta\theta}{\delta T_S} = \ln\frac{\nu_0}{\beta} + n \ln\theta - \frac{E_{des}}{k_B T_S}. \quad (2.5)$$

Figure 2.2 (a) - (c) show TPD curves with given ν_0 (10^{13} s^{-1}), E_{des} (2.0 eV), and colour coded coverages from 0.1 to 1.0 ML for $n = 0, 1, 2$, respectively. Zero-order desorption means that the desorption rate is independent of the coverage. This is the case for multilayer desorption as underneath any desorbed molecule another one from the next layer appears. The peak shifts to higher temperatures with increasing coverage, falls abruptly to zero at T_{max} and the rising edges lay on top of each other.

2. Experimental Methods and Setup

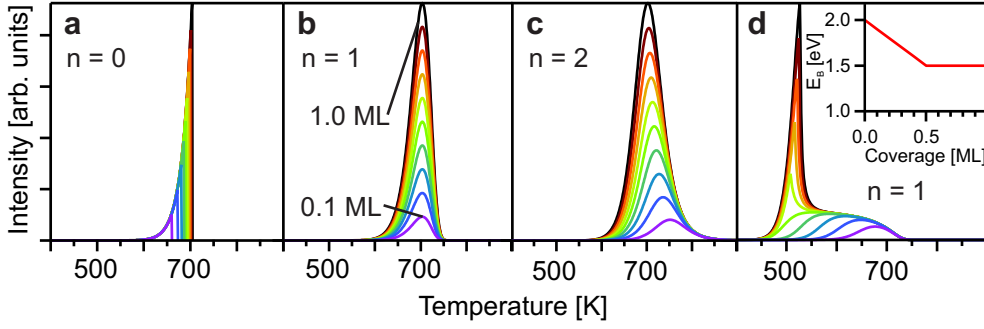


Figure 2.2.: Desorption spectra (obtained by numerically solving eq. 2.3) with coverages from $\theta = 0$ to 1.0 ML in steps of 0.1 ML, constant heating rate $\beta = 1 \text{ K s}^{-1}$ and prefactor $\nu_0 = 10^{-13} \text{ s}^{-1}$ (a)-(d); a constant desorption energy $E_{des} = 2.0 \text{ eV}$ and desorption orders $n = 0$ (a), 1 (b), 2 (c); and in (d) desorption order $n = 1$ and a desorption energy dependence on coverage $E_{des}(\theta)$ as shown in the inset of (d).

Second-order desorption is typical for recombinative desorption such as $\text{H}_{ads} + \text{H}_{ads} \rightarrow \text{H}_{2,gas}$ and shows a peak shift towards lower temperatures for higher initial coverages. The most common desorption kinetics for atomic or non-associative molecular desorption are first-order processes. Without any other interactions the position of the peak maximum in a first-order desorption curve is coverage independent (see Figure 2.2 b), but it has been shown, that coverage dependent lateral interactions can play a major role in desorption processes and let ν_0 and E_{des} , therefore, become coverage dependent as well [89–92]. These interactions can be attractive or repulsive leading to peak shifts to lower or higher temperatures for increasing coverages, respectively. Due to the similarities in lineshape, attractive interactions often lead to so-called pseudo-zero-order desorption and repulsive interactions to pseudo-second-order desorption. Figure 2.2 (d) shows a common case where two “phases” or desorption sites with different properties exist on the surface. The higher binding energy site provides the broad peak at higher temperatures and the lower binding energy site the sharp peak at 500 K. It is $\nu_0 = 10^{-13} \text{ s}^{-1}$, $n = 1$ as in Figure 2.2 (b), but E_{des} is now coverage dependent with a decreasing desorption energy from 2.0 eV to 1.5 eV for a rise in coverage from 0 ML to 0.5 ML, respectively. For coverages higher than 0.5 ML, E_{des} remains constant at 1.5 eV, as shown in the inset. A possible scenario: Repulsive lateral interactions lead to a decrease in binding to the surface with increasing coverage as the mean distance to neighbouring molecules decreases and therefore the repulsive forces increase. For coverages above the exemplarily chosen $\theta = 0.5 \text{ ML}$, the molecules are ad-

2.1. Temperature-Programmed Desorption (TPD)

sorbed on less favourable sites with a coverage independent desorption energy of 1.5 eV. The occurrence of such a second monolayer peak is often described with the existence of a so-called “compressed phase” [93]. In many systems ν_0 and E_{des} vary together with coverage following more or less strictly the so-called *compensation effect* where

$$\ln \nu_0(\theta) = E_{des}(\theta)/RT_i + const. \quad (2.6)$$

with isokinetic temperature T_i [86] and ideal gas constant R . This effect can occur due to experimental inaccuracies as surface inhomogeneities [94] and low signal to noise ratios [95] but can also follow from thermodynamics. For non-activated desorption E_{des} and ν_0 are connected to the standard enthalpy and standard entropy of desorption by

$$E_{des} = \Delta H_{des}^\circ + RT \quad (2.7)$$

and

$$\nu_0 \propto \frac{k_B T}{h} \exp\left(\frac{\Delta S_{des}^\circ}{R}\right), \quad (2.8)$$

respectively. A compensation effect now occurs if H_{des}° and ΔS_{des}° are strongly coverage dependent in a way that the resulting standard Gibb’s energy of desorption

$$\Delta G_{des}^\circ(\theta) = \Delta H_{des}^\circ(\theta) - T\Delta S_{des}^\circ(\theta) \quad (2.9)$$

remains rather independent of coverage. This compensation in the sense that a rise in enthalpy with coverage is balanced by a rise in entropy and a decrease in enthalpy by a decrease in entropy was first observed for reactions in solutions [96] where strong attractive interactions with solvent molecules lower the enthalpy and by frustrating vibrational and rotational degrees of freedom likewise the entropy. Transferred to desorption from surfaces, attractive lateral interactions weaken the binding to the substrate and the decrease of ΔH_{des}° with higher coverages goes along with a decrease of ΔS_{des}° due to restricted diffusion and hindered vibrations [88].

There exist a couple of methods to evaluate TPD data and NIEMANTSVERDRIET [48] performed a competitive test to check what the restrictions of each method are. As shown above, a prediction that desorption energy and pre-factor are coverage independent cannot simply be done for many systems, so

2. Experimental Methods and Setup

that suitable methods have to take this into consideration. There are only two methods providing this for a useful range of coverages, the so-called *leading edge analysis* by HABENSCHADEN and KÜPPERS [97] and the *complete analysis* by KING [49]. The crucial part of getting information about coverage dependence is to do the evaluation process for the individual $E_{des}(\theta_1)$ and $\nu_0(\theta_1)$ data at a somehow constant coverage θ_1 . The first method provides this by evaluating only a small part of the spectrum (the *leading edge*) where the coverage can be considered as a constant within a reasonable error. But it is obvious to lose information by evaluating only a fraction of the measured data or *vice versa* it is absolutely necessary to have high-quality data with a high signal-to-noise ratio to get reliable values from the *leading edge* analysis. The latter method, developed by KING, evaluates the *complete* spectrum and the challenge of the constant coverage is achieved by regarding several spectra with different initial coverages. However, also the *complete analysis* requires good quality data otherwise the coverage dependence of E_{des} and ν_0 cannot be distinguished adequately and a so-called “forced” compensation effect can occur [95].

2.1. Temperature-Programmed Desorption (TPD)

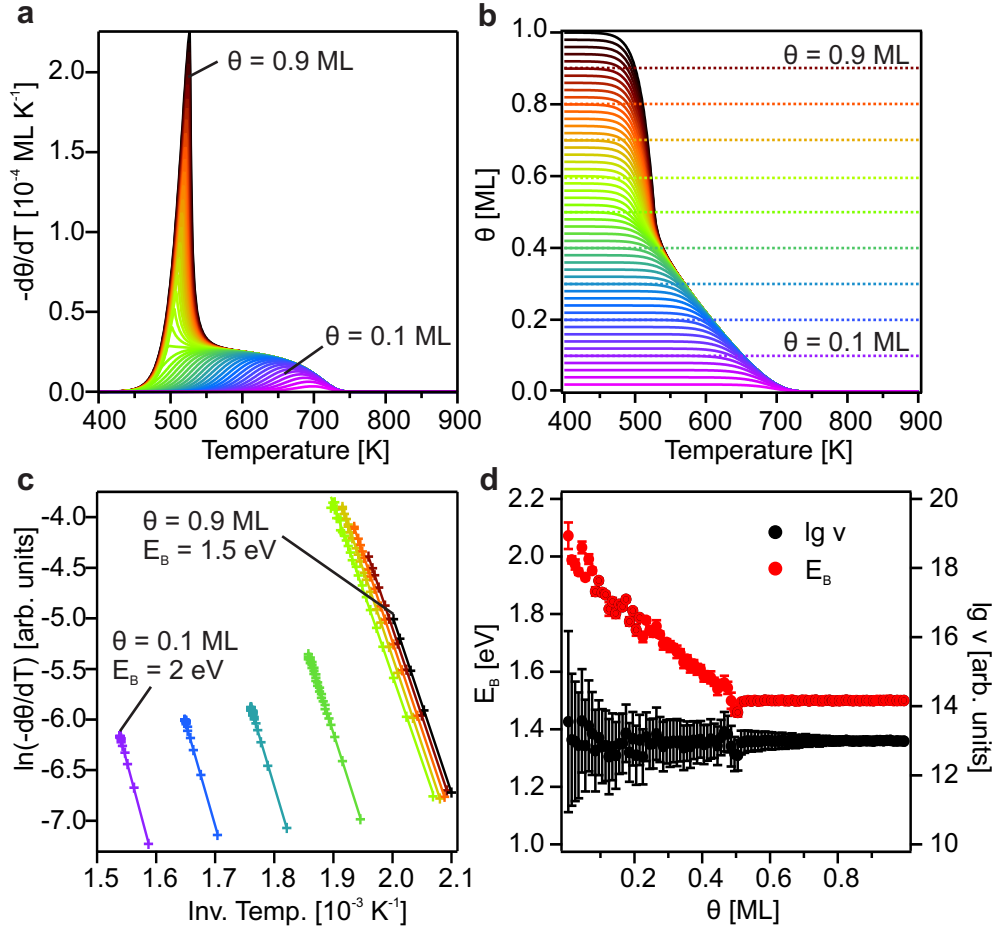


Figure 2.3.: TPD spectra (obtained by numerically solving eq. 2.3) (a) and evaluation scheme (b) - (d) to illustrate the *complete analysis* as in ref. [98]. (a) TPD spectra (as in Fig. 2.2 (d)), (b) corresponding integrated spectra with the residual coverage at any given temperature $\theta(T)$ on the y-axis and intersections for coverages from 0.1 to 0.9 ML (dotted lines), (c) Arrhenius-plots for “constant” coverages from 0.1 to 0.9 ML from the intercept temperatures in (b) and the corresponding QMS-intensities at these temperatures in (a), (d) resulting desorption energies E_{des} (red, left axis) and prefactors ν (black, right axis) depending on coverage.

Figure 2.3 illustrates the particular evaluation steps. The measured series of TPD spectra with different initial coverages (a) needs to be integrated in the way that the y-axis corresponds to the remaining coverage on the surface at the respective temperature (b). Now the intercepts for a chosen coverage (dashed lines, e.g. $\theta_1 = 0.1$ ML) with the integrated TPD curves give the temperatures where the respective TPD spectra possess the remaining cover-

2. Experimental Methods and Setup

age θ_1 and these temperatures now deliver the $\delta\theta/\delta T_S$ values needed for the Arrhenius plots in (c). According to eq. 2.5 the slope provides $E_{des}(\theta_1)$, the intercept with the y-axis $\nu_0(\theta_1)$. Examined for a reasonable number of coverages the coverage dependence of E_{des} and ν_0 can be evaluated as shown in (d). Another important aspect of TPD used in this work is the convenient way to quantify adsorbate coverage by simply integrating a measured spectrum. This approach is described in section 2.4.2.

2.2. High-Resolution Electron Energy-Loss Spectroscopy (HREELS)

TPD leads to information such as coverage and binding energy that tells something about the general lateral adsorbate-adsorbate and vertical adsorbate-substrate interactions. To get more information about the adsorbate morphology, the view is now more focused on the molecular adsorption geometry and electronic structure. Therefore high-resolution electron energy-loss spectroscopy (HREELS) is a versatile tool giving in one experiment information about the orientation of molecules with respect to a planar surface *via* vibrational spectroscopy and about the electronic properties by exciting electronic transitions. There are well-written and detailed descriptions of HREELS in textbooks [99] [63], reviews [74], theses [100], and in previous works using the same experimental setup as used here [101], therefore only a brief introduction and the inevitable information is given here. The surface sensitivity of HREELS comes from the use of low-energy electrons with kinetic energies from 3 to 100 eV which correspond to a penetration depth of a few monolayers independent of the investigated substrate according to the universal curve for the mean free paths of electrons [102]. There are several methods using this surface sensitivity due to slow electrons. Diffraction-based techniques like low-energy electron diffraction (LEED), but also spectroscopic techniques like ultraviolet and X-ray photoemission spectroscopy (UPS, XPS), Auger electron spectroscopy and electron energy-loss spectroscopy (EELS). To receive measurable low-energy electrons from a sample UPS and XPS work with photons, AES with photons or electrons, LEED and EELS with an accelerated and focused electron beam. Whilst LEED evaluates the angular distribution of elastically scattered electrons to get information about the periodicity of the surface, EELS analyzes inelastically scattered electrons, which give hints to

2.2. High-Resolution Electron Energy-Loss Spectroscopy (HREELS)

excitations at the surface. However, the angular distribution is also important in the latter case as it tells something about the dominating scatter mechanism and therefore about the local symmetry at the surface. EELS is connected to a technique with high electron energies and only poor resolutions done not only in reflection but also in transmission. Experimental improvements by IBACH lead to better resolutions of up to 0.5 meV (high-resolution electron energy-loss spectroscopy, HREELS) and therefore allowed to resolve vibrational spectra of adsorbates [103]. Such an Ibach-type spectrometer was used in this work and is shown in Figure 2.4 (a) as a photograph of the dismantled spectrometer and in (b) as a schematic draw.

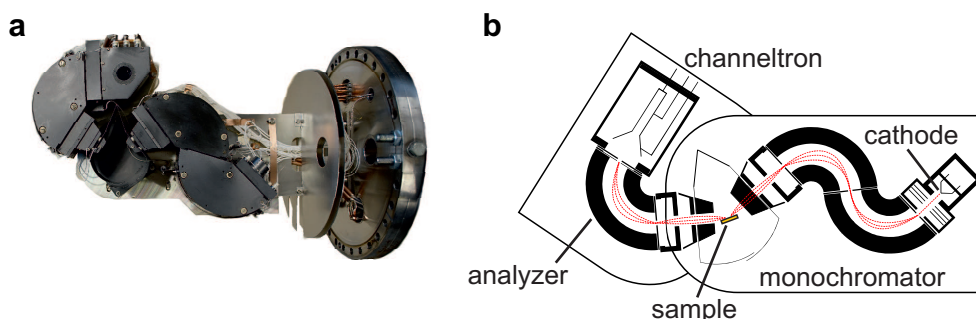


Figure 2.4.: Picture (a) and corresponding schematic draw ((b), adapted from ref. [101]) of the SPECS[®] Delta 0.5 high-resolution electron energy loss spectrometer. For a detailed description of labeled parts, see text.

The low-energy electrons (trajectories, red curves) are emitted from a LaB cathode, monochromatized and accelerated to the desired primary electron energy by a series of lenses. After being scattered on the sample, the electrons are detected energy- (by varying analyzer potentials) and angle-resolved (by analyzer rotation) with a channeltron. HREELS can be divided roughly into two regimes with different dominating excitations which require different primary electron energies, vibrational and electronic HREELS. The transition between the two is smooth but for the first, the chosen electron energy is rarely above 5 eV and for the latter usually 15 eV or more. The main reason for the low primary electron energy in the case of vibrational HREELS is that a good resolution is necessary, and the resolution of the energy dispersive 127°-monochromators and analyzer in the setup is proportional to the corresponding pass energy of the electrons. With this, a resolution of 2 meV can be achieved. A problem of low energies is, to keep the desired current (and therefore intensity) of electrons constant, the number of electrons per volume

2. *Experimental Methods and Setup*

has to increase with reduced electron velocity. This causes space charge effects leading to energy divergence and poorer achievable resolutions. So the flux and measured intensity have to be reduced which makes high scattering cross-sections necessary. That is the reason why the so-called dipole scattering mechanism with its high cross-sections for small electron energies [104] is so important. With higher electron energies of several ten eVs, the resolution decreases to above 10 meV which is not problematic as electronic excitations in this energy region itself have widths of several hundred eVs due to their high energy and corresponding short lifetime. A general expression for the scattering cross section which takes all interactions into account does not exist due to the high complexity of the scattering mechanism [105]. So these interactions are divided into several classes. For vibrational measurements three scattering mechanisms are important, the above-mentioned dipole scattering, impact scattering, and the formation of negative ion resonance. The latter involves short living [106] negative ions by attached electrons which decay under the emission of an electron with a characteristic kinetic energy. These resonances are dependent on the primary electron energy and two primary electron energy-resolved measurements showed no signs for such resonances, thus a more detailed description is omitted. Impact scattering describes the scattering of electrons at local potentials with ranges in the order of atomic scales. The range allows conclusions on the momentum transfer parallel to the surface q_{\parallel} . In the *kinematic theory of electron diffraction* [107] the Fourier transformed scattering potentials at the surface are important parameters of the scattering cross-section. For the Fourier expression of small range potentials large expansion coefficients with large q_{\parallel} values are necessary, hence the scattering cross-section shows a high isotropy.

2.2. High-Resolution Electron Energy-Loss Spectroscopy (HREELS)

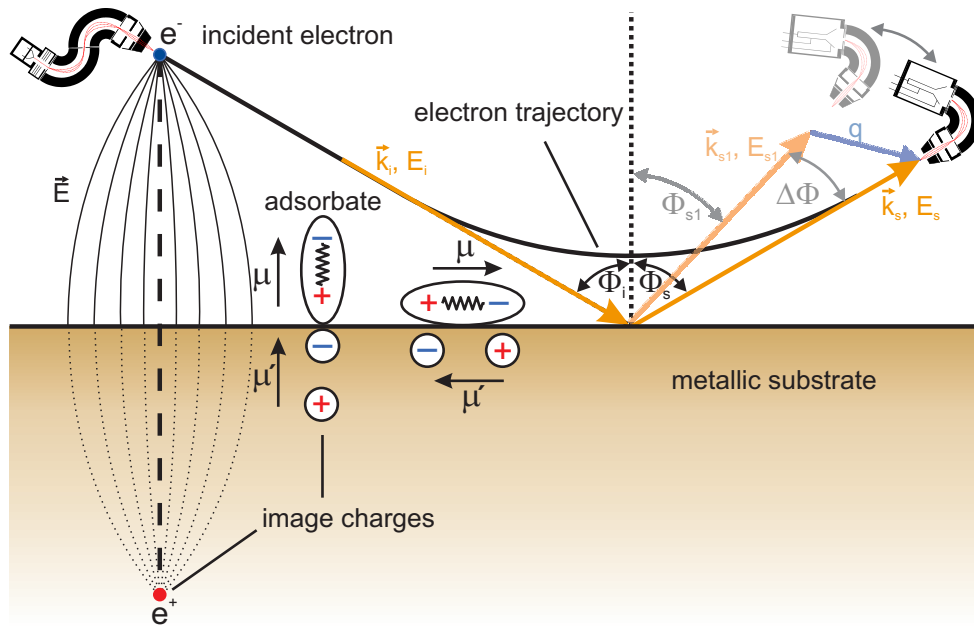


Figure 2.5.: Illustration of dipole scattering and the surface selection rule. The monochromatized electrons e^- (\vec{k}_i, E_i) leave the monochromator (upper left) approach the sample under an angle of incidence Φ_i and are reflected due to long-range Coulomb interactions in specular direction $\Phi_s = \Phi_i$ ($\vec{k}_s, E_s = E_i$ elastic scattering, $E_s \neq E_i$ inelastic scattering). These electrons can be measured energy and angle-resolved (to identify dipole scattered electrons) by the analyzer (upper right). Between the incident electrons and their corresponding image charge e^+ in the metal an electric field \vec{E} is formed (left). This electric field can couple to dynamic dipole moments μ of vibrations in adsorbed molecules (centre). These dipole moments are enhanced due to image charge effects if they have a significant contribution perpendicular to the surface (left, upstanding molecule) and are diminished if they are orientated mainly parallel to the surface (right molecule). This coupling only to vibrations with a dynamic dipole moment normal to the surface is called surface selection rule and leads to a huge increase in the intensity of such modes. Detailed description, see text.

In contrast, dipole scattering is based on the coupling of long-range dipole fields of excitations located at or near the surface with the electric field of the incident electron. Dipole scattering shows characteristically large scattering cross sections within small angles around specular direction ($\Phi_i = \Phi_s$ in Fig. 2.5). Due to these long-range interactions the Fourier expression can be discontinued after small momenta $q_{||}$ so that large transferred momenta are negligible. Figure 2.5 depicts the involved processes. Cathode and monochro-

2. Experimental Methods and Setup

mator are shown in the upper left. As the incident electron e^- , with wave vector \vec{k}_i and kinetic energy E_i , approaches the surface an electric field \vec{E} between the electron and its image charge e^+ in the metal is established. This long-range dipole field can now couple to likewise long-range dipole fields connected to adsorbate vibrations with a dynamic dipole moment μ . The reflected electron (\vec{k}_s, E_s) is detected under an angle Φ_s . Figure 2.5 also shows schematically the surface selection rule for HREELS. Two exemplary vibrations are shown, one with a dynamic dipole moment oriented parallel to the surface, one oriented perpendicular, i.e. parallel to the surface normal in z -direction. These z -parts of dynamic dipole moments are increased due to image dipole effects (μ') whereas the parts parallel to the surface are diminished. Excitation of vibrations with dynamic dipole moments perpendicular to the surface after the dipole scattering mechanism leads to a huge increase in intensity at the corresponding energy loss in the spectrum. In effect, dipole scattered electrons can only be detected under small angles around specular direction and can, therefore, be discriminated from impact scattered ones by measuring under different analyzer angles.

Angular-resolved measurements in the electronic regime offer the opportunity to measure dispersions, according to eq. 2.10.

$$q_{\parallel} = k_{i,\parallel} - k_{s,\parallel} = \frac{1}{\hbar} \left(\sqrt{2m_e E_i} \sin\Phi_i - \sqrt{2m_e (E_i - E_s)} \sin\Phi_s \right) \quad (2.10)$$

Here q_{\parallel} is the parallel component of the difference q of the wave vectors k_i (incident electron) and k_s (scattered electron). m_e is the electron mass, E_i and E_s the kinetic energies of the incident and scattered electron, respectively ($\Delta E = E_i - E_s = \hbar\omega$ is the measured electron energy-loss). Φ_i and Φ_s are the angles of the incident and scattered electron, respectively, with respect to the surface normal. The plot of an energy loss over the transferred parallel momentum is called dispersion curve and gives information about the localisation parallel to the surface of the excited electrons. Within this notation, energy-loss processes with positive $\Delta\Phi$ (electrons scattered towards the surface normal) lead to positive q_{\parallel} values.

2.3. Density Functional Theory (DFT)

The following section gives only a brief introduction to density functional theory (DFT) as detailed descriptions can be found in literature [108]. Today, DFT is a well established versatile tool in chemistry and as such it is used in this work. To receive the described information from the vibrations detected in HREELS measurements it is necessary to know something about the nature of these adsorbate vibrations, i.e. they need to be assigned. This can be roughly done with textbook tables but it is much more constructive to know exactly what the observed vibration looks like and, more important, what the orientation of its dynamic dipole moment is. DFT offers easy access to data like this and as only pure organic (C, N, O, and H atoms) molecules are part of this thesis well established standard functionals and basis sets lead to satisfactory results. However, only gas-phase single molecule data is used as calculations on surfaces are still a challenging problem in theoretical chemistry. A short history of quantum chemistry shall enable to understand and rank the obtained results and to define the scope of DFT in comparison to other theoretical chemical methods. In contrast to force-field methods (“molecular mechanics”) DFT is based on quantum mechanics. But compared to *ab-initio* methods like Hartree-Fock (HF) or configuration interaction (CI) it consumes much less computing capacity for similar accuracy. The most important disadvantages of DFT are the inability to improve results systematically and the complexity of depicting crucial properties like van-der-Waals interactions. DFT is based on the assumption by HOHENBERG and KOHN [109], that the ground-state energy E of a system is explicitly defined by its electron density ρ which itself depends only on the three space coordinates x, y , and z , where the maxima of $E(\rho)$ reflect the positions of the nuclei, the respective height the atomic number and the integral reflects the number of electrons in the system. So $E(\rho) = E(x, y, z)$ depends on three variables independent of the number of electrons N involved. Compared to this, wave function based approaches have the three space coordinates plus a spin coordinate for each electron and therefore need $4N$ variables to describe a given system of N electrons. The problem of DFT is, that there is no established functional for the dependence of E on $\rho(x, y, z)$, there are only approximations. The functional can be separated as

$$E(\rho) = T(\rho) + E_{ne}(\rho) + J(\rho) \quad (2.11)$$

2. Experimental Methods and Setup

with the kinetic energy of the electrons T , the attractive electron-nuclear interaction E_{ne} , and the problematic electron-electron interaction described by a Coulomb-term J . The nuclear-nuclear interactions are assumed to be constant within the Born-Oppenheimer approximation [110]. THOMAS [111] and FERMI [112] and later on BLOCH [113] and DIRAC [114] obtained first results with this “orbital-free” approach but the accuracy of the results was insufficient mainly due to the lack of knowledge of an appropriate functional for the kinetic energy of the electrons. This problem was solved by the reintroduction of orbitals in the form of one-electron Schrödinger equations which increased the number of variables from 3 to $3N$ wherefore the breakthrough of DFT needed the extreme increase in computing capacity over the last decades. The one-electron wavefunctions or Kohn-Sham equations [115] have the form

$$\left(-\frac{1}{2}\nabla^2 + v_{eff}(\vec{r}) - \epsilon_j\right)\varphi_i(\vec{r}) = 0 \quad (2.12)$$

with energy ϵ_j , Kohn-Sham function φ_i , and the effective potential v_{eff} :

$$v_{eff}(\vec{r}) = v(\vec{r}) + \int \frac{n(\vec{r}')}{|\vec{r} - \vec{r}'|} d^3r' + v_{XC}(\vec{r}) \quad (2.13)$$

with the external (electron-nuclear) potential $v(\vec{r})$, electron density n , and the exchange-correlation potential v_{XC} . With this formalism, all difficulties occurring in calculations for many-particle systems are concentrated in this exchange-correlation potential named after its consistency of an exchange term due to interacting electrons and a correlation term due to derivations from 0 and 1 of occupancy parameters in HF. There exist several approaches, functionals, to find the exchange-correlation potential which can be divided into three groups: (a) local density approximation (LDA), where v_{XC} is assumed to be dependent on n which is a good solution for relatively homogenous systems like the conduction band electrons of a metal; (b) generalized gradient approximation (GGA), where v_{XC} is also dependent on the derivative n' ; and (c) hybrid methods with one DFT-derived part of v_{XC} and one HF derived part. The latter is well established for molecules and offer a higher accuracy than simple DFT functionals. The most common hybrid functional which is also used in this thesis is B3LYP [116] with contributions of BECKE [117], LEE, YANG, and PARR [118].

As important as choosing the right functional is the use of the right set of basis functions, called basis set, for the one-electron wavefunctions. Usually, a

2.3. Density Functional Theory (DFT)

linear combination of several Gaussian-type orbitals (GTO) is used to appropriately describe an atomic (Slater-type) orbital. The number of GTOs used to describe an orbital determines the accuracy but also the computational “costs” of a calculation. For core electrons, a high number of GTOs is necessary to get reliable energy values for the molecule as these electrons contribute most of the energy. The minimal basis set is the one with sufficient orbitals to include all electrons. To describe chemical bonds a larger basis set is necessary like one with the doubled (Double Zeta), or tripled (Triple Zeta) number of orbitals. In most cases, not all basis functions are doubled as only the valence electrons take part in chemical bonding. An important set of such so-called split-valence basis sets was established by Pople [119]. Here it is taken into account, that core electrons need a basis function described by many GTOs to obtain the correct energy and valence electrons need more basis functions with different exponents to form new molecular orbitals by a combination. For example, the 6-311G basis set contains 1 basis function described by 6 GTOs for the core electrons and has 3 basis functions described by 3, 1, and 1 GTOs for each valence orbital. This means, a second-row element is described by one 1s-type basis function (6 GTOs), three 2s-type basis functions (3 + 1 + 1 GTOs), nine 2p-type basis functions (3 × 3 + 3 × 1 + 3 × 1 GTOs) or 13 basis functions (26 GTOs) in total. Another common way to improve the accuracy is to add additional polarization and diffuse functions. Polarization functions are higher angular momentum (p, d, f, g) functions to polarize the corresponding lower angular momentum functions and are labelled by a * (5 d-type functions for non-hydrogen atoms) or ** (5 d-type for non-hydrogen, 3 p-type for hydrogen). Diffuse functions are needed for the calculation of anions or excited states when loosely bound electrons are present. They consist of s- and p-functions for non-hydrogen atoms (labeled +) or additional s-functions for hydrogen (++).

All calculations have been performed with the Gaussian09[®] program package [120] and vibrations are visualized with the Facio 19.1.4 [121] program. An exemplary Gaussian09[®] input file and all calculated structures in Cartesian coordinates can be found in Appendix C and J, respectively.

2.4. Experimental Setup

As mentioned above the used setup was not altered significantly wherefore only the basics are introduced and for a more detailed description, previous theses are referenced [101, 122]. Also included in this section is a brief discussion of the used substrates, especially the Au(111) single crystal, and the sample preparation with sputtering, annealing, dosing and coverage determination.

2.4.1. Ultra-high Vacuum System

For the detection of low-energy electrons it is mandatory to work under ultra-high vacuum (UHV) conditions ($\approx 10^{-10}$ mbar), but also for the work with well-defined surfaces, it is of great value to have residual gas pressures as low as possible. Corresponding to

$$F = p/\sqrt{2\pi k_B T} \quad (2.14)$$

with the molecular flux towards the surface F , chamber pressure p , and the mass of the residual gas m [87], a monolayer coverage (under the assumption of a sticking coefficient of 1) is reached after 3 hours (typical HREELS measurement time) at a pressure of 10^{-10} mbar. To achieve such low pressures the chamber is pumped in three stages. A 520 L s^{-1} turbo-molecular pump is backed by a 60 L s^{-1} turbo-molecular pump which itself is backed by a membrane pump to provide pre-vacuum. The UHV system is subdivided into a (upper) preparation chamber (Figure 2.6 (a) top; (b) 13) and a (subjacent) spectrometer chamber (Fig. 2.6 (a) bottom; (b) 14). The latter is individually pumped by an ion getter pump and can be separated from the first with a gate valve and stay under UHV conditions for months without being externally pumped. With this system, base pressures around 10^{-11} mbar are achievable. The preparation chamber is equipped with a sputter gun for surface cleaning, a doser for evaporative adsorbate deposition, a quadrupole mass spectrometer (QMS) for dosing supervision or TPD measurements, and an IR-lamp for small over-night bake-outs if necessary. The doser system was changed from a home-built effusion cell to a commercial one with three quartz crucibles which can be individually heated (and cooled) during this work. The doser can be separated from the preparation chamber with a gate valve and is individually pumped with a turbo-molecular and a membrane pump. Both the doser and the QMS can be shifted in linear position (z-shift) which gives additional flexibility in

2.4. Experimental Setup

adjusting dosing parameters and QMS detection limits. Located below the QMS there is a transfer rod to easily exchange samples without breaking the vacuum. The spectrometer chamber contains the Delta 0.5 HREEL spectrometer and the possibility for illuminating the sample during measurements (not used in this thesis). Figure 2.6 (b) shows an external picture of the setup with sample heater power supply (1), LakeShore-340 temperature control unit (2), pumping control units (3), QMS control unit (4), sputter gun power supply (5), doser power supply and temperature control (6), channeltron power supply (7), HREELS power supply (8), liquid nitrogen cryostat (9), x-y-z- β -manipulator (10), sputter gun (11), QMS (12), dosing system (13), HREEL spectrometer (14), spectrometer angle-control (15), transfer rod (16), and doser cooling unit (17).

2. Experimental Methods and Setup

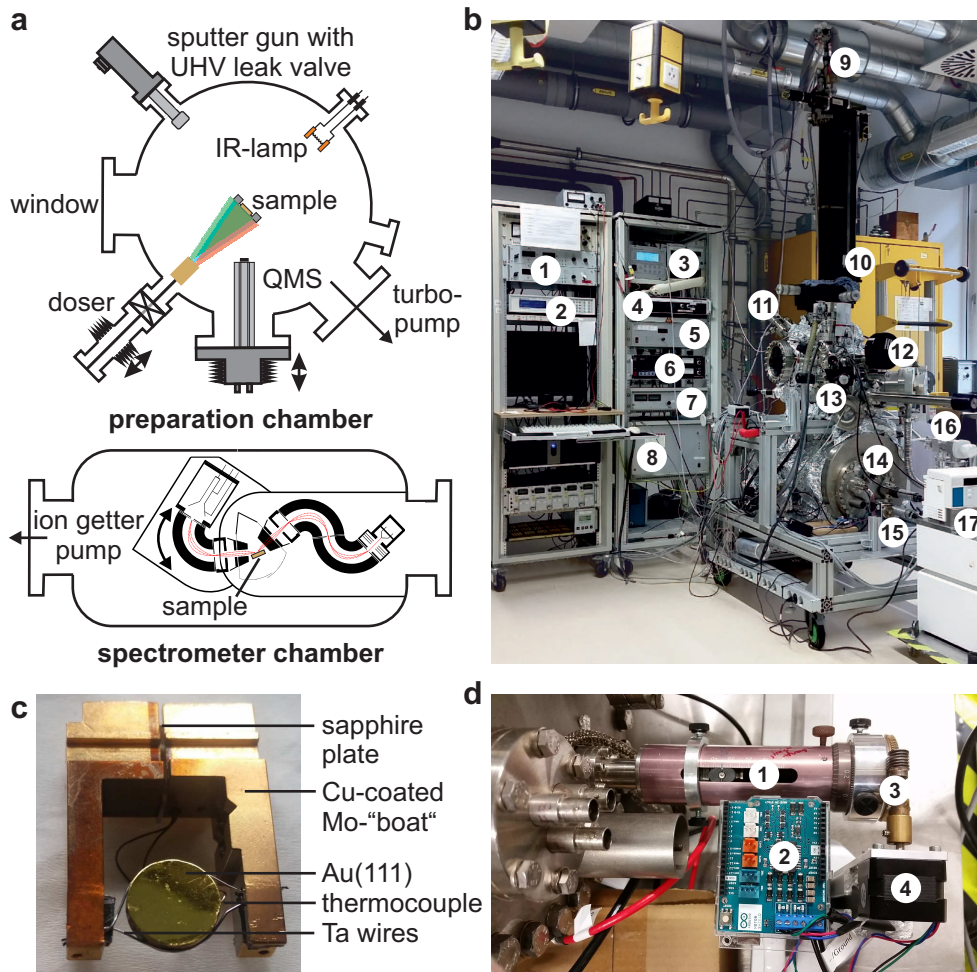


Figure 2.6.: (a) Ultrahigh vacuum system consisting of a preparation chamber (upper scheme) for single-crystal preparation (sputter gun) and adsorbate evaporation (Knudsen cell doser) or characterization (QMS). A transfer rod to exchange samples without breaking the vacuum is located underneath the QMS (not shown). The individually pumped spectrometer chamber is located below the preparation chamber and can be isolated from the latter with a gate valve. It contains the Delta 0.5 HREEL spectrometer. Adapted from ref. [101]. (b) Picture of the experimental setup, numbered parts described in the text. (c) Sample holder. (d) Arduino[®] controlled angle alteration.

Figure 2.6 (c) shows the molybdenum sample holder with an Au(111) sample fixed by two tantalum wires. These wires also feature the possibility to resistively heat the sample. Together with the thermal connection to a liquid nitrogen cooled crystal and a thermocouple connected directly to the sample precise temperature control from 100 to 900 K is possible. An additional setup adjustment is shown in Figure 2.6(d), (1) is the linear shifting to adjust the HREELS' analyzer angle. To provide automatized angle-resolved HREEL measurements a conversion unit (3) was connected to the shifting stage and powered by a stepper motor (4) which is controlled by an Arduino[®] single-board microcontroller (exemplary program code in Appendix I.1). Together with the spectrometer software's ability to automatically measure up to 999 succeeding spectra, it offers the possibility to measure small angle steps. The maximum parameters during this thesis were a 40 h measurement in 61 steps from -6.9° to $+6.9^\circ$ off-specular angle. Related to the Delta 0.5 HREEL spectrometer it needs to be mentioned that in some measurements there occurs a previously reported artefact apparently specific for this type of spectrometer [123]. Its energetic position depends on the settings of distinct lenses in the analyzer part of the spectrometer. See, e.g., Figures 4.7 (a) (at 2000 cm^{-1}) and 4.9 (top, between 1 and 2 eV) in chapter 4 where the artefact appears at different positions due to different primary electron energies.

2.4.2. Au(111) Surface and Sample Preparation

In this section, a short overview of the investigated metal surfaces and their preparation is given. Except for two benzene investigations on Cu(111) and Ag(111) this was an Au(111) sample, wherefore the focus lies on the latter. Figure 2.7 (a) shows a face-centered cubic (fcc) unit cell and the 111 plane (golden spheres). A gold (or copper, or silver) single crystal cut along this 111 plane delivers the used Au(111) surface. Figure 2.7 (b) shows an STM image of the energetically more stable $22 \times \sqrt{3}$ -“herringbone”-reconstruction with alternating hcp (hexagonal closest packing) and fcc areas ((c): schematic draw of the yellow area in (b)). Figure 2.7 (d) shows a calculated top-view of the blue-shaded area in (c) with first-layer Au-atoms (red) and second-layer atoms (yellow). The first layer atoms alter between hcp (between three second-layer atoms) and fcc (between two second-layer atoms) positions.

The Au(111) surface is a suitable substrate as it shows small reactivity towards adsorbates which provides the possibility to study well-defined intact

2. Experimental Methods and Setup

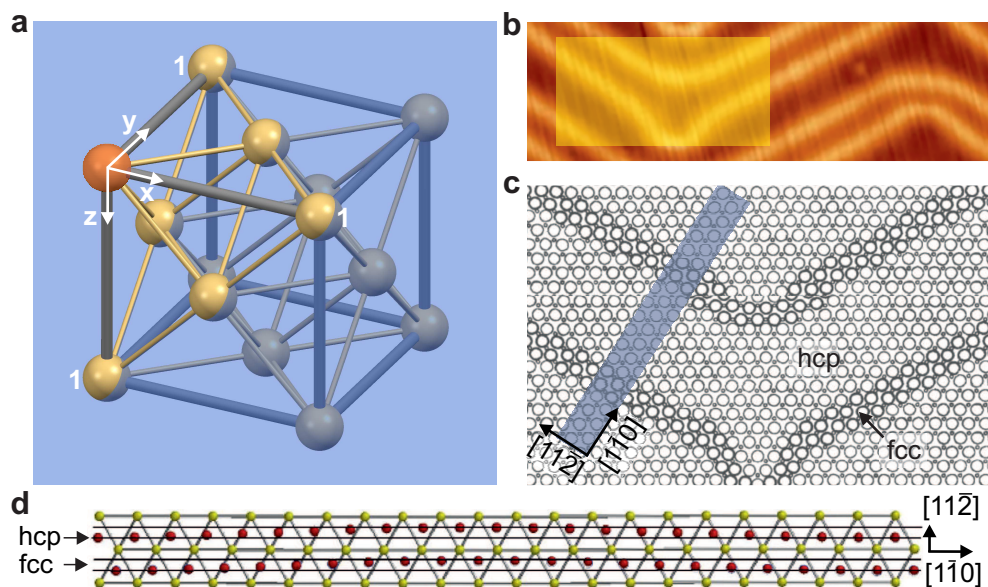


Figure 2.7.: (a) Face-centered cubic (fcc) unit cell, (b) STM image, adapted from ref. [124], (c) herringbone scheme adapted from ref. [125], (d) calculated positions adapted from ref. [126]

molecular layers, furthermore it is stable so that after a cleaning cycle simple heating restores the herringbone reconstruction, and last but not least, gold is a common electrode material in micro electronics and therefore the study of Au/semiconductor interfaces is of great interest. The standard [127] (daily) cleaning procedure (for all three used substrates) consists of 15 min sputtering with 10^{-6} mbar Ar^+ at 1 keV kinetic energy succeeded by 20 min annealing at 750 K. After exchanging the substrate, ten or more of such cycles have to be performed consecutively until the sample shows no more impurities in HREELS. The so cleaned samples are ready to be covered with adsorbate films. For this three different dosing systems were used in this work. The two above mentioned heatable solid evaporators and an additional liquid doser connected to the preparation chamber *via* the same gate valve as the other dosers and consisting of a leak valve with a connected UHV-flask allowing freeze-pump-cycles to degas the liquids.

Figure 2.8 (a) shows the residual gas QMS intensities of suitable m/z during dosing benzene with the liquid doser (black) and F_4TCNQ with the solid doser (red, timescale $\times 0.2$). As can be seen from the curvy red spectrum, the leak valve of the liquid doser allows a better dosing control (straight black spectrum) than the heating of the solid doser does. The sharp rises (and falls)

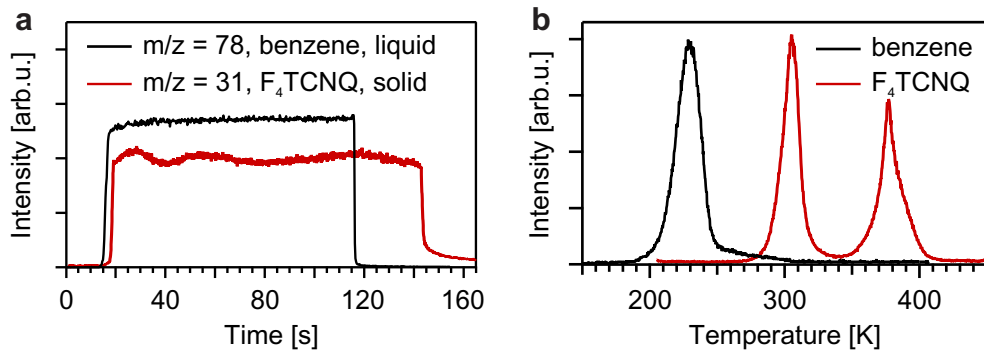


Figure 2.8.: (a) Exemplary background pressure mass spectra measured during dosing of a liquid (benzene, black) and a solid (F_4TCNQ , red, timescale $\times 0.2$). Characteristic masses are observed with the QMS. The sharp rises (and falls) in intensity correspond to opening (closing) the gate valve between the preparation chamber and the doser. (b) Corresponding TPD spectra on Au(111) show a sub-monolayer of benzene (black) and 2.2 ML of F_4TCNQ (red).

correspond to the opening (and closing) of the gate valve between doser and preparation chamber. The QMS monitored dosing offers a good opportunity to obtain a desired coverage. The precise coverage determination follows after other potential measurements (like HREELS) and is pictured for the previous dosings in Figure 2.8 (b). The black and red spectra are the TPD spectra of benzene and F_4TCNQ , respectively, received after the dosings shown in (a). Benzene shows a sub-monolayer coverage whereas for F_4TCNQ a clear multilayer desorption peak is visible. This separated mono- (370 K) and multilayer (310 K) desorption peaks allow on the one hand a precise coverage determination by simply integrating the QMS intensity and normalizing this integral with the monolayer peak area, and on the other precise and reproducible preparation of monolayer samples by heating (and therefore multilayer desorbing) the sample to (in this case) 340 K. However, the monolayer preparation is only possible when the two peaks are fairly separated and the coverage determination requires a non-degradative desorption of the monolayer. As the dosing parameters vary slightly from measurement to measurement general information is difficult. Hence, the dosing parameters for all measured samples in this thesis are summarized in Appendix B.

2. *Experimental Methods and Setup*

3. Binding of Aromatic Molecules on Coinage Metal Surfaces

Due to their small band gaps, aromatic molecules are appropriate candidates as semiconducting materials in organic electronic devices [52]. The behavior of corresponding devices like transistors, OLEDs, or photovoltaic cells often depends strongly on properties of the metal/organic interface as they appear at the boundary between an electrode and the semiconducting material [34]. To get the ability to modify such interfaces in a way that desired properties are achieved demands a deeper quantitative understanding of the molecule/surface system. The work in this chapter is part of a DFT supported multi-technique approach to get this quantitative understanding by comparing several theoretical modelling methods due to their reproduction of precisely experimentally determined characteristics. The most basic class of aromatic molecules are the acenes (see Figure 3.1 (a)). Starting from benzene they are achieved by adding subsequently benzene rings in a linear way: two rings, naphthalene, three rings, anthracene, four rings, tetracene, and five rings, pentacene. Due to the enlargement of the aromatic system, the HOMO-LUMO gap decreases from roughly 6 eV for benzene to 2 eV for pentacene [128] and thus the higher acenes are suitable organic semiconductors [52].

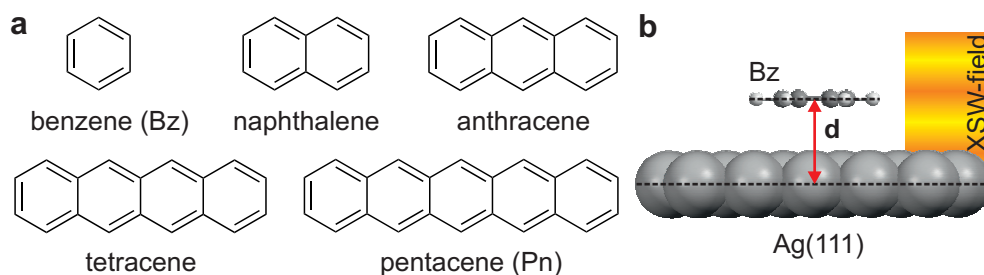


Figure 3.1.: (a) Structural formulas of the investigated acenes. (b) Schematic draw of XSW-measurements to determine the distance d between the first adsorbate layer and the surface.

One essential characteristic of such a metal/organic interface is the distance

3. Binding of Aromatic Molecules on Coinage Metal Surfaces

between the molecular plane of the adsorbed molecules in the monolayer and the uppermost layer of metal atoms. Such distance can be obtained by normal incidence X-ray standing wave (XSW) measurements as it is depicted in Figure 3.1 (b) schematically for the Bz/Ag(111) system. Thereby a standing X-ray wave is produced by the superposition of the incoming with the reflected beam under Bragg-conditions leads to a standing wave in front of the surface [129, 130]. The so created distance dependent X-ray intensity allows precise, element-specific measurements of adsorption heights. Measurements at the Bz/Ag(111) interface revealed with unprecedented accuracy a value of $3.04 \pm 0.02 \text{ \AA}$ [131]. A second important property of the molecule/metal system is the binding energy between the two. Most exact as possible experimental values for these properties allow the development of new and improvement of existing quantum chemical methods which then allow the precise simulation of simple aromatic molecules on metal surfaces [132–135]. As described in section 2.1 such energy values can be obtained from TPD spectra with different initial coverages. In section 3.2 the influence of the underlying metal is investigated by comparing the binding energy of Bz adsorbed on the coinage metal surfaces, namely Au(111), Ag(111), and Cu(111). To study the influence of the size of the aromatic system on this fundamental property, section 3.4 shows the results and their discussion for the acenes on Au(111).

3.1. Background: The Metal/Organic Interface

For a better understanding of the obtained results, it is useful to give a brief introduction into the physical properties of metal/organic interfaces. The focus will lie on vertical adsorbate-substrate and lateral adsorbate-adsorbate interactions. As all parts of this thesis treat metal/organic interfaces it is a useful introduction not only for this chapter.

3.1.1. Adsorbate-Substrate Interactions

Interfaces often show properties, the single components do not [33, 44]. At metal/organic interfaces both the metal states which are located close to the surface (*sp*-, and *d*-bands, surface state) and the frontier orbitals of the adsorbed molecules are affected. As aromatic systems like the ones investigated in this work often have relatively small HOMO-LUMO gaps, the metal/organic junction can be described adequately with well-established metal/semiconductor

3.1. Background: The Metal/Organic Interface

models. Depending on the interactions between metal and semiconductor several scenarios can occur. At such an interface, the Fermi levels, or in the case of molecules the charge neutrality level (CNL), of the two materials must match and therefore states are induced in the semiconductor's band gap. This often goes along with an interfacial charge-transfer as charge flows from the material with the higher Fermi level to the other. The arising space charge region often expands only a few atomic diameters into the metal but several nanometers into the semiconductor, as the free carrier concentration and therefore screening is by orders of magnitude lower in the latter [104]. The charge accumulation is dependent on the distance to the interface. This so-called band bending is shown in Figure 3.2 (a) to (d) for four different exemplary cases. Figure 3.2 (a) depicts the situation at the interface of a low work function (Φ , see Fig. 3.2 (a)) metal and an n-type semiconductor. When the two materials are connected, charge flows from the metal to the semiconductor and forms an accumulation region. Figure 3.2 (b) shows the respective case with a p-type semiconductor. Figure 3.2 (c) and (d) describe the situation for a high work function metal. Here, an electron injection barrier (also Schottky-barrier, Φ_{SB} , Fig. 3.2 (c)) or hole injection barrier (Fig. 3.2 (d)) arise, which hinder an ohmic contact. The energy level alignment can be separated into two model-like regimes. The vacuum level alignment if the work function stays constant during adsorption and the Fermi level alignment where some point of the band gap is pinned to the Fermi level.

3. Binding of Aromatic Molecules on Coinage Metal Surfaces

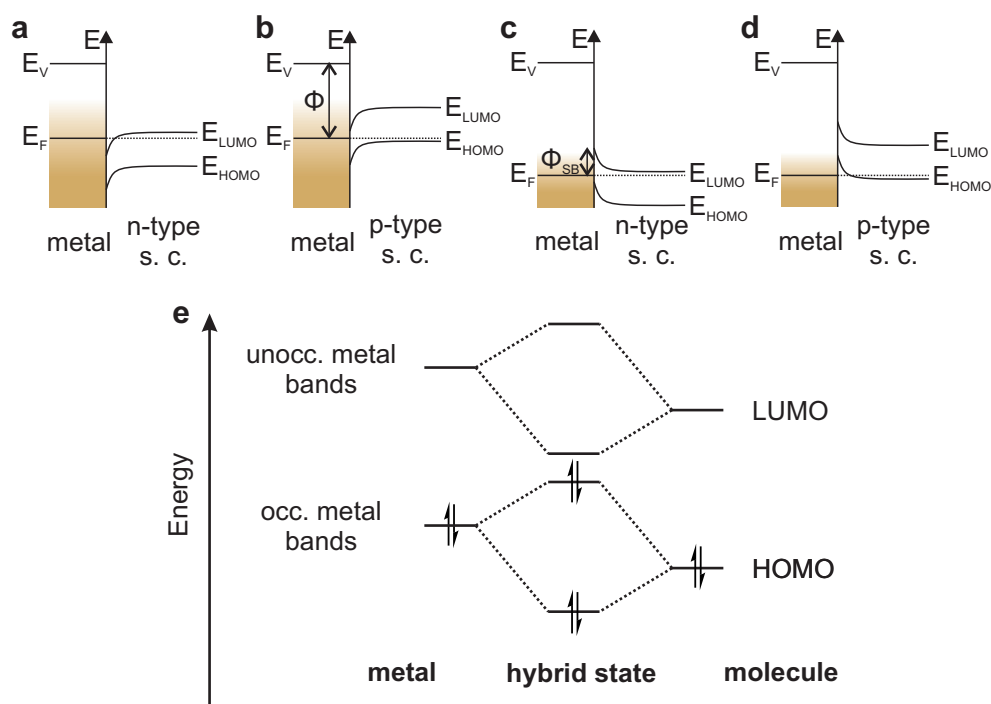


Figure 3.2.: (a) - (d) Schematic band diagrams of metal-semiconductor (s. c.) interfaces with energy E , vacuum energy E_V , Fermi energy E_F , LUMO energy E_{LUMO} (or conduction band), HOMO energy E_{HOMO} (or valence band), Schottky-barrier height Φ_{SB} , and metal work function Φ . (a) and (b) show low work function metals with n- and p-type semiconductors, respectively. (c) and (d) high work function metals with n- and p-type semiconductors, respectively. (a) – (d) adapted from ref. [104]. (e) Simplified picture of the orbitals/bands involved in the hybridization of a metal substrate and an adsorbed molecule.

But it is, of course, a simplification if small organic molecules with localized orbitals are assumed as an infinite system with bands. Figure 3.2 (e) depicts the metal/organic interface from the molecular point of view. Occupied and unoccupied metal bands (left) mix here with the molecule's frontier orbitals (right) to form new hybrid orbitals (centre). In the case of weak interactions these new orbitals would be hard to differ from the single components' ones but for stronger interactions, depending on the localization more at the metal or more at the adsorbate these hybrid orbitals can go along with a (partial) charge transfer and an alteration of properties like the HOMO-LUMO gap [136–138]. Models, where only an integer charge transfer is possible should be handled with care as hybridization is the more flexible model and integer charge transfer is only one limiting case.

3.1.2. Adsorbate-Adsorbate Interactions

In the current chapter, both the influence of the substrate and the influence of intermolecular interactions shall be investigated by comparing Bz adsorption on different coinage metal surfaces and by comparing different acenes on the Au(111) surface, respectively. For the Bz adsorption, the metal/substrate interactions as introduced in the last section are relevant. For the acene study also intermolecular lateral and substrate-mediated interactions are important. The adsorption behavior and especially the adsorbate superstructures depend strongly on the balance between van-der-Waals- (vdW), Pauli-, Coulomb- (dipole-dipole), and the mentioned substrate-mediated interactions [139, 140].

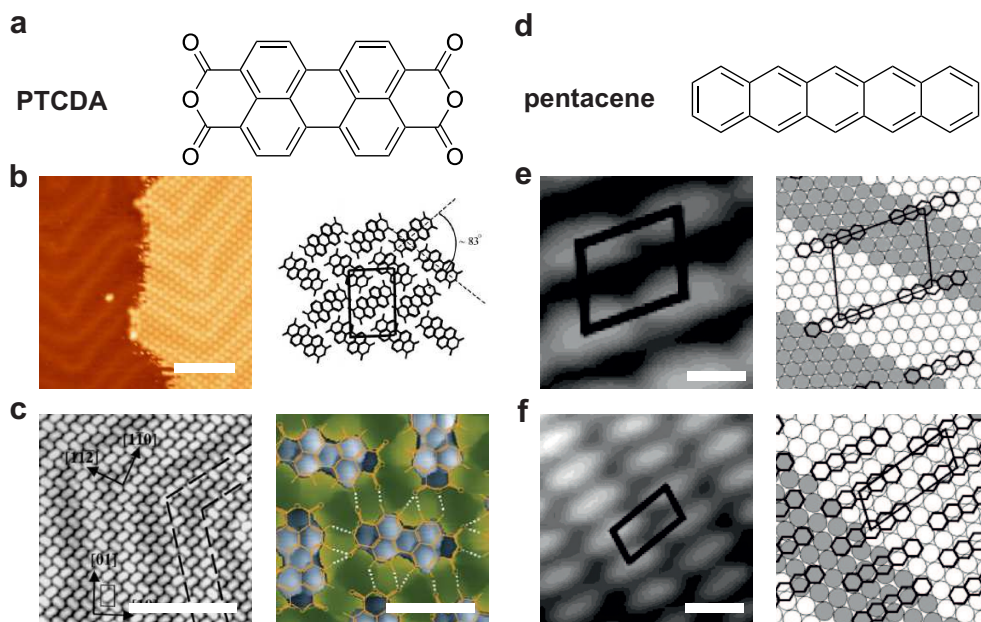


Figure 3.3.: (a) Structural formula of PTCDA. (b) left, STM image of a sub monolayer coverage of PTCDA on Au(111), scale bar 10 nm, adapted from ref. [141]. (b) right, schematic molecular orientation, adapted from ref. [142]. (c) left, monolayer PTCDA on Au(111) STM image, scale bar 10 nm, adapted from ref. [142]. (c) right, STM image visualizing the hydrogen bonds which cause the attractive lateral interactions, scale bar 1 nm, adapted from ref. [143]. (d) Structural formula of pentacene. (e) and (f) left, 0.5 ML and 1 ML pentacene on Au(111) STM images, respectively. Scale bars 1 nm, right, modelled adsorption geometries. (e) and (f) adapted from ref. [144].

Figure 3.3 shows two exemplary cases. On the left, perylenetetracarboxylic dianhydride, PTCDA, (Fig. 3.3 (a)), a well-established organic semiconduc-

3. Binding of Aromatic Molecules on Coinage Metal Surfaces

tor [44, 145]. In the sub-monolayer regime, large islands are formed with a herringbone-like structure (Fig. 3.3 (b)) due to attractive lateral interactions. Figure 3.3 (c) shows the complete monolayer coverage with a close-up of a scanning-tunnelling microscopy (STM) image with an improved resolution due to an H-functionalized tip. Attractive hydrogen-bonds between C-H groups and O atoms are depicted with dashed lines. So here the attractive interactions predominate and lead to a coagulative self-assembly. On the right-hand side, (d) to (f), the corresponding situation for pentacene is shown. And here we see a separation of the individual molecules by several Ångströms in the sub-monolayer (Fig. 3.3 (e)). Actually, there are several phases observable in the sub- to monolayer regime, but they can be divided into two groups with different molecular densities. Figure 3.3 (e) represents the low-density phase with roughly 4×10^{13} molecules cm^{-2} , (f) represents the high-density phase with 1×10^{14} molecules cm^{-2} [144]. Hence, up to a coverage of about 0.4 to 0.5 ML, the molecular self-assembly leads to space between the molecules. The resulting space is filled up with increasing coverage. Thus, for pentacene the overall intermolecular forces are repulsive. A similar behavior is also observed for tetrathiafulvalene (TTF) on Au(111) [146] where it is attributed to a charge-transfer and clear chemisorption. But compared to TTF, pentacene contains no sulfur atoms, which lead to the strong adsorbate-substrate interactions in the TTF/Au(111) system. The reason for the strong repulsive forces in the pentacene/Au(111) system lies in the substrate-mediated interactions. They occur due to the perturbation of surface-related electronic states of the perfectly clean and flat substrate by adsorbates (or step edges and point defects). These substrate-mediated interactions control the superstructure of self-assembled adsorbates as they transmit a lateral adsorbate to adsorbate interaction *via* the substrate. Han *et al.* [140] define two types of substrate-mediated interactions due to different perturbation mechanisms. The first type is based on chemisorption and shows a short interaction range of 1.5 - 3 Å (comparable to chemical bonds) and a strong interaction potential of 0.5 - 10 eV. The second is based on the electron scattering properties of the adsorbate (e.g. for surface state electrons, see scattering pattern in Fig. 3.4 (b)) and is more long-range (up to 10 Å) but weaker (0.001 - 0.1 eV).

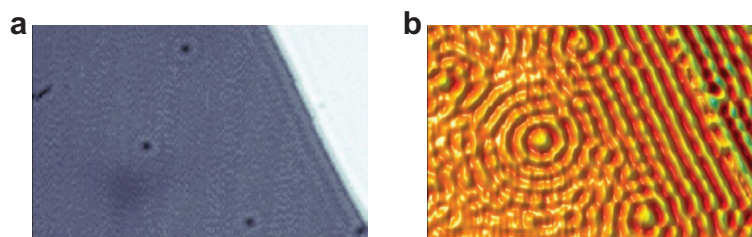


Figure 3.4.: (a) Topographic STM image (460 Å width, $V_S = -200$ mV, $I_t = 500$ pA, 4 K) of atomically flat Cu(111) with a monoatomic step-edge (diagonal line), and single-atom defects (dark spots). (b) dI/dV map of (a) showing standing waves propagating from the step edge and being scattered at defect sites. Adapted from ref. [147].

Figure 3.4 (a) shows a topographic STM image of a clean Cu(111) surface with a step-edge and some point-defects. Fig. 3.4 (b) shows the corresponding dI/dV -map with an increased contrast of the electronic features due to the mapping of electronic states at the bias determined energy level. The periodic structures are interference patterns of the surface state electrons scattered at defect sites. These so-called Friedel oscillations [148] were first observed by Crommie *et al.* on Cu(111) [149] and by Hasegawa *et al.* on Au(111) [150]. The image shows clearly how particular perturbations influence the electronic structure at the surface by electron scattering even for relatively long distances. Going back to the pentacene/Au(111) sub-monolayer films, these electronic substrate-mediated interactions can now serve as an adequate explanation for the observed patterning. In the end, the perturbation of the surface's electronic structure due to these long-range interactions is observed as strong lateral repulsive interactions. To summarize, the self-assembling properties of adsorbates at interfaces rely on a subtle balance between attractive vdW interactions or hydrogen bonds and repulsive Pauli or surface-mediated interactions. The distinct strength of each component determines to a great extent the first adsorbate layer's structure.

3.2. Benzene on Coinage Metals

Although the adsorption properties of benzene (Bz) on the coinage metal surfaces Au(111), Ag(111), and Cu(111) have already been studied extensively [139, 151–156], the experimentally determined values for the binding en-

3. Binding of Aromatic Molecules on Coinage Metal Surfaces

ergy remain surprisingly uncertain and cover a range from 0.43 eV up to 0.84 eV for low coverages. This uncertainty makes them useless for the improvement of the quantitative understanding of such interfaces as it is needed for the further development of quantum chemical methods. The origin of the wide range is due to the uncertainties in the methods used to determine the binding energy. Many groups only use the temperature of the maximum desorption rate at a given coverage and under the assumption of a pre-factor (Redhead method [85]). But as the present coverage and the chosen pre-factor differ from one experiment to the other also the determined values for the binding energy differ. With the use of the complete analysis as explained in detail in section 2.1 the binding energy, as well as the pre-factor, can be determined coverage dependent without any further assumptions. By extrapolating to zero coverage a benchmark for the use in calculations can be obtained [131]. Figure 2.3 in section 2.1 illustrated the complete analysis with calculated data obtained by solving numerically the Polanyi-Wigner equation (eq. 2.3) with arbitrary parameters. Figure 3.5 now uses the same scheme but experimental data obtained for Bz on Au(111). The evaluation and its specific problems are explained for the Bz/Au(111) system in detail whereas for Bz/Ag(111), and Bz/Cu(111) only the results are presented. Figure 3.5 shows TPD spectra of initial Bz coverages from 0.03 monolayers (ML) up to 1.3 ML on the Au(111) surface. The preparation conditions can be found in App. B. Three peaks can be identified labeled as α_1 , α_2 , and α_3 . The peak at the highest temperature (α_3), is assigned to desorption from the monolayer and the highest coverage spectrum not showing the α_2 -shoulder is defined as 1 ML coverage (labelled in Fig. 3.5). It shifts from 235 K at a coverage of 0.03 ML by 45 K to 190 K for a full monolayer coverage. This shift indicates lateral repulsive interactions as described in section 2.1. Peak α_2 arises as a shoulder at the left side of α_3 and is attributed to a compressed phase as reported for other organic molecules on noble metal surfaces [157–159] including Bz on Ag(111) [139]. The integrated coverage of α_2 exceeds not more than 0.1 ML. α_3 represents multilayer desorption showing clear zero-order desorption behavior. This monolayer definition from the TPD spectrum is important and corresponds to the idea of a monolayer as a complete layer of molecules with a direct metal contact where no additional molecules can be adsorbed at positions with equal or higher substrate-adsorbate interaction. This definition is also widely used in TPD- and STM-based publications [139, 153]. Other definitions of a monolayer re-

ferring to the relation of adsorbed molecules to substrate atoms [160] are not useful here. Shall results based on different definitions be compared, a conversion is necessary. From STM measurements [153] a conversion factor for Bz on Au(111) of 1 ML (TPD/STM definition) equals 0.18 ML (Bz molecules per surface atom) can be obtained. For Ag(111) such value should be similar due to the comparable surface atom density, for Cu(111) it should be significantly smaller due to the smaller Cu-radius [161] and hence higher surface atom density.

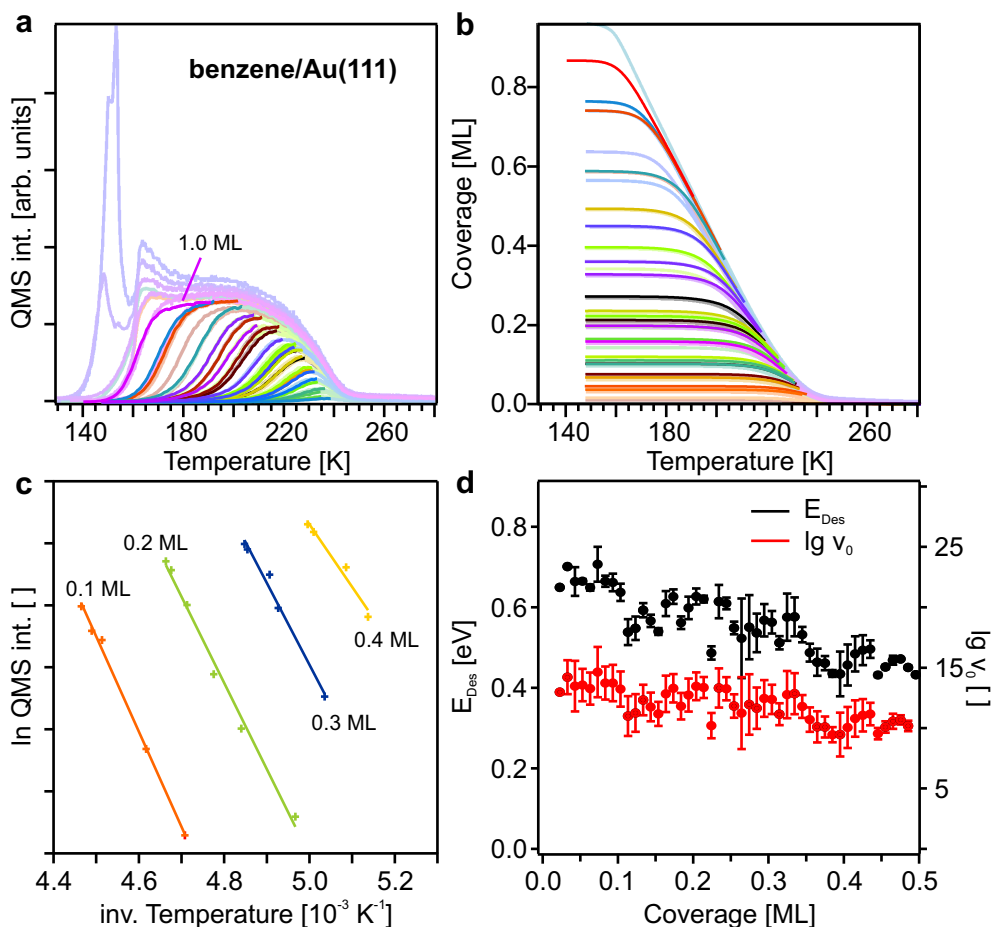


Figure 3.5.: Detailed description of the *complete analysis* evaluation for Bz on Au(111) analogue to Figure 2.3. (a) the measured TPD spectra, (b) the integrated spectra, (c) four exemplary Arrhenius plots, and (c) the resulting E_B and $\lg v$ vs. coverage relation.

According to section 2.1 the TPD spectra need to be integrated in the way that they show the actual coverage on the surface at a given temperature (see Fig. 3.5 (b)). Horizontal lines in this graph stand for a constant chosen cover-

3. Binding of Aromatic Molecules on Coinage Metal Surfaces

age and the intersections with the curves lead to temperature values at which each spectrum in Fig. 3.5 (a) has this coverage. With these T -values Fig. 3.5 (a) delivers the corresponding desorption rates and the resulting value pairs lead to the Arrhenius plots shown in Fig. 3.5 (c). The intercept with the y-axis (infinite temperature) and the slope lead to the coverage dependence of the pre-factor (red) and the desorption energy E_{des} (black) in Fig. 3.5 (d), respectively. Extrapolation to a coverage of $\theta_i = 0$ ML leads to $E_{des}(0 \text{ ML}) = 0.68 \pm 0.03 \text{ eV}$ and $\nu(0 \text{ ML}) = 10^{13.9 \pm 0.3} \text{ s}^{-1}$. The slope of linear fits between 0 and 0.5 ML are $-0.48 \pm 0.04 \text{ eV/ML}$ for the desorption energy (see Fig. 3.6 (b)) and $-8.08 \pm 1.36 \text{ 1/ML}$ for the log of the pre-factor. This coverage dependency of the binding energy is the quantification of the before mentioned peak shifting to lower temperatures with higher initial coverages. It means in a descriptive way that the binding between an adsorbing molecule and the substrate weakens rapidly with an increasing number of already present neighboring molecules, which indicates strong repulsive interactions [162–164]. In literature, there exists one coverage dependent TPD study for the Bz/Au(111) system which delivers comparable data, with the exception, that no compressed phase is observed [165]. However, this data was not evaluated in detail and the desorption energy was only determined with the use of the Redhead equation and a supposed pre-factor of 10^{13} s^{-1} giving a desorption energy of 0.64 eV for a coverage of 0.1 ML. Nevertheless this is in good agreement with the present study ($E_{des}(0.1 \text{ ML}) = 0.63 \pm 0.03 \text{ eV}$ and $\nu(0.1 \text{ ML}) = 10^{13.2 \pm 0.3} \text{ s}^{-1}$).

As it is expected, on the higher temperature side the edges of the monolayer TPD peaks lie on top of each other (see Fig. 3.5 (a)) and so do the integrals of the residual coverage above a given temperature (Fig. 3.5 (b)). This leads to an accumulation of data points on the low $1/T$ -side of the Arrhenius-plots which should be itself not a problem, but due to non-infinite pumping rates and other experimental inaccuracies, a scattering of these accumulated data points leads to huge scattering of the determined binding energies (see ref. [95]). Several experimental and evaluation related arrangements face these problems and reduce their impact. First, a small integration time ($t_I = 200 \text{ ms}$) is used for one data point to improve temperature resolution. Second, a small QMS to sample distance ($d = 10 \text{ mm}$) is used to increase the signal-to-noise ratio. Additionally, the raw data is binned by using a moving average over 10 data points. The fact, that the falling edges lie on top of each other includes that no additional information is given by these additional TPD curves. Therefore only

3.2. Benzene on Coinage Metals

the lowest initial coverage spectrum of such a set of curves is used to reduce the influence of the increased background pressure in the spectra of higher initial coverages. To apply this reproducibly, only the TPD data from the initial coverage (low temperature) to the desorption maximum is used (marked as solid, non-shaded lines in Fig. 3.5 (a)). A compensation effect as described in section 2.1 seems not to affect the obtained results largely as the total E_{des}/θ dependence varies significantly from the corresponding ν/θ dependence (see Fig. 3.5 (d) for Au(111) and Fig. 3.6 (d) together with Fig. E.1 in App. E for Ag(111)).

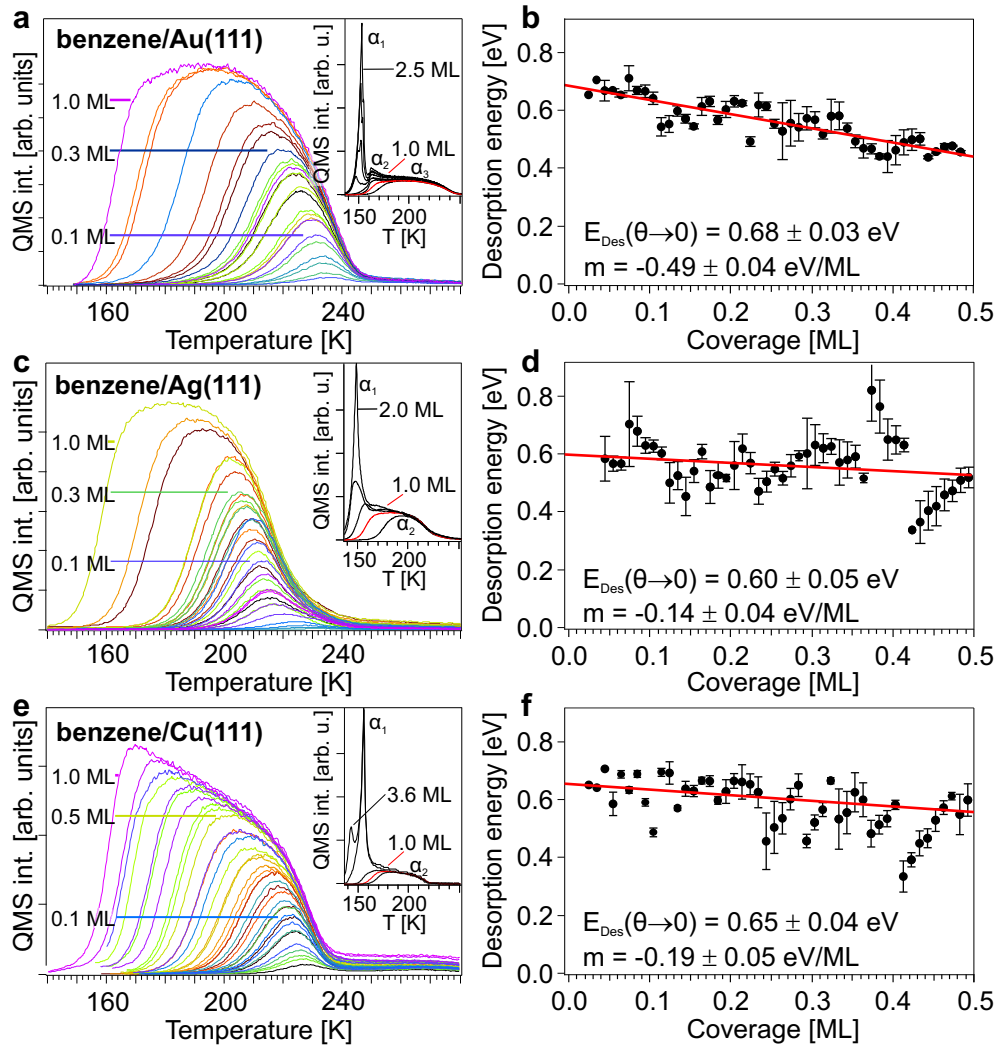


Figure 3.6.: (a), (c), (e) Measured (sub-)monolayer and multilayer (insets) TPD spectra for Bz on Au(111), Ag(111), and Cu(111), respectively. (b), (d), and (f) show the corresponding E_B vs. coverage plots with linear fits (red) between 0.0 and 0.5 ML coverage.

3. Binding of Aromatic Molecules on Coinage Metal Surfaces

Figure 3.6 is an overview of the measured TPD spectra ((a), (c), (e)) and the corresponding desorption energies ((b), (d), (f)) for Bz on Au(111), Ag(111), and Cu(111), respectively. The results for Bz on Au(111), (a) and (b), have been discussed above. (d) and (e) show the results for Bz on Ag(111). As can be seen from the inset of Fig. 3.6 (c) the compressed phase α_2 is less separated compared to the Bz /Au(111) system. The corresponding peak merges with the multilayer peak (α_3) in a way that α_1 and α_2 seem to be one single phase with a zero-order shape (steep fall) but contradictory shifting to lower temperatures with higher initial coverages. Rockey *et al.* already analyzed this behavior and assigned it to a compressed phase [139]. The overall shapes of the sub-monolayer TPD spectra (see Fig. 3.6 (c)) are comparable to the Bz/Au(111) system, however, the falling edge on the high-temperature side is shifted by 15 K to lower temperatures thus indicating a slightly lower binding energy. The complete analysis (Fig. 3.6 (d)) leads to a desorption energy in the single molecule limit of $E_{des}(0 \text{ ML}) = 0.60 \pm 0.05 \text{ eV}$ with a coverage dependency between 0 and 0.5 ML of $-0.14 \pm 0.04 \text{ eV/ML}$. The extrapolated pre-factor for zero coverage and the corresponding coverage dependency of the logarithm are $\nu(0 \text{ ML}) = 10^{12.7 \pm 0.8} \text{ s}^{-1}$ and $-0.17 \pm 2.58 \text{ 1/ML}$, respectively (see App. E). The most significant difference between the gold and silver measurements is the coverage dependency which is 70% smaller compared to Au(111), thus indicating weaker intermolecular interactions. A Redhead derived literature value is 0.57 eV at a coverage of 0.1 ML using a pre-factor of 10^{13} s^{-1} [156]. For 0.1 ML the complete analysis of the spectra in Fig. 3.6 (c) delivers $E_{des}(0.1 \text{ ML}) = 0.59 \pm 0.05 \text{ eV}$ and $\nu(0.1 \text{ ML}) = 10^{12.7 \pm 0.8} \text{ s}^{-1}$. It needs to be mentioned, that desorption from defects (tail above 240 K in Fig. 3.6 (c)) is increased compared to the gold surface, which made data evaluation even more challenging.

For Cu(111) the compressed phase seems completely vanished (inset of Fig. 3.6 (e)) and the overall shape differs slightly, with increasing peak maxima for higher initial coverages and simultaneous shifting to lower temperatures. This causes the occurrence of two falling edges, a steep one up to 0.5 ML and an additional flat one for higher coverages up to 1 ML (see Fig. 3.6 (e)). Evaluation analogous to the before mentioned systems (Fig. 3.6 (f)) leads to $E_{des}(0 \text{ ML}) = 0.65 \pm 0.04 \text{ eV}$, with a slope of the linear fit between 0 and 0.5 ML of $-0.19 \pm 0.05 \text{ eV/ML}$ and $\nu(0 \text{ ML}) = 10^{13.8 \pm 0.5} \text{ s}^{-1}$ with the corresponding slope $-3.06 \pm 2.15 \text{ 1/ML}$. (see App. E). Thus the interaction strength measured

3.3. Discussion: Equal Stability on Different Metals

as coverage dependency of the desorption energy is comparable to Ag(111). TPD data from literature gives a binding energy of 0.59 eV at 0.1 ML coverage [154,166]. For 0.1 ML $E_{des}(0.1 \text{ ML}) = 0.59 \pm 0.05 \text{ eV}$ and $\nu(0.1 \text{ ML}) = 10^{12.7 \pm 0.8} \text{ s}^{-1}$ can be obtained from the linear fit. The desorption from defect sites (between 240 and 280 K in the TPD spectra in Fig. 3.6 (e)) is even more pronounced on Cu(111) compared to Ag(111) and is visible as a higher baseline on the high-temperature side compared to the low-temperature side in Fig. 3.6 (e). Additional HREEL measurements concerning the adsorption geometry of Bz on Cu(111) are shown and discussed in App. D. It has to be noted that all cited values for E_{des} have been reevaluated by Silbaugh *et al.* [160] with pre-factors obtained from calculations. These pre-factors deviate from the ones obtained via the complete analysis by one or two orders of magnitude.

3.3. Discussion: Equal Stability on Different Metals

The surprising finding of our study is, that despite the different electronic structure and general chemical “reactivity” of the investigated coinage metal surfaces, the difference in desorption energy is rather small and within the error bars equal.

Table 3.1.: Desorption energies of benzene on Au(111), Ag(111), and Cu(111). Linear fit parameters corresponding to the data in Figure 3.6.

E_{des}	slope [eV/ML]	intercept [eV]
Au(111)	-0.49 ± 0.04	0.68 ± 0.03
Ag(111)	-0.14 ± 0.04	0.60 ± 0.05
Cu(111)	-0.19 ± 0.05	0.65 ± 0.04

Table 3.1 and 3.2 summarize the linear fit parameters for the coverage dependent E_{des} and $\lg \nu$, respectively, obtained from the complete analysis. This suggests a universal trend for the binding energy of aromatic molecules. With increasing coverage, the desorption energy decreases for all investigated systems which indicates repulsive lateral interactions. The pre-factors’ behaviors show similarities but they decrease less strongly than the desorption energy with increasing coverage.

3. Binding of Aromatic Molecules on Coinage Metal Surfaces

Table 3.2.: Obtained coverage dependent prefactors for benzene on Au(111), Ag(111), and Cu(111). Linear fit parameters corresponding to the data in Figure 3.5 and Figure E.1 in App. E.

	$\lg \nu$	slope [1/ML]	intercept
Au(111)	-8.08 ± 1.36	13.95 ± 0.34	
Ag(111)	-0.17 ± 2.58	12.73 ± 0.78	
Cu(111)	-3.06 ± 2.15	13.76 ± 0.53	

Together with XSW results from Willenbockel *et al.*, the obtained TPD results served Tkachenkov *et al.* [131] as experimental benchmarks for a comparison of the best available theoretical methods to calculate adsorbate covered metal surfaces with special attention to binding distance and binding energy. Despite huge progress of DFT based quantum chemical methods, surface-related calculations still face several problems. On the one hand, there is the self-interaction error of the exchange energy leading to wrong energy levels and electrostatics, on the other hand, there is the missing possibility to adequately reflect long-range vdW-interactions. To face these problems, different exchange-correlation functionals (see section 2.3; Heyd-Scuseria-Ernzerhof (HSE) [167, 168] and Perdew-Burke-Ernzerhof (PBE) [169]) were combined with methods to simulate long-range interactions (vdW^{surf} [135] and many-body dispersion (MBD) [170, 171]) and the results of the different combinations were compared with the experimentally obtained values. The combination of HSE and MBD correctly predicts the desorption energies and the binding distances [131]. Our results together with the corresponding calculations suggest that this universal binding energy trend for aromatic molecules on coinage metal surfaces results from the subtle balance between vdW attraction and Pauli repulsion.

3.4. Acenes on Au(111)

The former section showed that the binding energy of aromatic molecules on coinage metal surfaces is rather independent on the kind of metal which is used and that the adsorption properties rely mainly on intermolecular or substrate-mediated interactions. This chapter now focuses on the influence of the extent of the aromatic system on the binding properties, which is obligate to know for the aim of finding rational routes to tailor organic semiconductors. The easiest way to “increase” the size of an aromatic system starting from benzene is to add additional phenyl rings to it and thus getting the acenes from benzene to pentacene (see Fig. 3.1).

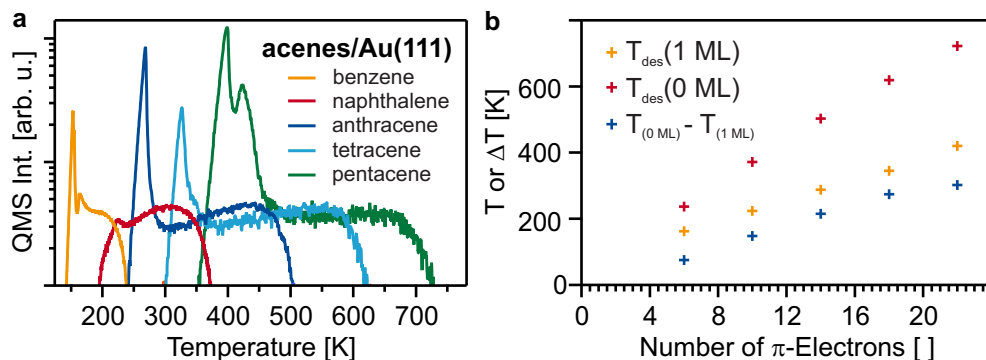


Figure 3.7.: (a) Acene TPD spectra (log-scaled intensity). (b) Desorption temperature ($T_{des}(1 \text{ ML})$ of a respective acene molecule at a coverage of 1 ML (yellow crosses; left edge of the TPD spectra in (a))-temperature), desorption temperature ($T_{des}(0 \text{ ML})$ of a respective acene molecule at a coverage of 0 ML (red crosses; right edge of the TPD spectra in (a)), and temperature range of the respective 1 ML TPD spectra (blue crosses) *vs.* the number of π -electrons in the corresponding acene.

Figure 3.7 (a) shows TPD spectra (coverage $> 1 \text{ ML}$, preparation conditions in App. B) for all acenes on Au(111). The “position” of the desorption peaks shifts to higher temperatures for larger systems. This is somehow expected, as the strength of an interaction depends on the number of interaction partners. In the case of Bz, 6 H-atoms and 6 C-atoms interact with $\approx 5 \text{ Au}$ -atoms whereas pentacene has 14 H-atoms and 22 C-atoms interacting with $\approx 13 \text{ Au}$ -atoms. But another obvious feature is, that the broad monolayer peak already observed for Bz is increasing its width rapidly with increasing the size of the aromatic system. Figure 3.7 (b) shows in red the temperatures corresponding to the beginning of monolayer desorption, in orange the end of monolayer

3. Binding of Aromatic Molecules on Coinage Metal Surfaces

desorption, and in blue the respective temperature ranges depending on the number of π -electrons of the investigated system. For Bz, the width of the desorption peak has been correlated to intermolecular interaction strength, adopting this, the interaction strength increases strongly with the size of the aromatic system. In a combined TPD and STM study [144] of pentacene on Au(111), this long tail was not identified as part of the monolayer due to the weak QMS signal caused by being stretched over a large temperature range. A further study of all acenes on Au(111) identified it but did not analyze it quantitatively [172]. The TPD spectra in Figure 3.7 (a) have roughly the same initial coverage, except a slightly lower one for naphthalene (red). As can be seen, only Bz (orange) and pentacene (green) show a compressed phase. While in the case of Bz this phase corresponds to roughly 0.1 ML, it is 0.5 ML in the case of pentacene on Au(111). In the following analysis, the length of the tail is correlated with the strength of intermolecular interactions. Another covered aspect is the nature of the compressed phase in the case of pentacene.

Figure 3.7 (b) shows, that the length of the low coverage tail increases with the size of the aromatic system. For Bz, it ranges over 80 K for pentacene over 320 K. But a closer look at the ΔT values (blue crosses) shows, that the dependency of the size of the system is not linear, it flattens for larger molecules. The increase in the temperature range from Bz to naphthalene is 65 K, the one from tetracene to pentacene 45 K. It has to be noted that the number of H-atoms is neglected here, although they also deliver a contribution to the binding to the substrate. With the complete analysis, there is a tool to quantify such qualitative statements. The before mentioned difficulties concerning the complete analysis and repulsive interactions are even more compromising here. The m/z -restriction of the used QMS (max. 200 m/z) prohibits the detection of the M^+ ion of pentacene (278 amu) and tetracene (228 amu) thus leading to low signal-to-noise ratios, especially in the area of the long tail. A complete series of 30 or more TPD spectra with different initial coverages, as it is needed to use the complete analysis, has only been performed for tetracene and pentacene, which should be sufficient to get a first quantification of the trend of the dependency of the binding energy on the system size. But for manifestation, it is appropriate to measure TPD series also for naphthalene and anthracene.

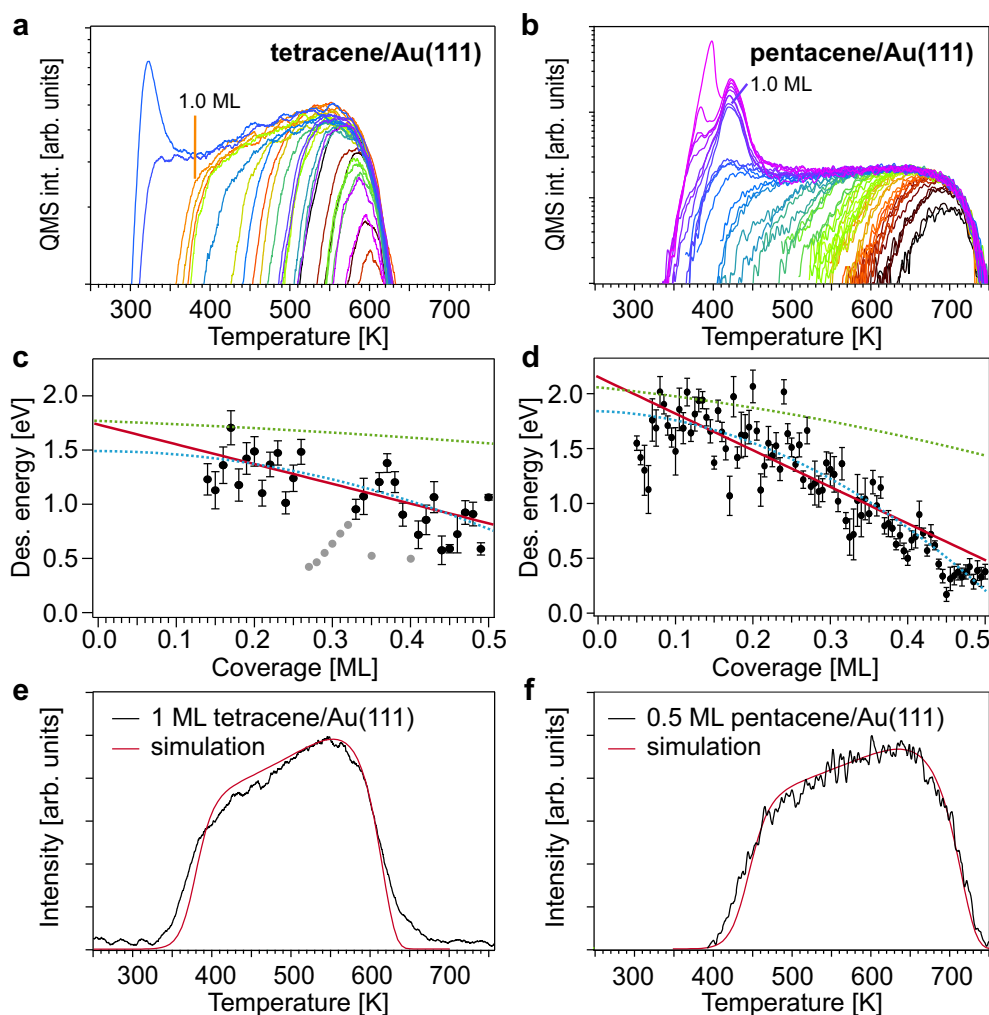


Figure 3.8.: (a), (c), and (e) refer to tetracene, (b), (d), and (f) to pentacene. (a) and (b) show series of (sub-)monolayer TPD spectra (log scaled intensity). (c) and (d) show the resulting dependencies of the desorption energy on the coverage with linear and second-order polynomial fits to the data between 0 and 0.5 ML (red solid and blue dashed lines, respectively). The green dashed line refers to the parameters used for the simulated TPD curves (red solid) in (e) and (f). Details, see text.

Figure 3.8 (a) and (b) show the measured TPD spectra for tetracene/Au(111) and pentacene/Au(111), respectively. The logarithmic intensity axis allows displaying the multilayer/compressed phase and the high-temperature tail in one graph. For tetracene, no additional compressed phase can be observed whereas for pentacene a clear separated peak evolves before the infinite rise of the multilayer peak with increasing coverage. This separated peak has exactly the same integrated area as the low coverage tail within the scope of measuring

3. Binding of Aromatic Molecules on Coinage Metal Surfaces

accuracy. Theoretically, this peak could also be assigned to desorption from the second layer, but there is no explanation why second-layer desorption should lead to a separated peak for pentacene but not for tetracene. Figure 3.8 (c) and (d) show the resulting E_{des} vs. coverage plots for tetracene and pentacene, respectively. The database for pentacene is much better whereas fit models were established here and transferred to tetracene afterwards. The TPD measurements of the tetracene/Au(111) system were problematic in a way that artefacts like additional shoulders or varying intensity levels occurred. In Figure 3.8 (c), the grey dots are ignored as they can be identified as artefacts from the Arrhenius plot evaluation. The solid red lines are linear fits to the shown data between 0 and 0.5 ML coverage analogue to the linear fits, applied to the Bz systems. For tetracene a desorption energy in the single molecule limit of $E_{des}(0 \text{ ML}) = 1.68 \pm 0.11 \text{ eV}$ with a coverage dependency of $-1.79 \pm 0.32 \text{ eV/ML}$. For pentacene, linear fitting gives $E_{des}(0 \text{ ML}) = 2.14 \pm 0.06 \text{ eV}$ with a coverage dependency of $-3.50 \pm 0.20 \text{ eV/ML}$. Especially in the case of pentacene, a clear non-linear behavior is visible. This might be explained with the long intermolecular distances in the low-coverage limit [144] where an additional molecule should not have such a large effect on the desorption energy as for higher coverages when the distances are reduced. A more suitable pure quadratic fit ($y = ax^2 + c$, blue dotted lines) gives $E_{des}(0 \text{ ML}) = 1.4 \pm 0.2 \text{ eV}$ (scale factor -2.8 ± 0.5) in the case of tetracene, and $E_{des}(0 \text{ ML}) = 1.78 \pm 0.05 \text{ eV}$ (scale factor -6.45 ± 0.31) in the case of pentacene. The green dotted lines represent a fitting model based on the manual modification of the desorption energy's dependence on coverage in TPD simulations to most perfectly reproduce a measured monolayer (tetracene) and half-monolayer (pentacene) TPD (see Fig. 3.3 (e) and (f)). The coverage dependence behind the simulated TPD (red lines) is a second grade polynomial like $y = ax^2 + bx + c$ with $a = -0.27$, $b = -0.27$, and $c = 1.7 \text{ eV}$ for tetracene and $a = -1.1$, $b = -0.7$, and $c = 2 \text{ eV}$. Note that c represents the desorption energy in the zero-coverage limit. The pre-factor was coverage independent and held constant at 10^{13} s^{-1} for the simulations. However, such simulations do not yet have a quantitative meaning. But with the establishment of a procedure which is able to fit the coverage dependence of the desorption energy and the pre-factor a huge step forward to easy and reliable TPD evaluation can be made.

3.5. Discussion: Binding Energy and the Size of the Aromatic System

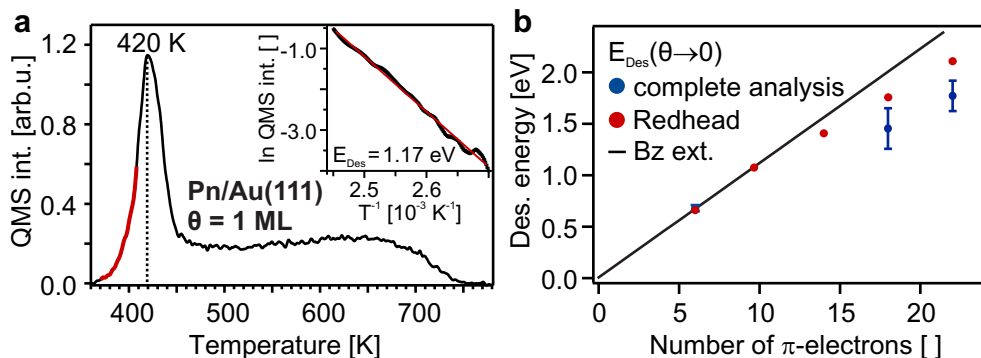


Figure 3.9.: (a) TPD data of a pentacene monolayer on Au(111), the dotted line marks the position of the high-coverage (compressed) phase peak. The red part of the spectrum is evaluated *via* leading edge analysis as shown in the inset, leading to a desorption energy of $E_{Des} = 1.17 \text{ eV}$. (b) shows the desorption energies *vs.* the number of π -electrons in the the zero-coverage limit after Redhead (red) and after complete analysis (blue). The black line indicates the linear extrapolation of the Bz value for larger aromatic systems.

Figure 3.9 (a) shows a TPD spectrum of 1 ML pentacene on Au(111) with the low-coverage tail from 450 to 750 K and the compressed phase centred at 420 K, both representing half a monolayer each. France *et al.* [144] (see Fig. 3.3 (e) and (f)) showed that there exist two coverage regimes with different molecular densities in the monolayer. Different in a way, that the high-coverage phase has roughly two times the density of the low-coverage phase. In other words, in the case of pentacene, the repulsive interactions lead to a molecular low-coverage pattern, where exactly one additional pentacene molecule (with a then lowered desorption energy) fits in the gaps of the pattern. The symmetric peak at 420 K suggests, that E_{des} is independent of coverage here. The leading edge analysis [97] of this peak (see inset of Fig. 3.9 (a)) leads to desorption energy of $1.17 \pm 0.05 \text{ eV}$. So overall, in the pentacene/Au(111) system, it seems to be the case, that from 0 to 0.5 ML the molecules adsorb in a pattern like it is shown in Fig. 3.3 (e), whereas the desorption energy drops from 1.8 eV for the single molecule to 1.2 eV with an increasing number of neighboring molecules. From thereon all adsorption sites in the gaps of the low-coverage pattern have the same environment and therefore binding energy (1.2 eV). Due to their long-

3. Binding of Aromatic Molecules on Coinage Metal Surfaces

range character (several Ångströms), the repulsive forces in the low-coverage regime cannot be simple direct intermolecular interactions of vdW or Coulomb type but must be substrate-mediated like the ones introduced in section 3.1.2. So all investigated systems show the low-coverage tail associated to the repulsive interactions and in the case of pentacene on Au(111) a subtle balance between molecular structure, substrate geometry, and substrate-mediated interactions leads to an interesting self-assembling system with large intermolecular distances leaving additional space for adsorption in the monolayer. A quantitative understanding of this relation might allow reliable simulations of such behaviors. Today, self-assembling is focused mainly on attractive intermolecular interactions, from attractive vdW interactions between the alkyl chains of thiols [173] *via* coordinated networks [174] up to covalently bound systems [53]. The target-oriented use of repulsive substrate-mediated interactions opens up new ways to tailored interfaces which can be easily modified e.g. by co-adsorption of a second adsorbate.

Figure 3.9 (b) shows a comparison of the determined desorption energies (single molecule limit) in dependency of the size of the systems measured as the number of π -electrons. The black line is an extrapolation of the value for Bz obtained with the complete analysis. The red dots mark the desorption energies for all systems calculated with the Redhead formula using the temperatures of the falling edges in Fig. 3.7 (b) and a coverage independent pre-factor of 10^{13} s^{-1} . The blue dots mark the complete analysis values. The latter clearly shows a nonlinear dependence on the system size and thus suggest, that the interaction strength is not only determined by the molecular size. First theoretical insights [175] suggest that many-body effects play an important role here. This has to be explained in detail by future theoretical work. Additional experimental work should cover analogous measurements with naphthalene and anthracene to complete the acene series. Beneficial would be the parallel development of a new simulation-based evaluation routine for TPD spectra allowing more reliable results and fewer requirements on data quality as the here used complete analysis. Further theoretical approaches should try to reproduce the adsorption behavior of pentacene which would allow the simulation of the behavior of other comparable molecules leading to tailored self-assembled adsorbate structures.

4. Adsorption and Growth of Functional Molecules on Au(111)

4.1. Background: N-Heteropolycyclic Aromatic Molecules

The former chapter brought general insights into the strengths of lateral and vertical interactions of planar aromatic molecules on coinage metal surfaces. The next step is to investigate the consequences of these interactions on the adsorbate geometry and thin-film morphology. Both have huge influence on device properties [33, 176–179] and despite long research [42, 180, 181], rules explaining aggregate morphology from the single molecule's structure are rare. As mentioned in the introduction, the variety of small organic molecular compounds suitable for organic electronics is too big to find general structure-property relationships for millions of substances. But for a small but representative and versatile sub-group, it should be possible and constructive. The use of aromatic systems offers small band gaps, suitable for organic electronics, as already explained in chapter 3. The further constraint on π -conjugated systems limits the aggregation pathways, but still allows the morphology tuning by varying substituents which cause different intermolecular forces. Also, the processability (e.g. solubility) can still be tuned by introducing aliphatic side chains or functional groups [182]. The basic electronic properties like the character as an electron or hole acceptor remain unchanged due to these substitutions. The introduction of hetero-atoms (N, O, S) into the aromatic system of such molecules allows even the tuning of the electronic properties (e.g., the energetic positions of the frontier orbitals) [183, 184]. Nitrogen plays a special role here as it can be introduced in aromatic systems with three single bonds as N-H (like in pyrrole) or with a double bond as in pyridine [185, 186]. The so manipulated systems can even switch between the two oxidation states with its corresponding oxidation potentials and electron affinities. Nitrogen in the pyridine form decreases the energy of both the HOMO and the LUMO

4. Adsorption and Growth of Functional Molecules on Au(111)

and hence leaves the optical gap almost constant but improves air- and water-stability due to an increased ionization potential and electron affinity. On these grounds, N-heteropolycycles were chosen to be investigated in a collaborative research centre (SFB 1249). As a part of an involved project, this work investigates the adsorbate geometry and electronic interfacial properties with means of HREELS, TPD, and DFT.

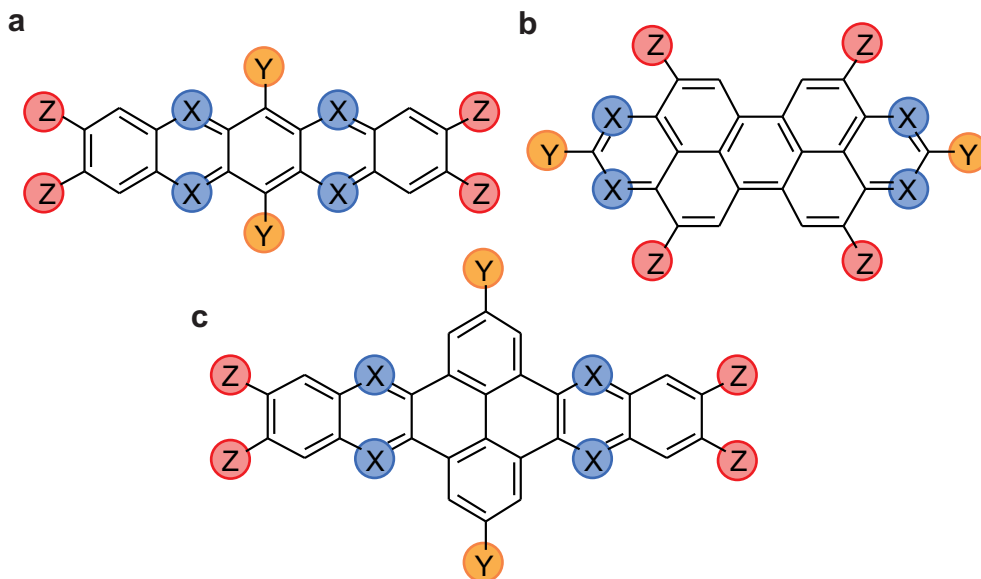


Figure 4.1.: The three basic molecular frameworks investigated in this thesis, (a) pentacene, (b) peropyrene, and (c) dibenzohexacene with the corresponding positions for substitutions to tune film morphology and electronic properties. For detailed description, see text.

Figure 4.1 shows the structural variability of the chosen basic frameworks pentacene (a), Pn, peropyrene (b), PP, and dibenzo[*hi,uv*]hexacene (c), DBH. X, Y, and Z represent the possible substitution points. X determines the basic electronic properties and can be C-H, N or N-H. Y can be hydrogen (H) or any other side chain, e.g. long aliphatic chains to increase solubility or bulky groups to adjust the morphology. At the Z-positions, hydrogen, electron-withdrawing like halogens [187] or electron donating groups can influence the electronic properties but also morphology and solid state structure. Pentacene and peropyrene as pristine hydrocarbons (X = C-H; Y, Z = H) are well studied organic semiconductors [144, 188, 189] but for their N-heterocyclic analogous this is not the case. Table 4.1 shows all investigated systems. Substituent positions (X, Y, Z) are equivalent to Fig. 4.1.

4.1. Background: *N*-Heteropolycyclic Aromatic Molecules

Table 4.1.: Investigated molecules, the positions of substituents X, Y, and Z can be obtained from Fig. 4.1. ¹ triisopropylsilylethynyl

framework	X	Y	Z	notation
Pn	H	TIPS ¹	H	TIPS-Pn
	N	TIPS	H	TIPS-TAP
DBH	N	H	H	QPP
	N	tBu	H	tBu-QPP
PP	N	H	H	TAPP
	N	C ₃ F ₇	H	TAPP-H
	N	C ₃ F ₇	Cl	TAPP-Cl
	N	C ₃ F ₇	Br	TAPP-Br
	N	C ₃ F ₇	I	TAPP-I

For all investigated molecules, gas-phase DFT calculations have been carried out to get information about the electronic structure and, in particular, the vibrational modes of the respective molecule (a detailed description of the used theoretical method as well as an exemplary calculation input file can be found in App. C). Figure 4.2 shows exemplary TAPP-Br with its structural formula (a), DFT-based geometry optimization (B3LYP/6-311G) (b), and DFT-derived electron densities (colors reflect the sign of the wave function) for the HOMO and LUMO, (c) and (d), respectively. The π -conjugation of the carbon-nitrogen structure forces a planar geometry of the aromatic part of the molecule (see Fig. 4.2 (b)) with all atoms in one plane. The C₃F₇-substituents are due to their sp^3 -hybridization not in-plane. Both, HOMO and LUMO, show a nodal plane along the long molecular axis. This causes the independence of the electronic structure on the nature of the Y-substituents, which makes it easy to adjust properties like the molecular packing or the solubility of a pre-designed n- or p-channel organic semiconductor. Another important aspect in this chapter is the epitaxial growth, hence the formation of crystalline thin films on crystalline surfaces. These films are mainly prepared by vapor deposition techniques. The growth behavior is determined by adsorbate-adsorbate interactions, surface energies, as well as lattice parameters and is described by three growth modes [87, 190].

4. Adsorption and Growth of Functional Molecules on Au(111)

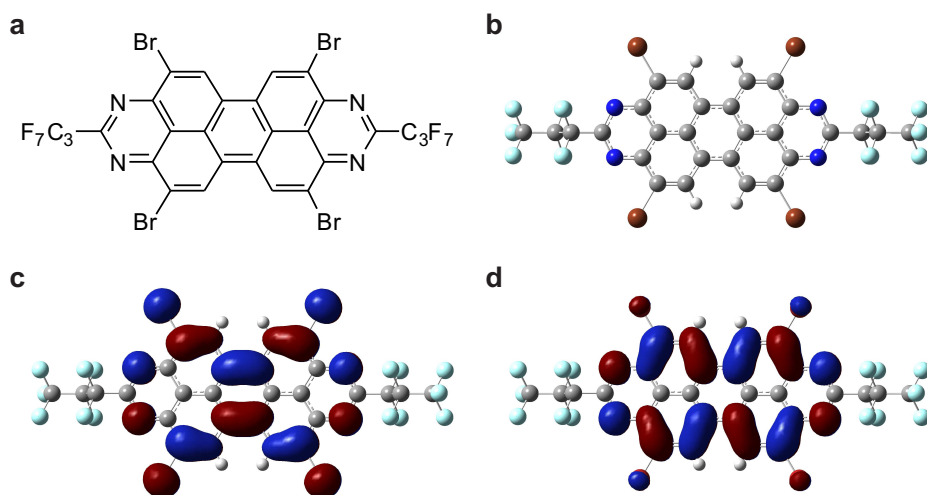


Figure 4.2.: Molecular structure of TAPP-Br (a), DFT-derived optimized molecular geometry (b) and frontier orbitals (HOMO (c) and LUMO (d), (B3LYP/6-311G).

First, Volmer-Weber growth with the formation of islands and three-dimensional adsorbate clusters due to stronger lateral (adsorbate-adsorbate) than vertical (adsorbate-substrate) interactions. Second, Frank-van der Merwe growth with preferred adsorption on surface sites and thus a layer-by-layer growth due to strong adsorbate-substrate interactions. Third, a mixture of both, Stranski-Krastanov growth with the adsorption of one or several “wetting” layers in the Frank-van der Merwe mode and subsequent island formation in the Volmer-Weber mode [191, 192]. The difference in the lattice parameters of the substrate and the thin film leads to strain in the film. Close to the surface (e.g. in the monolayer) strong vertical interactions outweigh the strain in the film. With increasing coverage (i.e. distance to the surface) the vertical interactions decrease and at a critical coverage the adsorption switches to island formation. In all presented systems monolayer formation as in Frank-van der Merwe or Stranski-Krastanov growth is observed. The situation for multilayer adsorption often is not that clear and discussed in the section of the particular system. Stranski-Krastanov growth allows to measure excitations in the monolayer even at higher coverages, this can be an explanation for the similarities of mono- and multilayer spectra. All in all, there is more evidence for layer-by-layer growth but with the used methods a clear distinction was not possible. Additional Auger electron spectroscopy (AES) experiments can help to get

more insight into this aspect.

The presentation of all systems starts with a brief introduction and motivation, a short description of the respective TPD spectra, which are shown for TIPS-Pn and which can be found in the appendix for the other systems. Afterwards, the vibrational spectra are discussed. At last, a view on the electronic spectra gives insight into the electronic properties at the surface. The results start with TIPS-Pn, followed by QPP, and the TAPP system. Preparation conditions for all shown measurements are summarized in App. B. The assignments of all observed vibrational modes in tabular form together with visualizations of these vibrational modes can be found in the respective part of the Appendix. The relevant (and discussed) vibrations are labelled in the spectra.

4.2. TIPS-Pentacene

The first presented molecule belongs to the pentacene derivatives (Fig. 4.1 (a)). Pentacene itself is a well-known organic semiconductor [193] and as it is still widely and successfully used in devices [194] it has the rank of a prototype material for semiconducting small molecules. Pentacene single-crystals have one of the highest mobilities in field effect transistors (FET) found for organic semiconductors. But lacks in other properties such as solubility and hence processability lead to developments like the investigated triisopropylsilylethynyl pentacene (TIPS-Pn) (structural formula in Fig. 4.3) which shows a fundamentally different crystal structure [195]. Whilst pentacene crystallizes in a herringbone-like structure with stacks of tilted molecules (related to the stack axis) and two different tilting angles in neighboring stacks, TIPS-Pn crystallizes in a brick-like structure with all pentacene planes parallel to each other. Another interesting aspect is, that pentacene, as well as TIPS-Pn, undergo a process called singlet fission [196–198]. First discussed for anthracene [199], this process describes the creation of two excited molecules in the triplet state from one optically excited molecule in its singlet state. In general, the purpose is to overcome the Shockley-Queisser [200] limit of theoretical photovoltaic efficiency by creating two excited states with only one photon. To allow this process, the energy levels must be in a way that the singlet state (S_1) has roughly twice the energy of the triplet state (T_1) which is the case for acenes. However, studies showed that the singlet fission efficiency depends strongly on

4. Adsorption and Growth of Functional Molecules on Au(111)

the orientation of neighboring molecules [201] which strongly depends on the substituents. So it was a surprising discovery that also the brick-like order of TIPS-Pn lead to a high singlet fission efficiency. The first aim of this study is to show that the preparation of well-defined TIPS-Pn films on Au(111) *via* evaporation is possible as this is still under discussion in the literature. Anthony et al. [202] proclaim that heating TIPS-Pn to temperatures above 140°C leads to a phase transition in TIPS-Pn single crystals which destroys the singlet fission ability. Furthermore, they state that TIPS-Pn decomposes after melting and before evaporation if the vacuum is not good enough for sublimation. The second goal is the investigation of these films with respect to morphology and electronic structure. This may include the direct observation of transitions involving triplet states as it is possible with EELS [203, 204]. The third goal is the extension of this study to new nitrogen substituted derivatives.

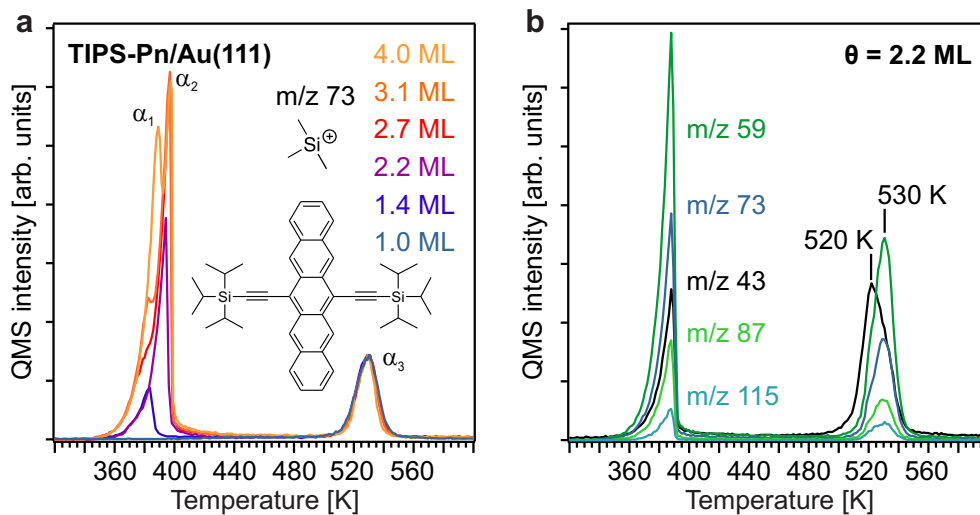


Figure 4.3.: (a) TPD spectra of TIPS-Pn on Au(111) for different coverages from $\theta = 1.0$ ML to 4.0 ML. The structural formulas of TIPS-Pn and of the observed fragment ($m = 73$ amu) are depicted. The observed fragment belongs to the TIPS group. Peaks are labeled from α_1 to α_3 with increasing desorption temperature. (b) TPD spectra of a $\theta = 2.2$ ML TIPS-Pn film on Au(111) for different observed fragments. The isopropyl-fragment ($m = 43$ amu) shows a monolayer desorption peak shifted by 10 K (see labeled temperatures). Figure adapted from ref. [73].

The presentation of the results starts with coverage- (Fig. 4.3 (a)) and fragment-mass-resolved (Fig. 4.3 (b)) TPD spectra. The coverage dependent spectra show three peaks. The high-temperature peak (530 K, α_3) shows sat-

uration before the other peaks start to increase. This clearly indicates the development of a complete wetting layer before multilayer adsorption takes place (Stranski-Krastanov or Frank-van-der-Merwe growth mode). The peak is highly symmetric which reveals simple first-order desorption without extensive lateral adsorbate-adsorbate or substrate-mediated interactions. This is in strong contrast to the pentacene results presented in the former chapter. α_2 is assigned to second layer desorption as it shows zero-order desorption behavior and saturation for higher coverages. α_1 arises as a shoulder of α_2 , shows no saturation for higher initial coverages and also shows zero-order desorption behavior, it is therefore assigned to desorption from higher layers. The observed fragment (73 amu) is a silicon-containing fragment of the TIPS group (structural formula is shown in Fig. 4.3 (a)). The shown coverage is determined by integrating the spectra and comparing the area of α_3 to the total integral. Monolayer coverages are prepared by evaporating significantly more than one monolayer and heating the sample to a temperature between 420 K (above multilayer desorption) and 500 K (below monolayer desorption). The exact dosing and preparation conditions can be found in App. B. Figure 4.3 (b) shows TPD spectra of the same initial coverage of $\theta = 2.2$ ML for different observed fragments. All fragments belong to the TIPS group and show a comparable behavior for mono- and multilayer desorption. Only the iso-propyl fragment ($m/z = 43$ amu) shows a different behavior and its monolayer desorption peak is shifted to lower temperatures by 10 K to 520 K compared to the other fragments. This indicates a degradation before the monolayer can desorb intact which is supported by TPD measurements of the doubly charged pentacene backbone ($m/z = 198$ amu) which is only visible in the multilayer desorption peak (see Fig. F.2 (c) in App. F). This on-surface degradation of TIPS-Pn around 520 K was already proposed by temperature-dependent X-ray photoelectron (XPS) measurements [205]. However, the degradation at 520 K indicates an intact evaporation and annealing (monolayer preparation) process where the maximum temperatures do not exceed 450 K.

4. Adsorption and Growth of Functional Molecules on Au(111)

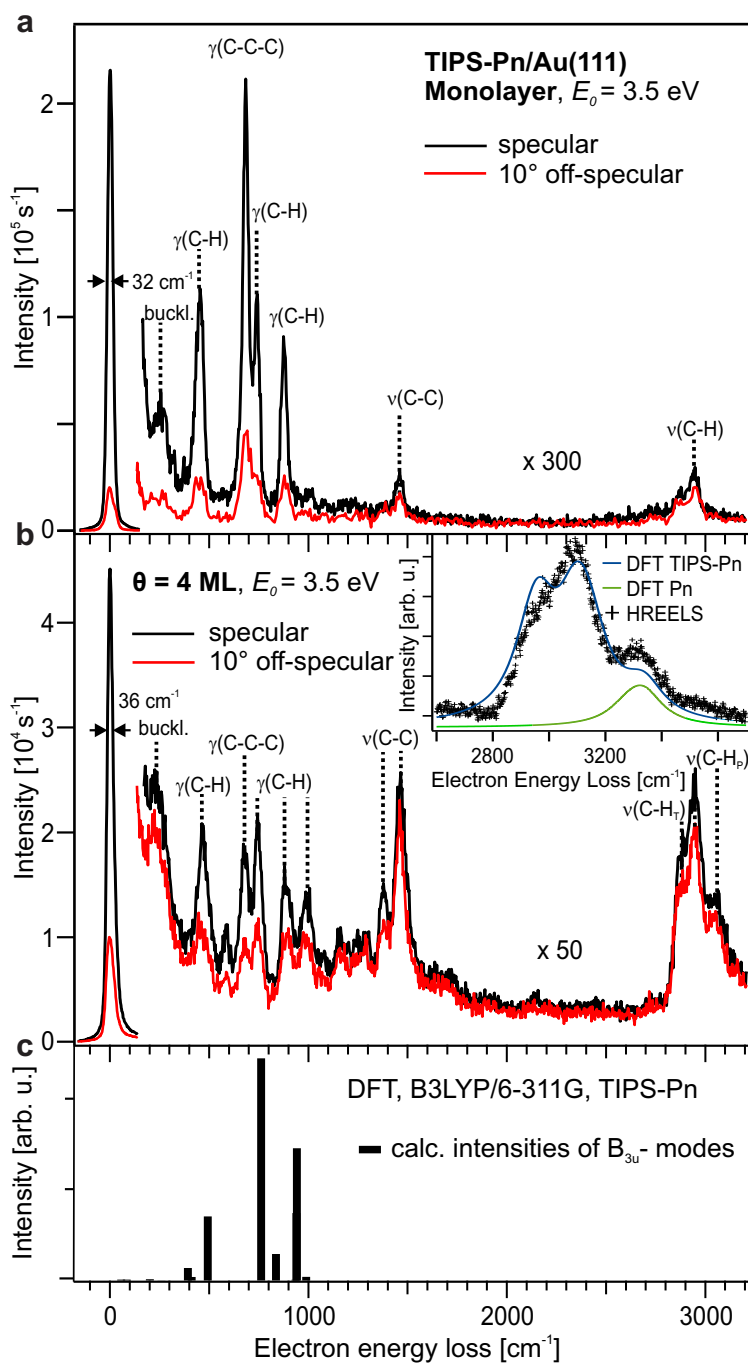


Figure 4.4.: HREEL spectra in specular (black) and off-specular (red) scattering geometry for mono- (a) and multilayer (b) coverages of TIPS-Pn on Au(111). $E_0 = 3.5$ eV is the primary electron energy of the incident electrons. The energy resolution measured as FWHM of the elastic peak (zero loss peak) is labeled in the graphs. The inset of (b) shows the enlarged $\nu(\text{C-H})$ stretching vibration region with corresponding DFT data for TIPS-Pn (blue) and pentacene (green). (c) shows calculated B_{3u} -mode (dynamic dipole moment perpendicular to the pentacene plane) frequencies and intensities (B3LYP/6-311G). Figure adapted from ref. [73].

The second goal after the shown general probability of evaporative thin film preparation is the investigation of the molecular orientation relative to the substrate within these thin films. For non- or weak-interacting substrates like SiO₂ grazing incidence X-ray diffraction (GIXD) measurements showed, that one TIPS group of the lowermost layer is oriented towards the substrate and hence the alkyne bond and the pentacene plane (with its short axis) are oriented perpendicular to the surface [206]. Complementary angle-resolved near-edge X-ray absorption fine structure (NEXAFS) measurements of TIPS-Pn on Au(111) showed, that due to the strong metal-aromatic interaction the pentacene plane is oriented parallel to the metal surface. From the data, a tilting angle between the molecular plane and the substrate (rotation around the short axis) is extracted [205]. However, the authors assume to overestimate their value of 30° due to contributions of additional resonances leading to increased intensities under the specific measuring angles. Vibrational HREELS is now used to further investigate the adsorption geometry of the evaporated thin films. Figure 4.4 shows HREEL spectra in specular (black) and 10° off-specular geometry (red) for a monolayer coverage (a) and a coverage of $\theta = 4$ ML (b). Figure 4.4 (c) shows calculated frequencies and intensities (B3LYP/6-311G) of vibrational modes with B_{3u} symmetry (dynamic dipole moment perpendicular to the pentacene plane). The specular spectrum in (a) is dominated by four intense modes ($\gamma(\text{C-H})$ and $\gamma(\text{C-C-C})$) which can be attributed to clear out-of-plane pentacene-related vibrations as a comparison with the DFT data in Fig. 4.4 (c) shows. Figure 4.5 (a) and (b) visualize the $\gamma(\text{C-H})$ at 449 cm⁻¹ and the $\gamma(\text{C-C-C})$ at 692 cm⁻¹ modes, respectively. The black arrow indicates the orientation of the corresponding dynamic dipole moment vector which is in both cases clearly perpendicular to the pentacene plane. All dominant modes show a much higher intensity in specular than in off-specular geometry and are therefore dipole-active. The observed $\nu(\text{C-C})$ and $\nu(\text{C-H})$ vibrations are attributed to modes located primarily in the TIPS groups. Equivalent modes of the pentacene part with a dynamic dipole moment parallel to the molecular plane (in-plane modes; visualized in Fig. 4.5 (c) and (d), respectively) show no significant intensity. From these observations, it can be derived that the TIPS-Pn molecules lie with its pentacene plane parallel to the Au(111) surface. But it has to be noted that a slight tilting as proposed in [205] cannot be excluded from these data, whereas 30° seems far too high as in that case modes with its dynamic dipole moment parallel to the long pentacene axis should show sig-

4. Adsorption and Growth of Functional Molecules on Au(111)

nificant dipole activity and therefore high intensity in the specular spectrum. The multilayer spectrum ($\theta = 4$ ML; Fig. 4.4 (b)) still shows dipole active out-of-plane modes ($\gamma(\text{C-H})$ and $\gamma(\text{C-C-C})$) but the difference in intensity is much smaller. Also, the elastic peak intensity is reduced by one fifth when increasing the coverage from 1 to 4 ML.

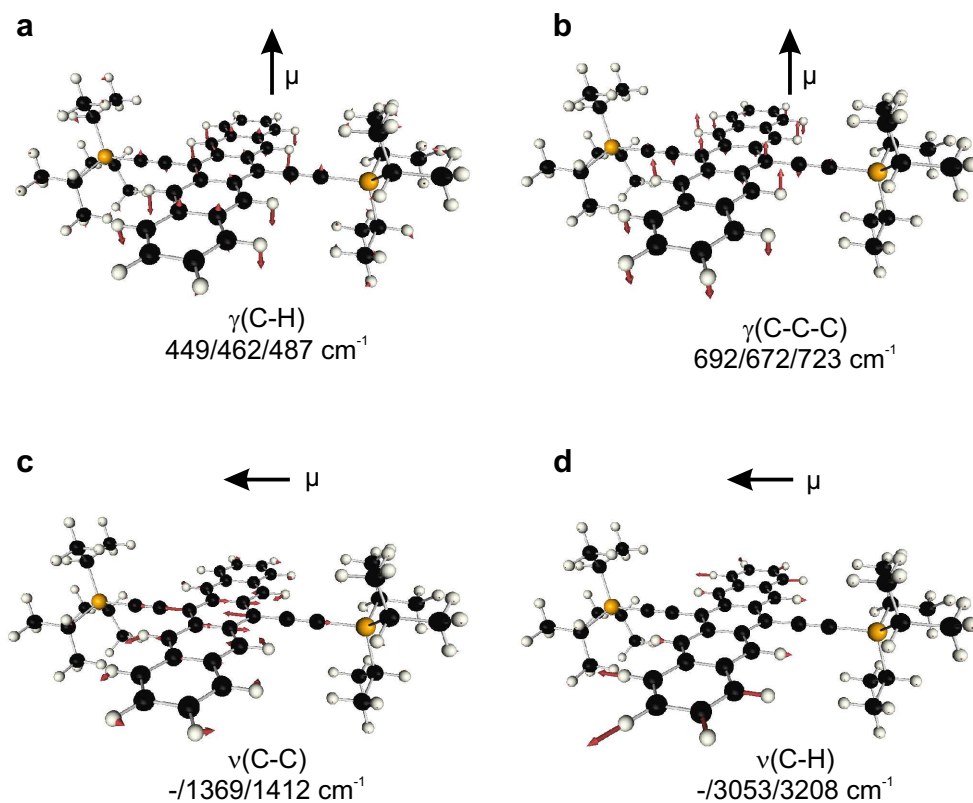


Figure 4.5.: Visualized characteristic vibrational modes (red arrows, atomic displacements) of TIPS-Pentacene derived by DFT calculations (B3LYP/6-311G) with their corresponding dynamic dipole moment orientations (μ), energies (HREELS monolayer/HREELS multilayer/DFT) and assignments. In all cases the dipole moment vector lies in the plane of the paper.

This can be attributed to the larger distance to the surface. The in-plane modes, $\nu(\text{C-C})$ and $\nu(\text{C-H})$, are still not dipole active, their intensities, however, are higher than the dipole active ones'. It is therefore concluded that TIPS-Pn adopts a molecular orientation with the pentacene plane parallel to the surface on Au(111) even at higher coverages. However, the uncertainty regarding a tilting around the short pentacene axis is still present. Note, that all observed vibrational modes and their corresponding assignments and visual-

izations can be found in App. F in Table F.1 and Figure F.1, respectively. The inset of Figure 4.4 (b) shows the enlarged region of the C-H stretching vibrations around 3000 cm^{-1} (black crosses) together with DFT calculated spectra of TIPS-Pn (blue) and pentacene (Pn, green). It is obvious, that the measured spectrum is well reproduced by the DFT calculation for TIPS-Pn. The two contributions below 3200 cm^{-1} are attributed to the aliphatic $\nu(\text{C-H})$ modes of the TIPS groups. The aromatic $\nu(\text{C-H})$ vibrations at 3300 cm^{-1} belong to the pentacene part. This is a further clear indication for intact TIPS-Pn molecules on the surface which confirms the previous TPD results.

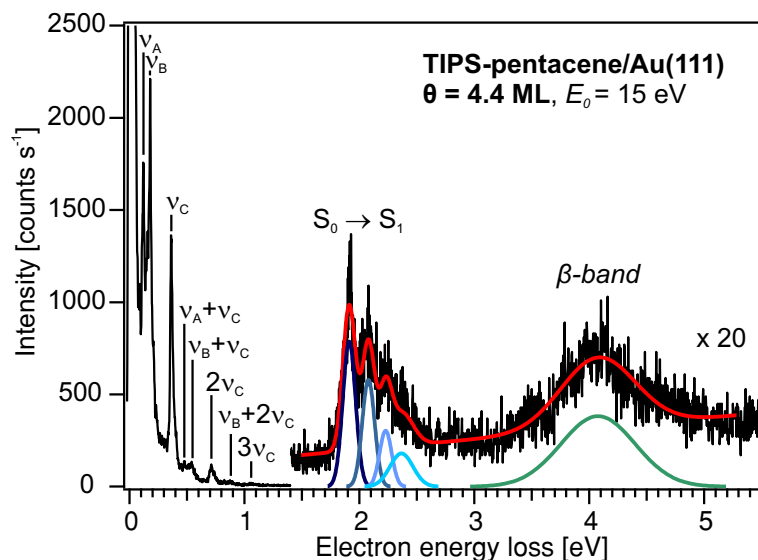


Figure 4.6.: Electronic HREEL spectra of 4.4 ML TIPS-Pn on Au(111) including fits to the $S_0 \rightarrow S_3$ (β -band) and vibronic $S_0 \rightarrow S_1$ transition peaks. The primary electron energy E_0 is 15 eV. In the low-energy regime vibrations ν_a ($\gamma(\text{C-H})$), ν_b ($\nu(\text{C-C})$), and ν_c ($\nu(\text{C-H})$) and visible overtones or combinations are labeled. Figure adapted from ref. [73].

For the spectrum in Figure 4.6, the primary electron energy was increased from 3.5 to 15 eV to allow the excitation of electronic transitions like the optical gap or a direct singlet-to-triplet excitation. The coverage was $\theta = 4$ ML. The monolayer spectrum is not shown, as adsorbate-induced features are screened there by the Au surface as already observed in electronic HREELS before [207] (see App. F for the monolayer spectrum). This is somewhat surprising as the increased distance between the surface and the aromatic backbone due to the bulky TIPS groups should cause a significant decoupling.

4. Adsorption and Growth of Functional Molecules on Au(111)

In contrast the 4 ML spectrum shows several low-energy features ($E_{loss} < 1$ eV) which are attributed to the $\gamma(\text{C-H})$ (ν_A), $\nu(\text{C-C})$ (ν_B), and $\nu(\text{C-H})$ (ν_C) vibrations and corresponding combinations or overtones. On the high-energy side the β -band ($S_0 \rightarrow S_3$ transition) is located at 4.1 eV. At 1.9 eV the optical gap ($S_0 \rightarrow S_1$ transition) shows the typical vibronic excitations (“acene fingers”) which are attributed to additional excitations of the $\nu(\text{C-C})$ breathing mode of the pentacene backbone at 1667 cm^{-1} . The optical gap determined by ultraviolet-visible measurements in solution is also 1.9 eV [208], whereas spin-cast films show an additional feature at 1.75 eV which is attributed to aggregation [208]. This indicates that in a 4 ML thin film both intermolecular interactions and the surface have negligible influence on the size of the optical gap and that the TIPS-Pn molecules are electronically decoupled. A possible triplet transition is not observed which can be explained by small cross sections for the given primary electron energy. In addition, a systematic primary electron energy dependent study [203, 204] may help to resolve these interesting excitations.

A further goal was the investigation of the aza-derivative triisopropylsilylethynyl tetraazapentacene (TIPS-TAP; $X = \text{N}$, $Y = \text{TIPS}$, $Z = \text{H}$ in Fig. 4.1). The molecules were synthesized by Fabian Paulus (Bunz group of the institute for organic chemistry at the University of Heidelberg). Routinely the received substance was investigated before loading the doser and after unloading it with electron ionization mass spectrometry at the organic chemistry institute’s core facility to get information about possible degradation. If the molecular ion (which cannot be detected by the QMS used for the TPD investigations as the observable m/z range is restricted to values below 200 amu) is present in the obtained mass spectrum it is concluded that the dosing procedure did not lead to degradation. The TIPS-TAP measurement showed a molecular ion 2 amu larger than expected suggesting a hydrogenation (reduction) of two out of the four nitrogen atoms. However, an expected increase of the optical gap due to the altered electronic structure (DFT calculations, B3LYP/6-311G: TAP $E_{HOMO-LUMO} = 2.3$ eV, Dihydro-TAP $E_{HOMO-LUMO} = 2.9$ eV) was not observed in the electronic HREELS measurements. These showed as well as the corresponding vibrational measurements comparable results to the ones obtained for TIPS-Pn. Another possible explanation for the higher mass is, that hydrogen attachment took place inside the mass spectrometer when the particular ionization method was applied. Because of this

4.3. Quinoxalinophenanthrophenazine (QPP) and *t*Bu-QPP

uncertainties, the results are only shown and briefly discussed in App. F.

To summarize the TIPS-Pn results, the TPD measurements showed clearly that the introduction of spatially demanding TIPS-substituents suppresses strong adsorbate-adsorbate or substrate-mediated interactions by increasing the lateral distance between two molecules as well as the vertical distance between substrate and adsorbate. Together with the vibrational HREELS measurements they also showed that intact sample preparation *via* evaporation is possible. The annealing to 450 K leads to smooth and well-ordered (high elastic peak intensity, good resolution) monolayer films which adopt a parallel orientation of the pentacene planes relative to the Au(111) substrate. The electronic HREELS data indicate only small intermolecular interactions as with 1.9 eV the optical gap in a 4 ML thin film is not significantly different from that in solution. However, the screened HOMO-LUMO transition in the monolayer is a sign for relevant electronic coupling of adsorbate and substrate here.

4.3. Quinoxalinophenanthrophenazine (QPP) and *t*Bu-QPP

The next investigated systems are based on the dibenzohexacene framework (see Fig. 4.1 (c)). Quinoxalino[2',3':9,10]-phenanthro[4,5-*abc*]-phenazine (QPP; X = N, Y = H, Z = H in Fig. 4.1 (c)) and the 2,11-di-*tert*-butyl-substituted QPP (*t*Bu-QPP; X = N, Y = (*t*Bu, Z = H in Fig. 4.1 (c)) give the opportunity to directly investigate the effect of the introduction of bulky substituents on adsorption morphology and electronic structure, i.e., to get insights into the structure-property relationship. QPP already has been studied in p-channel transistors and showed rather low field-effect mobilities [209]. *t*Bu-QPP has been used as a triptycene connected trimer to form hexagonal cage structures [210, 211] with the intention to act as a light-harvesting material in organic photovoltaic cells. The structural formulas can be found as insets in Figure 4.7 (a) and (d) for QPP and *t*Bu-QPP. The detailed sample preparations can again be found in App. B. The TPD spectra are shown and briefly discussed in App. G. They show the clear multilayer desorption peak (splitting into 2nd-layer and multilayer peak visible up to 7 ML) around 450 K whilst the monolayer desorption is only barely visible for both molecules. The monolayer preparation is possible by annealing the sample to 500 K.

4. Adsorption and Growth of Functional Molecules on Au(111)

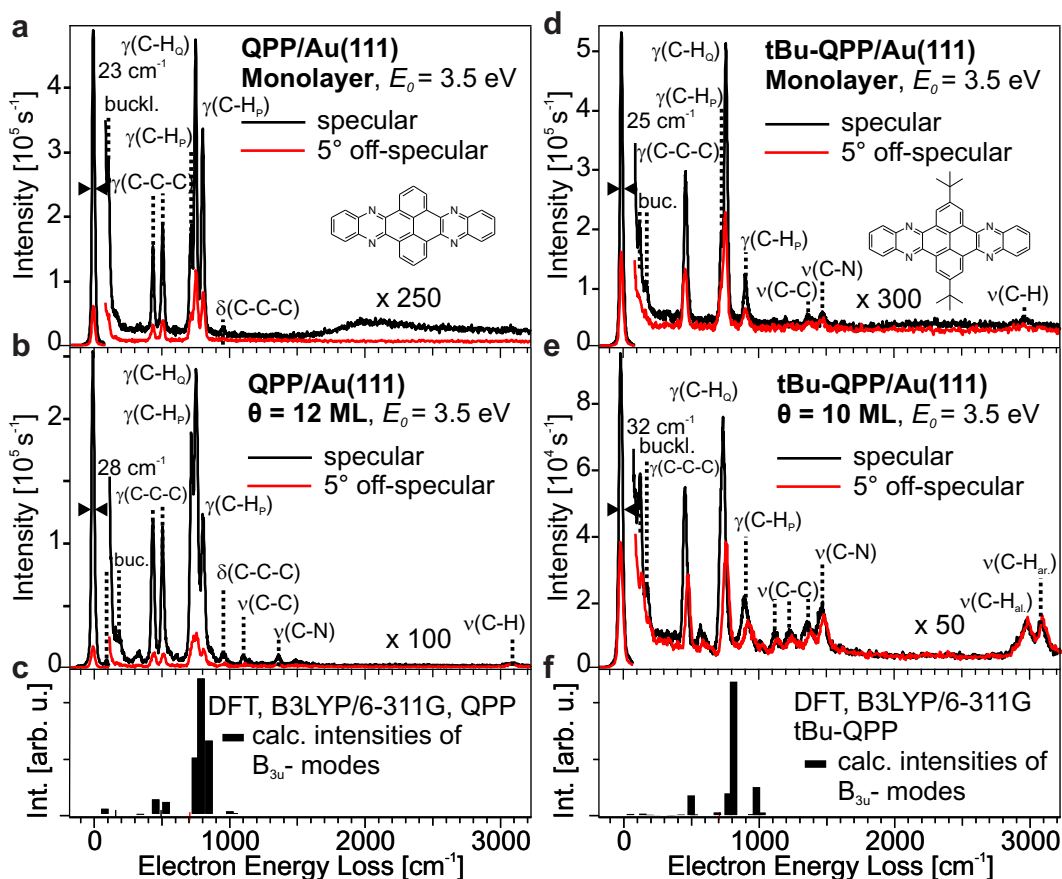


Figure 4.7.: HREEL spectra in specular (black) and off-specular (red) scattering geometry for mono- (top) and multilayer (center) coverages of QPP (left) and tBu-QPP (right), corresponding structural formulas shown in the upper graphs. E_0 is the primary energy of the incident electrons. The energy resolution measured as FWHM of the elastic peak (zero loss peak) is labeled in the graphs. At the bottom, (c) and (f), calculated B_{3u} -mode (dynamic dipole moment perpendicular to the molecular plane) frequencies and intensities are shown. Figure adapted from ref. [55].

The coverage determination was done by separating the multilayer peak and normalizing it with the 2nd-layer peak. Figure 4.7 (a) shows the vibrational HREEL spectra (specular in black, 5° off-specular in red) for a QPP monolayer on Au(111). The spectrum shows a high resolution of 23 cm^{-1} measured as full width at half maximum (FWHM), which indicates smooth well-ordered films. As in the case of TIPS-Pn, the specular spectrum is dominated by five out-of-plane $\gamma(\text{C-H})$ and $\gamma(\text{C-C-C})$ vibrations, which have a high specular to off-specular ratio and are therefore assigned as dipole active. The DFT data in Figure 4.7 (c) shows calculated (B3LYP/6-311G) intensities of infrared ac-

4.3. Quinoxalinophenanthrophenazine (QPP) and *t*Bu-QPP

tive vibrational modes with B_{3u} symmetry, hence a dynamic dipole moment perpendicular to the molecular plane. The five out-of-plane modes are well represented by these calculations. Two of them are visualized in Figure 4.8 (a) and (b) where the molecular plane is perpendicular to the paper plane while the dynamic dipole moment vector μ lies in the latter. Impact scattered modes are due to their small cross sections nearly invisible here. The broad feature around 2000 cm^{-1} can be assigned to a spectrometer related artefact (see section 2.4.1 and ref. [123]). Again, all observed vibrational modes and their corresponding assignments and visualizations can be found in App. G in Table G.1 and Fig. G.1, respectively. The multilayer spectrum in Figure 4.7 (b) reveals that still in a 12 ML thick film the spectrum is extremely dominated by the before seen dipole active out-of-plane modes suggesting a still nearly perfect planar adsorption. Due to the larger amount of molecules on the surface, the small impact scattering cross section is sufficient for showing some in-plane stretching modes like $\nu(\text{C-C})$, $\nu(\text{C-N})$, and $\nu(\text{C-H})$. The latter consists of several individual modes, two are visualized in Figure 4.8 (c) and (d) which show either dynamic dipole moment vectors oriented parallel to the long molecular axis or parallel to the short axis, respectively. Note, that the molecular plane lies now in the paper plane as well as the dynamic dipole moment does. As mentioned in section 4.1 the similarities of mono- and multilayer HREEL spectra could also be explained by Stranski-Krastanov growth but then more impact scattering from islands and an overall worse resolution and elastic peak intensity due to a rougher, less-ordered surface would be expected. The comparison with the *t*Bu-QPP spectra in Figure 4.7 (d), (e), and (f) shows high conformity. The only dipole-active modes are the specific out-of-plane wagging vibrations $\gamma(\text{C-H})$ and $\gamma(\text{C-C-C})$. The specular to off-specular intensity ratio of the dipole active modes as well as the elastic peak intensity is significantly smaller than for QPP, indicating a rougher, less ordered layer due to the bulky *t*Bu-groups. However, again no other vibrations show any significant dipole activity a relevant tilting can be excluded. Increasing the thickness to $\theta = 10$ ML leads to a further reduction of the elastic peak intensity by almost an order of magnitude which is a sign for a rougher film but is also grounded in the increased distance to the surface which decreases the dipole scattering efficiency.

4. Adsorption and Growth of Functional Molecules on Au(111)

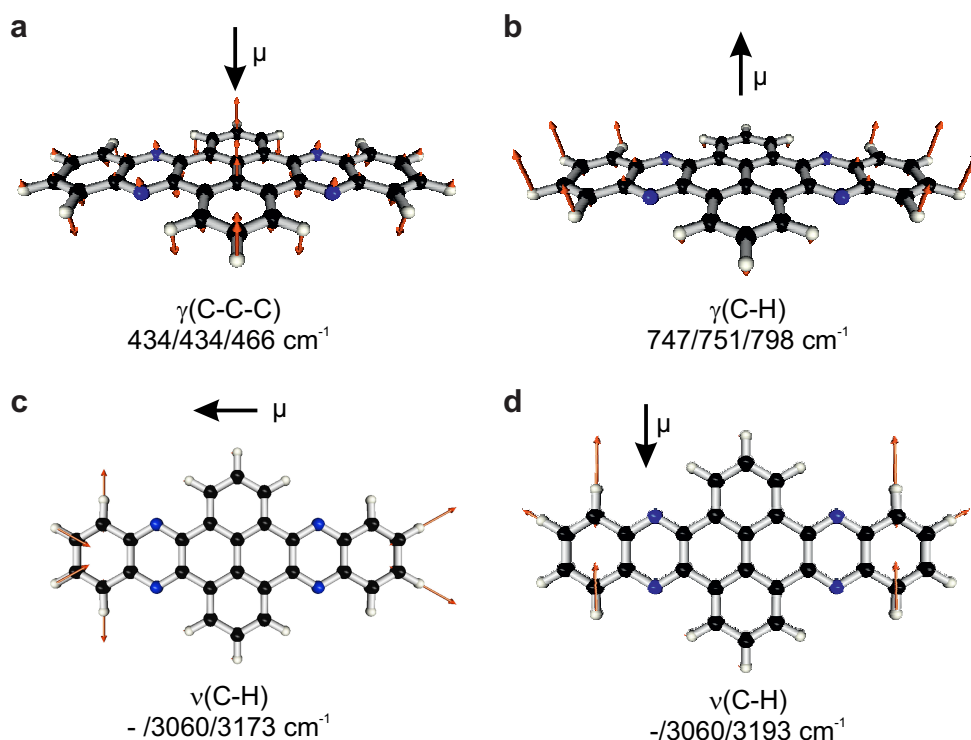


Figure 4.8.: Visualized characteristic vibrational modes (red arrows, atomic displacements) of QPP derived by DFT calculations (B3LYP/6-311G) with their corresponding dynamic dipole moment orientations (μ), energies (HREELS monolayer/HREELS multilayer/DFT) and assignments. In all cases the dipole moment vector lies in the plane of the paper as well as the molecule in (c) and (d). In (a) and (b) the molecular plane is orientated perpendicular to the paper plane. Figure adapted from ref. [55].

Nevertheless, the obtained picture is similar to the one for QPP (and TIPS-Pn), there is clearly no dipole activity of in-plane modes like the $\nu(\text{C-C})$ and $\nu(\text{C-H})$ stretching vibrations, and hence, the molecules adsorb in a planar orientation on the Au(111) surface. Note that the latter now resolves the separation of aromatic (at the QPP core) and aliphatic (at the *t*Bu groups) C-H bonds. Table G.1 in App. G also lists frequencies obtained by attenuated total reflectance Fourier-transform infrared spectroscopy (AFT FT-IR) of the condensed material. The data for the out-of-plane modes of the QPP in direct metal contact (HREELS) show a redshift of 10 cm^{-1} indicating a significant adsorbate-substrate binding which weakens the intramolecular bonds. For *t*Bu-QPP this shift is not existent showing that the bulky side groups decouple the adsorbate from the metal.

4.3. Quinoxalinophenanthrophenazine (QPP) and *t*Bu-QPP

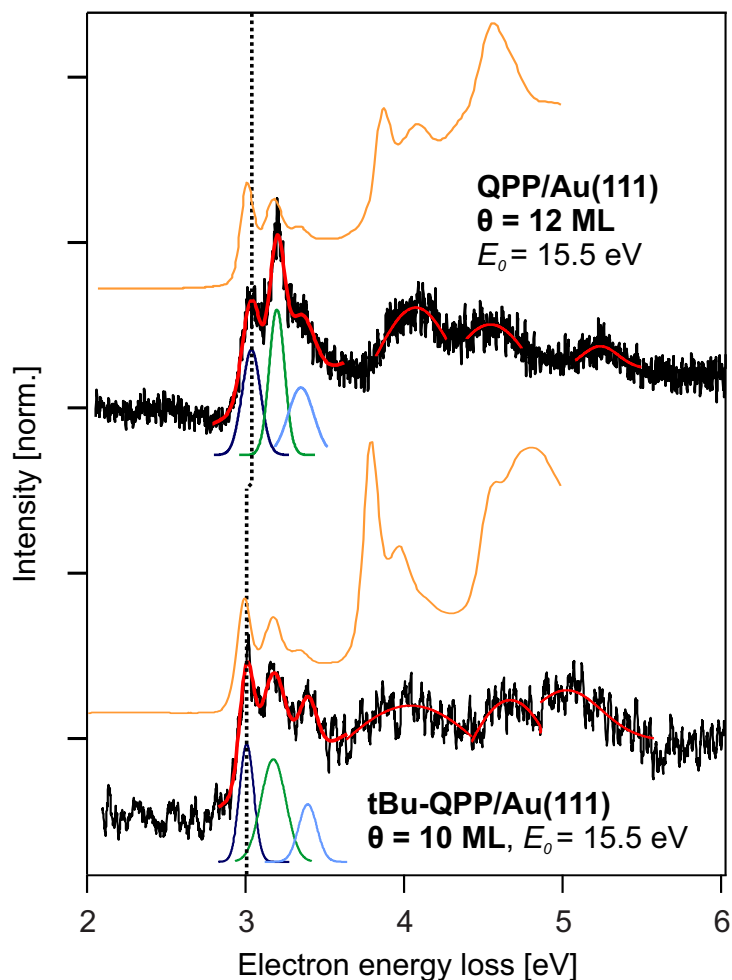


Figure 4.9.: Electronic HREEL spectra including fits to the vibronic $S_0 \rightarrow S_1$ transition peaks of 12 and 10 ML QPP and *t*Bu-QPP on Au(111), respectively. The primary electron energy E_0 is 15.5 eV, the spectra are normalized with respect to the $S_0 \rightarrow S_1$ transition peak (dashed line), and UV-vis spectroscopic data by Bernd Kohl *et al.* are shown for comparison. Figure adapted from ref. [55].

The electronic HREEL spectra are shown together with the respective UV/Vis data in Figure 4.9. The focus lies on the multilayer spectra as the relevant features are much better resolved here due to higher intensities. The monolayer spectra show in addition the conventional Au(111) surface plasmon at 2.5 eV. The HOMO-LUMO transition is observable in the monolayer, which indicates a rather weak adsorbate-substrate interaction as otherwise the frontier orbitals would be screened by the metal influence. This is in contrast to the

4. Adsorption and Growth of Functional Molecules on Au(111)

presented results for TIPS-Pn and suggests that the introduction of nitrogen into a polycyclic aromatic molecule leads to a decreased electronic coupling between adsorbate and substrate (see App. G for the respective monolayer spectra). The shown spectra are dominated by strong features around 3 eV which are assigned to the $S_0 \rightarrow S_1$ transition, the HOMO-LUMO transition or the optical gap. The visible vibronic features are due to simultaneous exciting the molecular breathing modes (sym. $\nu(\text{C-C})$ and $\nu(\text{C-N})$ around 1500 cm^{-1}) and are typical for extended aromatic systems (“acene fingers”, compare to the TIPS-Pn results in Fig. 4.6). The comparison with the UV/Vis spectroscopic data measured in solution surprisingly shows no significant differences like energetic shifts. The determined optical gaps are 2.98 eV (HREELS) and 3.00 eV (UV/Vis) for QPP, and 2.96 eV (HREELS) and 2.99 eV (UV/Vis) for *t*Bu-QPP. The optical gap is therefore not affected by the molecular packing and the metal contact in thin films or by the introduction of bulky substituents in this specific position. The latter was expected due to the calculated electronic structure (compare Fig. 4.1 and 4.2). Several additional higher energetic transitions can be observed which are also confirmed in the UV/Vis spectra. Note also the well visible (*t*Bu-QPP) and barely visible (QPP) $\nu(\text{C-H})$ overtone around 0.8 eV and the previously mentioned artefact in the QPP spectrum between 1.2 and 2 eV. As a short summary, it is noted that the bulky side chains decouple the adsorbate (no surface related frequency shift in the case of *t*Bu-QPP) significantly but have no effect on the orientation relative to the substrate. However, the surface roughness seems to increase with the introduction of bulky substituents indicated by a reduced dipole activity. The electronic spectra show almost no difference between thin films and solutions and therefore suggest only weak substrate-adsorbate and adsorbate-adsorbate interactions. The optical gap for both molecules is roughly 3 eV showing, that the introduction of hydrocarbon substituents in the specific positions does not affect the energetic position of the frontier orbitals.

4.4. Tetraazaperopyrene (TAPP) and its Halogenated Derivatives

The third investigated system, based on the peropyrene structure [212], was studied with variation in both the Y- and Z-position as the structural formulas in Figure 4.10 (a) show. The development of the TAPP system goes back to 2007 when Gade et al. [213] showed the synthesis of TAPP itself but also for a variety of derived compounds. The synthesis is based on the dimerization of diamidonaphthalene to 4,9-diamino-3,10-perylenequinone diimine (DPDI). This substance is easily treated with a variety of compounds to get either the pristine TAPP or several in Y-position substituted derivatives. The perfluorinated propyl groups showed promising behavior regarding solubility and electron-conduction and are therefore studied here. TAPP-Cl and TAPP-Br have already been successfully studied as n-channel semiconductors in devices like complementary circuits [214, 215]. So it was part of this work to complete the investigation of the structure-property relationship of halogenated TAPP derivatives by investigating their on-surface behavior in detail to allow a target-oriented development of new n-channel organic compounds in the future. With an STM study of the TAPP/Cu(111) system [216], so far only the pristine TAPP has been investigated on a single crystal surface. It showed interesting aggregation phenomena and on-surface reactivity like oligomerisation. The study carried out here is the first on Au(111), a more relevant substrate for device application due to its smaller reactivity compared to Cu(111). Parts of the TAPP, TAPP-H, and TAPP-Cl investigations have already been done and published in previous works [55, 122, 217, 218] but all shown spectra were measured during this work with improved resolutions. The results are presented again for a better understanding of the obtained insights.

4. Adsorption and Growth of Functional Molecules on Au(111)

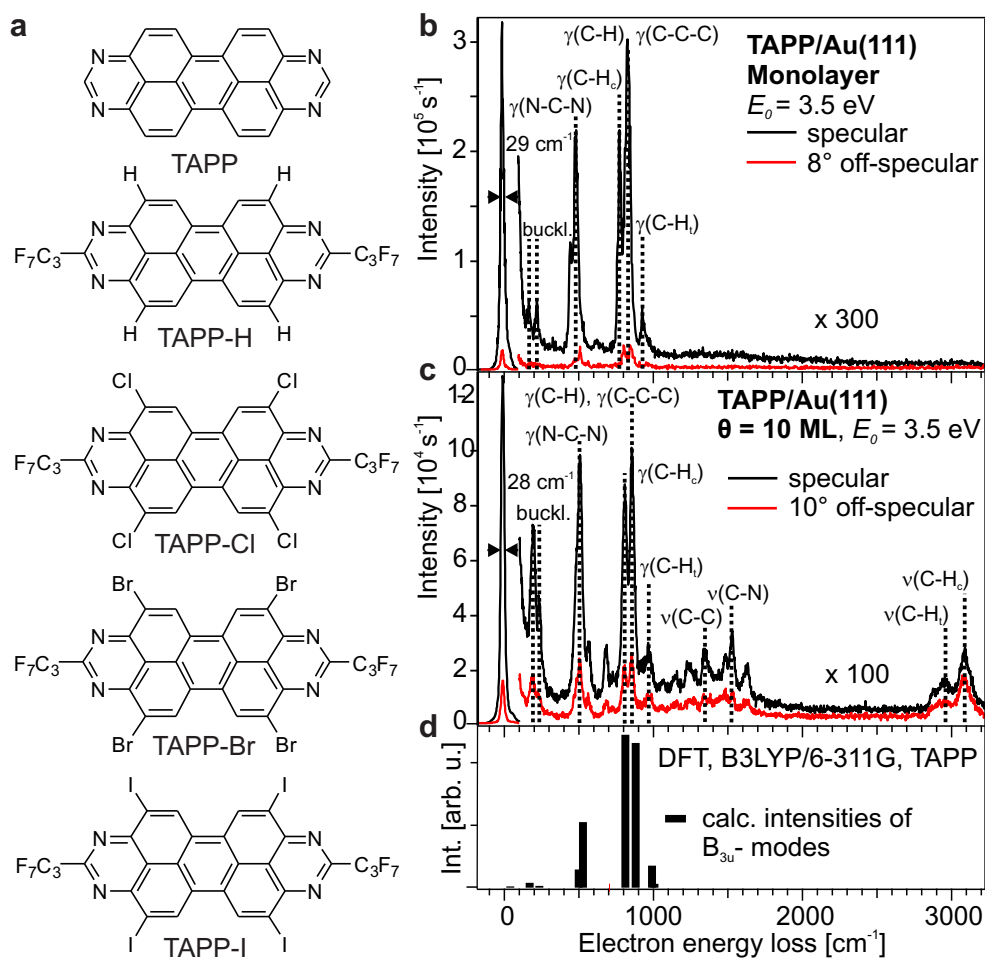


Figure 4.10.: (a) Molecular structures of all investigated TAPP derivatives. (b) - (d) HREEL spectra in specular (black) and off-specular (red) scattering geometry for a TAPP monolayer (b) and a coverage of 10 ML TAPP (c) on the Au(111) surface. E_0 is the primary energy of the incident electrons. (d) shows calculated B_{3u} -modes (dynamic dipole moment perpendicular to the molecular plane) frequencies and intensities (B3LYP/6-311G). Figure adapted from ref. [55].

4.4. Tetraazaperopyrene (TAPP) and its Halogenated Derivatives

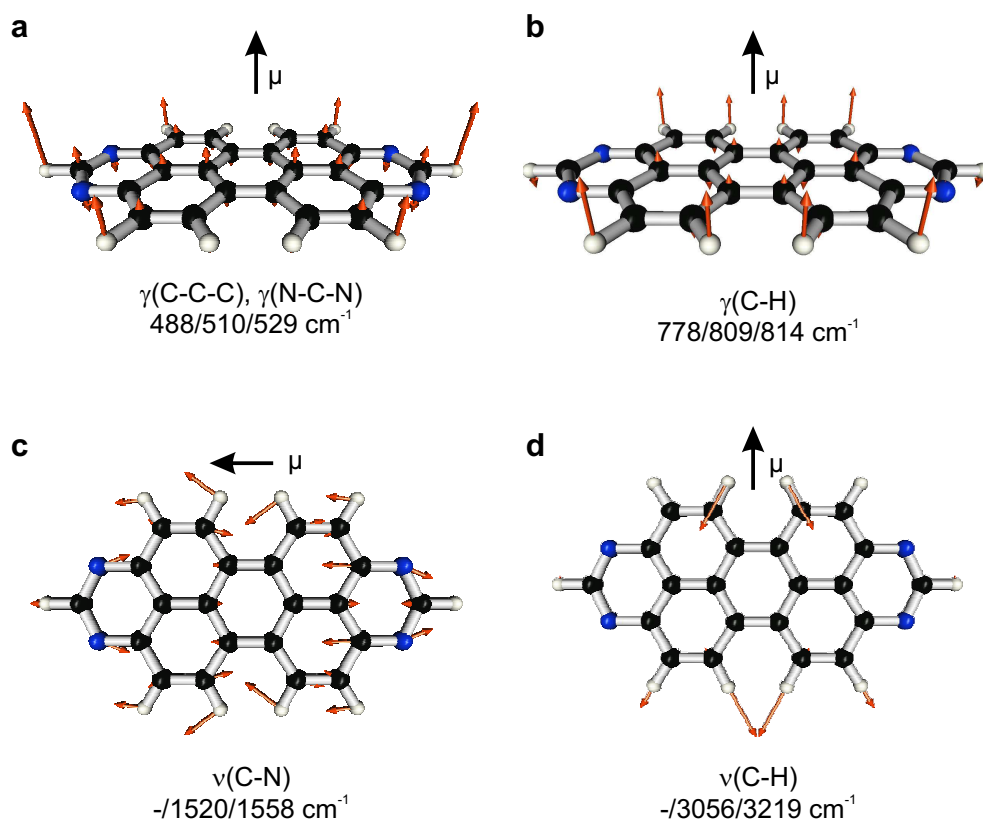


Figure 4.11.: Visualized characteristic vibrational modes (red arrows, atomic displacements) of TAPP derived by DFT calculations (B3LYP/6-311G) with their corresponding dynamic dipole moment orientations (μ), energies (HREELS monolayer/HREELS multilayer/DFT) and assignments. In all cases the dipole moment vector lies in the plane of the paper as well as the molecule in (c) and (d). In (a) and (b) the molecular plane is orientated perpendicular to the paper plane. Figure adapted from ref. [55].

Like for the previous systems, dosing, coverage determination, and distinct monolayer preparation were monitored with TPD (exemplary TPD spectra, see App. H). The precise dosing parameters for the samples corresponding to each shown spectra are listed in Table B in App. B. The TAPP multilayer desorbs intactly at 320 K, the monolayer decomposes and fragments desorb between 500 and 650 K showing a compressed phase desorbing at 530 K. The vibrational HREEL spectra of TAPP on Au(111) are shown in Figure 4.10 (b) for the monolayer and (c) for a coverage of $\theta = 10$ ML. Figure 4.10 (d) shows the calculated intensities and frequencies of all B_{3u} modes (B3LYP/6-311G). Again it is obvious that the specular (black) spectra of the TAPP mono- and multilayer are dominated by modes which are well represented by the calculated B_{3u}

4. Adsorption and Growth of Functional Molecules on Au(111)

modes. They are all assigned to out-of-plane modes and show a large specular to off-specular ratio, hence, they are dipole active. The $\gamma(\text{C-C-C})$ and $\gamma(\text{N-C-N})$ wagging modes around 500 cm^{-1} as well as the $\gamma(\text{C-H})$ mode at 778 cm^{-1} are visualized in Figure 4.11 (a) and (b), respectively. Note, that all observed vibrational modes and their corresponding assignments and visualizations can be found in App. H in Table H.1 and Fig. H.1, respectively. Whilst the monolayer spectra show almost no contributions from in-plane modes, like the $\nu(\text{C-N})$ and $\nu(\text{C-H})$ stretching vibrations they are well visible in the multilayer spectra. The significant specular to off-specular is assigned for the most part to the higher background level of the specular compared to the off-specular spectrum and not to a significant tilting of the molecules in the multilayer (see the area between 2000 and 2500 cm^{-1} in Fig. 4.10 (c)). The mentioned in-plane modes are visualized in Figure 4.11 (c) and (d). For the pristine TAPP a picture can be, that goes with the one derived for QPP. The gold metal surface forces the TAPP molecules to adopt a planar adsorption geometry to increase the metal- π interaction for the cost of intermolecular π - π interaction which could be obtained for tilted molecules with overlapping π -systems in the monolayer. A different behavior was observed before for octithiophene (8T) on Au(111) [219,220]. Here the molecules are tilted and thus overlapping in the monolayer. For QPP/Au(111), the further layers seem to adopt also a planar (relative to the substrate) adsorption geometry as the now predominant intermolecular π - π interactions are thus increased. The investigations of *t*Bu-QPP compared to QPP and TIPS-Pn compared to previous investigations of pentacene gave insight into the consequences of the introduction of a bulky but rigid substituent – they are rather small. The molecules still adopt a planar adsorption geometry in the monolayer as well as they do it in the multilayer in the limits of the experimental inaccuracies. Now, with perfluorinated propyl groups, a smaller but more flexible substituent is investigated.

4.4. Tetraazaperopyrene (TAPP) and its Halogenated Derivatives

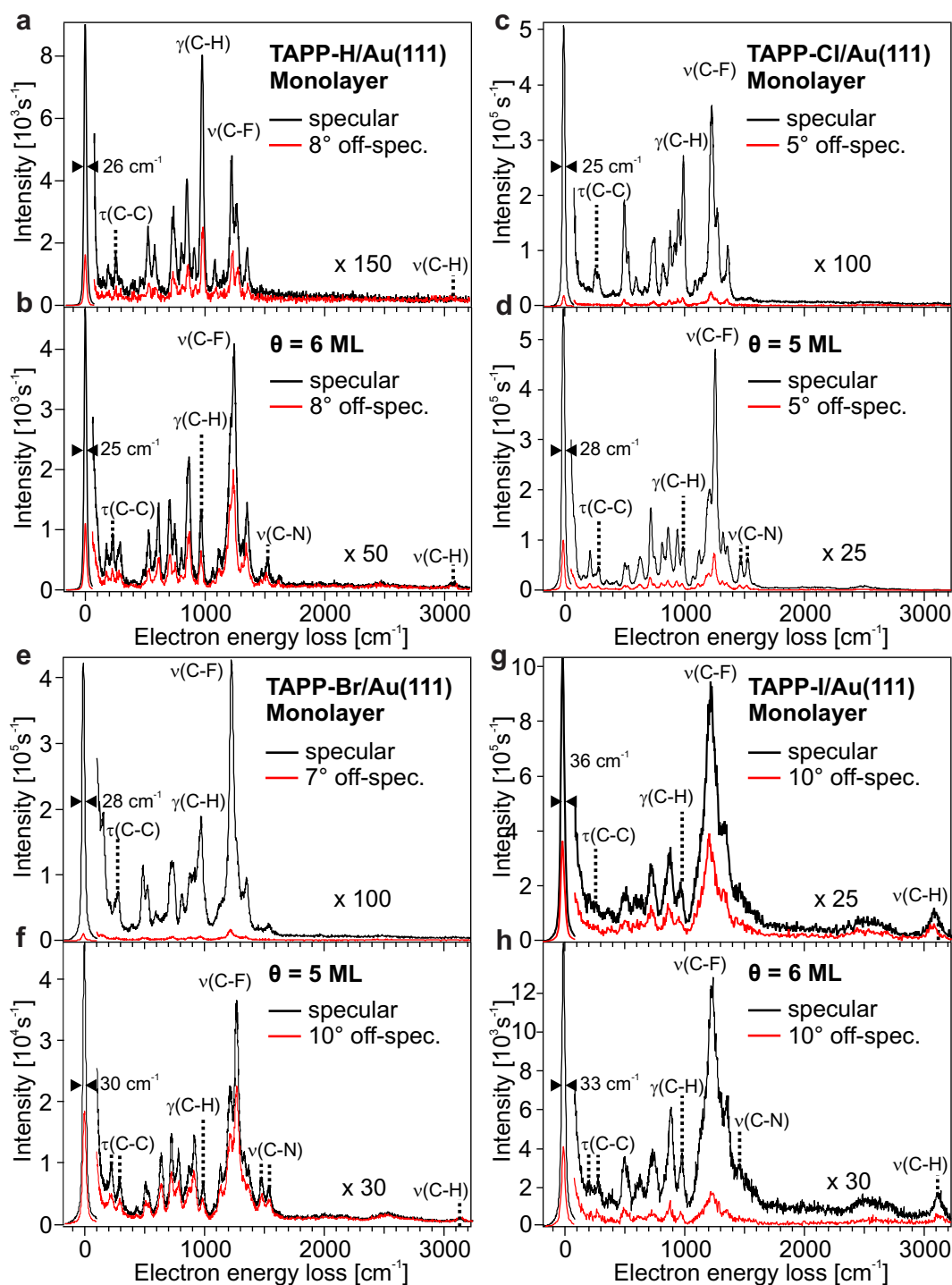


Figure 4.12.: HREEL spectra in specular (black) and off-specular (red) scattering geometry for mono- (top) and multilayer (bottom) coverages of TAPP-H (a), TAPP-Cl (b), TAPP-Br (c), and TAPP-I (d), corresponding structural formulas are shown in Figure 4.10 (a). E_0 is the primary energy of the incident electrons, θ the particular multilayer coverage. Figure adapted from ref. [218].

4. Adsorption and Growth of Functional Molecules on Au(111)

The TAPP-H on Au(111) HREEL spectra in specular (red) and off-specular geometry (black) for the monolayer and a coverage of 6 ML are shown in Figure 4.12 (a), and (b). Analogue spectra for TAPP-Cl, TAPP-Br, and TAPP-I are shown in Figure 4.12 (c) and (d), (e) and (f), and (g) and (h), respectively. The monolayer spectra show in all cases high specular to off-specular intensity ratios especially for the $\gamma(\text{C-H})$ out-of-plane mode around 1000 cm^{-1} suggesting a planar adsorption of the aromatic backbone on the metal surface. The relative intensity of this mode is reduced for higher coverages pointing to a less strict planar adsorption whilst now in all cases, the spectra are dominated by the $\nu(\text{C-F})$ stretching vibration which is hard to interpret as the C-F bonds point to several directions due to the tetrahedral geometry of the propyl carbon atoms. Another hint for a tilting of the peropyrene plane relative to the substrate above a coverage of 1 ML lies in the intensity and dipole-activity of the $\nu(\text{C-N})$ stretching modes around 1500 cm^{-1} which show dynamic dipole moments parallel to the long molecular axis (see e.g. the spectrum for the 5 ML film of TAPP-Cl on Au(111) in Fig. 4.12 (d) and compare to Fig. 4.11 (c) for the visualized analogue vibration in TAPP). On the other hand, the $\nu(\text{C-H})$ stretching modes with dynamic dipole moments parallel to the long molecular axis (compare to Fig. 4.11 (c)) show no dipole activity even in the multilayer spectra except a little in the case of TAPP-I (see Fig. 4.12 (h)). This indicates that these dynamic dipole moments are still oriented parallel to the surface hence, the multilayer molecules must be tilted around the short molecular axis. The multilayer spectra are a superposition of the contributions of the flat-lying monolayer molecules and the tilted ones in the upper layers which makes it hard to identify and interpret especially the modes between 500 and 1000 cm^{-1} (assignments and visualizations in App. H). The planar adsorption in the monolayer and the tilting around the short axis for higher coverages seems universal for the perfluoropropyl substituted TAPPs. The size of the substituent in Z-position has an influence on the general molecular (long-range) ordering. For the smaller substituents H and Cl the multilayer spectra show a good resolution suggesting a well-ordered surface structure where all molecules are oriented equally. This resolution (note the broad peaks in Fig. 4.11 (f) and (h)) decreases for bromine and iodine-substituted TAPPs indicating a rougher surface and less strictly defined adsorption geometry. All findings are illustrated in Figure 4.14 and summarized at the end of this chapter.

4.4. Tetraazaperopyrene (TAPP) and its Halogenated Derivatives

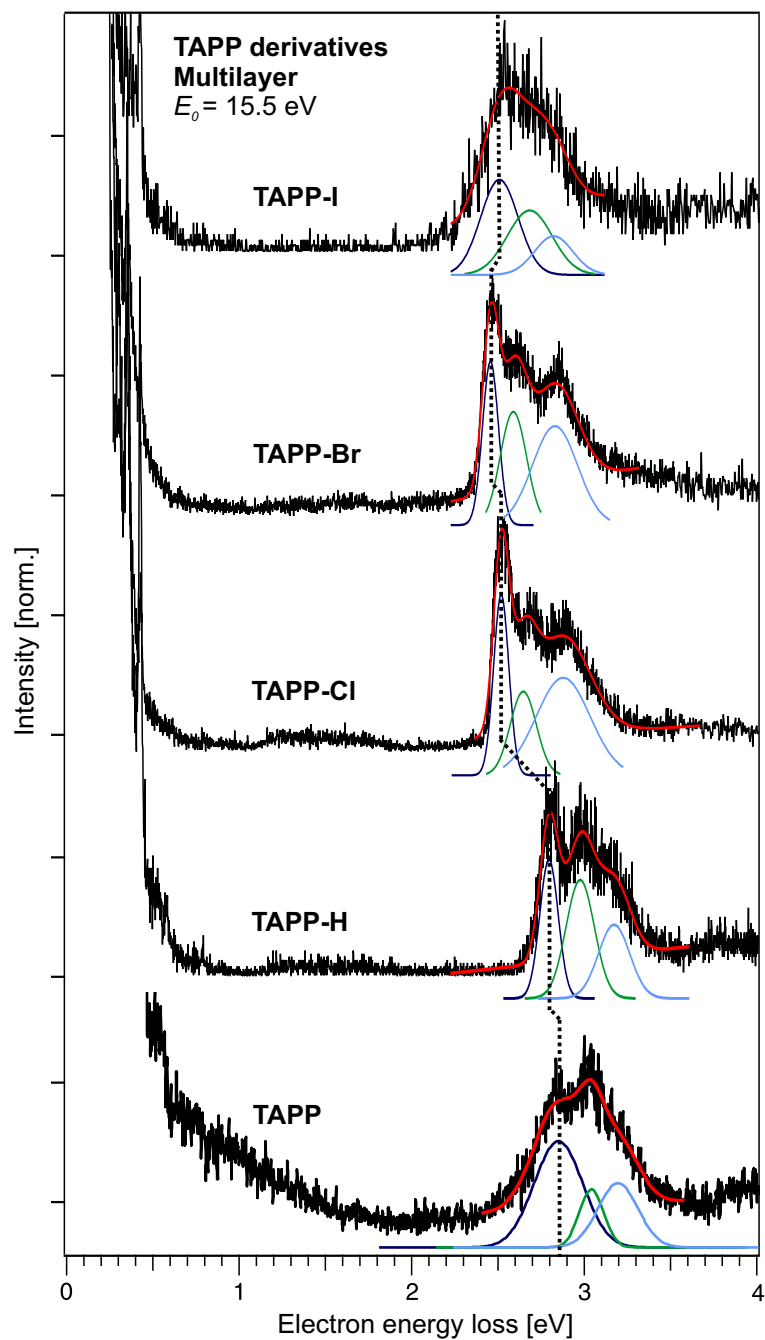


Figure 4.13.: Electronic HREEL spectra including fits to the vibronic $S_0 \rightarrow S_1$ transition peaks of multilayer coverages of the denoted TAPP derivatives on Au(111). The primary electron energy E_0 is 15.5 eV, the spectra are normalized with respect to the $S_0 \rightarrow S_1$ transition peak (dashed line). Figure partly adapted from ref. [218].

4. Adsorption and Growth of Functional Molecules on Au(111)

The electronic ($E_0 = 15.5$ eV) multilayer HREEL spectra of all measured TAPP derivatives are summarized in Figure 4.13. The monolayer spectra show no clear adsorbate induced peaks and are therefore not shown here. The screening of adsorbate features requires a significant adsorbate-substrate interaction which is underpinned by the dissociation of the monolayers in the TPD measurements. The observed HOMO-LUMO gaps ($S_0 \rightarrow S_1$ transitions, dark blue Gaussian fits) range from 2.42 eV (TAPP-Br) to 2.84 eV (TAPP). In all spectra, the already mentioned vibronic features are visible, which are assigned to additionally excited breathing modes (sym. $\nu(\text{C-N})$ and $\nu(\text{C-C})$ around 1500 cm^{-1} and overtones; green and light blue Gaussian fits). The HREELS derived optical gap of the pristine TAPP ($\theta = 10$ ML) of 2.84 eV is surprisingly close to the UV/Vis derived (solved in toluene [182]) of 2.86 eV showing negligible molecule-molecule interactions in the thin film. The introduction of the perfluorinated propyl chains in Y-positions shifts the gap slightly to 2.77 eV (UV/Vis in THF: 2.84 eV [218]). As proposed, only a small reduction by 0.07 eV is observed, indicating a weak influence of substitution in this position due to the fact that a nodal plane goes through the long molecular axis in the HOMO as well as in the LUMO (see Fig. 4.2 (c) and (d), respectively). The replacement of hydrogen in position Z with chlorine shifts the optical gap clearly stronger by 0.28 eV to 2.49 eV (UV/Vis in THF: 2.64 eV) indicating a strong influence of the electron withdrawing halogen on the energetic positions of HOMO and LUMO. The nature of the halogen and so also their differences in electronegativity seem to play a surprisingly non-relevant role in thin film HREELS measurements as the similar values for TAPP-Br of 2.42 eV (UV/Vis in THF: 2.61 eV) and TAPP-I of 2.48 eV (UV/Vis in THF: 2.51 eV) show (all UV/Vis data from ref. [218]). The UV/Vis values for solutions show significant differences here which may be caused by solvent effects or due to less good resolution in the HREEL spectra. Exemplary for the perfluoropropyl-substituted TAPPs, the observed vibrations are listed visualized for TAPP-H in Table H.2 and Figure H.2 in App. H.

4.5. Discussion: Substrate-Directed Growth and the Influence of Substituents

The described adsorption properties of all investigated compounds are now placed in a more general context by comparing them with the bulk crystal structures. Figure 4.14 shows in the top the derived adsorption behaviors for QPP, *t*Bu-QPP, TIPS-Pn, and TAPP and in the middle the corresponding crystal structures. The bottom section shows the adsorption behavior for the TAPP derivatives. The first row repeats the generally observed substrate-directed planar adsorption in the monolayer and up to at least 10 ML thick films. This was observed in a strict way for the pure planar molecules QPP and TAPP and less strict when bulky substituents were symmetrically introduced (*t*Bu-QPP, TIPS-Pn). For all investigated systems and all investigated thicknesses, the HREELS data show no tilting angles between the molecular planes and the substrate of more than 20°. Nevertheless, an exact quantification is challenging, especially for increased film thicknesses. On the other side, the bulk crystal structures show tilting angles between neighboring stacks of molecules of 82° for QPP, 69° for *t*Bu-QPP [221] and 35° for TAPP [216], whilst TIPS-Pn crystallizes in a brick-like structure [222] with no tilting like the substrate-directed growth mode. The bottom row summarizes the behavior of the C₃F₇-substituted TAPP derivatives. The monolayer adsorbs in a planar geometry, but the flexible substituents disturb an analogue adsorption of the further layers. These layers adopt a crystal-like growth mode as long as the substituent in Z-position is small enough (TAPP-H, TAPP-Cl). The bigger bromine and iodine substituents suppress a smooth and homogenous film growth.

4. Adsorption and Growth of Functional Molecules on Au(111)

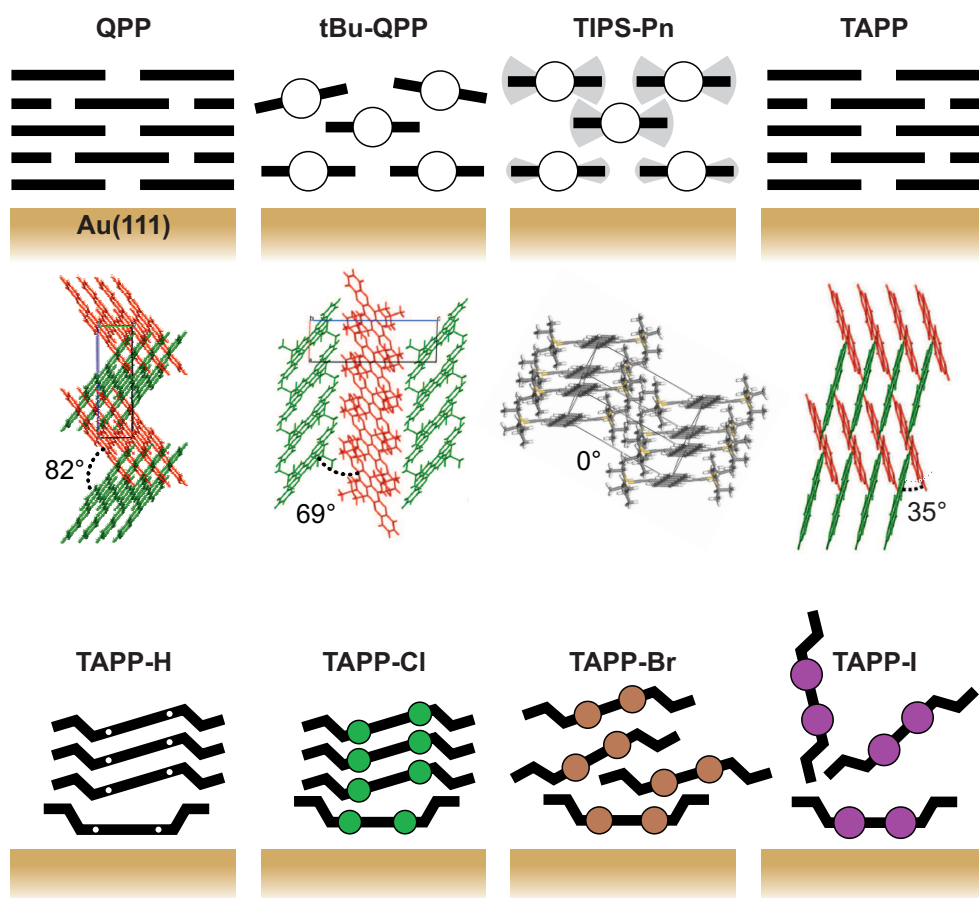


Figure 4.14.: Developed adsorption geometry models for the investigated molecules. For QPP [221], tBu-QPP [221], TIPS-Pn [222], and TAPP [216] the corresponding bulk crystal structures measured by X-ray diffraction are shown. Figure adapted from ref. [218].

To summarize, if an adsorbing molecule shows a reasonable large planar aromatic system it will adsorb in a planar fashion on interacting metal substrates to increase the metal- π interaction, also if there are bulky substituents. This flat monolayer now acts as a template for the second layer to now increase the intermolecular π - π interaction between two layers and so on (QPP, textittBu-QPP, TIPS-Pn, TAPP) as long as such a behavior is not prevented by the orientation of flexible substituents in the monolayer (C_3F_7 -substituted TAPP derivatives). There is no observation of a critical coverage from whereon another adsorption geometry is adopted. However, it is self-evident, that the number of defects increases with an increasing number of layers and therefore more and more seed crystals exist that will lead to the bulk like crystal structure.

4.5. Discussion: Substrate-Directed Growth and the Influence of Substituents

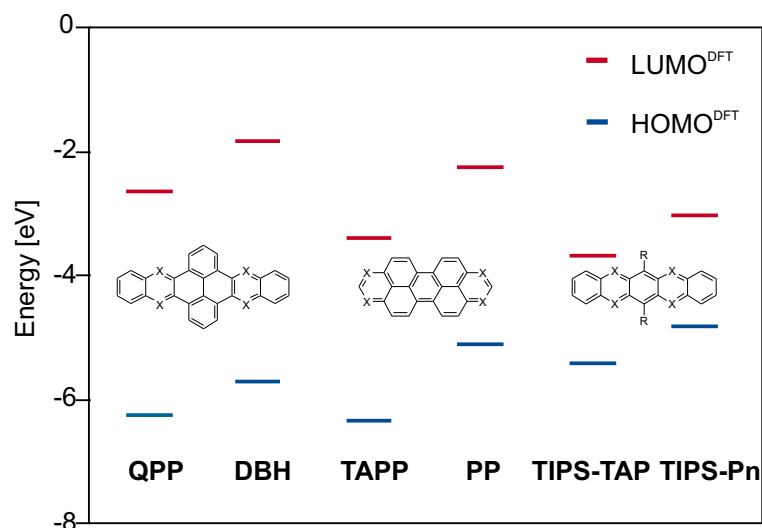


Figure 4.15.: Overview of the calculated HOMO and LUMO energies of the N-heteropolycyclic molecules (X = N in the depicted structural formulas) QPP, TAPP, and TIPS-TAP and their respective hydrocarbons (X = C-H in the depicted structural formulas) dibenzo[*hi,uv*]hexacene (DBH), peropyrene (PP), and TIPS-pentacene (TIPS-Pn). Figure adapted from ref. [55].

Regarding the electronic HREELS measurements, it has to be noted, that in all cases the monolayer was hard to investigate due to screening effects from the substrate or poor signal-to-noise ratios. The study of thin films with a coverage between 4 and 10 ML showed a surprisingly well agreement with UV/Vis data obtained from bulk or solution investigations showing negligible intermolecular interactions. This study lead also to qualitative and for the distinct cases also quantitative understanding of the influence of substituents at the particular positions on the optical gap. The comparison of *t*Bu-QPP with QPP, as well as the comparison of the substituted TAPPs with the pristine one, confirm the assumption, that substitution in Y-position (compare to Fig. 4.1) has no influence on the optical gap as the participating frontier orbitals show no electron density there. The substitution in Z-position was only studied at the TAPP system and showed a shift of 0.28 ± 0.09 eV when substituting H with a halogen. In contrast to UV/Vis measurements, the nature of the halogen (chlorine, bromine, or iodine) had only a small influence on the size of the optical gap, which may be due to the poor resolution of the underlying spectra. The introduction of nitrogen into an aromatic hydrocarbon system

4. Adsorption and Growth of Functional Molecules on Au(111)

(X = N in Fig. 4.1) has only little influence on the size of the optical gap. Complementary DFT calculations in Figure 4.15 for the HOMO and LUMO energies of the studied N-hetero/hydrocarbon pairs clearly show the collective shifting of both the HOMO and the LUMO due to the substitution of C-H with N.

The small band gap of the pentacene derivatives compared to, e.g. TAPP or QPP, is due to the number of participating π -electrons. In the case of pentacene (and TIPS-Pn or TIPS-TAP; 22 π -electrons) it fulfills the rule of Hückel [223] whereas $4n + 2$ π -electrons lead to aromaticity and $4n$ π -electrons to anti-aromaticity. PP or TAPP with 28 and QPP or DBH with 32 π -electrons are anti-aromatic. This classification is only strict for small aromatic systems but as the observed differences show, there are still effects in larger systems.

5. Collective Excitations at Metal/Organic Interfaces

Regarding the electronic structure, interfaces can show exceptional properties. Bulk behavior is completely altered due to the reduction from a three-dimensional to a two-dimensional system. This also concerns collective excitations of electrons, known as plasmons. Surface plasmons are located at interfaces and can be sensitive to the charge density distribution at this interface [87] and therefore deliver information about the underlying electronic structure. This is used e.g. in surface plasmon resonance-based techniques like biosensors or lab-on-a-chip sensors [224] which all work with the high sensitivity of the surface plasmon behavior on layer thickness or molecular adsorption. The smaller wavelength of surface plasmons compared to optical photons also allows the confinement of photons into smaller structures and the merging of electronics and photonics at the nanoscale [225] that offers opportunities in applications like nanolithography [226] or light generation [227]. Collective excitations are widely studied at metal/vacuum interfaces [76, 80, 228–233] but only rarely at metal surfaces covered with thin organic films [82]. At such interfaces, the electronic structure of the metal and the organic film can be changed drastically. Tautz *et al.* [44, 83] observed a screening of the adsorbate's frontier orbitals, a shift of the substrate's surface plasmon frequency and the arising of new low-energy features at 0.4 eV in electronic HREELS measurements of thin perylene-3,4,9,10-tetracarboxylic dianhydride (PTCDA) films on Ag(111) and Ag(110) (see also Fig. 5.11 (c)). The group of T. Angot investigated similar low-energy transitions in detail with angle-resolved electronic HREELS at the ZnPc/Ag(001) and observed an interesting dispersion behavior [82, 234].

Earlier investigations of surface plasmons at metal/vacuum interfaces were done with optical techniques or high-energy EELS (≈ 50 keV) [235, 236]. The first need special conditions or rough surfaces as light cannot directly excite surface plasmons due to different phase velocities and therefore different wave vectors which prohibit a direct coupling [74]. The latter lack of surface sensitivity due to the large penetration depth of high-energy electrons. The obtained

5. Collective Excitations at Metal/Organic Interfaces

results with both techniques were ambiguous and the surface plasmon dispersion was either positive or zero [229, 237]. Electronic HREELS instead is a powerful technique for the investigation of plasmonic transitions as it combines the surface sensitivity and the possibility of direct excitation [74, 238]. Angle-resolved electronic HREELS can further give detailed information about the dispersion. The first part of this chapter shows and discusses the results obtained by angle-resolved HREELS, first for the pristine gold surface, followed by adsorbate-covered Au(111) surfaces. The second part deals with particular vibrational features which correspond to the electronic HREELS measurements. For a better understanding, a brief introduction into surface plasmons with a focus on the properties of the Au(111) surface is given first.

5.1. Background: Plasmons at Metal Surfaces

For many applications, it is sufficient to describe electrons in metals with the classical Drude model [239]. Here the metal is described as an ionic crystal and the electrons move freely as a so-called *electron gas*. This term refers to similarities to the kinetic gas theory whereas without an external electrical field the electrons in a conductor behave like gas particles in an enclosed volume. Due to long-range Coulomb interactions, the electrons in an electron gas can show collective behavior [240]. For metals, such collective oscillations of the charge-density are a fundamental property. The corresponding quasiparticle is the plasmon. The plasma frequency of such a bulk plasmon (BP) ω_{BP} derived from Poisson's equation of the electrostatics, the continuity equation, and Newton's second law [107, 241] is

$$\omega_{BP} = \sqrt{\frac{n_e e^2}{\epsilon_0 m_e}} \quad (5.1)$$

with the electron density n_e , the elementary charge e , the vacuum permittivity ϵ_0 , and the electron mass m_e . With the surface plasmon, Ritchie [242] introduced a corresponding collective excitation at the metal/dielectric interface. Its frequency ω_{SP} with the dielectric's permittivity ϵ_2 is given by

$$\omega_{SP} = \omega_{BP} \sqrt{\frac{1}{1 + \epsilon_2}}. \quad (5.2)$$

Within a metal which has a dielectric function described by the Drude model, there exists a collective excitation above the plasma frequency with both pho-

5.1. Background: Plasmons at Metal Surfaces

tonic and plasmonic character, the bulk plasmon polariton (BPP). In a simple (local) model, the longitudinal bulk plasmon is dispersion-less whereas the BPP shows dispersion and its frequency ω_{BPP} dependence on the wave vector q is given by

$$\omega_{BPP} = \sqrt{\omega_{BP}^2 + c^2 q^2} \quad (5.3)$$

with c , the speed of light. A similar excitation can also take place at the metal/dielectric interface or in two-dimensional systems like artificially structured semiconductors [243], graphene [244, 245] or ultra-thin metal layers on dielectric substrates [246] and is named surface plasmon polariton (SPP). Here, the strong localization of the charges in the dimension perpendicular to the surface causes a completely altered dispersion relation which shows a square-root-like dependence on the wave vector:

$$\omega_{SPP} = \sqrt{\frac{\epsilon_1 + \epsilon_2}{\epsilon_1 \epsilon_2}} c q \quad (5.4)$$

with the permittivity of the metal and the dielectric material ϵ_1 and ϵ_2 , respectively. In the long wavelength limit, the SPP behaves like a photon (dispersion relation $\omega = cq$), for higher q it approaches asymptotically the surface plasmon frequency.

The influence of the considered dimension on plasmonic dispersion was studied within the random phase approximation (RPA) by Das Sarma *et al.* [247] and the obtained dispersions are depicted in Figure 5.1 showing for $q \rightarrow 0$ the finite value, the \sqrt{q} -dependence, and the $\sqrt{\ln(q)}$ for 3D, 2D, and 1D, respectively.

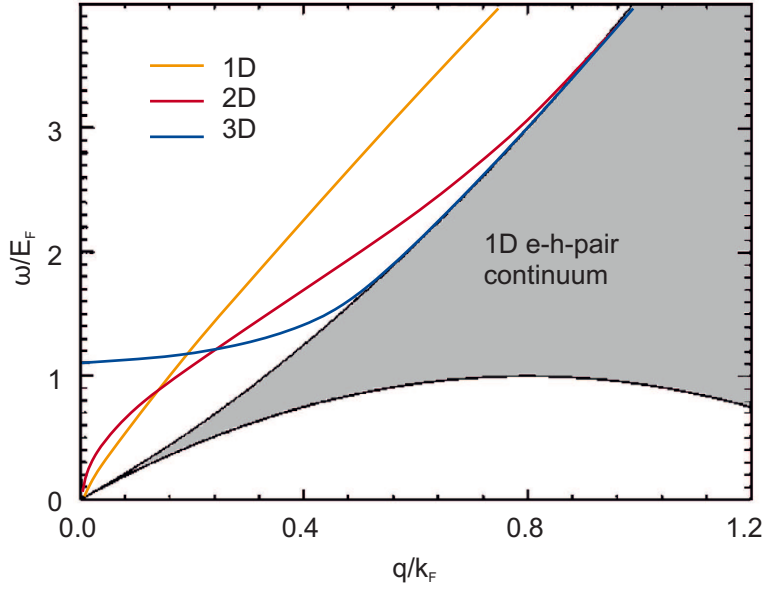


Figure 5.1.: Calculated 1D (orange), 2D (red), and 3D (blue) plasmon dispersion with frequency ω and wavevector q . The grey shaded area is the calculated region of the single-particle electron-hole-pair continuum in one dimension (adapted from ref. [247]).

The combined photonic and plasmonic character of an SPP is visualized in Figure 5.2 (a) where the longitudinal charge oscillation is shown as circles at the metal surface and the corresponding transversal electrical field lines are shown above and below. The interaction of a two-dimensional system of free electrons with another two- or three-dimensional electron gas (see Fig. 5.2 (b)) can lead to a novel excitation which shows a sound-like behavior (linear dispersion in the long wavelength limit) and is therefore called *acoustic* plasmon [248]. This new excitation attracted notable interest as it offers possible explanations for dynamics near the Fermi level or the mediation of superconductivity which cannot be explained with conventional 2D or 3D plasmons due to different long wavelength behavior [249–251]. The acoustic plasmon was first considered for a collective excitation in a system of two different electronic carriers [252].

5.1. Background: Plasmons at Metal Surfaces

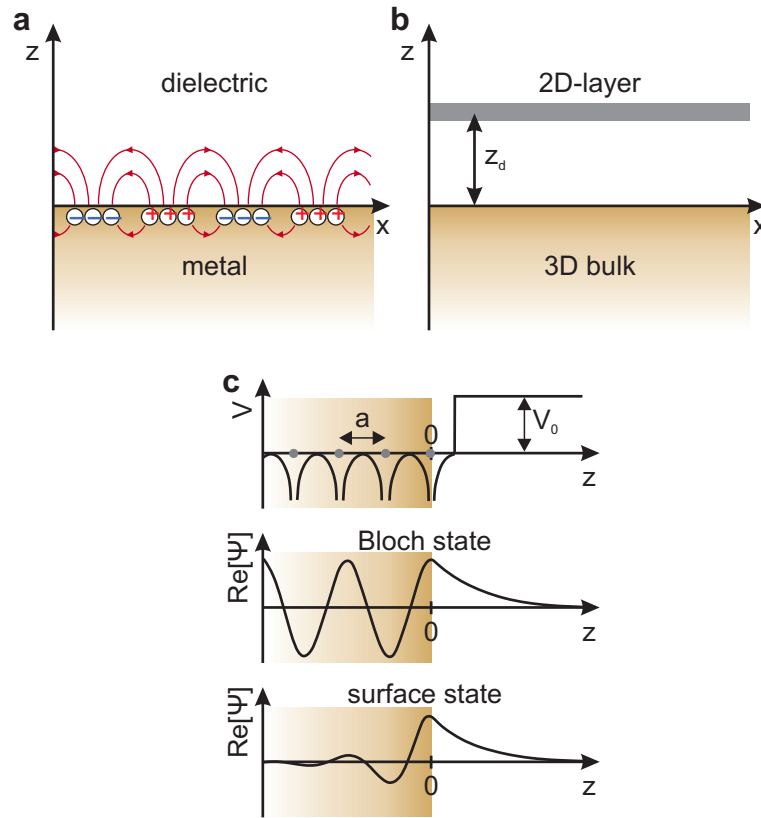


Figure 5.2.: (a) Surface plasmon at the metal/dielectric interface with its combined electromagnetic wave (red arrows) and surface charge (+ and -) character. (b) Interpretation of surface state electrons as a 2D sheet in the distance z_d to the surface of the 3D bulk material (adapted from ref. [253]). (c) top: Potential (V) vs. distance z with the metal/dielectric interface at $z = 0$ with lattice constant a and vacuum potential V_0 . (c) center: Real part of the one-dimensional Schroedinger equation solution corresponding to bulk (Bloch) states. (c) bottom: Real part of the one-dimensional Schroedinger equation solution corresponding to surface states. Adapted from ref. [254].

Chaplik *et al.* [255] later discussed acoustic plasmons in metal-insulator-semiconductor systems and found out that the valence electrons at the metal surface alter the plasmon in the semiconductor *via* screening from square-root to linear behavior. But the existence of acoustic plasmons was only considered for spatially separated free electron systems as depicted in Figure 5.2 (b) [256, 257]. In 2004 Silkin *et al.* [248] predicted that dynamical screening in metals

5. Collective Excitations at Metal/Organic Interfaces

with a partially filled surface state band should also lead to the formation of a 2D plasmon with acoustic-like dispersion. They suggested the Be(0001) surface as a promising candidate and in 2007 Diaconescu *et al.* [76] found the experimental affirmation in an angle-resolved HREELS study of Be(0001). Figure 5.2 (c) shows the potential in a crystal with lattice constant a (top, $z < 0$) and the (simplified) step to the vacuum potential (V_0 , $z > 0$). The Schrödinger equation offers two types of solutions for such a system [258]. The first type (centre) behaves in the crystal-like normal Bloch waves and decays exponentially into the vacuum (Bloch states), the second type (bottom) decays exponentially both into the crystal as well as into the vacuum, hence is located at the surface (surface states) [254].

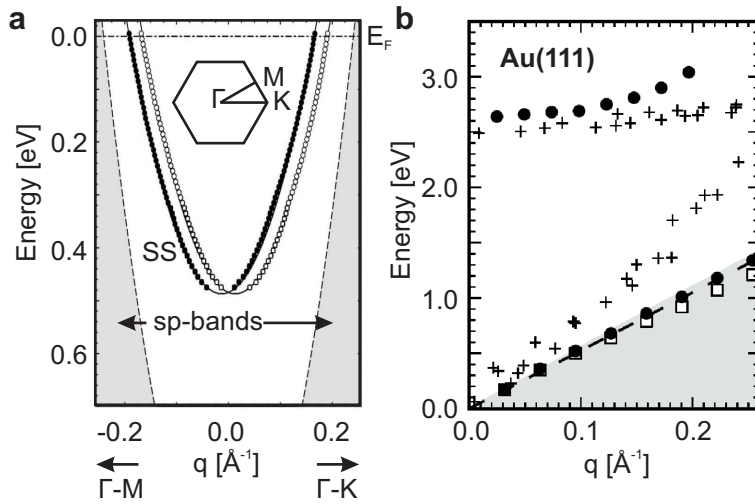


Figure 5.3.: (a) Dispersion of the surface state on Au(111) (note the Rashba-splitting [259]) in the depicted directions of the Brillouin-zone with the surface state (SS), the sp-band region (grey area) and the Fermi energy E_F (adapted from ref. [260]). (b) Calculated (solid dots and open squares, see ref. [261] for details) and measured (HREELS, crosses) data for the conventional (CSP) and acoustic (ASP) surface plasmon of Au(111) (adapted from ref. [261] with experimental data from ref. [78]).

Figure 5.3 (a) shows the surface state (SS) dispersion as obtained by angle-resolved photoelectron spectroscopy (ARPES) for Au(111) [260]. The splitting (white and black dots) occurs due to the Rashba-effect [259]. With the crossing of the Fermi level (see the top of the graph), the suggested requirement for the

5.2. Angle-Resolved electronic HREELS measurements

occurrence of acoustic plasmons is fulfilled here. Results for the plasmonic excitation at the Au(111) surface obtained experimentally with HREELS [78, 230] and theoretically with two different methods [261] are shown in Figure 5.3 (b). The experimental data (crosses) show clearly the two plasmonic branches, the “conventional” plasmon between 2.5 and 3 eV and the “acoustic” one with a linear dispersion below. These findings were later corrected by Vattuone *et al.* [79] who now investigated an Au(111) single crystal instead of a deposited 90 nm thick film in ref. [78] and showed that the observed peak which shows a linear dispersion essentially consists of two individual ones so that the actual acoustic plasmon agrees better with the theoretical predictions shown in Figure 5.3 (b). Experimental (Cu) [80, 81] and theoretical (Ag, Cu) [261] studies showed that the 111-surfaces of the other coinage metals have similar properties and can also exhibit a 2D plasmon with acoustic-like dispersion. The investigation in this study starts with a verification of the mentioned HREELS measurements on the pristine Au(111) surface before the results for adsorbate-covered samples are presented. A detailed compendium of the theory behind surface plasmons and surface plasmon polaritons can be found in ref. [262].

5.2. Angle-Resolved electronic HREELS measurements

Due to the mentioned mismatch of plasmonic and light wave vectors, direct coupling between light and plasmon and hence plasmonic excitations are hindered when metallic samples are investigated with optical techniques. This motivates the use of electrons for studying surface plasmonic properties of materials. EELS and HREELS have been widely used [76, 78–81, 230] in this field and the possibility of angle-resolved measurements offers the opportunity to measure sensitive to the participating wave vector parallel to the surface q_{\parallel} and thus detect dispersions. Nevertheless, it is still challenging to find the right scattering geometry and incident electron energy that the measured scan line (energy loss *vs.* momentum transfer) crosses the plasmonic dispersion curve. The transferred parallel momentum is for an angle-resolved EELS study given by equation 2.10 in section 2.2. A small angle step size in angle-resolved measurements increases the information about dispersion and dipole-activity. To enable this within reasonable experimental efforts an automated angle rotation was established during this work. The Arduino[®] controlled step motor

5. Collective Excitations at Metal/Organic Interfaces

allows together with the spectrometer software's ability to perform repeated measurements with variable energy and angle step size. The only limitation is the software's maximum number of subsequently recorded spectra of 999. The step motor unit is described in section 2.4.1, a commented program code can be found in App. I.1.

5.2.1. Au(111)

The pristine Au(111) surface was one of the first systems for which the existence of the proposed acoustic surface plasmon was experimentally proven [78]. The very first system, the Be(0001) surface, showed the collective excitation in a well-defined form up to almost 2 eV at an incident electron energy of $E_0 = 10.74$ eV [76]. On Au(111) the corresponding loss-intensity of the surface plasmon peak drops down faster with increasing off-specular angle measurements and becomes difficult to detect. The first step in this study on the influence of an adsorbate on such collective excitations is the reproduction of former results for the bare surface to see if sensitive parameters for sample preparation and measuring (E_0 , Φ_I , Φ_S) are appropriate for the detection of collective low-energy excitations. Figure 5.4 (a) shows the HREELS measurements for different angles $\Delta\Phi$ off-specular (in the sense, that rotating the analyzer towards the surface normal is counted as positive $\Delta\Phi$ according to Fig. 2.5). For angles between 1.8° and 4.7° , clearly, two peaks (ASP and X) can be identified which is in agreement with ref. [79] and in contradiction to ref. [78] where the split peak was not resolved. The conventional plasmon (CSP) [230] is barely visible in most spectra around 2.5 eV. The loss energies of the features *vs.* the corresponding transferred parallel wave vector $q_{||}$ are plotted in Figure 5.4 (b). They are in excellent agreement with the measurements of Vattuone *et al.* [79]. The ASP shows clearly a linear dependence on q and goes to 0 for $q \rightarrow 0$. It needs to be mentioned that the shown data only covers positive momentum transfer as the observed peaks in the negative $q_{||}$ regime were less well-defined and the intensity decreases rapidly with higher negative off-specular angles. Such a behavior was observed before in literature [76] and has been assigned to the narrow dipole lobe that can cause a low excitation probability in the respective regime.

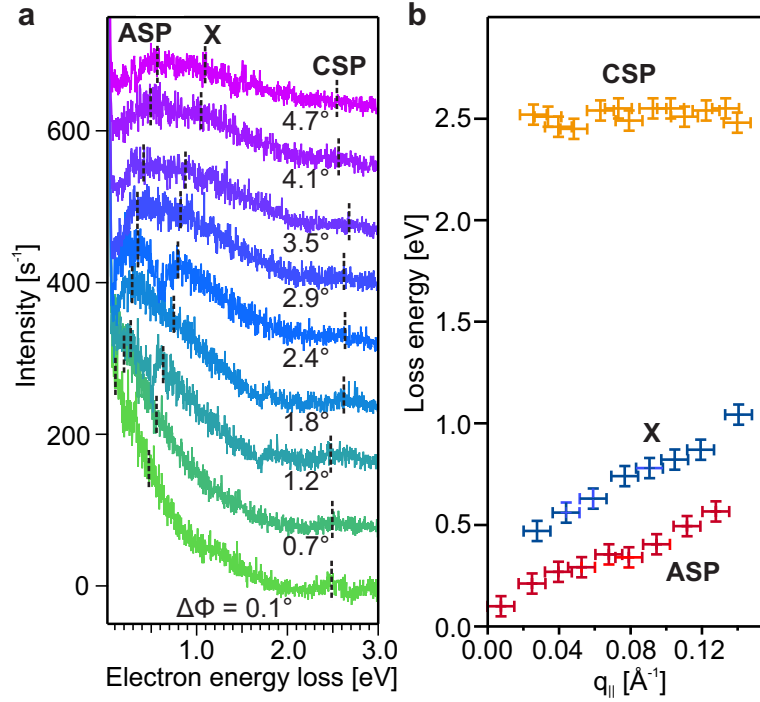


Figure 5.4.: (a) Series of electronic HREEL spectra recorded under $\Delta\Phi$ from 0.1° to 4.6° off-specular analyzer angles and with a primary electron energy $E_0 = 15.5$ eV. The spectra are separated vertically by 80 counts s^{-1} and peak positions are marked with dashed lines for clarity. (b) Corresponding dispersion relations of the marked transitions.

The CSP around 2.5 eV shows more or less no dispersion within the observed momentum range and small signal-to-noise ratio, but the reported [230] small positive dispersion lies in the error bars of the present experimental data. ASP and CSP show high accordance to the calculations by Yan *et al.* [261] shown in Fig. 5.3 (b). The feature X shows a dispersion almost parallel to the ASP, shifted by roughly 0.3 eV to higher loss energies and thus not vanishing for $q \rightarrow 0$. Vattuone *et al.* [79] described it as the upper threshold of interband transitions between bulk states and the surface state band but did not explain the situation for small $q_{||}$ where the surface state is occupied (see Fig. 5.3 (a)) and an excitation should be impossible.

With this knowledge of being able to excite and measure acoustic surface plasmons on the bare Au(111) surface the next step is the investigation of the influence of adsorbates.

5.2.2. TCNQ and F₄TCNQ on Au(111)

To recapitulate, in the case of bare metal surfaces like Be(0001), Au(111), and Cu(111), the collective low-energy excitation arises from the interplay of 3D bulk electrons with the electrons in the partially filled surface state band. Thus the influence of adsorbates on 2D plasmonic excitation is obviously connected with the influence of adsorbates on the surface state electrons. It is known from the literature that this influence ranges from quenching and thus frustrating a collective excitation [263] up to a transfer of the metallic properties to the adsorbate layer and band formation in a spatially separated 2D free-electron system [44,264]. A high electron affinity (EA) of the adsorbate helps to form a free-electron system due to withdrawing electron density from the substrate. Therefore a model system with tunable EA and well-studied adsorption properties was chosen for the present investigation. Tetracyanoquinodimethan (TCNQ) (structural formula, see Fig. 5.5 (b)) has an EA derived from inverse photoemission spectroscopy (IPES) of 4.23 eV.

Fluorination increases the EA up to 5.08 eV [265] for 2,3,5,6-tetrafluorotetracyanoquinodimethane (F₄TCNQ). This difference leads to a special situation for the adsorption on an Au(111) surface. While for TCNQ the EA is not high enough to allow charge transfer from the metal to the adsorbate, F₄TCNQ is charged. Due to highly ordering and epitaxial growth of F₄TCNQ on Au(111) the charge is spatially distributed and a space charge region extending up to a coverage of 10 ML into the organic film can be found [266].

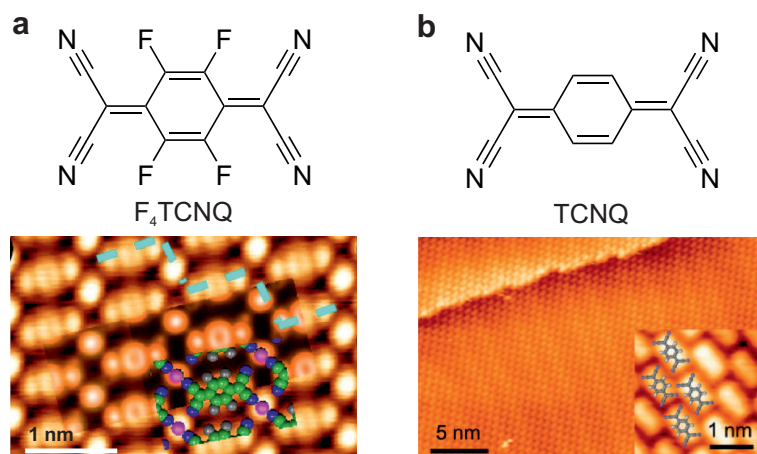


Figure 5.5.: Molecular structures and STM images of F₄TCNQ on Au(111) (a), adapted from ref. [267] and TCNQ on Au(111) (b), adapted from ref. [268].

5.2. Angle-Resolved electronic HREELS measurements

Both molecules have been intensively studied on single crystal surfaces [267–272] as well as in devices like photovoltaic cells [273] or transistors [274, 275]. STM investigations (see Fig. 5.5 (b)) revealed a brick-like adsorption geometry with stabilizing hydrogen bonds between neighboring molecules for TCNQ on Au(111) [268]. A study of F₄TCNQ on Au(111) showed significant differences [267]. The bright spots between the molecular features in the STM image in Figure 5.5 (a) are assigned to segregated Au adatoms [276]. The interaction between the Au(111) surface and the F₄TCNQ is thus strong, that single Au adatoms (purple in Fig. 5.5 (a)) are lifted and coordinated by two nitrogen atoms of neighboring molecules (blue) leading to a charge transfer from the metal to the molecule. Note, that at the corner of four adsorbed F₄TCNQ molecules with one Au adatom centered only two nitrogen atoms of two molecules are directly coordinated to the adatom while the distance to the other two nitrogen atoms is increased.

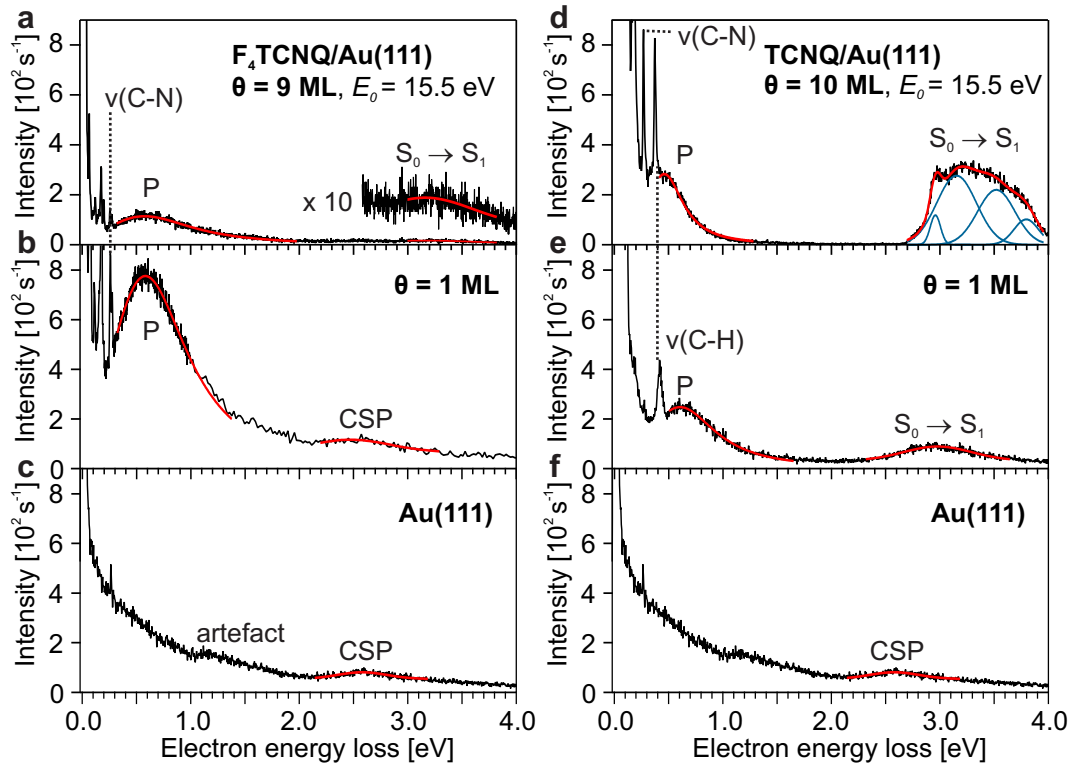


Figure 5.6.: Electronic HREEL spectra including fits for the relevant peaks for F₄TCNQ multi- (a) and monolayers (b), TCNQ multi- (d) and monolayers (e), and Au(111) ((c) and (f)). The primary electron energy E_0 is 15.5 eV. Labeled peaks are the plasmonic excitation (P), the conventional surface plasmon (CSP), and the vibronic $S_0 \rightarrow S_1$ transition peaks.

5. Collective Excitations at Metal/Organic Interfaces

Details about sample preparation and dosing for all shown measurements are summarized in Table B in App. B. The electronic HREELS results for F₄TCNQ on Au(111) in specular geometry are shown in the left part of Fig. 5.6. At the bottom, (c), the pristine Au(111) shows the CSP at 2.6 eV as introduced in the last section and the before mentioned spectrometer artefact between 1.2 and 1.8 eV. The ASP is not visible here as it vanishes for $q \rightarrow 0$ (specular measuring geometry) and the possible interband transition (X in Fig. 5.4) cannot be resolved as a separated peak as it is overlapped by the large Drude tail of the elastic peak. Figure 5.6 (b) now shows the surprising result for a monolayer of F₄TCNQ on Au(111). Not only a broad low-energy feature (P) around 0.5 eV loss energy is visible despite measuring in specular geometry but this feature also shows a drastically increased intensity and signal-to-noise ratio compared to the ASP measurements on the pristine Au(111) surface presented in section 5.2.1. The CSP is rather unaffected by the organic layer and still appears at 2.6 eV as a small peak only a little above the detection limit. Increasing the coverage up to 9 ML (Fig. 5.6 (a), note the unchanged y-axis range for comparison of absolute intensities) reduces the intensity of P but does not affect its energetic position. The CSP is vanished and a peak associated with the S₀ → S₁ transition (optical gap) is visible more as a step edge (see enlarged part of Fig. 5.6 (a)) than a well-defined peak around 3.3 eV (UV/Vis: 3.1 eV [277]). Interestingly the situation in the multilayer alters completely by changing the procedure of sample preparation. Whilst the presented multilayer spectrum was obtained after dosing on the sample at room temperature, Figure I.2 in App. I.2 shows a 3.5 ML thick F₄TCNQ layer dosed on a 120 K cold Au(111) substrate. Although the coverage is half of the amount of the coverage in Figure 5.6 (a), feature P has almost vanished and also shifted to lower energies, instead, the S₀ → S₁ is dominating the spectrum. The electronic HREELS results in chapter 4 and earlier investigations [44, 58] showed that a well-defined peak which can be assigned to the S₀ → S₁ transition in the multilayer is the usual case. For F₄TCNQ on Au(111) it is concluded that dosing on a 120 K cold sample leads to a less-ordered structure with non- or only weakly interacting molecules. In contrast, the thermal energy of a 300 K warm sample allows reorganization to a well-defined molecular crystal. The well-ordered, epitaxial film growth is also confirmed by low-energy electron diffraction (LEED) measurements which show a surprisingly similar pattern for the monolayer as well as for the 20 ML thick F₄TCNQ film dosed on

5.2. Angle-Resolved electronic HREELS measurements

Au(111) at 300 K sample temperature [266]. In the same study, two-photon photoemission revealed the already mentioned space charge region extending up to 10 ML into the organic film which explains the hindered HOMO \rightarrow LUMO ($S_0 \rightarrow S_1$) excitation. Note, that the decreased intensity of P but an overall similar spectrum of 1 ML and 9 ML F_4 TCNQ in Figure 5.6 cannot be explained by possible Stranski-Krastanov growth as the signal for the $S_0 \rightarrow S_1$ transition from molecules located in the multilayer islands should be much larger in that case (see section 4.1 for more details).

The corresponding data for TCNQ on Au(111) is shown in the second column of Figure 5.6. The CSP of the Au(111) surface (f) has now vanished in the monolayer spectrum (e). Interestingly and in contrast to F_4 TCNQ, the monolayer shows a well-defined peak at 3.0 eV which can be assigned to the $S_0 \rightarrow S_1$ transition by comparison to UV/Vis measurements in solution (3.1 eV [277]). Again there is a low-energy feature P observable, shifted slightly to 0.6 eV and with significantly reduced intensity, compared to F_4 TCNQ (note the ordinates' equal scaling). The present C-H bonds cause an additional well-pronounced peak assigned to the excitation of C-H stretching vibrations at 0.4 eV. The increase in coverage to 10 ML (spectrum Fig. 5.6 (d)) causes a shift of P to slightly lower energies and, more significant, a decrease in intensity especially when the broad Drude tail of the elastic peak is taken into account. On the other hand the intensity of the peak assigned to the optical gap rises and shows vibronic features, i.e., the $S_0 \rightarrow S_1$ and additional vibrational excitation of $\nu(\text{C-H})$ or $\nu(\text{C-C})$ bonds (compare to chapter 4 where similar features were observed in all systems). In this case, the slight deviations of feature P may be a hint to Stranski-Krastanov growth. Then, the excitation of feature P would still take place in the monolayer areas of the sample, the intense $S_0 \rightarrow S_1$ -peak instead is caused by intramolecular excitations in the islands.

The peaks labeled as P in Figure 5.6 can be precisely fitted (red lines) with a Drude function [82] which arises from the dielectric function for metals consisting of the interband transition contribution ϵ_∞ and a Drude term for the contribution of free carriers:

$$\epsilon(\omega) = \epsilon_\infty - \frac{\omega_{BP}^2}{\omega(\omega + [i/\tau])} \quad (5.5)$$

where ω_{BP} is the bulk plasma frequency and τ the relaxation time. The imaginary part Im now corresponds to the Drude-type loss function [63] and the measured HREEL intensity I_{loss} [82, 278, 279]

5. Collective Excitations at Metal/Organic Interfaces

$$\text{Im} \left\{ \frac{-1}{1 + \epsilon(\omega)} \right\} = \frac{1}{1 + \epsilon_\infty} \frac{\omega \omega_P \tau^{-1}}{(\omega^2 - \omega_P^2)^2 + \omega^2 \tau^{-2}} = I_{loss} \quad (5.6)$$

with the energetic position of feature P, ω_P . Note that $\frac{1}{1+\epsilon_\infty}$ and τ^{-1} define the maximum intensity and linewidth of P, respectively. The assumption of free carrier behavior leads to the need for investigation of the dependence on the transferred parallel momentum $q_{||}$, i.e., the dispersion.

As shown above, for Au(111), angle-resolved HREELS offers the opportunity to do so and the obtained results for F₄TCNQ and TCNQ are summarized in Figure 5.7. (a) and (b) show waterfall plots (x- and y-offset between the spectra) of 45 electronic HREEL measurements between -5° (black) and $+5^\circ$ (purple) degrees off-specular analyzer angle for monolayers of F₄TCNQ and TCNQ on Au(111), respectively. The most important finding here is, that the energetic position of feature P shows a dependency on the transferred momentum. In Fig. 5.7 (c) the respective energies at the maximum intensities in (a) and (b) are plotted against the transferred momentum and show clearly a dispersive behavior indicating delocalization. Note for comparison the feature assigned to the S₀ → S₁ excitation around $E_{loss} = 3.0$ eV in Figure 5.7 (b) which is clearly unaffected in energy, linewidth and intensity by the transferred parallel momentum indicating localization on single molecules. The spectra in Figure 5.7 (a) reveal also a strong dependency of the measured loss intensity on the off-specular angle, indicating a strong dipole activity of the respective excitation, i.e., a corresponding dynamic dipole moment perpendicular to the metal surface. This is depicted in Figure 5.7 (d), where blue data points refer to F₄TCNQ, red data points to TCNQ. The maximum intensity is about three times as large for F₄TCNQ as for TCNQ. Both curves show the highest intensity around $q_{||} = 0.04 \text{ \AA}^{-1}$ and an asymmetric behavior with a tail towards higher $q_{||}$ values.

5.2. Angle-Resolved electronic HREELS measurements

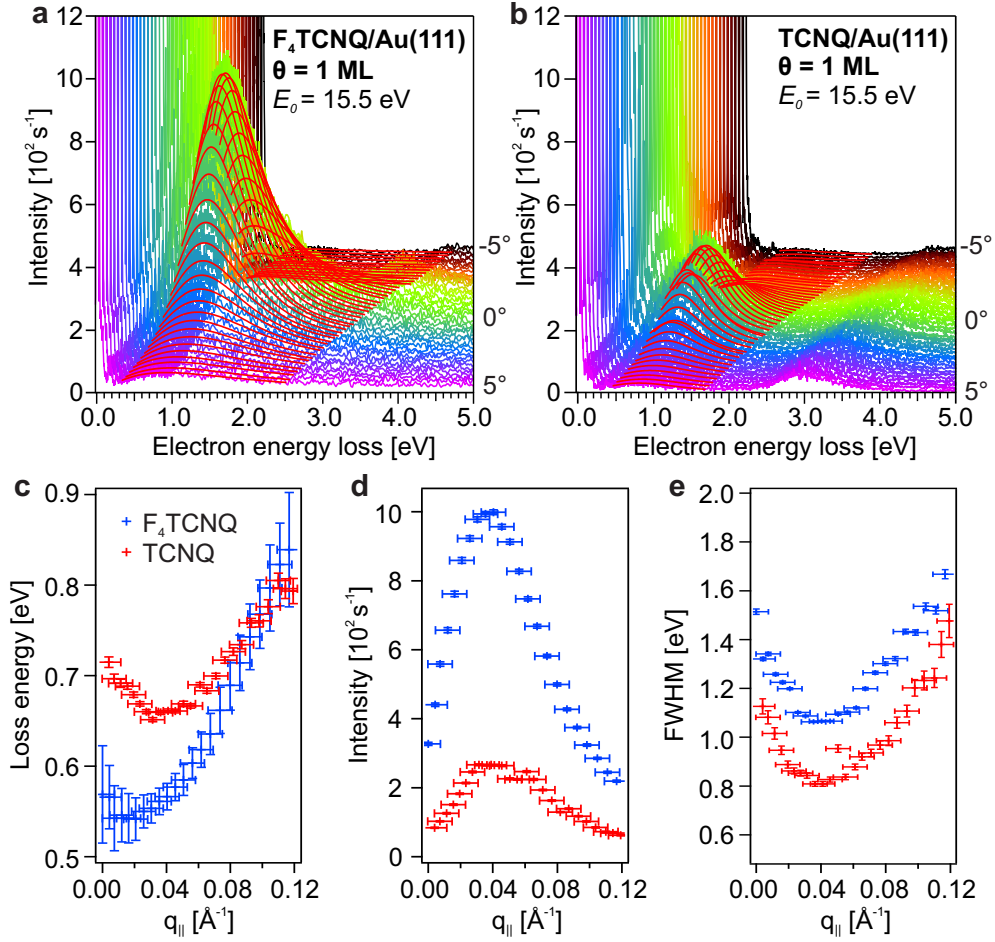


Figure 5.7.: (a) and (b) 45 angle-resolved electronic HREEL spectra from $\Delta\Phi = -5^\circ$ to 5° for monolayers of F_4TCNQ and $TCNQ$ on $Au(111)$, respectively. The primary electron energy E_0 is 15.5 eV. Drude-fits to the plasmonic excitation are shown in red. (c), (d), and (e) show the loss energy of the plasmonic excitation, the corresponding intensity, and linewidth depending on the wavevector component parallel to the surface $q_{||}$, respectively.

The curve for $TCNQ$ (red data points in Fig. 5.7 (c)) shows a minimum of 0.65 eV at $q_{||} = 0.03 \text{ \AA}^{-1}$, F_4TCNQ has its minimum of 0.53 eV at $q_{||} = 0.02 \text{ \AA}^{-1}$. It is hard to distinguish if the underlying dispersion relation is quadratic (as known from free electrons) or linear (as presented for the ASP in the last section). The dependency of the linewidth (in terms of the full width at half maximum, FWHM) on the transferred momentum is plotted in Fig. 5.7 (e). The almost quadratic curves are centred around 0.04 \AA^{-1} and have their minima at 0.8 and 1.1 eV for $TCNQ$ and F_4TCNQ , respectively. This behavior is comparable to the FWHM dispersion of surface plasmons for metals like Na,

5. Collective Excitations at Metal/Organic Interfaces

K, and Cs [74, 278, 280] indicating the existence of almost free carriers at the interface.

Other measurements which aimed at the influence of the primary electron energy E_0 and the coverage on the observed plasmonic feature need further investigations and are therefore only shown and briefly discussed in App. I.4 and App. I.5, respectively. It needs to be mentioned that all measurements are not performed along one of the high-symmetry axes as the used experimental setup does not contain a LEED spectrometer to determine the crystal orientation. The use of a crystal where the orientation was measured before at a different setup allowed a rough determination of the orientation during the HREELS measurements. A comparison of angle-resolved HREELS measurements in two different crystal orientations (one along the ΓK -direction) revealed no significant differences within the measurement uncertainty (see Fig. I.3 in App. I.3).

In a previous HREELS study [281], where only spectra recorded in specular geometry were shown, no electronic low-energy excitation was observed. A possible explanation would be a different surface cleanliness or a wrong coverage determination by using a quartz microbalance compared to the TPD based procedure in this work.

So far, the results suggest a collective excitation with a plasmonic character as the origin for the observed dispersive low-energy feature. Before the obtained results are compared to literature, discussed and interpreted in detail, complementary results obtained in the present study for additional metal/organic interfaces are presented.

5.2.3. Analogous Excitations in other Systems

As done before for, e.g. PTCDA/Ag(111) [44], the measured low-energy feature in the F_4 TCNQ/Au(111) system could be associated with the strong adsorbate/substrate interaction (chemisorption), charge transfer, and adatom coordination. Therefore the finding, that the particular excitation occurs also in a weaker interacting system such as TCNQ/Au(111) and is not depending on the special situation at the F_4 TCNQ/Au(111) interface is surprising. Hence, an extension of the current study to further well-defined adsorbate/substrate systems is appropriate. The structural formulas of the investigated further molecules are listed in Figure 5.8.

5.2. Angle-Resolved electronic HREELS measurements

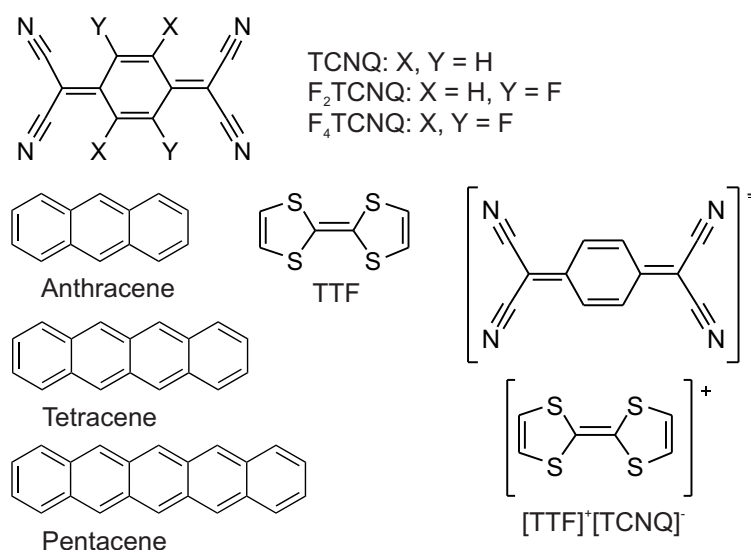


Figure 5.8.: Structural formula of the here studied molecules: F_nTCNQ ($n = 0, 2, 4$), TTF, $[\text{TCNQ}]^-[\text{TTF}]^+$, anthracene, tetracene and pentacene.

The study of 2,5-difluorotetracyanoquinodimethane (F_2TCNQ) on Au(111) can give hints if the difference of particular properties between $\text{F}_4\text{TCNQ}/\text{Au}(111)$ and $\text{TCNQ}/\text{Au}(111)$ occur abruptly or smooth. F_2TCNQ has been studied in charge transfer compounds [282] and transistors [283]. Its EA of 4.59 eV is located right in between TCNQ (4.23 eV) and F_4TCNQ (5.08 eV) [265]. The investigation of tetrathiafulvalene (TTF) on Au(111) extends the study to a system with an opposite charge transfer compared to F_4TCNQ , i.e., an electron transfer from the molecule to the gold substrate. TTF is widely used as n-dopant or pure single crystal in organic electronics [284, 285]. It is also part of the widely studied $[\text{TTF}]^+[\text{TCNQ}]^-$ salt, a charge-transfer system with interesting metallic properties [286, 287]. This donor/acceptor system with its positive charge on the TTF and the negatively charged TCNQ on Au(111) again completely alters the surface environment and is thus studied here to understand the influence of charged species. The investigation is completed by studying the acenes, namely pentacene, tetracene, and anthracene, which can lead to insights into the effect of more weakly bound adsorbates on the properties of the examined collective excitation and can give hints if the molecular size is critical for some collective properties at the interface. These larger acenes also have been used successfully in organic electronic devices [288–290].

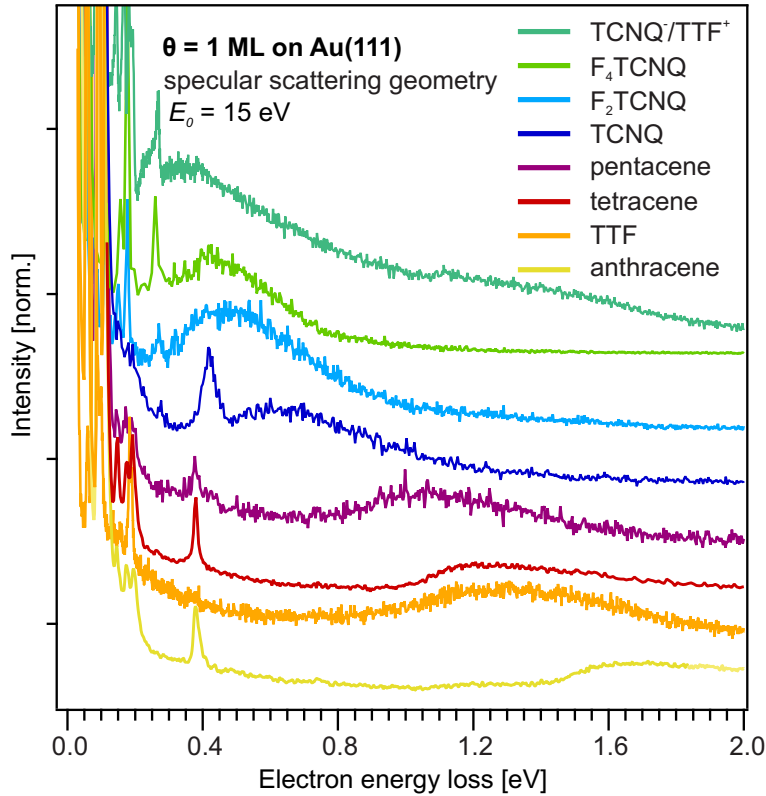


Figure 5.9.: Specular HREEL spectra for monolayer coverages on Au(111) of TCNQ/TTF salt (turquoise), F₄TCNQ (green), F₂TCNQ (light blue), TCNQ (blue), pentacene (purple, $\theta = 0.5$ ML), TTF (red), tetracene (orange), and anthracene (yellow). The primary electron energy E_0 is 15 eV.

Figure 5.9 shows electronic ($E_0 = 15$ eV) HREELS spectra for monolayers (0.5 ML for pentacene) of all mentioned organic molecules on the Au(111) surface recorded in specular scattering geometry. Preparation parameters are summarized in App. B, corresponding TPD measurements, specular and off-specular vibrational HREEL spectra, as well as angle-resolved electronic HREEL spectra and derived dispersions, can be found in App. I.6. In all spectra, a broad excitation is visible which shifts from 0.35 eV for the [TTF]⁺[TCNQ]⁻ salt to 1.67 eV for anthracene. All values are summarized in Table 5.1. The slightly different value for F₄TCNQ in Table 5.1 (0.44 eV) compared to the one from Fig. 5.6 (b) (0.5 eV) is attributed to the different primary electron energy ($E_0 = 15$ eV and 15.5 eV, respectively). The intensity is highest for the [TTF]⁺[TCNQ]⁻ salt, F₄TCNQ, and F₂TCNQ and decreases for the systems where the excitation is located at higher energies.

5.2. Angle-Resolved electronic HREELS measurements

Table 5.1.: Energetic position of feature P for [TTF]⁺[TCNQ]⁻, F₄TCNQ, F₂TCNQ, TCNQ, pentacene, tetracene, TTF, and anthracene on Au(111).

Organic adsorbate	energetic position [eV]
[TTF] ⁺ [TCNQ] ⁻	0.35
F ₄ TCNQ	0.44
F ₂ TCNQ	0.48
TCNQ	0.62
pentacene	1.05
tetracene	1.24
TTF	1.27
anthracene	1.67

In contrast to all other systems, where the plasmonic excitation shows its highest intensity at a monolayer coverage, in the pentacene/Au(111) system the highest intensity is observed for 0.5 ML coverage. This is shown in Figure I.8 in App. I.6 and assigned to the special adsorption behavior of pentacene. In section 3.4 it has been shown that up to 0.5 ML substrate-mediated interactions influence the adsorption and force pentacene to adsorb in a well-ordered pattern with large intermolecular distance. Before the observations are summarized and interpreted it is noted, that all molecules investigated in chapter 4 did not show a comparable excitation suggesting that the introduction of nitrogen into the aromatic system of planar molecules (TAPP and QPP) and/or the introduction of bulky substituents and therefore an increased distance between the metal surface and the organic film (TIPS-Pn, *t*Bu-QPP) suppresses the examined feature in the respective electronic HREEL measurements.

5.2.4. Discussion: Adsorbate Influenced Surface Plasmon Excitations

The observations of comparable broad low-energy electronic excitations at metal/organic interfaces are rare in literature. In the year 2000 Shklover *et al.* [264] found a similar feature at the PTCDA/Ag(111) interface at 0.4 eV which was assigned to a “monolayer exciton” due to the special properties at this particular interface with an electron transfer from the metal to the adsorbate and thus a completely altered electronic structure. The assumption

5. Collective Excitations at Metal/Organic Interfaces

of a localized molecular excitation can be excluded from the present measurements as off-specular electronic spectra (which were not carried out in the cited study) suggest clearly a dispersive behavior. A second observation at the perylene/Ag(111) interface in 2004 by Eremtchenko *et al.* [56] assigns a broad feature around 0.85 eV to an “interface excitation” without going more into detail. The first detailed angle-resolved study was realized by Salomon *et al.* in 2012 [82] at the ZnPc/Ag(001) interface. The measured dispersion is explained with a collective mode in a space charge layer between the metal surface and the organic adsorbate. As the origin of the space charge, they claim a vibrational excitation which leads to a dynamical charge transfer. This concept of an interfacial dynamical charge transfer (IDCT) is investigated and explained in detail in section 5.3.1 where it is also shown that it is not suitable to explain the plasmonic excitation in the systems studied in the present thesis.

But the assumption that the observed feature is a plasmonic excitation of a two-dimensional charge sheet seems likely. A well-studied system in this context is graphene, the prototype 2D-material [291] and with its delocalized π -electrons also a prototype for a 2D electron gas (for reviews regarding plasmonic excitations in graphene, see refs. [292] and [293]). Two-dimensional plasmons were observed e.g. for graphene on SiC, Si(111), and SiO₂ [244, 294–296]. The study of single-layer graphene on SiC(0001) [244] revealed an intensity *vs.* transferred momentum dependence similar to the measurements presented for F₄TCNQ and TCNQ on Au(111) in Figure 5.7 (c). The observed asymmetry and shift of the maximum to a positive q -value are assigned to characteristic properties of dipole scattering due to coupling to an image-charge electric field perpendicular to the charge sheet plane [297]. The more detailed investigation of Liu *et al.* [294] showed that an increase of graphene layers shifts the plasmon to lower energies and intensities, a behavior affirmed here especially for TCNQ on Au(111) (compare to Fig. 5.6 (d) and (e)).

The background section at the beginning of this chapter introduced the excitation of 2D plasmons and in particular the ASP on metal surfaces with a partially filled surface state (Be(0001) [76], Au(111) [78, 79], Cu(111) [80, 81]). Thus, it is known from the literature that there exists a low-energy plasmonic excitation on the bare metal surface and it is obvious that the participating charge sheet is strongly influenced by adsorbates. We propose, that the observed feature still originates from the same delocalized electrons as on the bare Au(111) surface but a pronounced influence on energetic position, intensity

5.2. Angle-Resolved electronic HREELS measurements

and dispersion is expected, depending on the molecular adsorbate. The most obvious deviation from the bare Au(111) is, that for the adsorbate/Au(111) systems the feature is observed most clearly in specular scattering geometry. For bare Au(111) it is due to the $E_{loss} \rightarrow 0$ for $q \rightarrow 0$ behavior not observable. An explanation could lie in the adsorbate domain size. Rocca *et al.* [298] showed in the year 1999 for ultrathin Ag films on Si(111)7×7 that the dispersion curves of an observed plasmon vary strongly with coverage and preparation procedure. Especially they observed that the dispersion curves show a break in the slope with a constant energy between $q = 0$ and that particular breakpoint. They explained it with different Ag island sizes due to the different deposition procedures and thus a minimal plasmon energy as the corresponding plasmon wavelength cannot extend the island size. Transferred to the here presented system it needs to be noted that on the hexagonal symmetry of Au(111) the build-up of domains is likely and thus there is evidence that the 2D charge sheet participating in a collective excitation is limited by these domains. In other words, on the bare surface, the infinite size leads to the observed $E_{loss} \rightarrow 0$ for $q \rightarrow 0$ dependence whereas the limited size due to adsorbate domains leads to the non-zero energy in the specular geometry shown in Fig. 5.7 and 5.9. This may not be relevant only for this work as there are several publications where a 2D plasmon is predicted either with \sqrt{q} or linear dependency on q but the experimental data suggest a non-zero plasmon energy for $q \rightarrow 0$ [244, 294, 299]. Therefore a detailed analysis of the dispersion curves with a comparison to theoretical models known from literature is set aside here as first theoretical input has to reveal insights into the conditions at these particular interfaces. The other peculiar observation in Figure 5.9 is the different plasmon energy for different adsorbates. For strong electron acceptors, it is small for less-strong acceptors or donors it is shifted to higher energies. An important parameter in this context seems to be the EA. Experimental values for the EA from inverse photoemission experiments (IPES) of thin films (e.g. 5 nm F₄TCNQ on polycrystalline Au, see references in Fig. 5.10 for details), except for TTF where no experimental data was found and a B3LYP/6-311G DFT calculation was used, are plotted against the observed plasmon energy in Figure 5.10 (a). The linear dependency suggests a strong influence of this particular parameter or a corresponding property. An explanation can give a study of K doped single-layer graphene [295] on SiC where a strong dependence of the observed 2D intraband π -plasmon energy

5. Collective Excitations at Metal/Organic Interfaces

at given transferred parallel momentum on the K-doping concentration and therefore charge carrier density in the sheet is observed. There an increase in the intrinsic electron density from $n = 1.2 \times 10^{13} \text{ cm}^{-2}$ to $7.0 \times 10^{13} \text{ cm}^{-2}$ lead to a plasmon energy shift from 0.5 eV to 0.75 eV (at $q_{\parallel} = 0.05 \text{ \AA}^{-1}$). Thus it is concluded that adsorbates with higher EA lead to a stronger decrease in electron density of the charge sheet at the metal surface and thus a lower plasmon energy.

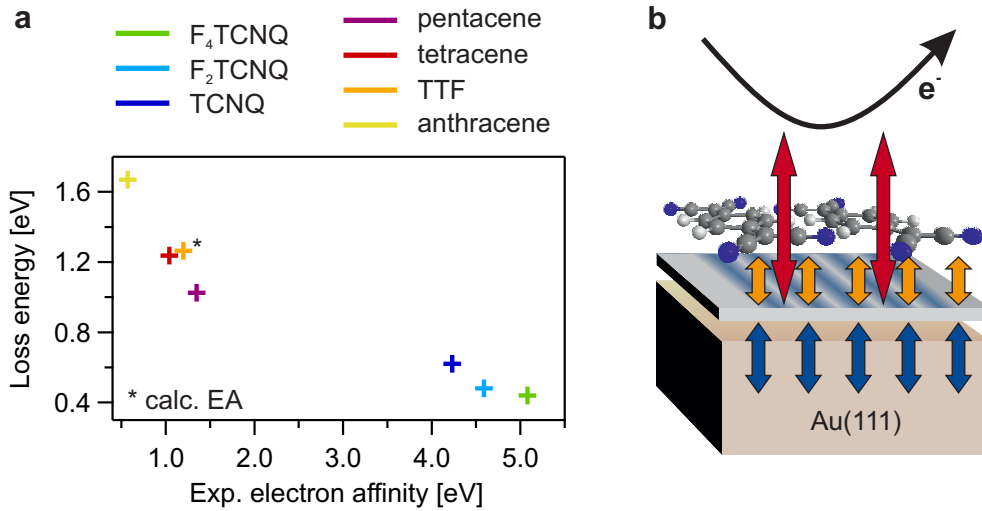


Figure 5.10.: (a) HREELS plasmonic loss energy *vs.* experimental electron affinities for anthracene (yellow [300]), tetracene (orange [300]), TTF (red, B3LYP/6-311G DFT calculation), pentacene (purple [300]), TCNQ (blue [265]), F₂TCNQ (light blue [265]), and F₄TCNQ (green [265]). (b) Schematic picture showing the embedding of the 2D surface state electrons (grey) in the 3D bulk (blue arrows), the pull- or push-like interaction with the adsorbate (orange arrows), and the screening interaction of the adsorbate with the incident electrons (red arrows).

To summarize the discussion of the results, the present study leads to a picture as visualized in Figure 5.10 (b). The collective excitation of the electrons delocalized in two dimensions in the surface state band (grey and blue sheet) by the incoming electron beam (red arrows) is influenced by the bulk electron gas (blue arrows). For the (111)-surfaces of the coinage metals Cu, Ag, and Au the surface state is partially filled which leads to two possible pathways for surface plasmon excitations, CSP and ASP as shown in section 5.2.1. The orange arrows in Figure 5.10 (b) now indicate the interaction of organic adsorbates with the 2D electron gas underneath. The molecular frontier orbitals interact with the metal states close to E_F thus the size of adsorbate domains

also determines the size of the delocalized electron system and so the minimal plasmon energy. The same interaction also influences the electron density in the charge sheet and thus leads to the observed shift of the plasmon energy.

But the all-in-all coherent picture still leaves open questions that require further investigations. First, additional experimental efforts have to include measurements along the high-symmetry axes to examine the influence of the crystal orientation on the observed excitation. Therefore the crystal geometry has to be determined with LEED before an angle-resolved HREELS investigation. Although there is already a lot of knowledge about the electronic structure and properties like the adsorption geometries and domain sizes for the particular systems, it is necessary to perform comprehensive measurements under exactly the same preparation conditions as these conditions largely influence the studied properties and in particular the observed low-energy excitation. Hence, the domain size on the investigated samples should be determined with STM. Additional photoemission experiments and theoretical calculations should study the band structures of the particular systems. With these larger data sets theory should be able to deliver a clear picture of the nature of the observed low-energy plasmonic excitation at metal/organic interfaces.

5.3. Vibrational Measurements

Salomon *et al.* [82] introduced a connection between a collective excitation at metal/organic interfaces and the so-called interfacial dynamical charge transfer (IDCT). The latter expresses itself in Fano-like line shapes in vibrational spectra. HREELS offers the opportunity to measure electronic and vibrational excitations in a single experiment, so looking also into the vibrational regimes of the investigated systems is likely. To keep the number of unknowns as small as possible, this part will focus only on TCNQ and its di- and tetra-fluorinated derivatives which show the most meaningful vibrational spectra regarding Fano-like line shapes. Before the presentation of the results, a brief background section will introduce Fano-resonances in general and additionally the concept of IDCT.

5.3.1. Background: IDCT and Fano-resonances

Ugo Fano introduced his theory for the occurrence of asymmetric line shapes in 1935 [301] and, gaining much more attention, in 1961 [302] which was applied successfully in many fields of experimental physics like atomic and nuclear physics [303], condensed matter physics [304], nanophotonics [305, 306], magnetic metamaterials [307], and mechanical waves [308]. The basic principle is depicted in Figure 5.11 (a).

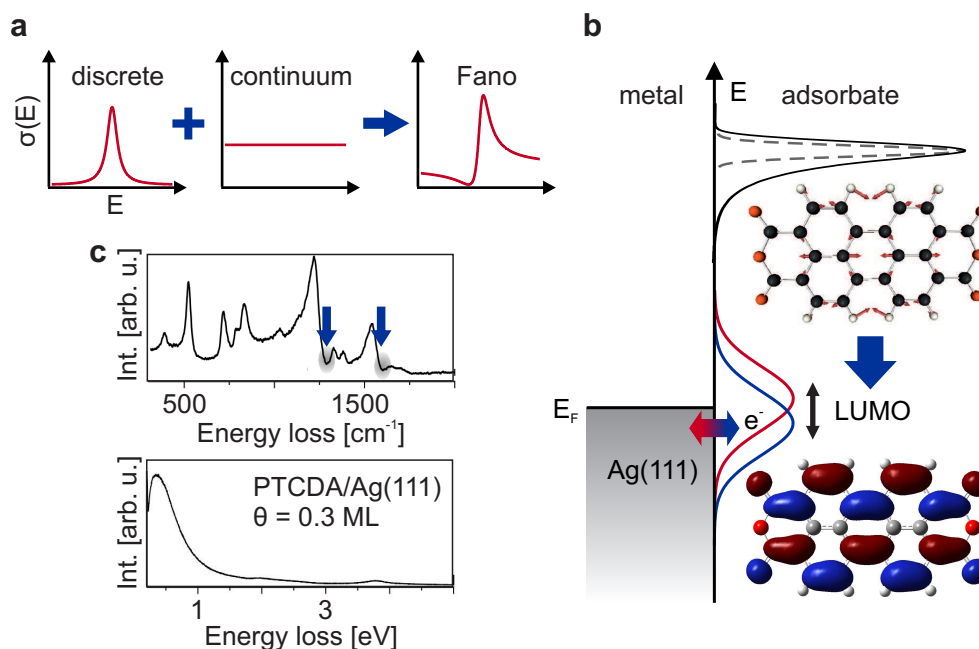


Figure 5.11.: (a) Energy dependent cross sections σ for a discrete excitation (left), a (ideal) continuum (middle) and a continuum coupled Fano resonance (right), adopted from ref. [306]. (b) IDCT model with an adsorbate (PTCDA) on a metal surface (Ag(111)) and corresponding energy levels. for the Fermi energy E_F , an adsorbate vibration (upper right), and the adsorbate LUMO close to E_F (blue and red). The involved vibration and LUMO are depicted (B3LYP/6-311G DFT calculations), adapted from ref. [44]. (c) Vibrational (top) and electronic (bottom) HREELS data for 0.3 ML PTCDA on Ag(111) from ref. [44], with blue arrows indicating proposed IDCT induced Fano-like vibrations.

A discrete excitation couples with a continuum and leads to a response with a minimum and a maximum, the Fano-resonance. The two (discrete and broad) excitations can be seen as a system of two coupled oscillators with eigenfrequencies ω_1 and ω_2 from which one is excited externally (see ref. [306] for a detailed description). In a weakly coupled system, both oscillators show reso-

nances at frequencies of the external force close to their eigenfrequencies. The directly excited oscillator shows a symmetric Lorentzian peak (Breit-Wigner resonance) close to its own eigenfrequency, but close to the resonance of the other oscillator, it shows an asymmetric peak due to both the (off-phase) excitation of the external force and the excitation by the in-resonance oscillating coupled oscillator. This leads to destructive followed by constructive interference and the well-known Fano-like peak shape [309]. In theory, a discrete excitation couples with a continuous one which is not given in most of the experimental cases. Here the continuum is given by a broad excitation which has to overlap energetically with a discrete one. An application is the concept of the interfacial dynamical charge transfer (IDCT), where a broad electronic excitation couples with a discrete vibrational one. First proposed for CO on Cu(100) [310] and O₂ on Pt(111) [311] and more recently for larger adsorbates like C₆₀ [312] and PTCDA [83,84] on Ag(111) it describes the coupling of electron-hole pair formation to adsorbate vibrations which leads to line shifts, increased line-widths and the suppression of surface selection rules and therefore increased intensities of selected modes. Figure 5.11 (b) illustrates the IDCT by the example of PTCDA on Ag(111). In contrast to CO on e.g. Cu(100) the bonding between molecule and substrate is not a clear chemical bond here and originates more from electrostatic interactions. These interactions lead to a hybridization of specific molecular orbitals with metal bands. In this case, the LUMO of the PTCDA molecule becomes a partially occupied hybrid orbital which contributes to the metal/molecule bonding. The energetic position of this hybrid orbital is affected by distinguished vibrational modes, in this case, the symmetric C-C stretching or “breathing” mode of the adsorbate. The dynamical manipulated energetic position leads to a dynamic degree of occupation and hence an oscillating charge transfer from metal to molecule and *vice versa*. As the charge transfer is oriented perpendicular to the surface and the vibration is coupled to this modulation, this specific vibration is connected to a dynamic dipole moment perpendicular to the surface and becomes thus dipole active. This allows measurements with techniques based on dipole moment changes like HREEL or IR spectroscopy.

Figure 5.11 (c) shows experimental data for the PTCDA/Ag(111) interface [44] showing the vibrational HREEL spectrum (top) with Fano-like modes in the breathing-mode region (marked with arrows) and the corresponding electronic HREEL spectrum with an intense low-energy excitation assigned to

electron-hole pair excitations from hybrid orbitals close to E_F . So the vibrational spectrum can give hints to broad continuum-like electronic excitations and its properties. The next section covers the results of vibrational HREEL measurements of TCNQ, F₂TCNQ, and F₄TCNQ on Au(111).

5.3.2. TCNQ and its Fluorinated Derivatives on Au(111)

The amount of occupation or hybridization of an originally unoccupied adsorbate orbital depends largely on the energetic position of the orbital with respect to the Fermi energy of the metal. Important parameters are the adsorbate's electron affinity (EA) and the work function of the metal. A partially filled hybrid orbital is one of the criteria for an IDCT as mentioned in the previous section. TCNQ and its fluorinated derivatives on the Au(111) surface are a perfect model system as with increased fluorination the EA increases from 4.23 eV for TCNQ, *via* 4.59 eV for F₂TCNQ to 5.08 eV for F₄TCNQ (see Fig. 5.10 (a) and ref. [265]) thus F₄TCNQ is charged on Au(111) whilst TCNQ is neutral. Figure 5.12 shows the vibrational HREEL measurements ($E_0 = 3.5$ eV) for monolayer coverages of F₄TCNQ (a), F₂TCNQ (b), TCNQ (c) on Au(111) in specular (black) and 5° off-specular geometry. For F₄TCNQ, all observed vibrational modes, the respective assignments and visualizations can be found in App. I.7 in Table I.1 and Figure I.12, respectively. All spectra show good resolutions and high specular count rates indicating smooth, well-ordered films. The high specular intensities and specular-to-off-specular ratios of the out-of-plane buckling ($100 - 300$ cm⁻¹) and γ (C-C-C) vibrations indicate flat adsorption in all systems as expected from STM investigations for TCNQ and F₄TCNQ (compare to section 5.2.2 and Fig. 5.5). For F₂TCNQ and TCNQ with its C-H bonds the out-of-plane γ (C-H) modes dominate the spectrum and show high specular/off-specular ratios as well. The in-plane C-H stretching vibrations around 3000 cm⁻¹ are barely visible further confirming planar adsorption. From the mentioned STM measurements it is known that F₄TCNQ lifts up Au adatoms from the surface and coordinates to them with two of its cyano-groups [267], which is not observed for TCNQ [268]. It is further known, that negative charge shifts the C-N triple-bond stretching mode to smaller wavenumbers [281] due to a transfer of charge into anti-bonding molecular orbitals located at the cyano groups and thus reducing their bond order. The spectra show for F₂TCNQ and TCNQ (barely visible) one mode around 2200 cm⁻¹ whilst F₄TCNQ shows two modes at 2200 and 2100 cm⁻¹.

5.3. *Vibrational Measurements*

As F₂TCNQ acts here like TCNQ it is concluded that no distinct charge transfer, as well as no coordination of adatoms, takes place as well. One possible explanation for the observation of two frequencies in the case of F₄TCNQ on Au(111) would be that not all molecules at the F₄TCNQ/Au(111) interface are charged. But there is no reason why one F₄TCNQ should be charged and another one not. Hence it is more probable that there is a balanced interplay of electron affinity, hybridization, charge transfer, adatom coordination, and charge distribution in the adsorbed F₄TCNQ that causes the two coordinating cyano groups to show vibrations with shifted intensities whilst the other two cause a non-shifted mode.

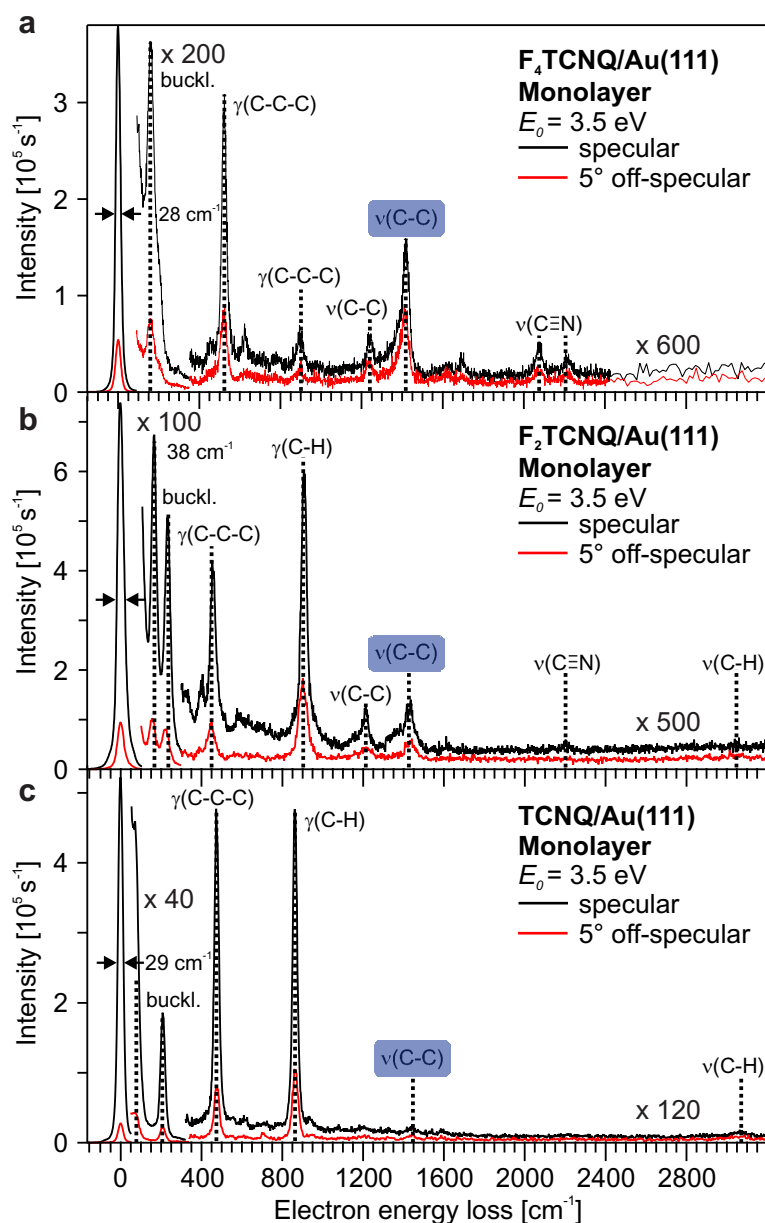


Figure 5.12.: HREEL spectra in specular (black) and off-specular (red) scattering geometry for monolayers of F_4TCNQ (a), F_2TCNQ (b), and $TCNQ$ (c). E_0 is the primary energy of the incident electrons. The energy resolution measured as FWHM of the elastic peak (zero loss peak) is labeled in the graphs. The relevant $\nu(C-C)$ stretching vibrations are shaded blue.

The focus in this section lies on the region of the symmetric C-C stretching modes ($\nu(\text{C-C})$) between 1200 and 1500 cm^{-1} as these breathing modes have the largest influence on the delocalized electrons in the frontier orbitals which are assumed to take part in potential IDCT processes or collective excitations as observed in the last chapter. In Figure 5.12 (c) the TCNQ monolayer shows the typical behavior for planar adsorption (compare to chapter 4 and refs. [55,218]). Only dipole active out-of-plane modes contribute to the spectrum and in-plane modes including the specific breathing modes are barely visible. For F_2TCNQ , Figure 5.12 (b) shows still almost no intensity for the in-plane $\nu(\text{C-N})$ and $\nu(\text{C-H})$ vibrations but the $\nu(\text{C-C})$ modes at 1200 and 1400 cm^{-1} show higher intensities and also a significant specular-to-off-specular ratio. A closer look also reveals an asymmetry as both modes show a tail on their low-energy sides. These observations occur in an even more pronounced fashion in Figure 5.12 (a) for a monolayer of F_4TCNQ on Au(111). The $\nu(\text{C-C})$ vibration at 1400 cm^{-1} becomes one of the dominating features of the spectrum and shows a clear Fano line shape with a tail on the low-energy side and a sharp fall as well as reduced intensity on the high-energy side. This suggests a dependence of the strength of Fano-like behavior on the electron affinity or the energetic position of the plasmonic excitation derived in the last chapter.

5.3.3. Discussion: Interactive Vibrational and Electronic Excitations

Tautz *et al.* [44] assigned the broad electronic low-energy excitation to electron-hole pair formation close to the Fermi energy and connected it to vibrational excitations *via* an IDCT, Salomon *et al.* [82] assigned a similar electronic excitation to a collective excitation of a space charge layer induced by an IDCT. Our study proofed the latter wrong as there is no need for an IDCT (expressed by Fano-like vibrations) to establish a collective excitation at a metal/organic interface as shown for e.g. TCNQ. The Fano line shape simply occurs if a discrete excitation couples to an energetically overlapping continuous-like one. The concept of IDCT implies that the coupling is based on an oscillating charge transfer into a partially occupied orbital. Transferred to the presented findings this leads to the insight, that an IDCT is not needed to explain the Fano-like vibrations. As proposed in chapter 5.2.2 the energetic position of the collective excitation depends on the electron affinity. A similar dependency is obviously

5. Collective Excitations at Metal/Organic Interfaces

present for a possible charge transfer. Hence, an IDCT-like behavior (Fano line shape) is observed in systems where the collective excitation is in the energetic region of the specific vibrations which implies that the electron affinity has to be that high that also the assumption of a (partial) charge transfer is reasonable. So in the derived picture, the collective excitation is a somewhat fundamental property of planar organic adsorbates on the investigated surface and the Fano lineshape simply occurs when both the discrete and the broad excitation overlap energetically. Now, there is still the question why certain modes can couple to the collective excitation and get dipole activated. Here, it is reasonable to adopt an argument from the IDCT concept. In the IDCT concept vibrations experience a Fano broadening if they affect the frontier orbitals' energies. In our concept, the molecules are assumed to adopt an orientation with their π -systems oriented parallel to the surface which leads to maximum interaction of the molecular π -electrons with the electrons located in the Au(111) surface state. The molecular π -electrons are located in the molecules' frontier orbitals which are largely affected spatially and energetically by the particular symmetric C-C stretching vibrations which are also important in the IDCT concept. When the energy of the collective excitation and the discrete vibration are in the same range a coupling occurs which transfers dipole activity from the plasmonic excitation to the coupled system.

Future works should include measurements along the high-symmetry axes with LEED, investigations of the growth mode with Auger electron spectroscopy (AES) and DFT studies with geometry optimizations and frequency calculations for adsorbate structures with and without adatoms. This will help to explain the dependence of the C-N stretching mode's frequency on charge distribution and adatom coordination. It needs to be mentioned that in the HREELS study by Lu *et al.* [281] also vibrational spectra were presented. Only spectra recorded in specular geometry were shown and neither the dipole active out-of-plane modes in the monolayer (and therefore flat adsorption) nor the split $\nu(\text{C-N})$ mode was observed. A possible explanation would be again a wrong coverage determination by using a quartz microbalance (e.g. no monolayer coverage) compared to the TPD based procedure in this work in which we were able to prepare well-defined covered surfaces with precisely determined adsorbate thicknesses.

6. Conclusion and Outlook

The presented work used a multi-technique approach to gain insight into fundamental aspects of metal/organic interfaces and corresponding structure/property relationships. Such relationships are crucial to establish guidelines for tailored organic semiconductors. This study focused on three aspects, the binding between substrate and adsorbate, the adsorption geometry, and the electronic structure at the interface. The examination of benzene on coinage metal surfaces lead to benchmarks of unrivalled accuracy for the binding energy of benzene on Au(111), Ag(111), and Cu(111) that helped to improve theoretical modelling of interface properties. The surprising finding of this study is the equal stability of benzene on these surfaces despite the metals' different electronic structures. First results from theory suggest, that this universal trend for the binding energy of aromatic molecules on coinage metal surfaces results from a subtle balance between repulsive Pauli- and attractive van der Waals-interactions. Future work should include improving the used evaluation routines of the experimental data to better face the problems originating from the analysis of systems with repulsive interactions.

The temperature-programmed desorption (TPD) study of the acene series from benzene *via* naphthalene, anthracene, and tetracene to pentacene on Au(111) revealed a strong coverage dependence of the binding energy on the coverage. This is interpreted as strong repulsive interactions, which increase with increasing molecular size. This leads to a shift by almost 300 K in desorption temperature between desorption from a coverage of 0 ML to desorption from a coverage of 1 ML in the case of pentacene. Pentacene additionally showed an extraordinary desorption behavior with a decreasing binding energy between 0 and 0.5 ML coverage and a constant one between 0.5 ML and 1 ML. This is assigned to substrate-mediated interactions that lead to the formation of a pattern in the low-coverage regime. The gaps in this pattern are filled in the high-coverage regime. The underlying long-range interactions can be used to build up tailored patterns and modify surface properties. The zero-coverage binding energies of the acene series showed that they deviate from a linear ex-

6. Conclusion and Outlook

trapolation of the value for benzene. The collaboration with Tkatchenko *et al.* (University of Luxembourg) lead to the suggestion that this deviation originates from many-body effects. Additional measurements of naphthalene and anthracene on Au(111) are currently performed. Together with additional results from theoretical modelling, this will complete the understanding of the influence of the size of the aromatic system on the binding energy. This first part helped to get insights into fundamentals of the aromatic/metal binding and showed ways to tailored self-assembly if substrate-mediated interactions can be used effectively.

The high-resolution electron energy-loss spectroscopy (HREELS) study of the adsorption behavior of N-heteropolycyclic aromatic molecules on Au(111) confirmed, that specific substitution can help to tailor particular properties of the resulting substrate/adsorbate systems. The most general finding is that planar aromatic molecules prefer a flat adsorption to increase the metal/ π -interactions and form well-ordered films. For purely planar molecules like TAPP or QPP this leads to a substrate-directed growth with the aromatic plane oriented parallel to the metal surface up to thicknesses of 10 ML and more – still surprisingly well-ordered. This originates from the fact that underlying flat molecules serve as a template for subsequently adsorbed ones and leads to a thin-film structure significantly different from the bulk crystal structure. The introduction of rigid bulky side chains to increase, e.g., solubility like the TIPS-groups in TIPS-Pn, or the *t*Bu-groups in *t*Bu-QPP increase the distance between metal and aromatic system, hence limiting the interactions that cause the strictly flat adsorption. Nevertheless, the respective monolayer HREEL spectra still suggest a flat adsorption but for higher coverages, the ordering seems less pronounced compared to the unsubstituted analogous. The introduction of flexible side chains like the C₃F₇-groups in the substituted TAPP derivatives also allows adsorption with a parallel orientation of the aromatic plane and the metal surface. In contrast to the systems with rigid side chains, the arrangement of the flexible chains in the monolayer prevents a planar adsorption in the second layer and leads to a crystal-like growth mode in the thin film. The introduction of halogens does not only affect the adsorption behavior but also the electronic structure, namely the optical gap. The influence on the adsorption is comparable to the introduction of bulky side chains. The larger the halogen, the more disordered is the multilayer morphology. Electronic HREELS investigations and comprehensive DFT-calculations

showed that the introduction of nitrogen into aromatic systems does not affect the size of the optical gap but shifts both HOMO and LUMO to lower energies thus increasing air- and water-stability. Monolayer coverages of TAPP and its derivatives show that the excitation of the optical gap is suppressed here, probably due to the screening of the participating frontier orbitals by the metal substrate. Electronic HREELS measurements of all systems at coverages between 4 and 10 ML showed surprising consistency with UV/Vis measurements in solution suggesting a negligible influence of packing on the optical gap in the thin film. The substitution of TAPP-H with halogens at side positions leads to a shift of the optical gap by 0.3 eV. In contrast to UV/Vis measurements, no alteration between the different halogens is observed which may be due to the lower resolution of HREELS compared to UV/Vis.

The last part of this work revealed interesting findings of collective excitations at adsorbate-covered surfaces. Angle-resolved HREEL spectra of several adsorbate/substrate systems showed broad and dispersive low-energy (0.4 – 1.6 eV) excitations in the monolayer regimes. The observed dispersion clearly suggests a delocalized electron gas wherefore the observed excitation was associated with a plasmonic excitation of the surface state electrons, known as acoustic surface plasmon (ASP). So far, ASPs were only reported for single crystal metal surfaces but the presented study of TCNQ, F₂TCNQ, F₄TCNQ, [TTF]⁺[TCNQ]⁻, TTF, pentacene, tetracene, and anthracene on Au(111) showed that it is not limited to bare metals. On pristine metals, the ASP shows an $E_{loss} \rightarrow 0$ for $q \rightarrow 0$ dispersion behavior, whereas our study on adsorbate-covered metal surfaces revealed finite energies. This deviation is explained by the different domain sizes (infinite on the pristine surface, finite on adsorbate-covered ones) which cause a break in the dispersion curve and finite values in the long-wavelength limit. The comparison of the different adsorbate-covered samples showed, that the observed excitation energy is also related to adsorbate properties like the electron affinity which determines the interactions of the adsorbate with the surface state electrons. A high electron affinity leads to a pull effect on the surface state electrons, thus increasing their spatial distribution and hence decreasing the effective electron density, which leads to a smaller excitation energy for surface plasmons. For all systems except F₄TCNQ /Au(111) the plasmonic excitation is apparently limited to monolayer coverages. For F₄TCNQ multilayers grown epitaxially at room temperature, a formed space charge region seems to suppress screening and

6. Conclusion and Outlook

thus this excitation is still possible in 10 ML thick films. Vibrational HREELS measurements showed a Fano-like coupling between the plasmonic excitations and particular vibrational modes leading to asymmetric, broadened vibrational peaks with significantly increased HREELS intensity. In contrast to earlier reports, the degree of coupling simply depends on the energetical overlap of both the vibrational and electronic excitation. This part about collective excitations definitely opens up the most entry points for future works. Measurements for different coverages and primary electron energies have to be evaluated and interpreted carefully. Experimental efforts have to concentrate on measurements along the high-symmetry axes of the sample and on measurements on different metal surfaces. Additionally, theoretical input has to confirm the assumptions made. However, the findings in this part can contribute to a better understanding of the electronic interaction mechanisms between organic adsorbates and the metal electrons located close to the surface. And the observed plasmonic excitations can play an important role in energy transport along the surface or as decay channels for other excitations.

In summary, this work contributed interesting experimental results, leading to causal relationships for several aspects of metal/organic interfaces. The studies of benzene on different metals and the acene series on Au(111) revealed insights into the interactions of aromatic π -electrons with metal surfaces. The investigation of the substituent depending adsorption geometry and electronic structure revealed important structure/property relationships and confirmed the possibility of tailoring interfacial properties by tailoring the organic compounds. The final study of collective excitations at metal/organic interfaces showed the strong influence of adsorbates on electronic properties of the metal surface. Future work in the scope of the collaborative research centre SFB1249 about N-heteropolycyclic molecules as functional materials can build upon the presented findings and continue the path to a better understanding of metal/organic interfaces and tailored organic semiconductors.

A. List of Acronyms

8T	Octithiophene
AES	Auger electron spectroscopy
AFT FT-IR	Attenuated total reflectance Fourier-transform infrared
ARPES	Angle-resolved photoelectron spectroscopy
ASP	Acoustic surface plasmon
B3LYP	Becke, Lee, Yang, and Parr (functional)
BP	Bulk plasmon
BPP	Bulk plasmon polariton
Bz	Benzene
CI	Configuration interaction
CNL	charge neutrality level
CPU	Central processing unit
CSP	Conventional surface plasmon
DBH	Dibenzo[hi,uv]hexacene
DFT	Density functional theory
DPDI	4,9-Diamino-3,10-perylenequinone diimine
EA	Electron affinity
EELS	Electron energy-loss spectroscopy
EI	Electron ionization
fcc	Face-centered cubic
FET	Field effect transistors
F₂TCNQ	2,5-Difluoro-7,7,8,8-tetracyanoquinodimethane
F₄TCNQ	2,3,5,6-Tetrafluoro-7,7,8,8-tetracyanoquinodimethane
FT-IR	Fourier-transform infrared
FWHM	Full width at half maximum
GGA	Generalized gradient approximation
GIXD	Gracing incidence X-ray diffraction
GTO	Gaussian-type orbitals
hcp	Hexagonal closest packing
HF	Hartree-Fock
HREELS	High-resolution electron energy-loss spectroscopy
HOMO	Highest occupied molecular orbital

HSE	Heyd-Scuseria-Ernzerhof
IDCT	Interfacial dynamical charge transfer
IPES	Inverse photoemission spectroscopy
IR	Infrared
LANL2DZ	Los Alamos National Laboratory Double Zeta (basis set)
LDA	Local density approximation
LEED	Low-energy electron diffraction
LUMO	Lowest unoccupied molecular orbital
MBD	Many-body dispersion
MO	Molecular orbital
ML	Monolayer
MS	Mass spectrometry
NEXAFS	Near-edge X-ray absorption fine structure
OLED	Organic light-emitting diode
PBE	Perdew-Burke-Ernzerhof
P_n	Pentacene
PP	Peropyrene
PTCDA	Perylene-3,4,9,10-tetracarboxylic dianhydride
QMS	Quadrupole mass spectrometers
QPP	Quinoxalino[2',3':9,10]-phenanthro[4,5-abc]-phenazine
RGA	Residual gas analysis
RPA	Random phase approximation
SFB	Sonderforschungsbereich
SI	Supporting information
SP	Surface plasmon
SPP	Surface plasmon polariton
SS	Surface state
STM	Scanning-tunnelling microscopy
TAP	5,7,12,14-Tetraazapentacene
TAPP	1,3,8,10-Tetraazaperopyrenes
TAPP-Br	2,9-Bisperfluoropropyl-4,7,11,14-tetrabromo-1,3,8,10-tetraazaperopyrene
TAPP-Cl	2,9-Bisperfluoropropyl-4,7,11,14-tetrachloro-1,3,8,10-tetraazaperopyrene
TAPP-H	2,9-Bisperfluoropropyl-1,3,8,10-tetraazaperopyrene
TAPP-I	2,9-Bisperfluoropropyl-4,7,11,14-tetraiodo-1,3,8,10-tetraazaperopyrene

A. List of Acronyms

tBu	<i>tert</i> -butyl
tBu-QPP	2,11-Di- <i>tert</i> -butyl-quinoxalino[2',3':9,10]-phenanthro[4,5- <i>abc</i>]-phenazine
TCNQ	7,7,8,8-Tetracyanoquinodimethane
TDS	Thermal desorption spectroscopy
THF	Tetrahydrofuran
TIPS	Triisopropylsilylethynyl
TIPS-Pn	6,13-Bis(triisopropylsilylethynyl)pentacene
TIPS-TAP	6,13-Bis(triisopropylsilylethynyl)-5,7,12,14-tetraazapentacene
TPD	Temperature-programmed desorption
TTF	1,4,5,8-Tetrathiafulvalen
TV	Television
UHV	Ultra-high vacuum
UPS	Ultraviolet photoelectron spectroscopy
UV/Vis	Ultraviolet–visible spectroscopy
vdW	van-der-Waals
XPS	X-ray photoelectron spectroscopy
XSW	X-ray standing wave
ZnPc	Zinc phtalocyanine

B. Dosing and Experimental Parameters

All dosing parameters for the shown measurements are summarized in the following table. Before the dosings, the crystals (obtained from CrysTec[®] and MaTeck[®]) were prepared with a standard sputter/annealing procedure. Ar⁺ ions (10^{-6} mbar) were accelerated with 1 keV towards the sample (15 min) and the clean but rough crystal surface was annealed at 750 K (for all surfaces) for 20 min. During this thesis, three different dosers have been used (labelled as 1, 2, and 3 in table B). (1) was a simple fine valve to dose liquids *via* the background pressure, (2) was a home-built doser with one single MACOR[®] crucible, and (3) a commercial Kentax[®] doser with three glass crucibles. Due to different positions of the temperature measurement in the dosers, the dosing temperature for the same substance can vary between doser (2) and (3) by up to 80 K. The experimental setup allowed the observation of the dosing with the QMS.

B. Dosing and Experimental Parameters

Table B.1.: The relevant dosing parameters for all measurements in this thesis: Obtained coverage θ (variable: many different dosed coverages), doser temperature T_D (RT: room temperature), dosing time t_D (variable: many different dosing times), sample temperature T_S , possible annealing temperature T_A , used doser (1: doser for liquids, 2: old home-built doser with one single MACCOR[®] crucible, 3: new Kentax[®] doser with three glass crucibles), source of the material, and purity.

Molecule	Substrate	θ [ML]	T_D [K]	t_D [s]	T_S [K]	T_A [K]	Doser	Source	Purity
benzene	Au(111)	variable	RT	variable	100-150	-	1	Sigma-Aldrich	99.8%
benzene	Ag(111)	variable	RT	variable	100-150	-	1	Sigma-Aldrich	99.8%
benzene	Cu(111)	variable	RT	variable	120-150	-	1	Sigma-Aldrich	99.8%
naphthalene	Au(111)	variable	RT	variable	150	-	3	Sigma-Aldrich	99%
anthracene	Au(111)	variable	RT	variable	150	-	3	Sigma-Aldrich	> 99%
tetracene	Au(111)	variable	388	variable	250	-	3	Sigma-Aldrich	98.9%
pentacene	Au(111)	variable	480	variable	300	-	2/3	Sigma-Aldrich	99%
TIPS-Pn	Au(111)	1	408	650	300	420	2	Sigma-Aldrich	> 99%
TIPS-Pn	Au(111)	4	418	2000	300	-	2	Sigma-Aldrich	> 99%
TIPS-TAP	Au(111)	1	411	1000	200	407	2	Fabian Paulus, AK Bunz	no data
TIPS-TAP	Au(111)	4.4	408	5000	200	-	2	Fabian Paulus, AK Bunz	no data
QPP	Au(111)	1	468	300	300	460	2	Bernd Kohl, AK Mastalerz	no data
QPP	Au(111)	23	460	1000	300	-	2	Bernd Kohl, AK Mastalerz	no data
<i>t</i> Bu-QPP	Au(111)	1	460	600	300	470	2	Bernd Kohl, AK Mastalerz	no data
<i>t</i> Bu-QPP	Au(111)	10	420	2200	320	-	2	Bernd Kohl, AK Mastalerz	no data
TAPP	Au(111)	1	447	1200	300	460	2	Lena Hahn, AK Gade	no data
TAPP	Au(111)	10	450	1200	300	-	2	Lena Hahn, AK Gade	no data

Molecule	Substrate	θ [ML]	T_D [K]	t_D [s]	T_S [K]	T_A [K]	Doser	Source	Purity
TAPP-H	Au(111)	1	460	1000	300	500	2	Lena Hahn, AK Gade	no data
TAPP-H	Au(111)	6	444	2000	300	-	2	Lena Hahn, AK Gade	no data
TAPP-Cl	Au(111)	1	435	500	300	480	2	Lena Hahn, AK Gade	no data
TAPP-Cl	Au(111)	5	438	1400	300	-	2	Lena Hahn, AK Gade	no data
TAPP-Br	Au(111)	1	440	1000	300	500	2	Lena Hahn, AK Gade	no data
TAPP-Br	Au(111)	5	435	1700	300	-	2	Lena Hahn, AK Gade	no data
TAPP-I	Au(111)	1	455	1500	200	460	2	Lena Hahn, AK Gade	no data
TAPP-I	Au(111)	6	433	1100	200	-	2	Lena Hahn, AK Gade	no data
F ₄ TCNQ	Au(111)	1	423	140	300	370	3	TCI	> 98%
F ₄ TCNQ	Au(111)	3.5	343	700	120	-	2	TCI	> 98%
F ₄ TCNQ	Au(111)	9	413	870	300	-	3	TCI	> 98%
TCNQ	Au(111)	1	383	200	300	370	3	TCI	> 99%
F ₂ TCNQ	Au(111)	1	393	500	300	355	3	TCI	> 98%
TTF	Au(111)	1	317	215	100	340	3	TCI	> 98%
TCNQ/TTF	Au(111)	1	378	600	200	340	3	Sigma-Aldrich	> 97%
pentacene	Au(111)	0.6	390	200	300	-	2	Sigma-Aldrich	99%
tetracene	Au(111)	1	388	740	250	-	3	Sigma-Aldrich	98.9%
anthracene	Au(111)	1	333	250	260	-	3	Sigma-Aldrich	> 99%

B. Dosing and Experimental Parameters

C. DFT Parameters and Commented Gaussian09 Input

All DFT calculations have been performed with the Gaussian09 program package [120]. This section describes the general procedure from the molecular structure to the calculated vibrations. First, the molecular structure is converted to Cartesian XYZ-coordinates with the ChemDraw program and Chem3D of PerkinElmer Informatics. Within the Chem3D program, a molecular mechanics based pre-optimization is performed and saved in a file format that can be imported to Gaussian09 (e.g. *.mol2). The so obtained coordinates are loaded into Gaussian09 and a DFT calculation with the appropriate parameters is started. A typical calculation is a geometry optimization with a subsequently performed frequency calculation to obtain the vibrational frequencies of the normal modes. Figure C.1 shows an exemplary Gaussian09 input for a TAPP-H. The blue shaded part contains the parameters for the calculation, the orange shaded part contains the input XYZ-coordinates.

```
%nprocshared=2 A
%chk=Y:\thesis\20180105TAPPH_OptFreqSym.chk B
#Copt freq=(raman,savenormalmodes) b3lyp/6-311+g(d,p)
guess=(huckel,save) F D E
geom=connectivity

20180105TAPPH_OptFreqSym G parameters

0 1 H
C 0.32685492 -2.73571451 2.29270120
C 0.16831251 -1.40543534 2.29940028
C 0.08104479 -0.67279321 1.16829114
C coordinates 0.15881552 -1.33280497 0.00000000
C 0.31981878 -2.67453656 0.00000000
C 0.40556024 -3.38577025 1.12592050
...
```

Figure C.1.: Prefactors for Bz on Au(111), Ag(111), and Cu(111) as a function of coverage. Adapted from the SI of ref. [313].

C. DFT Parameters and Commented Gaussian09 Input

The parameters are (A) the numbers of cores of the processor which should be used for the calculation, (B) the path for the checkpoint file (a useful file, for, e.g., molecular orbital visualization, with all calculation steps), (C) the important commands *opt* and *freq* for geometry optimization and subsequent frequency calculation (the parameter *raman* indicates that not only IR-active vibrations should be calculated), (D) the functional, (E) the basis set, (F) additional parameters for calculation, (G) the output file path, and (H) the charge and spin (1 = singulett). The output contains the optimized geometry, the normal modes and their corresponding IR- and/or Raman-activity, and the MO-energies. The normal modes can be visualized either within the Gaussview program or within the Facio program package [121]. Furthermore, there exists the possibility to draw mapped surfaces. E.g., the overall electron density surface can get a colour scale for the charge density at any point of the surface. The same is possible for the electron density surface of single molecular orbitals.

All calculations were performed for single molecules in the gas phase. To give a better comparability between calculated frequencies and experimental ones, the obtained frequencies were multiplied with 0.9614 as proposed for the chosen level of theory in ref. [314]. As the level of theory, usually, the functional B3LYP and the Pople style basis sets 6-311G were chosen as this level was used before to properly describe geometries and vibrational frequencies for pure (metal-free) organic compounds (for details, see section 2.3). Except for TAPP-I, where the iodine atoms could not be described by the 6-311G basis set and a LANL2DZ basis set was chosen instead.

D. Benzene on Cu(111): TPD and HREELS

As there exist contradictory findings concerning the morphology of the Bz/Cu(111) interface, additional HREELS measurements have been performed. XSW measurements by Willenbockel *et al.* [315] suggest a mixed monolayer phase of upstanding and flat-lying Bz molecules whereas earlier EELS measurements suggested a pure flat lying first layer and an eventually up-standing second layer [166]. The coverage dependent HREELS results from this work are summarized and explained in this section. The main result is that in the given experimental accuracy, Bz adopts an adsorption geometry with its plane parallel to the Cu(111) surface up to coverages of 12 ML. For the current topic, another finding of this investigation is more important. As Cu is (chemically) more reactive compared to Ag, and Au, CO from residual gas adsorbs more likely on this surface. This co-adsorption delivers a useful tool to determine the complete monolayer. To calculate the coverage by integrating TPD spectra, a definition of the area covered by one monolayer in such a spectrum is essential. In rather weak binding systems as aromatic molecules on coinage metal surfaces, there is often the problem that there is no clear separation of the mono- and multilayer desorption peaks (as can be seen in Figure D.1 (a) for the Bz/Cu(111) system).

D. Benzene on Cu(111): TPD and HREELS

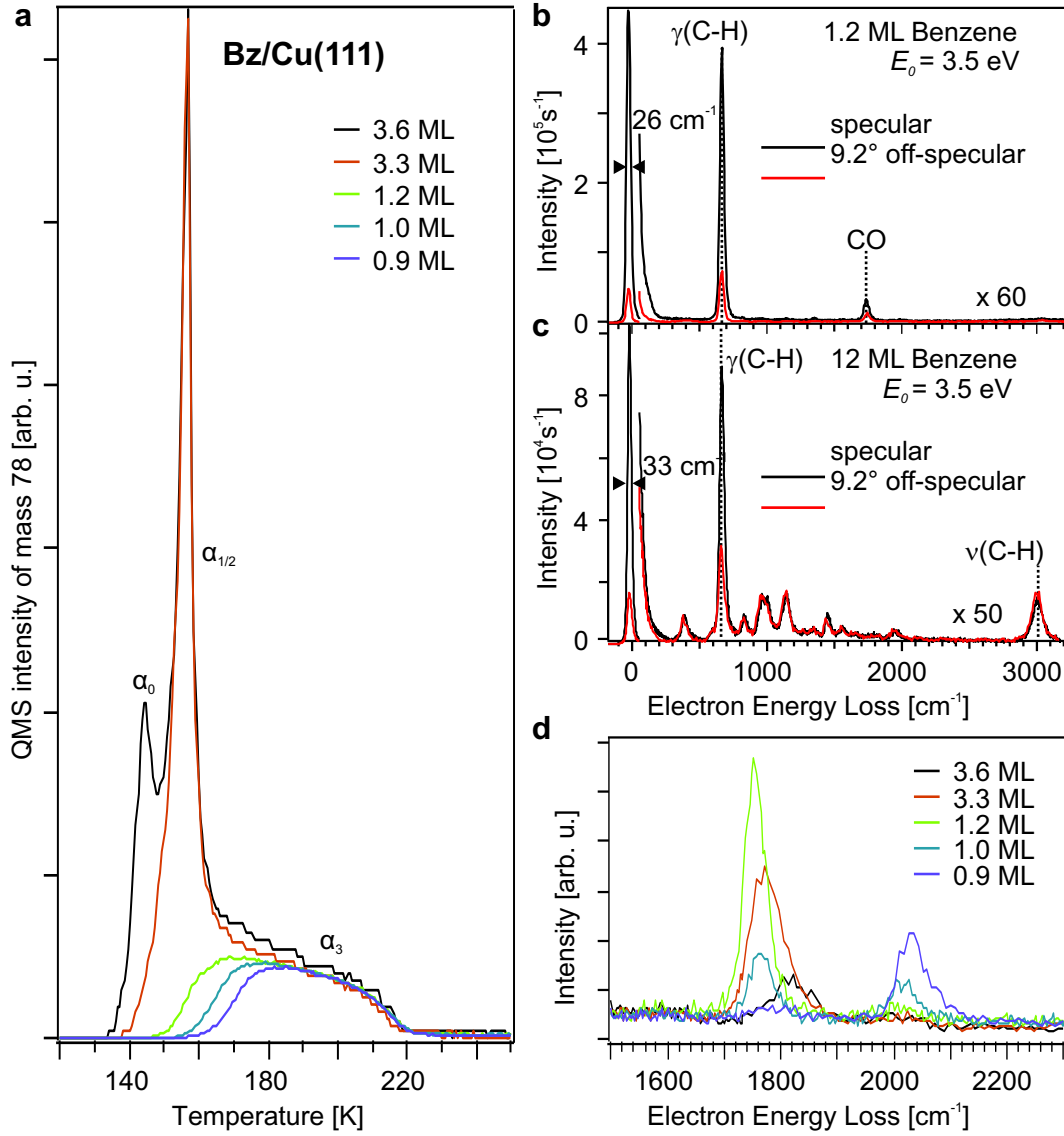


Figure D.1.: (a) TPD spectra of Bz on Cu(111) for several coverages from $\theta = 0.9$ ML to 3.6 ML, (b) specular (black) and off-specular (red) HREEL spectrum of 1.2 ML Bz on Cu(111), $E_0 = 3.5$ eV, $FWHM = 26$ cm^{-1} , (c) specular (black) and off-specular (red) HREEL spectrum of 12 ML Bz on Cu(111), $E_0 = 3.5$ eV, $FWHM = 33$ cm^{-1} , (d) enlargement of CO peak region between 1500 and 2300 cm^{-1} with specular HREEL spectra for the different Bz coverages shown in (a).

Such a separation would allow a simple integration of the monolayer part of the TPD spectrum and therefore a conclusion on to the total coverage. With means of high-resolution electron energy-loss spectroscopy (HREELS), we found a way to determine the monolayer more precisely than before. HREELS is a surface sensitive technique, which allows vibrational spectroscopy of ad-

sorbed molecules by exciting vibrations with monochromatic electrons and the measurement of their energy loss. [63] Figure D.1 (b) and (c) show a mono- and multilayer HREEL spectrum, respectively. From the relative intensities, we can derive a rather flat adsorption independent of the coverage. On the, compared to Au(111) and Ag(111), more reactive Cu(111) surface a distinct amount of carbon monoxide (CO) adsorbs from residual gas resulting in a clearly visible CO stretching vibration in the HREEL spectrum (see Figure D.1 (b)). The energy of this vibration is strongly coverage dependent (see Figure D.1 (d)). From literature we know, that there exist several sub-monolayer regimes for pristine CO on Cu(111) leading to electron energy loss peaks of 2080 cm^{-1} (top site, 1-fold) and 1850 cm^{-1} (bridge site, 2-fold) [316]. On Pt(111) and Rh(111) the co-adsorption of CO and Bz leads to a displacement of CO molecules also on hollow sites (3-fold) leading to a further reduction of the intra-molecular CO bonding strength and therefore of the corresponding vibrational frequency (clean Pt(111): hollow, 1800 cm^{-1} ; bridge, 1850 cm^{-1} ; top, 2100 cm^{-1}) [317]. From low-energy electron diffraction (LEED) studies a densely packed Bz layer with CO molecules in the resulting gaps is derived [318]. We assume a similar behaviour for the Cu(111)/Bz/CO system. In a simple picture, the small amounts of CO in our UHV chamber adsorb at the energetically most favourable adsorption sites, with increasing dosing time these sites get rarer and rarer until, when the monolayer is completed, none are left. That is the point where the frequency shifts from the 1-fold 2050 cm^{-1} (Figure D.1 (d) 0.9 ML) via a mixed 2050 cm^{-1} and 1760 cm^{-1} at 1 ML coverage to the only 3-fold 1760 cm^{-1} at a coverage of 1.2 ML. With the appearance of α_0 (see Figure D.1 (a), 3.6 ML) an additional shift to 1815 cm^{-1} is visible. This seems to be related to a third layer adsorption above the CO molecules, compressing them slightly and therefore strengthen the CO bond. As we know from residual gas measurements and from the total pressure, the amount of CO must be very small and therefore we do not think, that there is a significant influence on the adsorption behaviour of Bz.

D. Benzene on Cu(111): TPD and HREELS

E. Prefactors for Benzene on Coinage Metal Surfaces

Beside the binding energy *vs.* coverage dependence, the complete analysis [49] also gives the prefactor *vs.* coverage dependence as depicted in Figure 3.5 for Bz/Au(111). Figure E.1 shows the determined prefactors for benzene on (a) Au(111), (b) Ag(111), and (c) Cu(111) as a function of coverage.

E. Prefactors for Benzene on Coinage Metal Surfaces

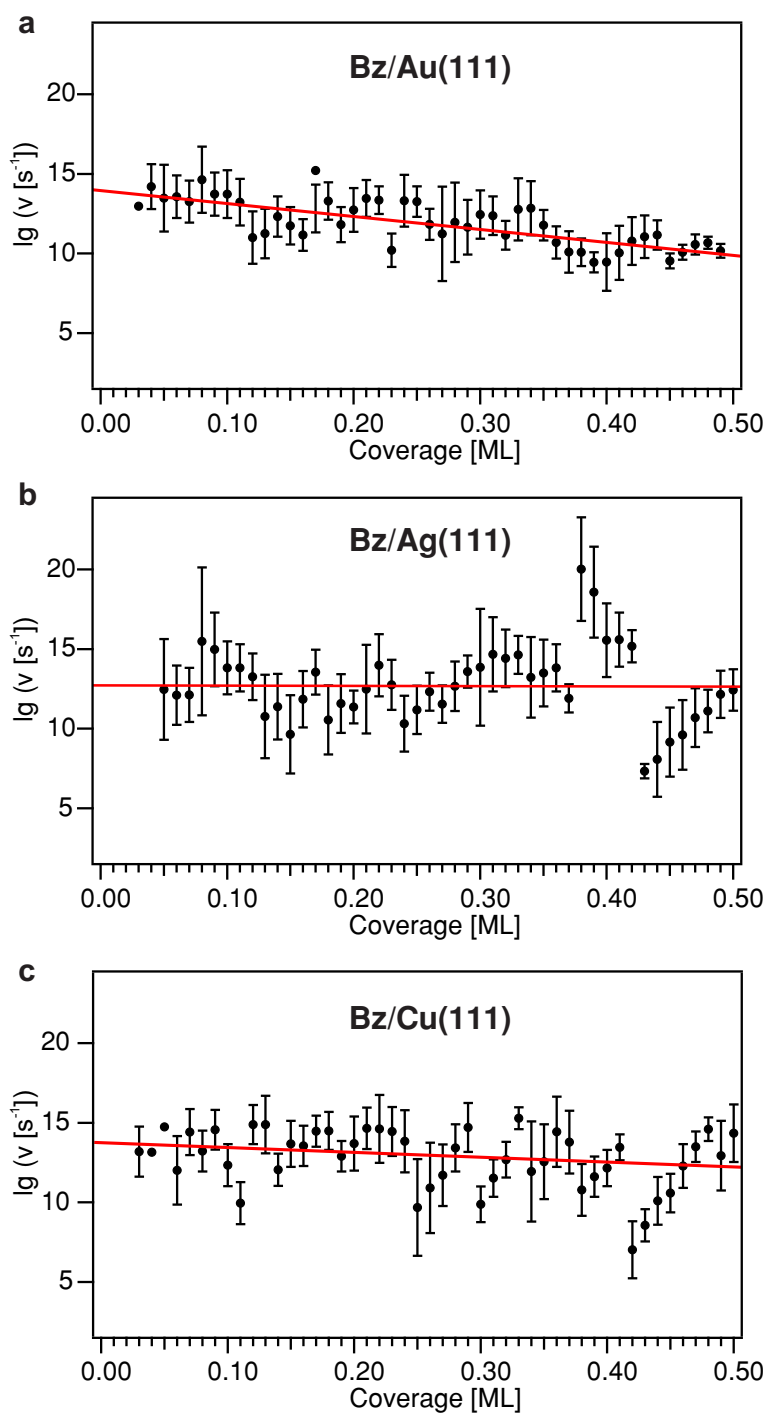


Figure E.1.: Prefactors for Bz on Au(111), Ag(111), and Cu(111) as a function of coverage. Adapted from the SI of ref. [313].

F. TIPS-P_n and TIPS-TAP: Further Studies and Vibrational Assignments

In Table F.1, all observed vibrational modes for TIPS-P_n are listed and assigned. In Fig. F.1, the listed vibrations for TIPS-P_n are visualized with the Facio19.1.4 program [121].

F. TIPS-Pn and TIPS-TAP: Further Studies and Vibrational Assignments

Table F.1.: TIPS-Pn - vibrational modes (in cm^{-1}) and assignments for 1 ML and 4 ML TIPS-Pn adsorbed on Au(111). *da* refers to dipole active modes. In addition DFT calculated frequencies based on the B3LYP functional and the 6-311G basis set of the free molecules are shown. ν , stretching; δ , in-plane bending; γ , out-of-plane bending; *P*, pentacene; *T*, TIPS; *E*, ethynyle; Repr, representation and in brackets corresponding orientation of the calculated dipole derivative vector with respect to the molecular geometry, *x* long axis, *y* short axis, *z* perpendicular to the pentacene plane).

#	TIPS-Pn 1 ML	TIPS-Pn 4 ML	DFT	Mode	Repr.
1	273	233	247	buckl. long	$B_{3u}(z)$
2	449 <i>da</i>	462 <i>da</i>	487	$\gamma(\text{C-H})_P$	$B_{3u}(z)$
3	-	586	597	$\delta(\text{C-C-C})_P$	$B_{2u}(y)$
4	692 <i>da</i>	672 <i>da</i>	723	$\gamma(\text{C-C-C})_P$	$B_{3u}(z)$
5	739 <i>da</i>	744 <i>da</i>	781	$\gamma(\text{C-H})_P$	$B_{3u}(z)$
6	886 <i>da</i>	878 <i>da</i>	936	$\gamma(\text{C-H})_P$	$B_{3u}(z)$
7	984 <i>da</i>	988 <i>da</i>	997	$\gamma(\text{C-H})_P$	$B_{3u}(z)$
8	-	1075	1117	$\delta(\text{C-C-H})_T$	
9	1203	1152	1186	$\delta(\text{C-H})_P$	$B_{2u}(y)$
10	-	1288	1297	$\delta(\text{C-H})_T$	
11	-	1369	1412	$\nu(\text{C}_P\text{-C}_E)$	$B_{2u}(y)$
12	1452	1457	1470	$\delta(\text{C-H})_T$	
13	-	1667	1691	$\nu(\text{C-C})_P$	$B_{1u}(y)$
14	-	2151	2228	$\nu(\text{C-C})_E$	$B_{2u}(y)$
15	2870	2859	3029	$\nu(\text{C-H})_T$	
16	2924	2942	3126	$\nu(\text{C-H})_T$	
17	-	3053	3208	$\nu(\text{C-H})_P$	$B_{2u}(y)$

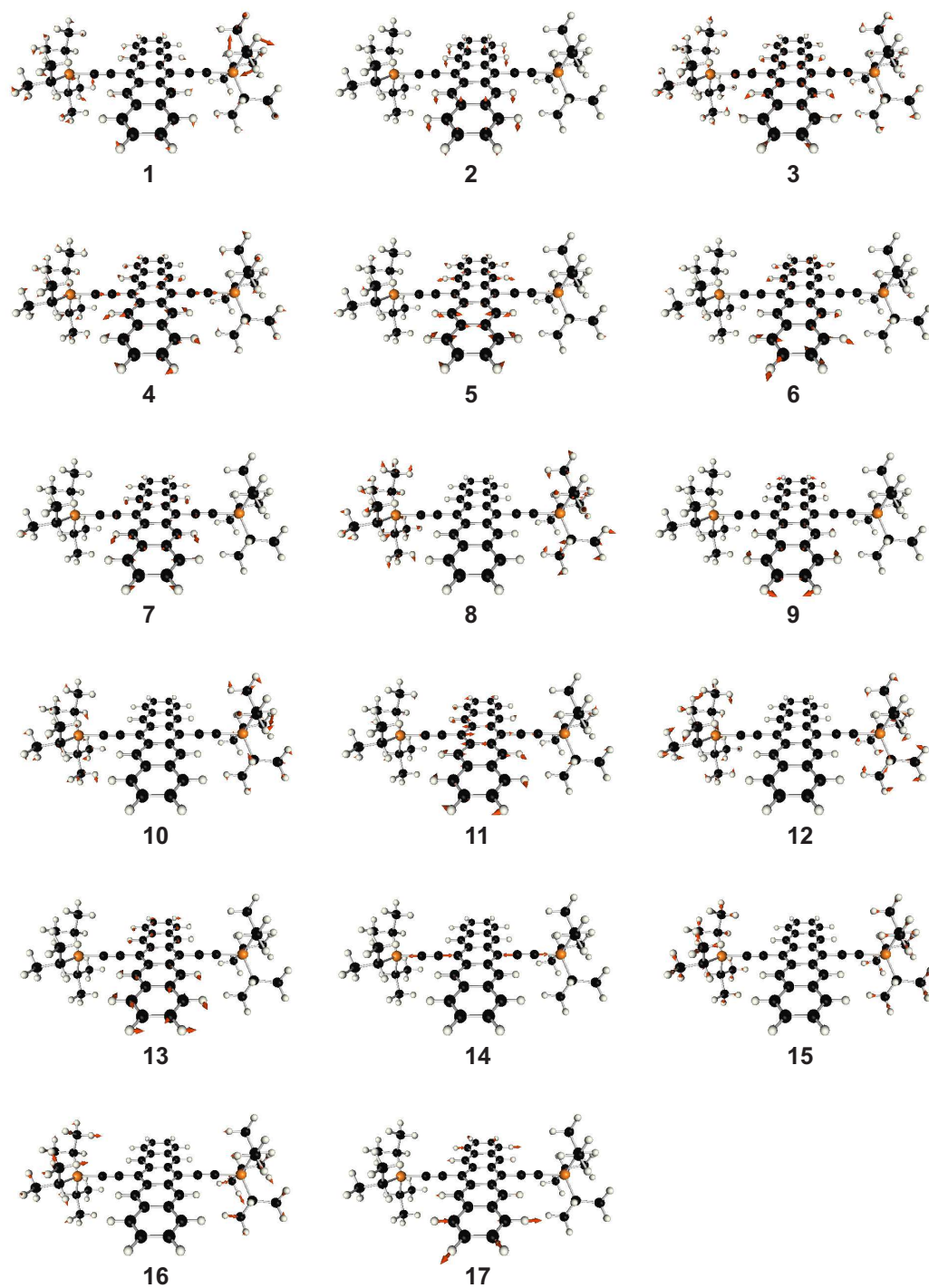


Figure F.1.: Visualizations of all observed and assigned vibrational modes for TIPS-Pn. Visualizations made with the Facio19.1.4 program [121]. The atomic displacement is indicated by the red arrows (enlarged by a factor of 5 for better visibility).

F.1. TIPS-Pn and TIPS-TAP: TPD and Mass Spectrometry

Figure F.2 (a) shows a comparison of a residual gas analysis (RGA) obtained during dosing at $T_D = 140^\circ$ (green) with electron ionization mass spectrometry data of the compound as bought (red) and after heating up to 140°C obtained from the mass spectrometry core facility of the Institute for Organic Chemistry, University of Heidelberg. The observed fragments belong to the TIPS sidechain, the differences in mass of 14 amu are associated with CH_2 dissociation. The similarities between the red and black curve suggest that the dosing does not lead to significant degradation of the substance.

Figure F.2 (b) shows a TIPS-TAP multilayer TPD with different observed masses. It needs to be noted that all fragments belong to the TIPS sidechain, except mass 200. The latter belongs to the TAP backbone and its observability suggests intact desorption from the multilayer and thus also intact adsorption. The fact that it is not visible in the monolayer is a clear indication of degradation during monolayer desorption. Also, the shift by 10 K to lower temperatures for mass 43 (compared to mass 59) indicates degradation as in the case of TIPS-Pn (see section 4.2). Figure F.2 (c) shows an additional TIPS-Pn multilayer TPD, here with mass 198 amu, the doubly charged molecular ion. As mass 200 in the case of TIPS-TAP, it is only visible in the monolayer. Both indicating degradation during monolayer desorption but also intact multilayer desorption and thus intact dosing.

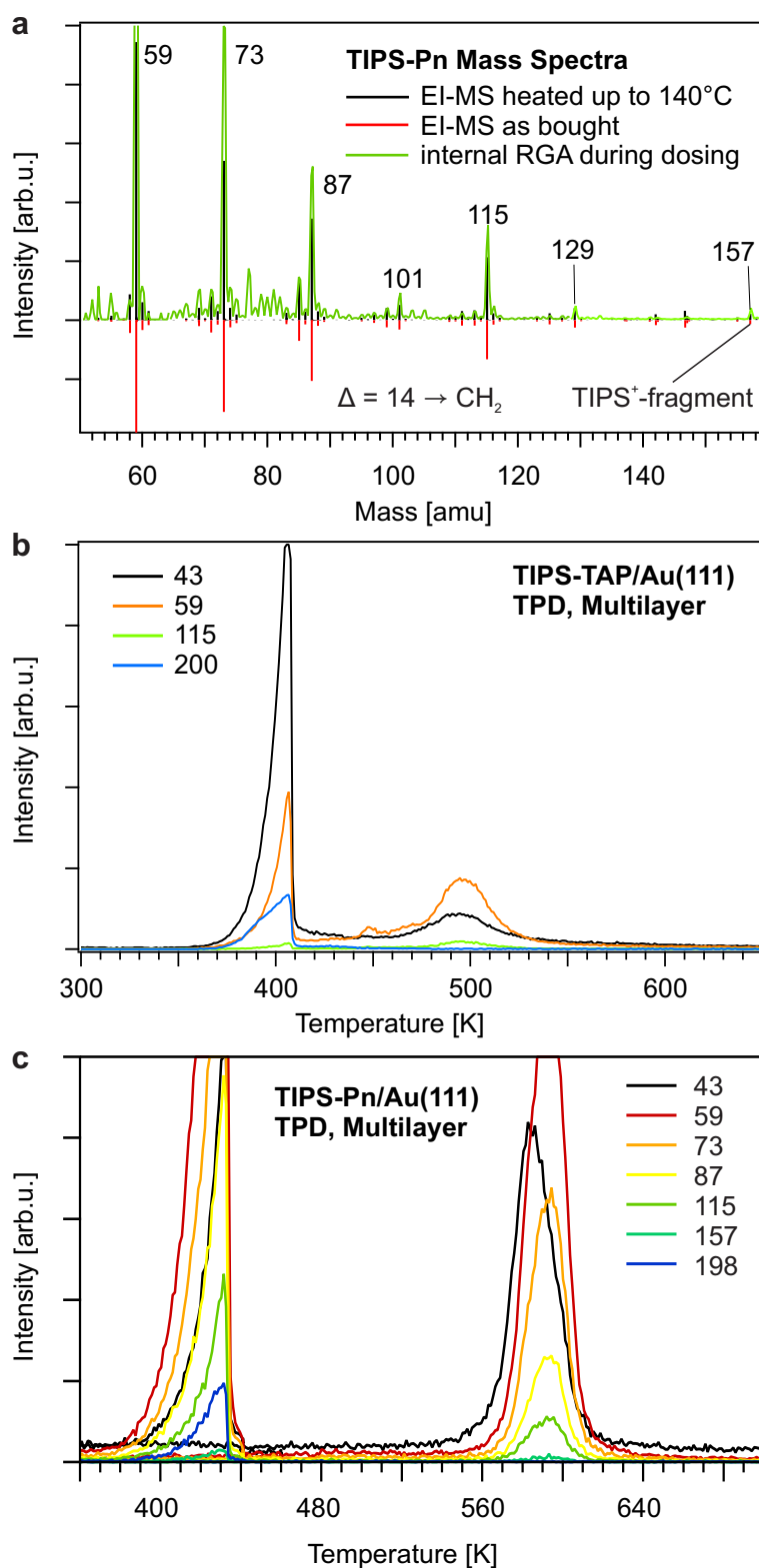


Figure F.2.: (a) Comparison of a residual gas analysis (RGA) obtained during dosing, green, with electron ionization mass spectrometry data of the compound as bought (red) and after heating up to 140°C obtained from the mass spectrometry core facility of the Institute for Organic Chemistry, University of Heidelberg. (b) TIPS-TAP multilayer TPD. (c) TIPS-Pn multilayer TPD including mass 198, the doubly charged molecular ion.

F.2. TIPS-Pn: Electronic HREELS

Figure F.3 shows the electronic HREELS data for a monolayer of TIPS-Pn on Au(111) in comparison to data for the pristine Au(111) surface. The Au(111) surface plasmon at 2.61 eV is still visible in the monolayer, whereas a feature which could be assigned to the excitation of the optical gap is not visible. Additionally, a broad feature at 0.94 eV is visible which could be associated to the plasmonic transition, which was also observed for the pentacene/Au(111) system (see chapter 5). Due to the low signal-to-noise ratio and the difficulty to distinguish between contributions from the substrate and the adsorbate, a detailed analysis is skipped here.

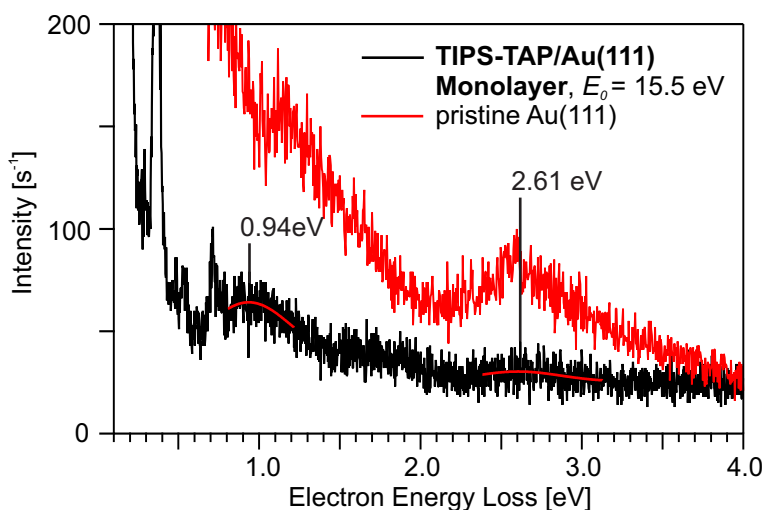


Figure F.3.: Electronic HREELS data of 1 ML TIPS-Pn on Au(111) (black) and for the pristine Au(111) surface (red).

F.3. TIPS-TAP: HREELS

In this section, the vibrational and electronics results for TIPS-TAP are presented. Due to the mentioned uncertainties, if the analyzed molecule is whether TIPS-TAP or the dihydrogenated derivative. Because of this problems, a detailed analysis and interpretation of the obtained results are skipped here.

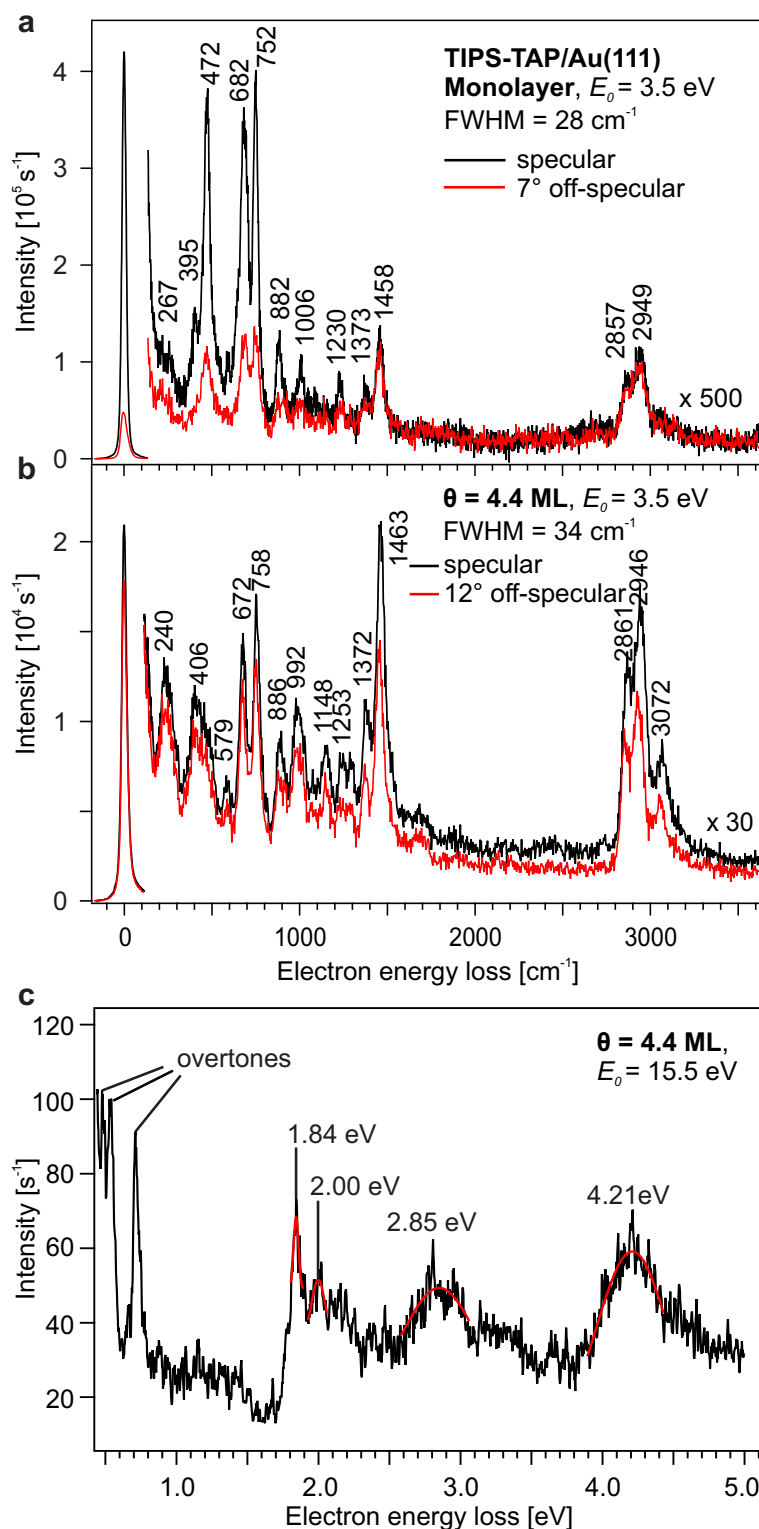


Figure F.4.: HREEL spectra in specular (black) and off-specular (red) scattering geometry for mono- (a) and multilayer (b) coverages of TIPS-Pn on Au(111). $E_0 = 3.5$ eV is the primary electron energy of the incident electrons. The energy resolution measured as FWHM of the elastic peak (zero loss peak) is labeled in the graphs. (c) shows the corresponding multilayer electronic HREELS data ($E_0 = 15.5$ eV) with gaussian fits to the relevant features.

F. TIPS-Pn and TIPS-TAP: Further Studies and Vibrational Assignments

G. QPP and *t*Bu-QPP: Further Studies and Vibrational Assignments

In Table G.1, all observed vibrational modes for QPP and *t*Bu-QPP are listed and assigned. In Fig. G.1, the listed vibrations for QPP are visualized with the Facio19.1.4 program [121]. We pass on a similar presentation for *t*Bu-QPP due to minor differences.

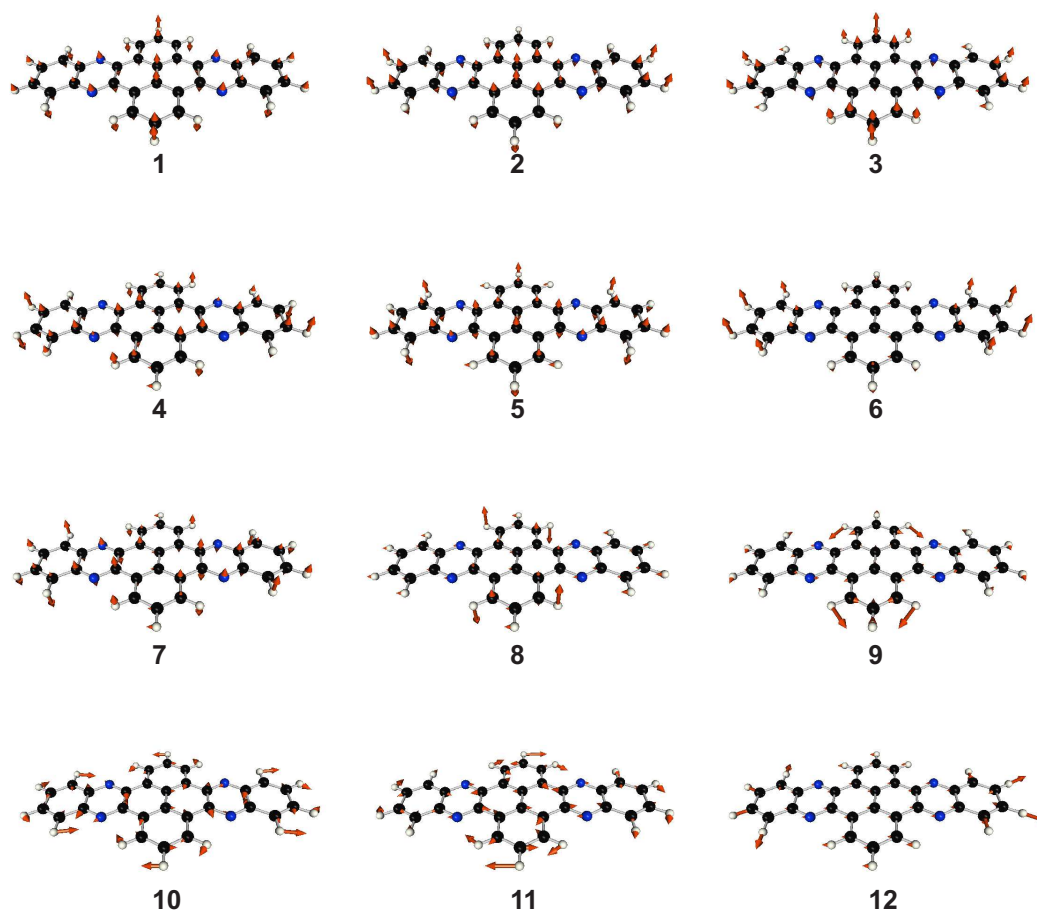


Figure G.1.: Visualizations of all observed and assigned vibrational modes for QPP. Visualizations made with the Facio19.1.4 program [121]. The atomic displacement is indicated by the red arrows (enlarged by a factor of 5 for better visibility).

G. QPP and *t*Bu-QPP: Further Studies and Vibrational Assignments

Table G.1.: QPP and *t*Bu-QPP - Vibrational frequencies (in cm^{-1}) and assignments for 1 ML and a multilayer QPP and *t*Bu-QPP, respectively, adsorbed on Au(111). *da* refers to dipole active modes. In addition attenuated total reflectance (ATR) FT-IR [221] measured and DFT calculated frequencies based on the B3LYP functional and the 6-311G basis set of the free molecules are shown. ν , stretch; δ , in-plane bending; γ , out-of-plane bending, *P*, pyrene; *Q*, quinoxaline; *tBu*, located at the tert-butyl groups; *al*, alyclic; *ar*, aromatic; in brackets: representation and corresponding orientation of the calculated dipole derivative vector with respect to the molecular geometry; *x* long axis, *y* short axis, *z* perpendicular to the molecular plane).

#	QPP 1 ML	QPP 12 ML	FT-IR (ATR)	DFT	<i>t</i> Bu-QPP 1 ML	<i>t</i> Bu-QPP 10 ML	FT-IR (ATR)	DFT	Mode	Repr.
1	109	96	-	97	138	142	-	130	buckl. long	$B_{3u}(z)$
2	166	190	-	173	180	190	-	187	buckl. short	$B_{3u}(z)$
3	434 <i>da</i>	434 <i>da</i>	-	466	469 <i>da</i>	468 <i>da</i>	-	487	$\gamma(\text{C-C-C})$	$B_{3u}(z)$
4	506 <i>da</i>	503 <i>da</i>	-	542	-	-	-	-	$\gamma(\text{C-C-C})_P$	$B_{3u}(z)$
5	711 <i>da</i>	722 <i>da</i>	720 (s)	755 <i>da</i>	730 <i>da</i>	744	728 (s)	758	$\gamma(\text{C-H})_P$	$B_{3u}(z)$
6	747 <i>da</i>	751 <i>da</i>	756 (s)	798	763	-	760 (s)	798	$\gamma(\text{C-H})_Q$	$B_{3u}(z)$
7	799 <i>da</i>	808 <i>da</i>	812 (s)	853	-	-	-	-	$\gamma(\text{C-H})_P$	$B_{3u}(z)$
8	950	954	975 (m)	995	905	900	897 (m)	966	$\gamma(\text{C-H})_P$	$B_{3u}(z)$
-	-	-	-	-	1017	950 (w)	1030	-	$\delta(\text{C-C-C})$	$B_{2u}(y)$
9	-	1096	1099 (s)	1136	1111	1119	1115 (m)	1159	$\nu(\text{C-C})_P$	$B_{1u}(x)$
-	-	-	-	-	1198	1221	1225 (m)	1238	$\nu(\text{C-C})_{tBu}$	-
10	-	1354	1356 (s)	1413	1359	1358	1360 (m)	1415	sym. $\nu(\text{C-C})$	A_g
11	-	1477	1477 (m)	1555	1467	1468	1476 (m)	1553	$\nu(\text{C-N})$	B_{3g}
-	-	-	-	-	-	2952	2862 (w)	3089	$\nu(\text{C-H})_{al}$	-
12	-	3060	3072 (w)	3215	-	3069	2961 (m)	3208	$\nu(\text{C-H})_{ar}$	$B_{1u}/B_{2u}(x/y)$

G.1. QPP and *t*Bu-QPP: TPD

Figure G.2 shows TPD measurements of QPP and *t*Bu-QPP multilayers on Au(111). Both molecules only show a peak assigned to multilayer desorption. This suggests destructive monolayer desorption. The peak for *t*Bu-QPP is shifted by 50 K to lower temperatures (400 K) compared to QPP (450 K), an indication for smaller intermolecular interactions between molecules in the monolayer and molecules in higher layers due to the bulky *tert*-butyl groups.

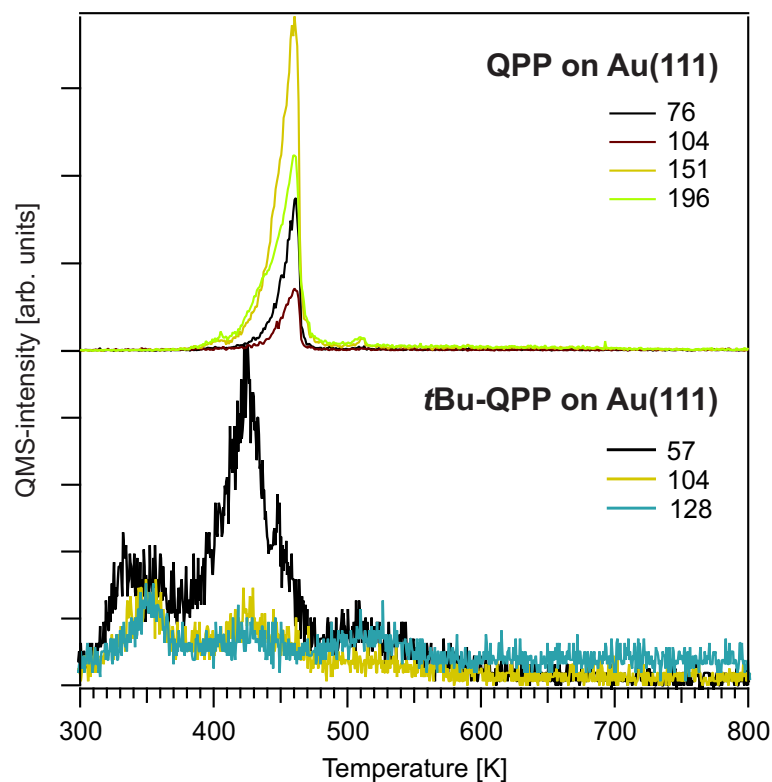


Figure G.2.: TPD measurements for multilayers of (a), QPP, and (b), *t*Bu-QPP. The observed fragments are listed in the graph.

G.2. QPP and *t*Bu-QPP: Electronic HREELS

Figure G.3 shows the electronic HREELS data for monolayers of QPP (blue) and *t*Bu-QPP (black) on Au(111) in comparison to data for the pristine Au(111) surface (red). The Au(111) surface plasmon at 2.61 eV is still visible in the monolayers, whereas a feature which could be assigned to the excitation of the optical gap is not visible. Due to the low signal-to-noise ratio and the difficulty to distinguish between contributions from the substrate and the adsorbate, a detailed analysis is skipped here.

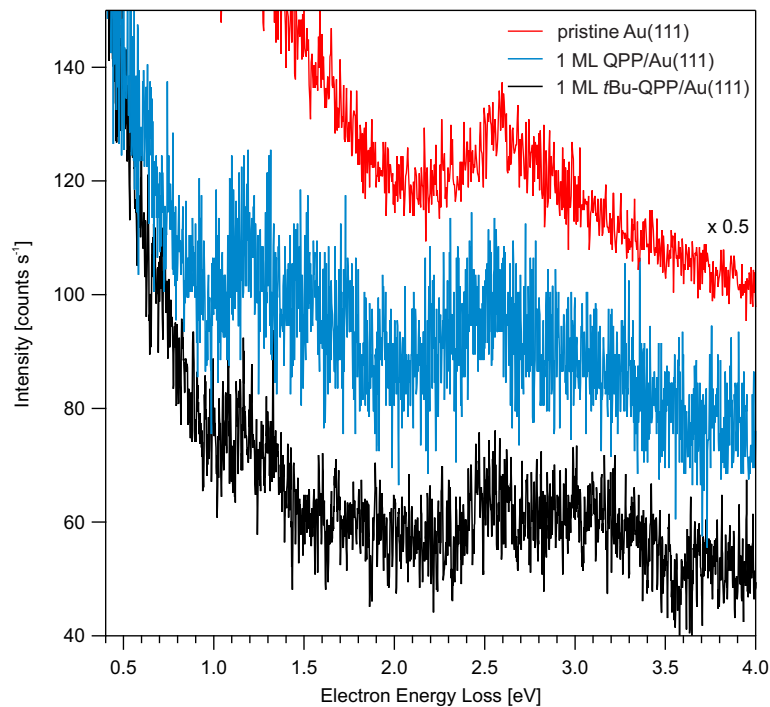


Figure G.3.: Electronic HREELS data of QPP (blue) and *t*Bu-QPP (black) monolayers on Au(111) and for the pristine Au(111) surface (red).

H. TAPP and its Derivatives: Further Studies and Vibrational Assignments

In Table H.1, all observed vibrational modes for TAPP are listed and assigned. In Fig. H.1, the listed vibrations for TAPP are visualized with the Facio19.1.4 program [121]. Exemplary for perfluoropropyl-substituted TAAPs, all observed vibrational modes for TAPP-H are listed and assigned in Table H.2. In Fig. H.2, the listed vibrations for TAPP-H are visualized. We pass on a similar presentation for TAPP-Cl, TAPP-Br, and TAPP-I due to minor differences.

H. TAPP and its Derivatives: Further Studies and Vibrational Assignments

Table H.1.: TAPP - Vibrational frequencies (in cm^{-1}) and assignments for 1 ML and 10 ML TAPP adsorbed on Au(111). *da* refers to dipole active modes. In addition DFT calculated frequencies based on the B3LYP functional and the 6-311G basis set of the free molecules are shown. ν , stretch; δ , in-plane bending; γ , out-of-plane bending; *C*, core; *T*, tips; representation and in brackets, corresponding orientation of the calculated dipole derivative vector with respect to the molecular geometry, *x* long axis, *y* short axis, *z* perpendicular to the molecular plane).

#	TAPP 1 ML	TAPP 10 ML	DFT	Mode	Repr.
1	178	199	176	buckl. long	B_{3u} (<i>z</i>)
2	229	237	239	buckl. short	B_{3u} (<i>z</i>)
3	449 <i>da</i>	-	465	$\delta(\text{C-C-C})$	B_{2u} (<i>y</i>)
4	488 <i>da</i>	510 <i>da</i>	504/529	$\gamma(\text{N-C-N})/\gamma(\text{C-C-C})$	B_{3u} (<i>z</i>)
5	-	565	572	$\delta(\text{C-C-C})$	B_{1u} (<i>x</i>)
6	-	687	692	$\delta(\text{C-C-C})$	B_{2u} (<i>y</i>)
7	778 <i>da</i>	809 <i>da</i>	814	$\gamma(\text{C-H})_C$	B_{3u} (<i>z</i>)
8	827 <i>da</i>	855 <i>da</i>	880	$\gamma(\text{C-H})/\gamma(\text{C-C-C})$	B_{3u} (<i>z</i>)
9	927	963	990	$\gamma(\text{C-H})_T$	B_{3u} (<i>z</i>)
10	-	1058	1080	$\delta(\text{C-C-C})$	B_{1u} (<i>x</i>)
11	-	1142	1163	$\delta(\text{C-C-H})$	B_{2u} (<i>y</i>)
12	-	1221	1242	$\delta(\text{N-C-N})$	B_{1u} (<i>x</i>)
13	-	1331	1350	$\nu(\text{C-C})$	B_{1u} (<i>x</i>)
14	-	1475	1510	$\delta(\text{N-C-H})$	B_{2u} (<i>y</i>)
15	-	1520	1558	$\nu(\text{C-N})$	B_{1u} (<i>x</i>)
16	-	1619	1663/1650	$\nu(\text{C-C})$	B_{1u}/A_g (<i>x/-</i>)
17	-	2929	3159	$\nu(\text{C-H})_T$	B_{1u} (<i>x</i>)
18	3056	3065	3219	$\nu(\text{C-H})_C$	B_{2u} (<i>y</i>)

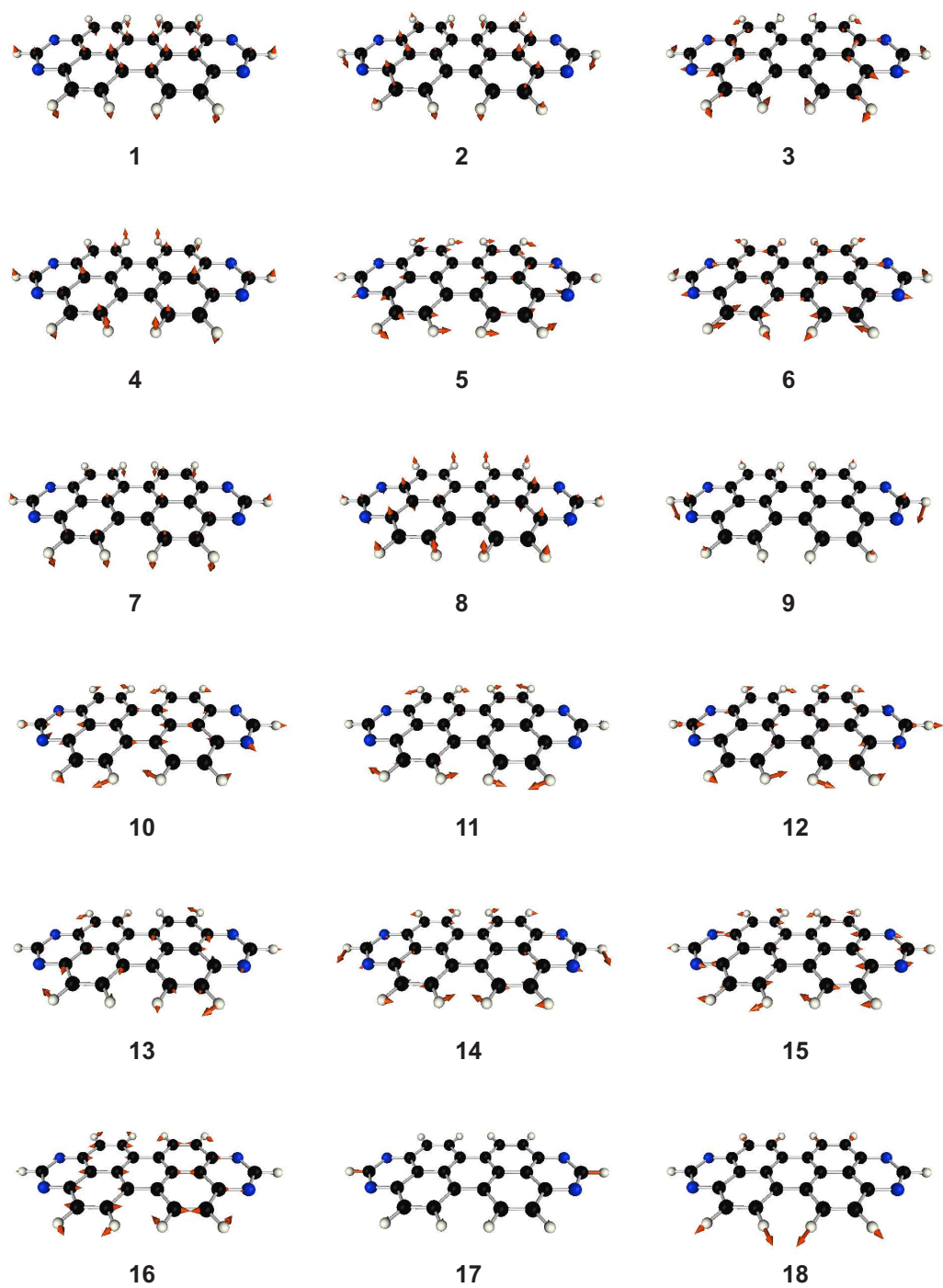


Figure H.1.: Visualizations of all observed and assigned vibrational modes for TAPP. Visualizations made with the Facio19.1.4 program [121]. The atomic displacement is indicated by the red arrows (enlarged by a factor of 5 for better visibility).

H. TAPP and its Derivatives: Further Studies and Vibrational Assignments

Table H.2.: TAPP-H - Vibrational frequencies (in cm^{-1}) and assignments for 1 ML and 6 ML TAPP-H adsorbed on Au(111). *da* refers to dipole active modes. In addition DFT calculated frequencies based on the B3LYP functional and the 6-311G basis set of the free molecules are shown. ν , stretch; δ , in-plane bending; γ , out-of-plane bending; *S*, side-chains; in brackets: corresponding orientation of the calculated dipole derivative vector with respect to the molecular geometry, *x* long axis, *y* short axis, *z* perpendicular to the molecular plane).

#	TAPP-H 1 ML	TAPP-H 6 ML	DFT	Mode	Repr.
1	190	176	168	$\tau(\text{C-C})$, buckl. short	(<i>x, z</i>)
2	255	232	188	$\tau(\text{C-C})$, buckl. long	(<i>x, z</i>)
3	-	290	282	side-chain wagging	(<i>x, z</i>)
4	523 <i>da</i>	526 <i>da</i>	493	$\delta(\text{C-C-C})_S$	(<i>z</i>)
5	581 <i>da</i>	607	586	$\delta(\text{C-C-C})_S + \delta(\text{C-H})$	(<i>x, z</i>)
6	-	704 <i>da</i>	662	$\gamma(\text{C-H})$	(<i>z</i>)
7	734 <i>da</i>	744 <i>da</i>	731	$\gamma(\text{N-C-N})$	(<i>x, z</i>)
8	806	802	767	$\gamma(\text{N-C-N})$	(<i>z</i>)
9	851 <i>da</i>	862 <i>da</i>	831	$\gamma(\text{C-H})$	(<i>x, z</i>)
10	911	-	866	$\gamma(\text{C-H})$	(<i>x, z</i>)
11	976 <i>da</i>	970 <i>da</i>	883	$\gamma(\text{C-H})$	(<i>z</i>)
12	1081	1062	968	$\delta(\text{C-C-C})_S + \gamma(\text{N-C-N})$	(<i>z</i>)
13	1225 <i>da</i>	1241 <i>da</i>	1206	$\nu(\text{C-F})$	(<i>z</i>)
14	1265 <i>da</i>	-	1241	$\nu(\text{C-F})$	(<i>z</i>)
15	1354	1349	1364	$\delta(\text{C-C-C})_S + \delta(\text{N-C-N})$	(<i>z</i>)
16	-	1527	1462	$\nu(\text{C-N})$	(<i>x</i>)
17	-	1617	1562	$\nu(\text{C-N})_T$	(<i>x</i>)
18	3057	3066	3258	$\nu(\text{C-H})_C$	(<i>y</i>)

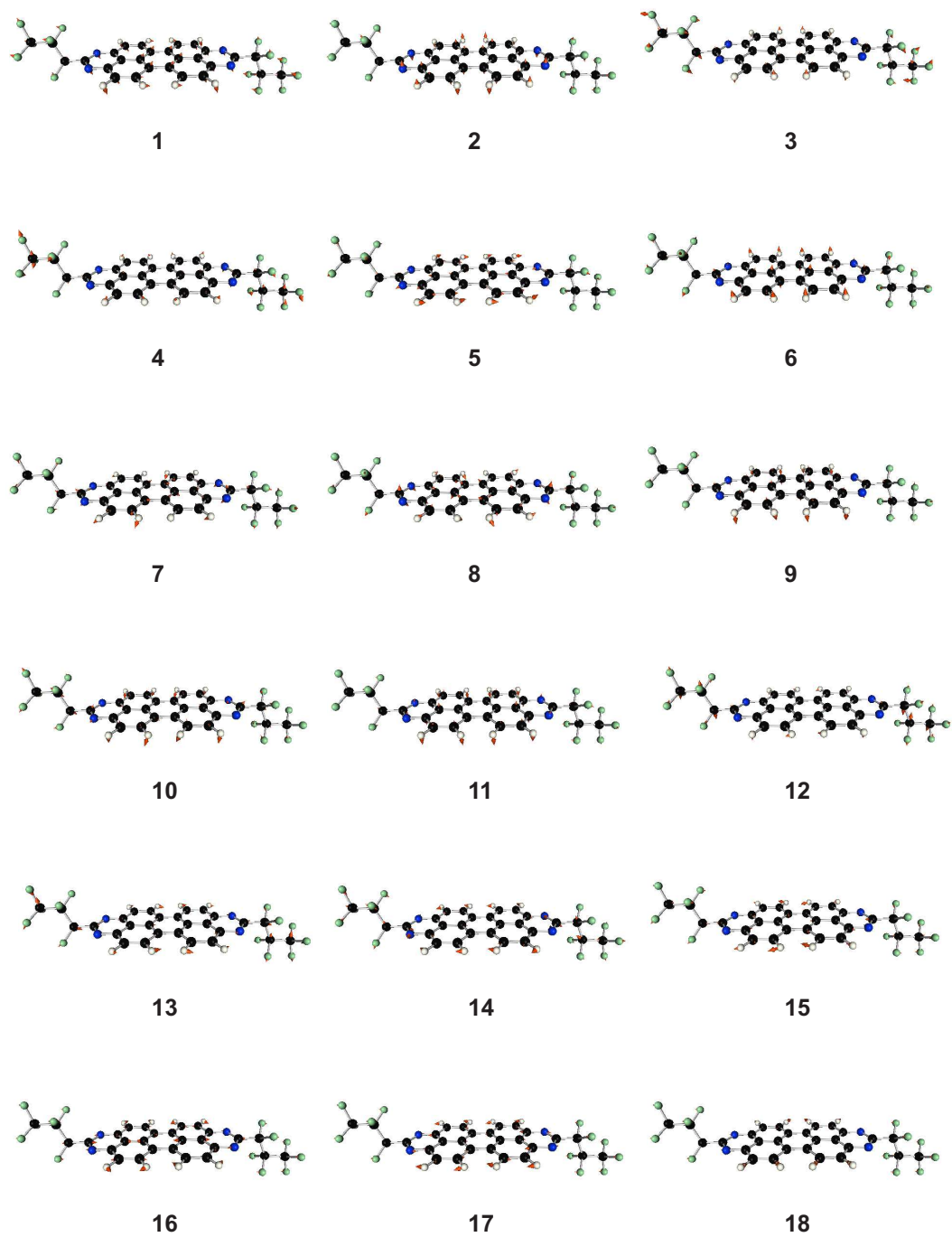


Figure H.2.: Visualizations of all observed and assigned vibrational modes for TAPP-H. Visualizations made with the Facio19.1.4 program [121]. The atomic displacement is indicated by the red arrows (enlarged by a factor of 5 for better visibility).

H.1. TAPP and its Derivatives: TPD

Figure H.3 shows TPD measurements of multilayers of TAPP and its derivatives on Au(111). All TAPPs show a peak assigned to multilayer desorption (note the zero-order desorption) around 450 K. The monolayer behaviour is rather different but suggests clearly destructive desorption.

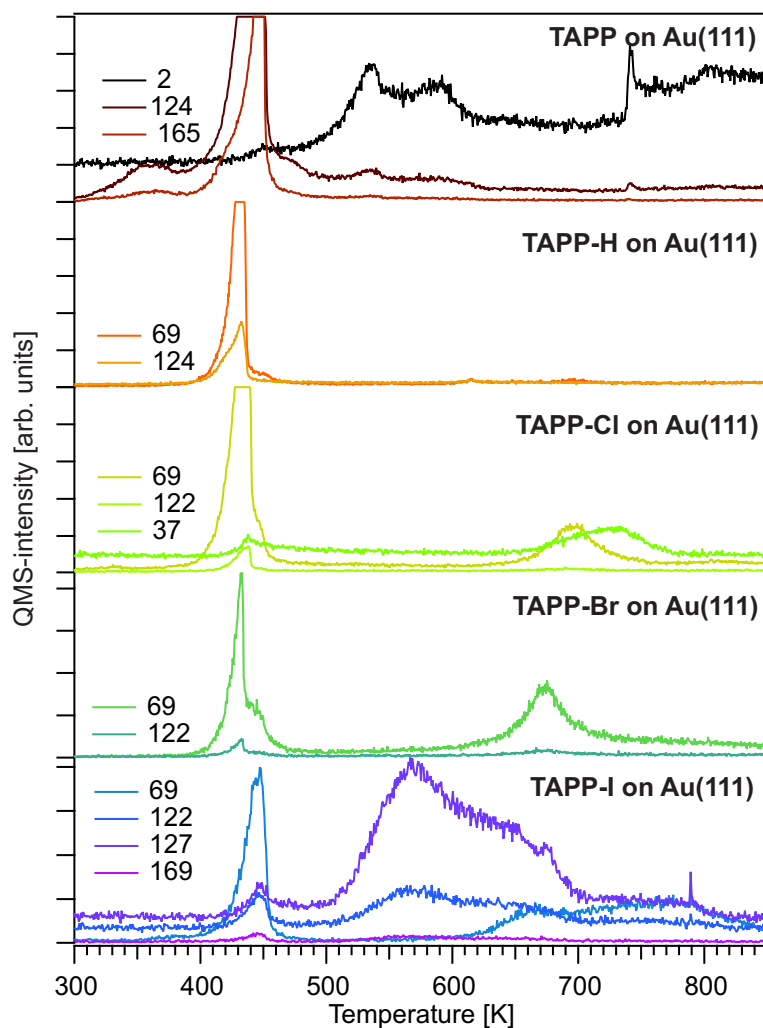


Figure H.3.: TPD measurements for all TAPP derivatives. Multilayers on Au(111), the observed fragments are listed in the graph.

H.2. TAPP and its Derivatives: Electronic HREELS

Figure H.4 shows the electronic HREELS data for monolayers of TAPP and its derivatives on Au(111) in comparison to data for the pristine Au(111) surface (red). It is hard to distinguish between contributions from the substrate and the adsorbate. Due to these difficulties, a detailed analysis is skipped here. But there is a significant influence of the halogenation on the monolayer spectra. The peaks associated to the excitation of the optical gap/Au(111) surface plasmon around 2.6 eV are shifted by 0.2 eV to higher energies for the non-halogenated TAPPs (TAPP (blue) and TAPP-H (dark green)).

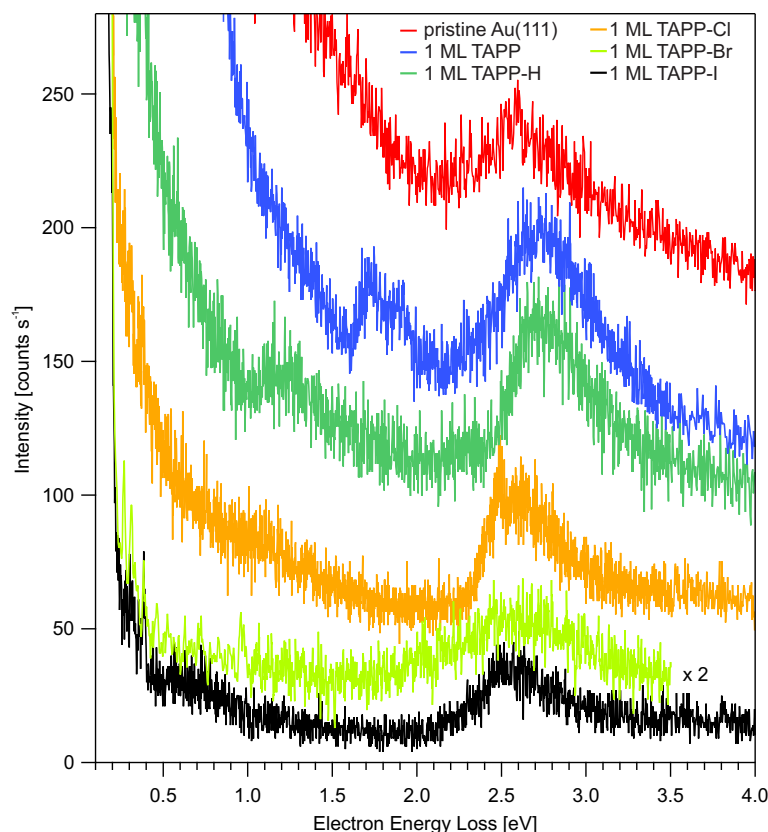


Figure H.4.: Electronic HREELS ($E_0 = 15.5$ eV) data in specular geometry for monolayers of all TAPP derivatives on Au(111) and for the pristine Au(111) surface (red).

H. TAPP and its Derivatives: Further Studies and Vibrational Assignments

I. Angle-Resolved HREELS: Further Measurements

The following section covers further measurements connected to the investigation of the plasmonic excitation in chapter 5. First, the automatized angle-resolved measurement is explained (section I.1), then the results about the influence of preparation conditions (section I.2), crystal orientation (section I.3), primary electron energy (section I.4), and coverage (section I.5) on the plasmonic excitation are shown. At last, TPD, as well as, vibrational and (angle-resolved) electronic HREELS measurements for systems that show analogous plasmonic excitations are presented (section I.6).

I.1. Explanation and Exemplary Arduino Input for Automated Measurements

This section provides a brief explanation of the developed automatized angle-resolved HREELS measurement. The requirement for the whole project was the possibility to measure subsequently up to 999 HREEL spectra within the “average” option of the Delta 0.5 control software. The task was to move the spectrometers angle-control by a specific value in a limited time between two measurements. The Arduino controlled stepper motor described in section 2.4.1 fulfils this function properly. However, it was not possible to establish a simple executable program which sends the relevant parameters to the Arduino, thus for any angle-resolved measurement, the program code has to be adjusted. An angle-resolved measurement is performed within several steps. First three things have to be considered: (1) The favoured angle step size, (2) the angular range, and (3) the length (and thus quality) of a single measurement. Together these values determine the number of measurements and the length of the complete job. The number of measurements and the parameters of the single measurements (energy step width, integration time etc.) is set in the Delta 0.5 control program. The stepper motor control needs only the num-

I. Angle-Resolved HREELS: Further Measurements

ber of steps (51 motor steps are 0.01 turns of the spectrometers angle control, thus a value of 500 leads to 0.1 turns (0.23°) between two measurements) and the time between two angle steps (measurement time in ms). Figure I.1 shows the used Arduino program. The orange part is called “Setup”, as the definition of variables and the assignments of the shield’s pins is located here. The “Loop” part (blue) is executed continuously. The first part is a simple “for”-loop which is repeated 500 times in the example and contains the control of each solenoid to perform motor steps. After 500 times (which is a change of the analyzer angle by 0.23°), a delay is performed. The delay should correspond to the measurement time minus the time which is needed for the rotation as between two HREEL spectra no break can be forced.

I.1. Explanation and Exemplary Arduino Input for Automated Measurements

```
/*
This is a sketch for automatized angle-resolved HREELS measurements for
the Adafruit assembled Motor Shield for Arduino v2
*/
int delaylength = 30;
int x;
void setup() {

  //establish motor direction toggle pins
  pinMode(12, OUTPUT); //CH A -- HIGH = forwards and LOW = backwards???
  pinMode(13, OUTPUT); //CH B -- HIGH = forwards and LOW = backwards???

  //establish motor brake pins
  pinMode(9, OUTPUT); //brake (disable) CH A
  pinMode(8, OUTPUT); //brake (disable) CH B
}

void loop(){
  for (x = 1; x < 500; x+=1) { //51 steps -> 0.01 turn
    digitalWrite(9, LOW); //ENABLE CH A
    digitalWrite(8, HIGH); //DISABLE CH B

    digitalWrite(12, HIGH); //Sets direction of CH A
    analogWrite(3, 255); //Moves CH A

    delay(delaylength);

    digitalWrite(9, HIGH); //DISABLE CH A
    digitalWrite(8, LOW); //ENABLE CH B

    digitalWrite(13, HIGH); //Sets direction of CH B
    analogWrite(11, 255); //Moves CH B

    delay(delaylength);

    digitalWrite(9, LOW); //ENABLE CH A
    digitalWrite(8, HIGH); //DISABLE CH B

    digitalWrite(12, LOW); //Sets direction of CH A
    analogWrite(3, 255); //Moves CH A

    delay(delaylength);

    digitalWrite(9, HIGH); //DISABLE CH A
    digitalWrite(8, LOW); //ENABLE CH B

    digitalWrite(13, LOW); //Sets direction of CH B
    analogWrite(11, 255); //Moves CH B

    delay(delaylength);
  }
  delay(1626666); // break in milliseconds
}
```

SETUP

number of steps

LOOP

time for one measurement in ms

Figure I.1.: Commented Arduino program code. (orange) Setup part, which determines the pin assignment on the board. (blue) Loop part, where the angle step size between two measurements and the length of a single measurement are defined.

1.2. Influence of the Preparation

Fig. I.2 shows the electronic HREEL spectra for different preparation conditions for the $F_4TCNQ/Au(111)$ system. Fig. I.2 (a) shows the spectrum for a deposition of 9 ML F_4TCNQ on a $Au(111)$ surface at room temperature. Feature P is well-visible in the low-energy region (0.58 eV) only slightly affected by the high coverage. A feature assigned to the excitation of the optical gap is only barely visible at 3.28 eV, suggesting screened frontier orbitals up to the investigated coverage of 9 ML. Fig. I.2 (b) shows the corresponding spectrum for dosing onto a 120 K cold substrate. The coverage is only half the coverage in (a) but Feature P has almost vanished and the intramolecular electronic excitations 3.35 eV and 5.46 eV are well pronounced. This different behaviour is assigned to well-ordering and band formation for the room temperature sample and a disordered multilayer at the 120 K sample.

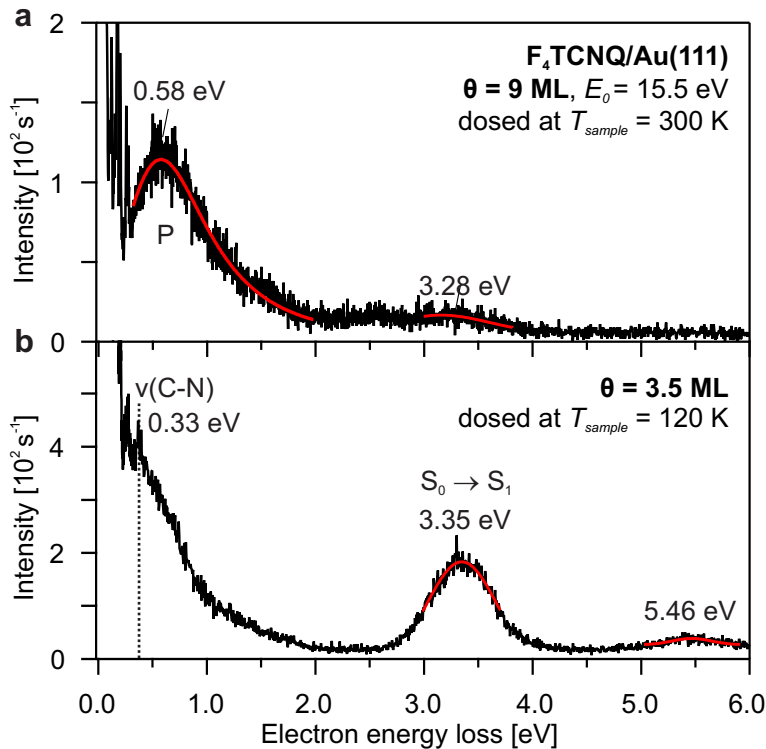


Figure I.2.: (a) Electronic HREEL spectrum ($E_0 = 15.5 \text{ eV}$) of 9 ML F_4TCNQ on $Au(111)$ dosed at a sample temperature of $T_{\text{sample}} = 300 \text{ K}$; (b) corresponding spectrum obtained for a coverage of 3.5 ML dosed at $T_{\text{sample}} = 120 \text{ K}$.

I.3. Influence of the Crystal Orientation

Figure I.3 shows the investigation of the plasmonic excitation with different crystal geometries. Unfortunately, the used experimental setup did not contain a LEED spectrometer to measure the actual crystal geometry. Therefore the orientation was measured in another setup (2PPE, LEED image in Fig. I.3 (b), and Brillouin-zone in (c)). From this measurement, it was concluded, that all measurements in this thesis have been performed in a direction between the Γ -M and Γ -K direction (blue dispersion curve in Fig. I.3 (f)). To investigate the influence of the crystal orientation, the sample was rotated in the sample holder by about 11° and thus the red curve in Fig. I.3 (f) was recorded in Γ -K direction. Within the measurement accuracy, no significant change could be observed.

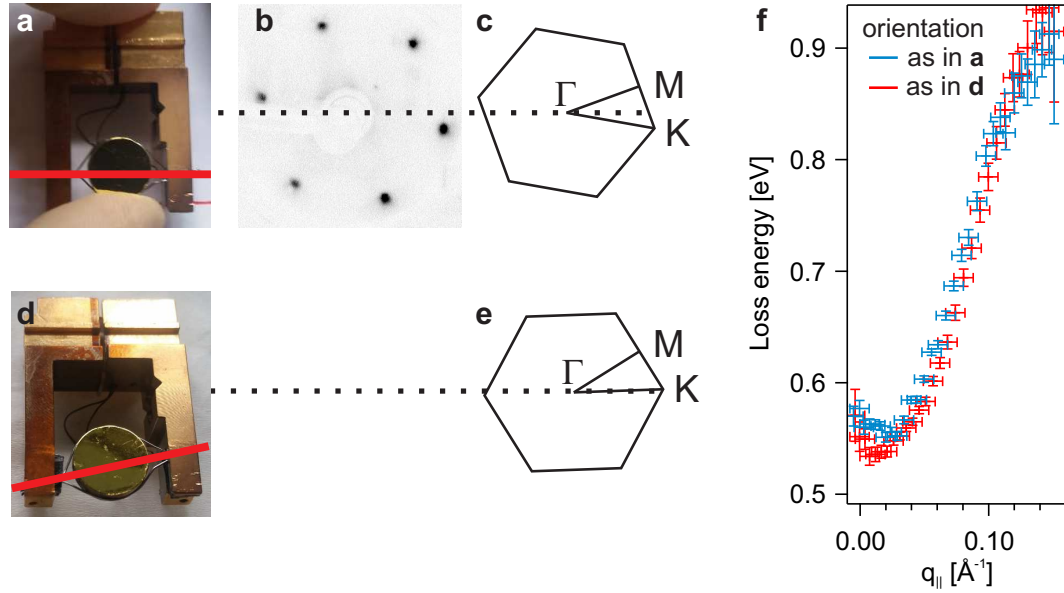


Figure I.3.: (a) and (d), pictures of the sample holder with the Au crystal in parallel orientation (a) and rotated by 12° (d); (b) LEED image obtained in 2PPE chamber in parallel orientation; (c) and (e), corresponding Brillouin-zone scheme with high-symmetry points (Γ , M, K) and measurement direction (dotted line); (f), q_{\parallel} dependence of the plasmon energy as obtained from angle-resolved HREELS measurements with the two different crystal orientations.

I.4. Influence of the Primary Electron Energy

Fig. I.4 shows the results for E_0 -dependent measurements for monolayers of F_4 TCNQ and TCNQ on Au(111). The measurements reveal an increasing loss energy with increasing E_0 for both systems. To draw reliable conclusions, first, the nature of the plasmonic excitation has to be elucidated in more detail.

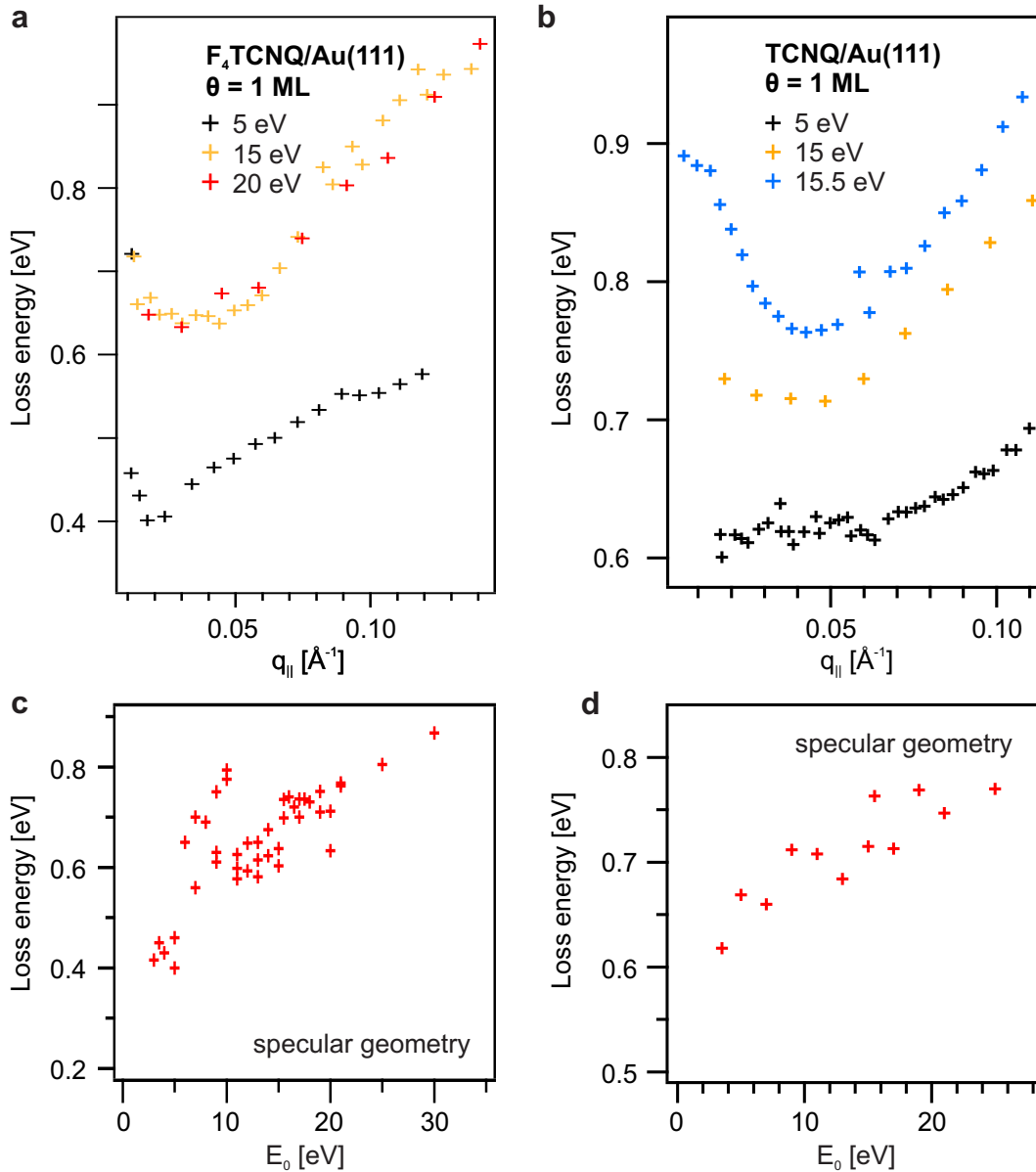


Figure I.4.: (a) and (b) show dispersion curves obtained with different E_0 for F_4 TCNQ and TCNQ monolayers on Au(111), respectively. (c) and (d) show the resulting loss energy of the plasmonic feature vs. E_0 for F_4 TCNQ and TCNQ, respectively.

I.5. Influence of the Coverage

Fig. I.5 shows the results for coverage-dependent measurements of F_4TCNQ and $TCNQ$ on $Au(111)$. The measurements reveal a decreasing loss energy with increasing coverage for both systems. To draw reliable conclusions, first, the nature of the plasmonic excitation has to be elucidated in more detail.

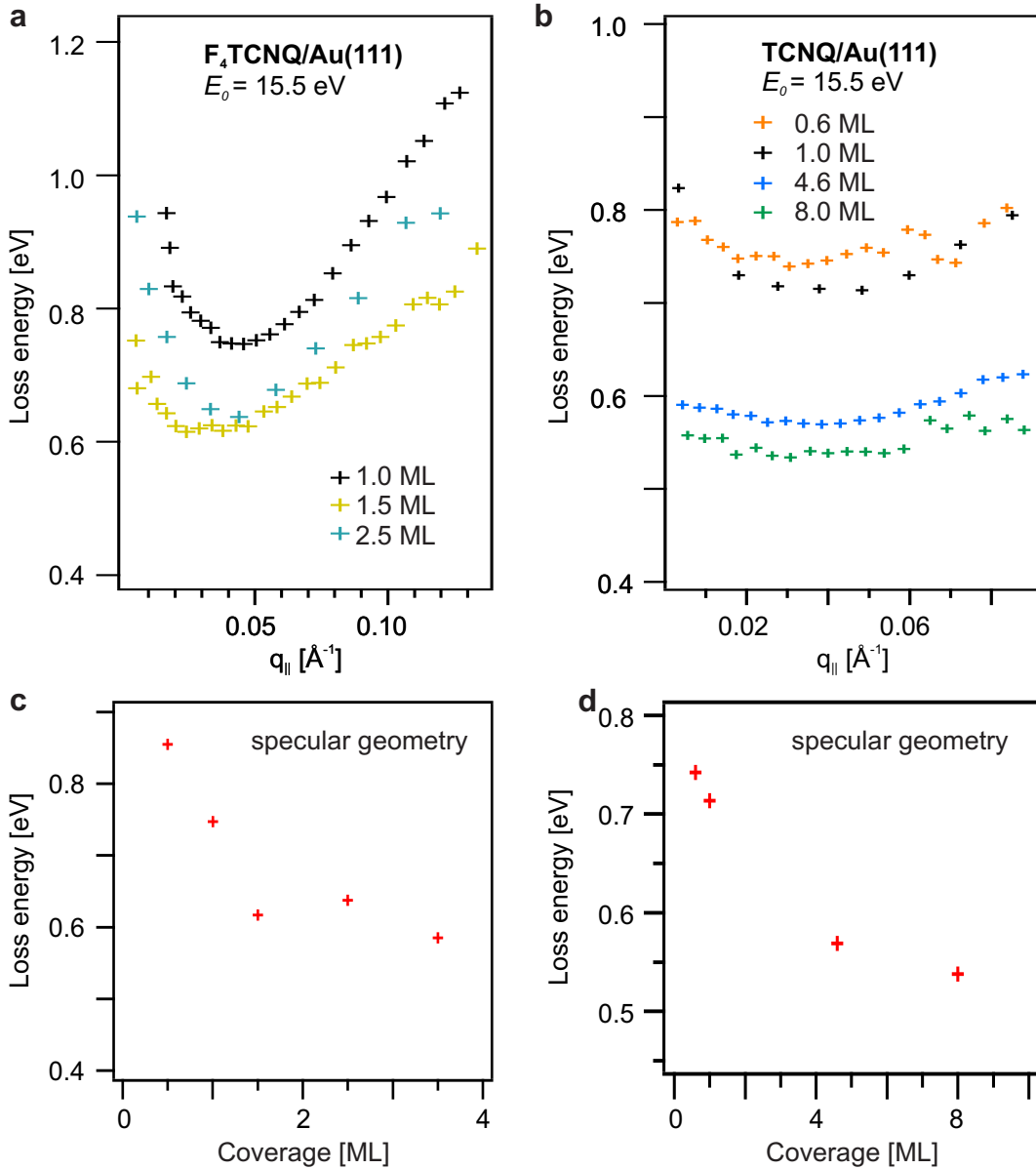


Figure I.5.: (a) and (b) show dispersion curves obtained with different coverages (θ) of F_4TCNQ and $TCNQ$ monolayers on $Au(111)$, respectively. (c) and (d) show the resulting loss energy of the plasmonic feature *vs.* θ for F_4TCNQ and $TCNQ$, respectively.

I.6. Analogous Excitations

This section of the Appendix covers all the data correlated to the measurement of the plasmonic excitation in several systems besides the F_4 TCNQ and TCNQ on Au(111) system. Figures I.6, I.7, I.8, I.9, I.10, and I.11, show the data for $[\text{TCNQ}]^-[\text{TTF}]^+$, F_2 TCNQ, pentacene, tetracene, TTF, and anthracene, on Au(111), respectively. All Figures show a multilayer TPD, vibrational HREELS measurements of the monolayer in specular and off-specular geometry, an electronic HREELS measurement in specular geometry, angle-resolved electronic HREELS measurements, and the obtained loss energy, intensity, and FWHM dependence on the transferred parallel momentum. Note, whereas usually, the electronic HREELS data is for monolayer coverages, for pentacene HREELS measurements for different coverages are presented to show the influence of the coverage on the plasmonic excitation. A brief discussion of the obtained results shall show the most pronounced similarities and differences. A more detailed analysis and interpretation will be part of future works.

The TPD spectra show a separation of mono- and multilayer peaks for $[\text{TCNQ}]^-[\text{TTF}]^+$ and F_2 TCNQ, for the other molecules the transition is fluent. The monolayer coverages for the HREELS measurements were obtained by annealing or dosing at specific temperatures that prevent multilayer adsorption. All vibrational HREELS measurements reveal a well-ordered film and an adsorption geometry with the plane of the aromatic system oriented parallel to the surface. All electronic spectra show a dispersive low-energy excitation and the more or less pronounced conventional Au(111) surface plasmon around 2.6 eV. Anthracene shows an additional low-energy excitation at 1.21 eV (see Fig. I.11 (c)). The angle-resolved measurements show a dispersive excitation in all systems. The slope of the dispersion curve is rather quadratic for $[\text{TCNQ}]^-[\text{TTF}]^+$ (see Fig. I.6 (e)) and rather linear for the other systems. Analogous to F_4 TCNQ and TCNQ on Au(111), the minimum of the loss energy and the linewidth (FWHM), as well as the maximum in intensity, are shifted from $q_{\parallel} = 0$.

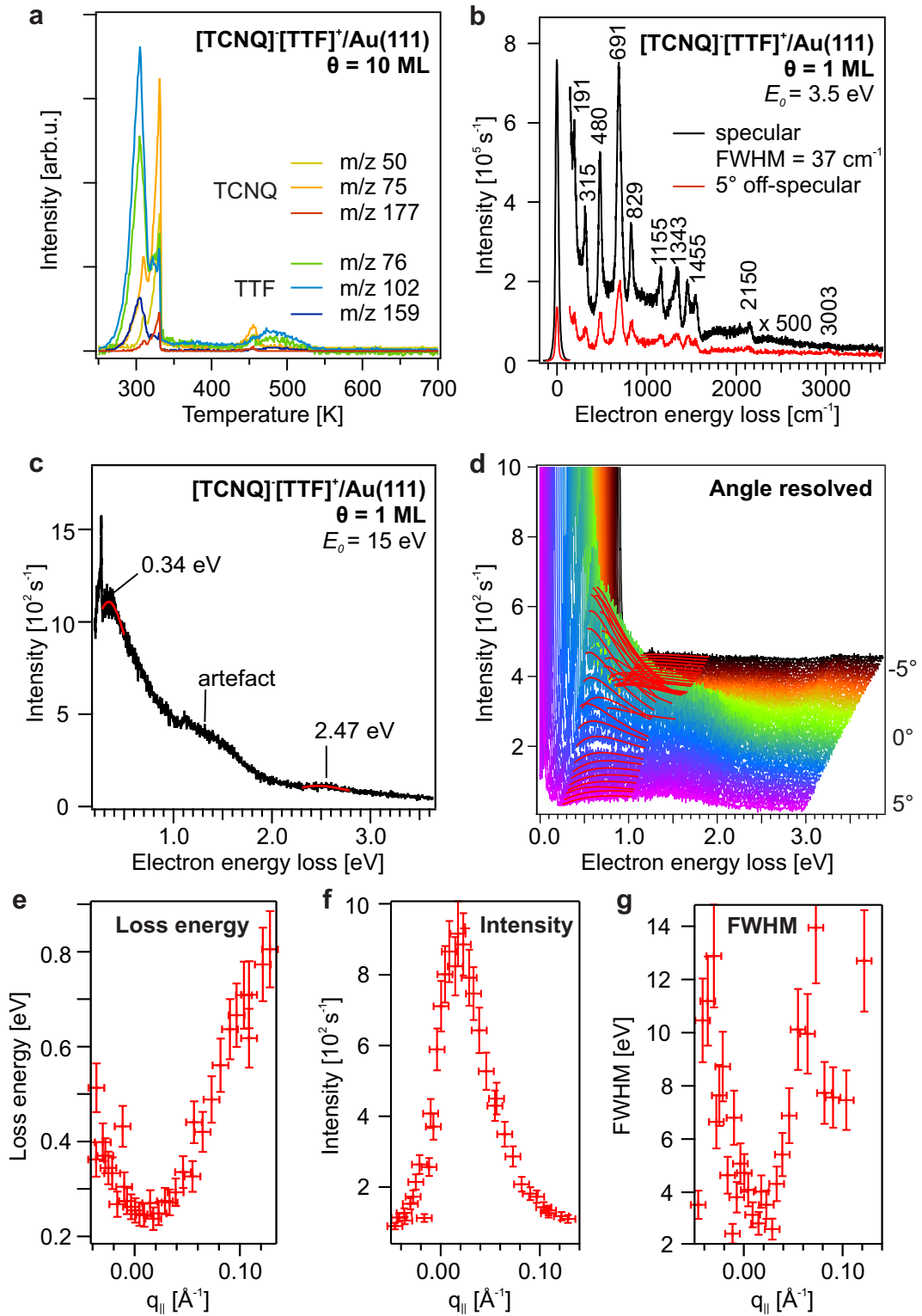


Figure I.6.: (a) TPD spectrum of 10 ML [TCNQ]⁻[TTF]⁺ on Au(111), (b) - (g) HREEL data for 1 ML [TCNQ]⁻[TTF]⁺ on Au(111), (b) vibrational HREEL spectra in specular and off-specular scattering geometry, (c) electronic HREEL spectra, (d) 45 angle-resolved electronic HREEL spectra (e), (f), and (g) show the loss energy of the plasmonic excitation, the corresponding intensity, and linewidth depending on $q_{||}$, respectively.

I. Angle-Resolved HREELS: Further Measurements

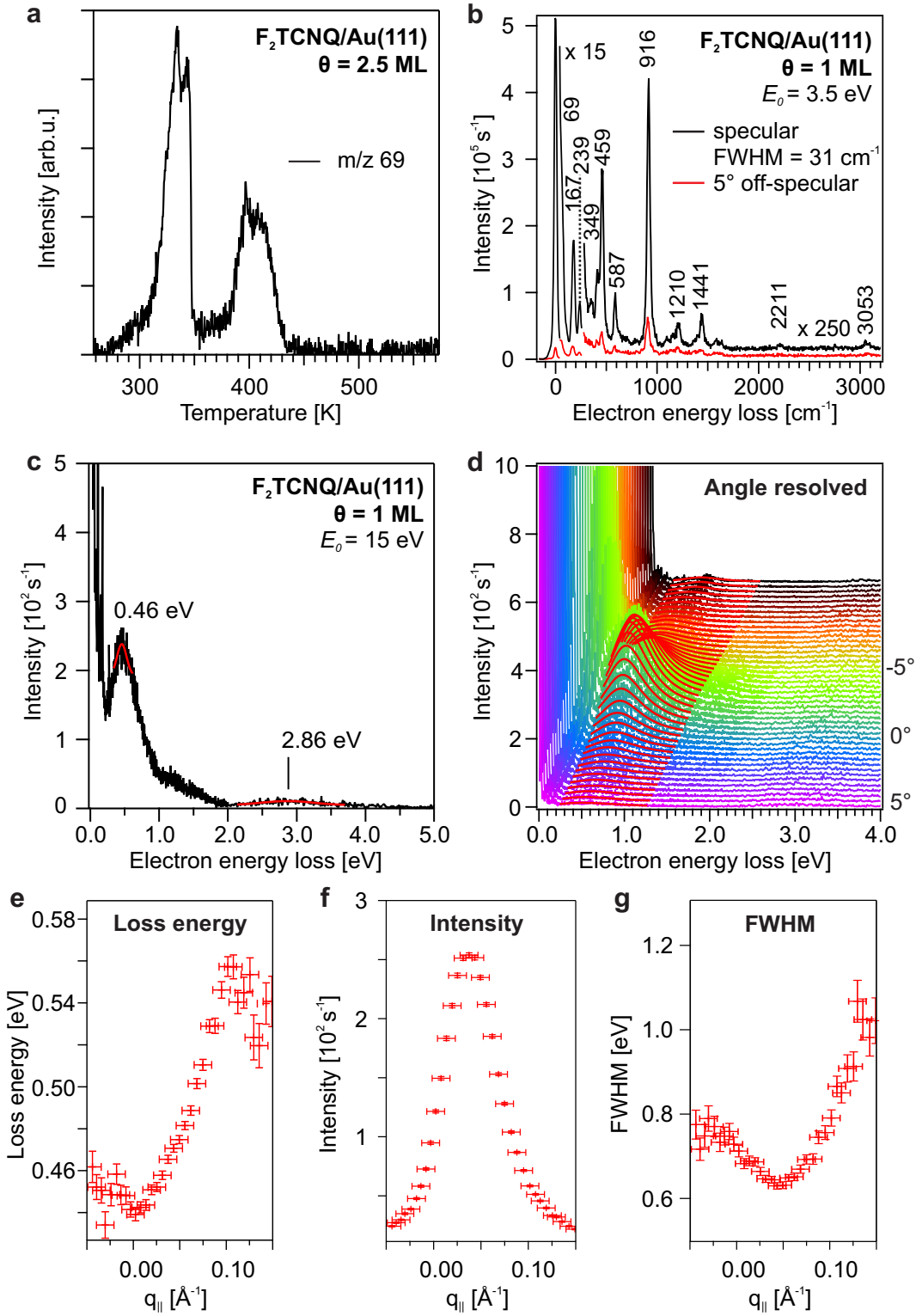


Figure I.7.: (a) TPD spectrum of 2.5 ML F₂TCNQ on Au(111), (b) - (g) HREEL data for 1 ML F₂TCNQ on Au(111), (b) vibrational HREEL spectra in specular and off-specular scattering geometry, (c) electronic HREEL spectra, (d) 45 angle-resolved electronic HREEL spectra (e), (f), and (g) show the loss energy of the plasmonic excitation, the corresponding intensity, and linewidth depending on $q_{||}$, respectively.

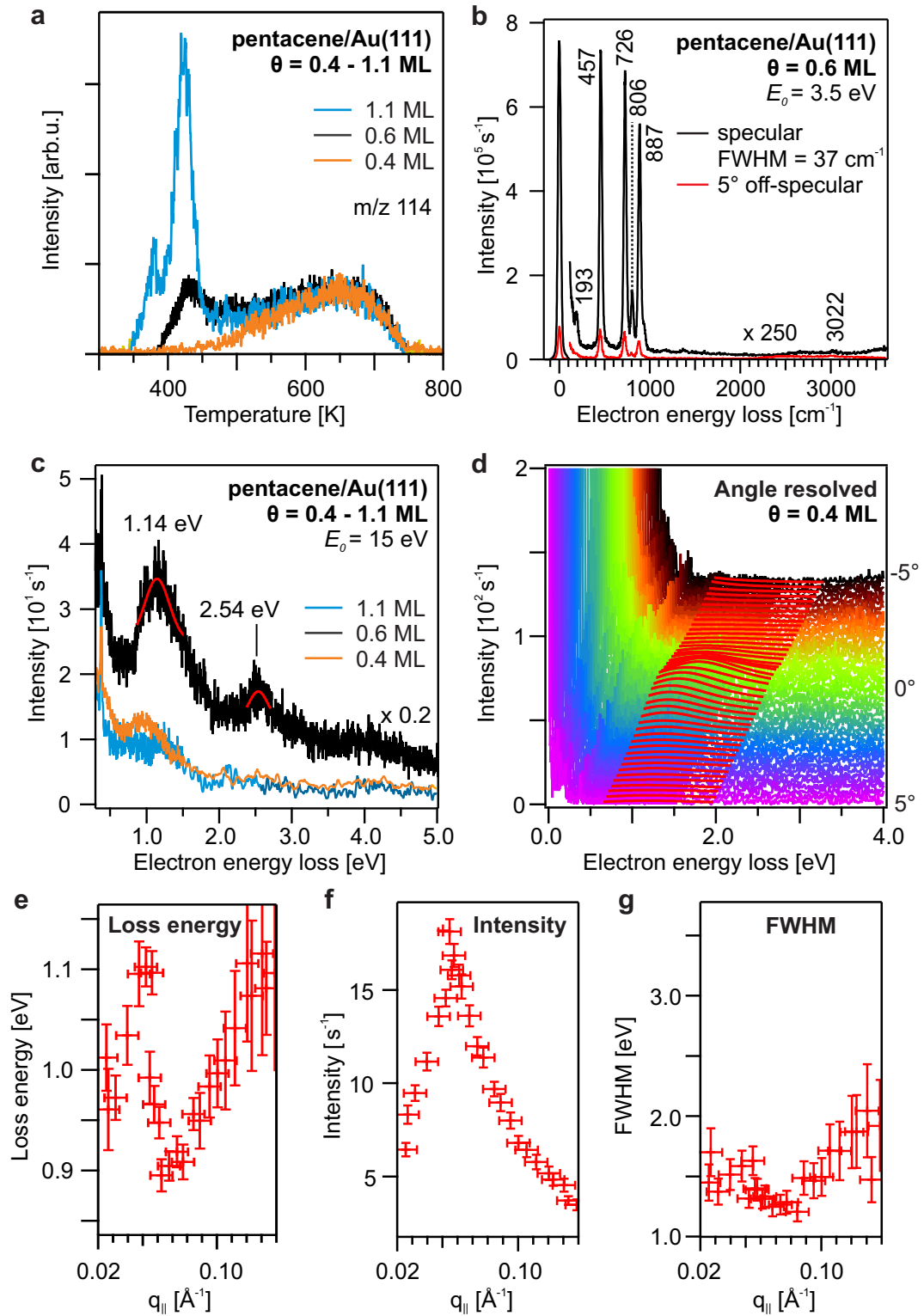


Figure I.8.: (a) TPD spectra of 0.4, 0.6, and 1.1 ML pentacene on Au(111); (b) vibrational HREEL spectra in specular and off-specular scattering geometry for $\theta = 0.6$ ML; (c) electronic HREEL spectra for the coverages from (a); (d) 45 angle-resolved electronic HREEL spectra for $\theta = 0.6$ ML; (e), (f), and (g) show the loss energy of the plasmonic excitation, the corresponding intensity, and linewidth depending on q_{\parallel} , respectively, as derived from (d).

I. Angle-Resolved HREELS: Further Measurements

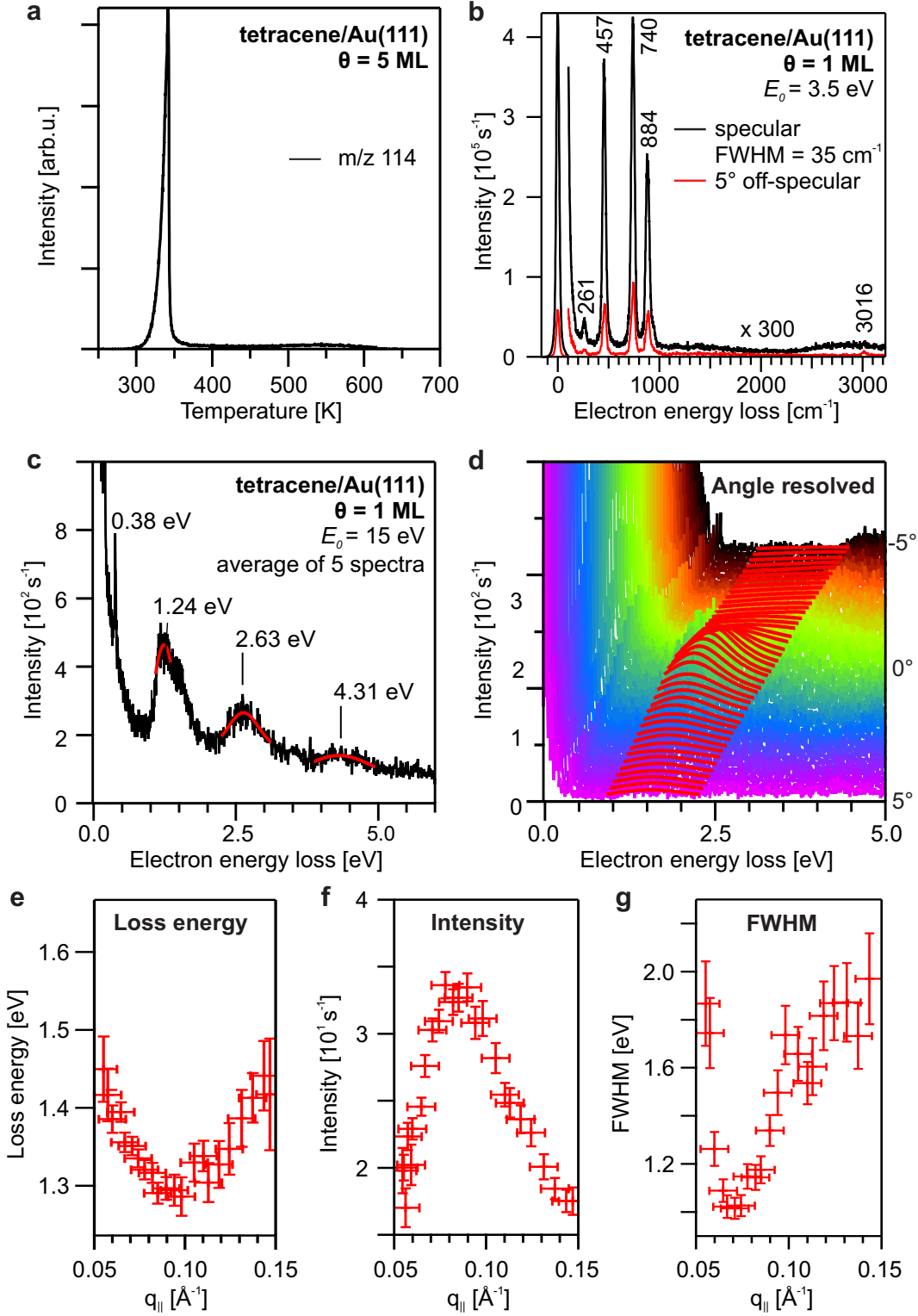


Figure I.9.: (a) TPD spectrum of 5 ML tetracene on Au(111), (b) - (g) HREEL data for 1 ML tetracene on Au(111), (b) vibrational HREEL spectra in specular and off-specular scattering geometry, (c) electronic HREEL spectra, (d) 45 angle-resolved electronic HREEL spectra (e), (f), and (g) show the loss energy of the plasmonic excitation, the corresponding intensity, and linewidth depending on $q_{||}$, respectively.

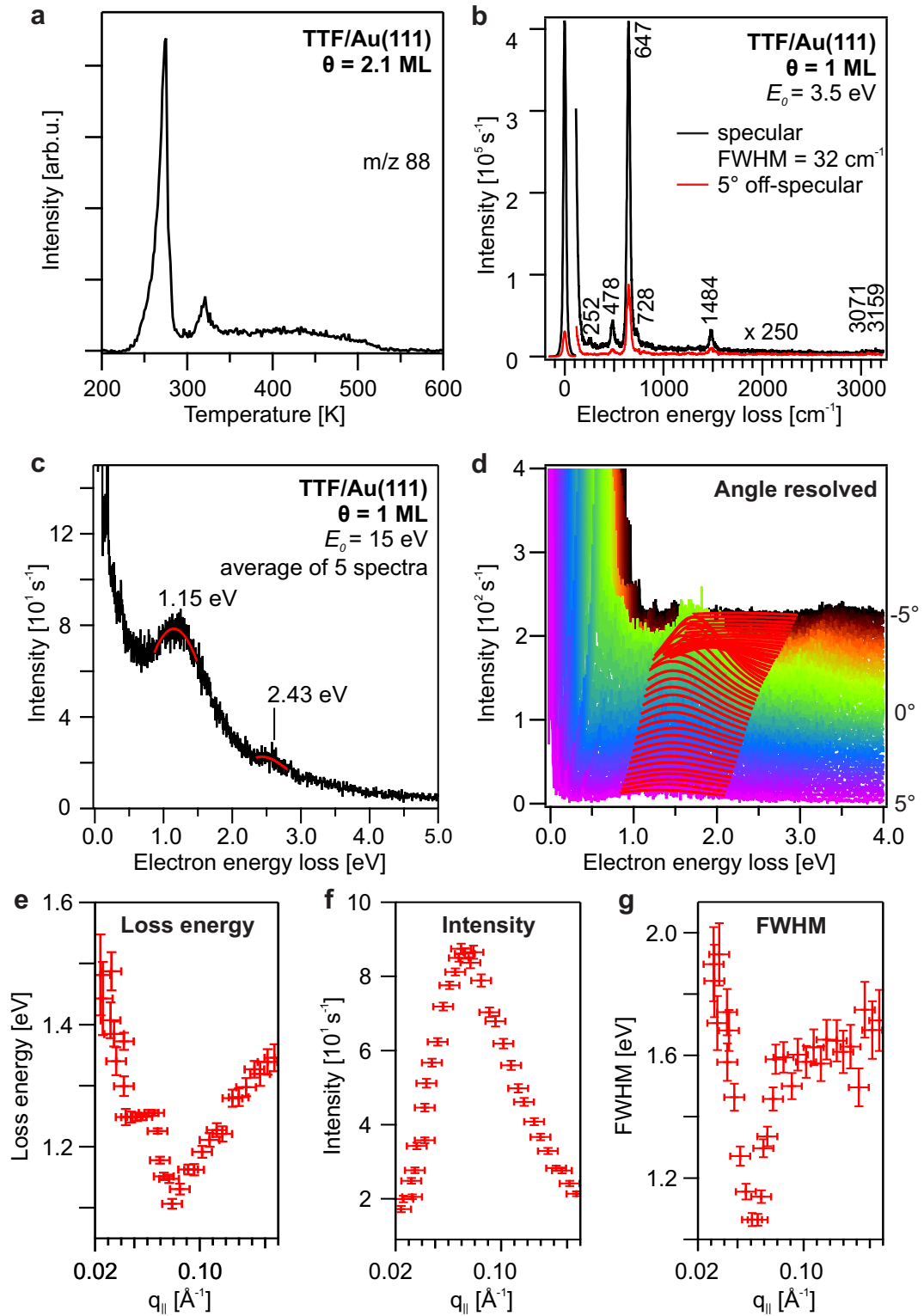


Figure I.10.: (a) TPD spectrum of 2.1 ML TTF on Au(111), (b) - (g) HREEL data for 1 ML TTF on Au(111), (b) vibrational HREEL spectra in specular and off-specular scattering geometry, (c) electronic HREEL spectra, (d) 45 angle-resolved electronic HREEL spectra (e), (f), and (g) show the loss energy of the plasmonic excitation, the corresponding intensity, and linewidth depending on $q_{||}$, respectively.

I. Angle-Resolved HREELS: Further Measurements

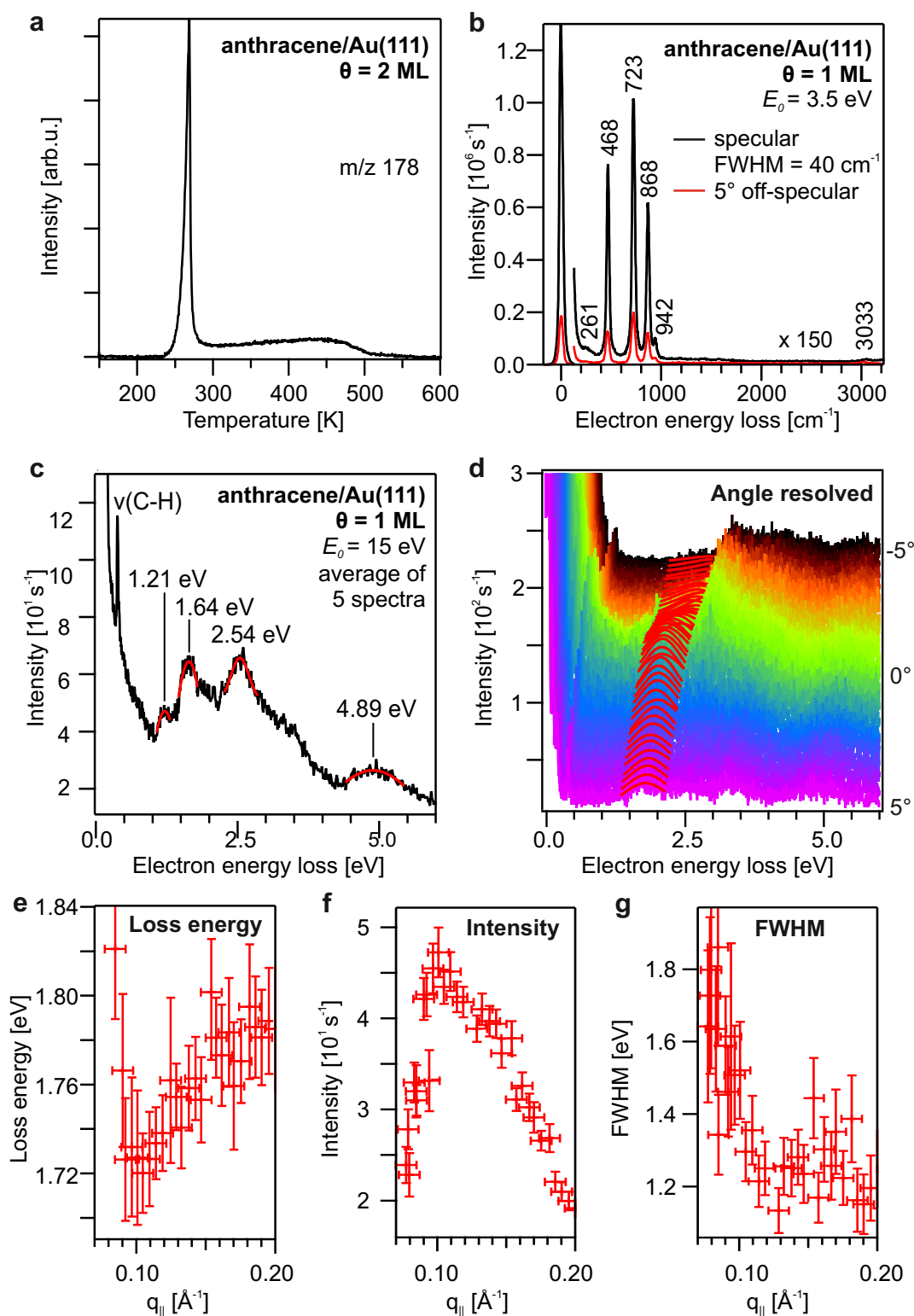


Figure I.11.: (a) TPD spectrum of 2 ML anthracene on Au(111), (b) - (g) HREEL data for 1 ML anthracene on Au(111), (b) vibrational HREEL spectra in specular and off-specular scattering geometry, (c) electronic HREEL spectra, (d) 45 angle-resolved electronic HREEL spectra (e), (f), and (g) show the loss energy of the plasmonic excitation, the corresponding intensity, and linewidth depending on q_{\parallel} , respectively.

I.7. Vibrational Assignments for F₄TCNQ

In Table I.1, all observed vibrational modes for F₄TCNQ are listed and assigned. In Fig. I.12, the listed vibrations for F₄TCNQ are visualized with the Facio19.1.4 program [121]. We pass on a similar presentation for TCNQ and F₂TCNQ due to minor differences, which can be attributed to the occurrence of H-atoms in TCNQ and F₂TCNQ.

Table I.1.: F₄TCNQ - Vibrational frequencies (in cm⁻¹) and assignments for 1 ML and 8 ML F₄TCNQ adsorbed on Au(111). *da* refers to dipole active modes. In addition DFT calculated frequencies based on the B3LYP functional and the 6-311G basis set of the free molecules are shown. ν , stretch; δ , in-plane bending; γ , out-of-plane bending; representation and in brackets, corresponding orientation of the calculated dipole derivative vector with respect to the molecular geometry, x long axis, y short axis, z perpendicular to the molecular plane).

#	1 ML	8 ML	DFT	Mode	Repr.
1	161 <i>da</i>	183	167	$\tau(\text{C-C})$, buckl. long	$B_{3u}(z)$
2	254 <i>da</i>	257	263	$\tau(\text{C-C})$, buckl. short	$B_{3u}(z)$
3	-	441	486	$\delta(\text{C-C-C})$	A_g
4	528 <i>da</i>	557	597	$\gamma(\text{C-C-C})$	$B_{3u}(z)$
5	632	609	638	$\delta(\text{C-C-N})$	A_g
6	-	803	811	$\delta(\text{C-C-C}) + \delta(\text{C-C-F})$	$B_{1u}(x)$
7	904	880	897	$\delta(\text{C-C-C})$	A_g
8	-	971	986	$\delta(\text{C-C-C}) + \nu(\text{C-F})$	$B_{2u}(y)$
9	-	1132	1152	$\delta(\text{C-C-C}) + \delta(\text{C-C-F})$	$B_{1u}(x)$
10	-	1187	1204	$\delta(\text{C-C-C})$	$B_{2u}(y)$
11	1248	1284	1354	$\delta(\text{C-C-C}) + \delta(\text{C-C-F})$	$B_{1u}(x)$
12	-	1358	1395	$\delta(\text{C-C-C}) + \nu(\text{C-C}) + \gamma(\text{N-C-N})$	$B_{2u}(y)$
13	1427 <i>da</i>	1455	1499	$\nu(\text{C-C})$	A_g
14	-	1584	1621	$\nu(\text{C-C})$	$B_{2u}(y)$
15	-	1652	1696	$\nu(\text{C-C})_S + \delta(\text{N-C-N})$	A_g
16	2084	2217	2311	$\nu(\text{C-N})$	$B_{2u}(y)$

I. Angle-Resolved HREELS: Further Measurements

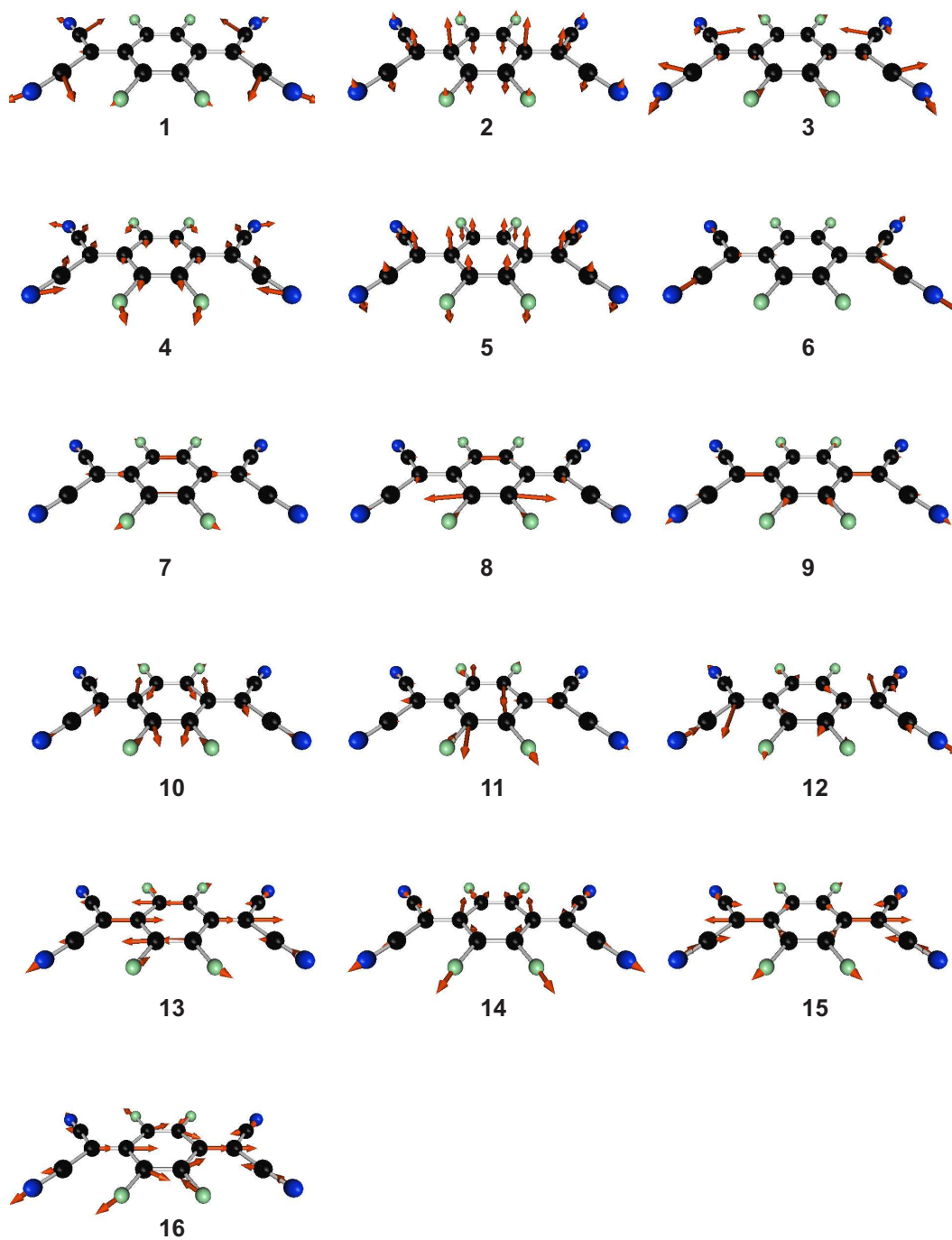


Figure I.12.: Visualization of all observed vibrational modes of F₄TCNQ. The numerization is corresponding to table I.1 and the visualization was made with the Facio19.1.4 program [121]. The atomic displacement is indicated by the red arrows (enlarged by a factor of 5 for better visibility).

J. Calculated Optimized Structures

Mode assignments in previous chapters are based on DFT frequency calculations performed after a geometry optimization (all within the Gaussian09[®] [120] program package). Therefore the cartesian coordinates of all calculated optimized molecular structures are summarized here. A brief DFT explanation can be found in section 2.3, a commented Gaussian09[®] input file can be found in App. C.

J. Calculated Optimized Structures

TIPS-Pn (B3LYP/6-311G)

#	Sym	X	Y	Z	#	Sym	X	Y	Z
1	Si	5.944175	-0.024622	0.101588	51	H	-2.500064	4.950522	0.018282
2	C	1.435925	0.001911	0.021098	52	H	-2.486783	2.472942	-0.006994
3	C	0.724783	1.237042	0.02518	53	H	7.573527	-0.456177	1.91148
4	C	1.399674	2.478964	0.049645	54	H	4.924499	0.712239	2.936248
5	C	0.721427	3.693938	0.053035	55	H	6.416452	1.620763	2.681122
6	C	1.405594	4.957138	0.076876	56	H	6.342234	0.382447	3.93251
7	C	0.709304	6.133942	0.079176	57	H	6.316983	-2.058462	3.377976
8	C	-0.724017	6.132425	0.057696	58	H	6.373347	-2.635255	1.713852
9	C	-1.417382	4.954131	0.034587	59	H	4.897256	-1.897651	2.344267
10	C	-0.730128	3.692405	0.031142	60	H	6.048809	-2.342673	-0.636254
11	C	-1.40561	2.476092	0.008066	61	H	8.284587	-2.568483	-1.674206
12	C	-0.727989	1.235452	0.003989	62	H	8.444187	-1.798663	-0.097155
13	C	2.856923	0.002853	0.042714	63	H	8.552143	-0.832327	-1.570114
14	C	4.078534	-0.002177	0.06492	64	H	6.400349	-0.496911	-3.058771
15	C	6.476661	-0.445396	1.918236	65	H	4.865439	-1.181592	-2.522036
16	C	6.0143	0.633895	2.919149	66	H	6.158827	-2.240552	-3.089939
17	C	5.988605	-1.841252	2.356973	67	H	6.032461	2.388811	0.403813
18	C	6.505098	-1.453203	-1.087459	68	H	8.404097	1.672289	0.823165
19	C	8.032861	-1.670899	-1.101034	69	H	8.318661	3.025086	-0.302504
20	C	5.946388	-1.330798	-2.519555	70	H	8.627517	1.401272	-0.906122
21	C	6.537713	1.768208	-0.346109	71	H	4.996717	2.115298	-1.873245
22	C	8.057566	1.970717	-0.168704	72	H	6.583298	1.722912	-2.536872
23	C	6.070226	2.254132	-1.732787	73	H	6.288046	3.319554	-1.857269
24	Si	-5.94419	0.024534	-0.10179	74	H	-2.480905	-2.47726	-0.067505
25	C	-1.435941	-0.001537	-0.02077	75	H	-2.488304	-4.955444	-0.092207
26	C	-0.724799	-1.236669	-0.024835	76	H	-1.235688	-7.07862	-0.096727
27	C	-1.399691	-2.478591	-0.049298	77	H	1.252706	-7.075962	-0.059597
28	C	-0.721445	-3.693566	-0.052684	78	H	2.500044	-4.950153	-0.017929
29	C	-1.405614	-4.956765	-0.076523	79	H	2.486765	-2.472572	0.007343
30	C	-0.709325	-6.13357	-0.07882	80	H	-7.573213	0.45703	-1.911752
31	C	0.723996	-6.132054	-0.05734	81	H	-4.923949	-0.710691	-2.936716
32	C	1.417362	-4.95376	-0.034234	82	H	-6.415818	-1.619512	-2.682166
33	C	0.730109	-3.692033	-0.030792	83	H	-6.341619	-0.380598	-3.93297
34	C	1.405592	-2.475721	-0.007719	84	H	-6.316502	2.060147	-3.377127
35	C	0.727973	-1.23508	-0.003643	85	H	-6.3731	2.635995	-1.712681
36	C	-2.856938	-0.002496	-0.04247	86	H	-4.896908	1.89878	-2.343322
37	C	-4.078547	0.002428	-0.064783	87	H	-6.050509	2.342276	0.636889
38	C	-6.47635	0.446267	-1.918308	88	H	-8.285981	2.565688	1.675992
39	C	-6.013762	-0.632487	-2.919694	89	H	-8.445702	1.796179	0.098804
40	C	-5.988253	1.842368	-2.356203	90	H	-8.551949	0.82931	1.571547
41	C	-6.505752	1.45223	1.088015	91	H	-6.399068	0.495324	3.05893
42	C	-8.033712	1.668507	1.102427	92	H	-4.865131	1.181759	2.521691
43	C	-5.946229	1.329868	2.519798	93	H	-6.159316	2.239204	3.090606
44	C	-6.537276	-1.768735	0.3448	94	H	-6.030777	-2.388893	-0.404651
45	C	-8.056799	-1.972154	0.165609	95	H	-8.402327	-1.67401	-0.826693
46	C	-6.071086	-2.25463	1.73193	96	H	-8.317403	-3.026677	0.299155
47	H	2.480888	2.477633	0.067855	97	H	-8.628004	-1.403026	0.902301
48	H	2.488284	4.955818	0.092561	98	H	-4.997808	-2.115246	1.873622
49	H	1.235666	7.078993	0.097086	99	H	-6.585357	-1.723817	2.53552
50	H	-1.252728	7.076333	0.059955	100	H	-6.288466	-3.320188	1.856003

Figure J.1.: Calculated optimized molecular structure for TIPS-Pn, cartesian coordinates (DFT level: B3LYP/6-311G).

QPP (B3LYP/6-31G)

#	Sym	X	Y	Z
1	C	0	7.238453	0.712701
2	C	0	7.238453	-0.712701
3	C	0	6.052876	-1.416943
4	C	0	4.81527	-0.717789
5	C	0	4.81527	0.717789
6	C	0	6.052876	1.416943
7	N	0	3.639018	-1.409726
8	C	0	2.490364	-0.71926
9	C	0	2.490364	0.71926
10	N	0	3.639018	1.409726
11	C	0	1.224634	-1.449849
12	C	0	0	-0.727268
13	C	0	0	0.727268
14	C	0	1.224634	1.449849
15	C	0	-1.224634	1.449849
16	C	0	-1.209791	2.853545
17	C	0	0	3.548751
18	C	0	1.209791	2.853545
19	C	0	1.209791	-2.853545
20	C	0	0	-3.548751
21	C	0	-1.209791	-2.853545
22	C	0	-1.224634	-1.449849
23	C	0	-2.490364	-0.71926
24	C	0	-2.490364	0.71926
25	N	0	-3.639018	-1.409726
26	C	0	-4.81527	-0.717789
27	C	0	-4.81527	0.717789
28	N	0	-3.639018	1.409726
29	C	0	-6.052876	-1.416943
30	C	0	-7.238453	-0.712701
31	C	0	-7.238453	0.712701
32	C	0	-6.052876	1.416943
33	H	0	8.185277	1.242649
34	H	0	8.185277	-1.242649
35	H	0	6.02326	-2.500619
36	H	0	6.02326	2.500619
37	H	0	-2.159671	3.37391
38	H	0	0	4.63367
39	H	0	2.159671	3.37391
40	H	0	2.159671	-3.37391
41	H	0	0	-4.63367
42	H	0	-2.159671	-3.37391
43	H	0	-6.02326	-2.500619
44	H	0	-8.185277	-1.242649
45	H	0	-8.185277	1.242649
46	H	0	-6.02326	2.500619

Figure J.2.: Calculated optimized molecular structure for QPP, cartesian coordinates (DFT level: B3LYP/6-31G).

J. Calculated Optimized Structures

tBu-QPP (B3LYP/6-311G)									
#	Sym	X	Y	Z	#	Sym	X	Y	Z
1	C	7.241403	-0.584626	-0.00025	51	H	-8.150061	-1.384515	-0.000212
2	C	7.216196	0.838951	-0.000196	52	H	-5.970646	-2.599411	-0.000087
3	C	6.020048	1.519991	-0.000126	53	H	-1.172812	-6.85152	0.000472
4	C	4.796464	0.800003	-0.000106	54	H	-1.850224	-5.48523	0.885908
5	C	4.821844	-0.63158	-0.000153	55	H	-1.850995	-5.484923	-0.883907
6	C	6.070155	-1.307673	-0.00023	56	H	0.944736	-6.690293	-1.27456
7	N	3.607232	1.471028	-0.000047	57	H	1.90086	-5.206195	-1.301226
8	C	2.470253	0.76306	-0.000023	58	H	0.366475	-5.278834	-2.172034
9	C	2.496059	-0.676649	-0.000054	59	H	0.367837	-5.278625	2.172293
10	N	3.656896	-1.344134	-0.000125	60	H	0.945676	-6.690103	1.274577
11	C	1.191537	1.471665	0.000019	61	H	1.901671	-5.20591	1.300522
12	C	-0.011824	0.725367	-0.000012	62	H	1.172812	6.85152	0.000471
13	C	0.011824	-0.725367	-0.000012	63	H	1.850209	5.485243	0.885936
14	C	1.243097	-1.430515	-0.000006	64	H	1.85101	5.484911	-0.883879
15	C	-1.191537	-1.471665	0.00002	65	H	-0.944719	6.690296	-1.274568
16	C	-1.15058	-2.873927	0.000088	66	H	-1.900848	5.206201	-1.301242
17	C	0.059274	-3.575976	0.000112	67	H	-0.366456	5.278835	-2.172036
18	C	1.247018	-2.828801	0.000052	68	H	-0.367857	5.278625	2.172291
19	C	1.15058	2.873927	0.000088	69	H	-0.945693	6.690101	1.274569
20	C	-0.059274	3.575976	0.000111	70	H	-1.901683	5.205904	1.300506
21	C	-1.247018	2.828801	0.000052					
22	C	-1.243097	1.430515	-0.000005					
23	C	-2.496059	0.676649	-0.000053					
24	C	-2.470253	-0.763059	-0.000022					
25	N	-3.656896	1.344134	-0.000125					
26	C	-4.821844	0.63158	-0.000153					
27	C	-4.796464	-0.800003	-0.000105					
28	N	-3.607232	-1.471028	-0.000046					
29	C	-6.070155	1.307673	-0.00023					
30	C	-7.241402	0.584626	-0.00025					
31	C	-7.216196	-0.838951	-0.000196					
32	C	-6.020048	-1.519991	-0.000126					
33	C	0.126822	-5.117409	0.000196					
34	C	-0.126822	5.117409	0.000196					
35	C	-1.275733	-5.764679	0.000702					
36	C	0.884178	-5.599452	-1.26594					
37	C	0.885004	-5.599269	1.265902					
38	C	1.275732	5.764679	0.000717					
39	C	-0.884165	5.599454	-1.265947					
40	C	-0.885017	5.599267	1.265895					
41	H	8.194	-1.096777	-0.000307					
42	H	8.150061	1.384515	-0.000211					
43	H	5.970647	2.599411	-0.000086					
44	H	6.059408	-2.388169	-0.000269					
45	H	-2.097784	-3.38762	0.000116					
46	H	2.210712	-3.315292	0.000056					
47	H	2.097784	3.38762	0.000114					
48	H	-2.210712	3.315292	0.000056					
49	H	-6.059409	2.388169	-0.000269					
50	H	-8.194	1.096776	-0.000308					

Figure J.3.: Calculated optimized molecular structure for *t*Bu-QPP, cartesian coordinates (DFT level: B3LYP/6-311G).

TAPP (B3LYP/6-311G(d,p))

#	Sym	X	Y	Z
1	C	0	1.205222	3.569869
2	C	0	2.444218	2.853335
3	C	0	2.453296	1.492957
4	C	0	1.247015	0.710616
5	C	0	0	1.402357
6	C	0	0	2.825537
7	C	0	-1.247015	0.710616
8	C	0	-2.453296	1.492957
9	C	0	-2.444218	2.853335
10	C	0	-1.205222	3.569869
11	C	0	1.247015	-0.710616
12	C	0	0	-1.402357
13	C	0	-1.247015	-0.710616
14	C	0	0	-2.825537
15	C	0	-1.205222	-3.569869
16	C	0	-2.444218	-2.853335
17	C	0	-2.453296	-1.492957
18	C	0	2.453296	-1.492957
19	C	0	2.444218	-2.853335
20	C	0	1.205222	-3.569869
21	N	0	1.198961	-4.914779
22	C	0	0	-5.499656
23	N	0	-1.198961	-4.914779
24	N	0	-1.198961	4.914779
25	C	0	0	5.499656
26	N	0	1.198961	4.914779
27	H	0	3.360555	3.430404
28	H	0	3.408812	0.98634
29	H	0	-3.408812	0.98634
30	H	0	-3.360555	3.430404
31	H	0	-3.360555	-3.430404
32	H	0	-3.408812	-0.98634
33	H	0	3.408812	-0.98634
34	H	0	3.360555	-3.430404
35	H	0	0	-6.586107
36	H	0	0	6.586107

Figure J.4.: Calculated optimized molecular structure for TAPP, cartesian coordinates (DFT level: B3LYP/6-311G(d,p)).

J. Calculated Optimized Structures

TAPP-H (B3LYP/6-31G)									
#	Sym	X	Y	Z	#	Sym	X	Y	Z
1	C	0.322116	-2.844246	2.455942	51	H	-0.105695	0.981151	3.420274
2	C	0.167071	-1.48524	2.464645	52	H	-0.385068	3.422812	3.369302
3	C	0.0813	-0.708456	1.253636	53	H	-0.385068	3.422812	-3.369302
4	C	0.161443	-1.396053	0	54	H	-0.105695	0.981151	-3.420274
5	C	0.325141	-2.811964	0					
6	C	0.4077	-3.547713	1.214258					
7	C	0.0813	-0.708456	-1.253636					
8	C	0.167071	-1.48524	-2.464645					
9	C	0.322116	-2.844246	-2.455942					
10	C	0.4077	-3.547713	-1.214258					
11	C	-0.0813	0.708456	1.253636					
12	C	-0.161443	1.396053	0					
13	C	-0.0813	0.708456	-1.253636					
14	C	-0.167071	1.48524	2.464645					
15	C	-0.322116	2.844246	2.455942					
16	C	-0.4077	3.547713	1.214258					
17	C	-0.325141	2.811964	0					
18	C	-0.4077	3.547713	-1.214258					
19	C	-0.322116	2.844246	-2.455942					
20	C	-0.167071	1.48524	-2.464645					
21	N	0.561507	-4.898703	1.203523					
22	N	0.561507	-4.898703	-1.203523					
23	N	-0.561507	4.898703	1.203523					
24	N	-0.561507	4.898703	-1.203523					
25	C	-0.639094	5.485873	0					
26	C	0.639094	-5.485873	0					
27	C	-0.803012	6.993421	0					
28	F	-1.519465	7.404805	-1.128778					
29	F	-1.519465	7.404805	1.128778					
30	C	0.803012	-6.993421	0					
31	F	1.519465	-7.404805	-1.128778					
32	F	1.519465	-7.404805	1.128778					
33	C	-0.533653	-7.765064	0					
34	F	-1.257909	-7.382302	-1.130787					
35	F	-1.257909	-7.382302	1.130787					
36	C	-0.469425	-9.302277	0					
37	F	0.1813	-9.771649	-1.11969					
38	F	-1.751694	-9.813907	0					
39	F	0.1813	-9.771649	1.11969					
40	C	0.533653	7.765064	0					
41	F	1.257909	7.382302	1.130787					
42	F	1.257909	7.382302	-1.130787					
43	C	0.469425	9.302277	0					
44	F	-0.1813	9.771649	-1.11969					
45	F	-0.1813	9.771649	1.11969					
46	F	1.751694	9.813907	0					
47	H	0.385068	-3.422812	3.369302					
48	H	0.105695	-0.981151	3.420274					
49	H	0.105695	-0.981151	-3.420274					
50	H	0.385068	-3.422812	-3.369302					

Figure J.5.: Calculated optimized molecular structure for TAPP-H, cartesian coordinates (DFT level: B3LYP/6-311G).

TAPP-Cl (B3LYP/6-311+G(d,p))

#	Sym	X	Y	Z	#	Sym	X	Y	Z
1	C	-0.311583	2.82861	2.445809	51	H	0.104373	-0.979639	3.410304
2	C	-0.161513	1.474272	2.451689	52	Cl	0.40621	-3.705534	3.940403
3	C	-0.078549	0.707639	1.246083	53	Cl	0.40621	-3.705534	-3.940403
4	C	-0.155036	1.391961	0	54	H	0.104373	-0.979639	-3.410304
5	C	-0.31291	2.804461	0					
6	C	-0.393917	3.553554	1.204385					
7	C	-0.078549	0.707639	-1.246083					
8	C	-0.161513	1.474272	-2.451689					
9	C	-0.311583	2.82861	-2.445809					
10	C	-0.393917	3.553554	-1.204385					
11	C	0.078549	-0.707639	1.246083					
12	C	0.155036	-1.391961	0					
13	C	0.078549	-0.707639	-1.246083					
14	C	0.161513	-1.474272	2.451689					
15	C	0.311583	-2.82861	2.445809					
16	C	0.393917	-3.553554	1.204385					
17	C	0.31291	-2.804461	0					
18	C	0.393917	-3.553554	-1.204385					
19	C	0.311583	-2.82861	-2.445809					
20	C	0.161513	-1.474272	-2.451689					
21	N	-0.541512	4.883561	1.192958					
22	N	-0.541512	4.883561	-1.192958					
23	N	0.541512	-4.883561	1.192958					
24	N	0.541512	-4.883561	-1.192958					
25	C	0.610818	-5.458232	0					
26	C	-0.610818	5.458232	0					
27	C	0.776642	-6.985293	0					
28	F	1.4702	-7.377258	-1.09598					
29	F	1.4702	-7.377258	1.09598					
30	C	-0.776642	6.985293	0					
31	F	-1.4702	7.377258	-1.09598					
32	F	-1.4702	7.377258	1.09598					
33	C	0.597728	7.730695	0					
34	F	1.293534	7.350046	-1.097328					
35	F	1.293534	7.350046	1.097328					
36	C	0.545559	9.291814	0					
37	F	-0.078786	9.753711	-1.08727					
38	F	1.800411	9.763373	0					
39	F	-0.078786	9.753711	1.08727					
40	C	-0.597728	-7.730695	0					
41	F	-1.293534	-7.350046	1.097328					
42	F	-1.293534	-7.350046	-1.097328					
43	C	-0.545559	-9.291814	0					
44	F	0.078786	-9.753711	-1.08727					
45	F	0.078786	-9.753711	1.08727					
46	F	-1.800411	-9.763373	0					
47	Cl	-0.40621	3.705534	3.940403					
48	H	-0.104373	0.979639	3.410304					
49	H	-0.104373	0.979639	-3.410304					
50	Cl	-0.40621	3.705534	-3.940403					

Figure J.6.: Calculated optimized molecular structure for TAPP-Cl, cartesian coordinates (DFT level: B3LYP/6-311+G(d,p)).

J. Calculated Optimized Structures

TAPP-Br (B3LYP/6-311G)									
#	Sym	X	Y	Z	#	Sym	X	Y	Z
1	N	4.901048	-1.198663	-0.496171	51	H	0.977288	-3.409764	-0.096125
2	C	5.491717	-0.00027	-0.5627	52	H	0.977589	3.409679	-0.096228
3	N	4.901146	1.198207	-0.496295	53	H	-0.977559	-3.409678	0.095686
4	C	3.5547	1.214618	-0.362856	54	H	-0.977259	3.409764	0.095569
5	C	2.813386	-0.000125	-0.28846					
6	C	3.554588	-1.214932	-0.362791					
7	C	1.397647	-0.000062	-0.143959					
8	C	0.709371	-1.248122	-0.07274					
9	C	1.477582	-2.456973	-0.149289					
10	C	2.834058	-2.45292	-0.286833					
11	C	2.834274	2.452672	-0.286934					
12	C	1.4778	2.456842	-0.149371					
13	C	0.709482	1.248059	-0.072784					
14	C	-0.70933	1.248122	0.072299					
15	C	-1.397601	0.000063	0.143562					
16	C	-0.709441	-1.248058	0.072345					
17	C	-2.813331	0.000126	0.288157					
18	C	-3.554639	-1.214617	0.362612					
19	C	-2.834227	-2.452671	0.286561					
20	C	-1.477761	-2.456842	0.148914					
21	C	-1.477544	2.456973	0.148822					
22	C	-2.834012	2.452921	0.286447					
23	C	-3.554528	1.214933	0.362539					
24	N	-4.90097	1.198664	0.496105					
25	C	-5.491625	0.000272	0.562753					
26	N	-4.901067	-1.198205	0.496238					
27	Br	3.806077	-4.111701	-0.382568					
28	Br	-3.806397	-4.11136	0.382308					
29	Br	-3.806038	4.111702	0.382121					
30	Br	3.806438	4.111362	-0.382728					
31	C	-7.003184	0.000221	0.703724					
32	F	-7.424467	1.132436	1.419711					
33	F	-7.423943	-1.129226	1.424443					
34	C	-7.759772	-0.002804	-0.64488					
35	F	-7.364589	-1.140323	-1.363361					
36	F	-7.358303	1.127225	-1.371876					
37	C	-9.300742	0.001654	-0.611854					
38	F	-9.793048	-1.116404	0.034603					
39	F	-9.787104	-0.004332	-1.909473					
40	F	-9.787029	1.129575	0.021822					
41	C	7.003305	-0.000221	-0.703353					
42	F	7.424229	1.129247	-1.423943					
43	F	7.424745	-1.132414	-1.419279					
44	C	7.759589	0.002762	0.645423					
45	F	7.358006	-1.127328	1.372262					
46	F	7.36419	1.140219	1.363881					
47	C	9.300567	-0.001624	0.61275					
48	F	9.786635	0.004268	1.910479					
49	F	9.792969	1.116515	-0.033495					
50	F	9.787047	-1.129467	-0.020918					

Figure J.7.: Calculated optimized molecular structure for TAPP-Br, cartesian coordinates (DFT level: B3LYP/6-311G).

TAPP-I (B3LYP/LANL2DZ)

#	Sym	X	Y	Z	#	Sym	X	Y	Z
1	N	-4.934959	-1.188166	0.462923	51	H	-0.981472	-3.416498	0.089279
2	C	-5.522424	0.018897	0.52402	52	H	-0.957264	3.423937	0.085031
3	N	-4.925905	1.222655	0.464118	53	H	0.957351	-3.423358	-0.085365
4	C	-3.572686	1.237004	0.334747	54	H	0.981583	3.417076	-0.089455
5	C	-2.826398	0.010359	0.266461					
6	C	-3.581553	-1.210778	0.336271					
7	C	-1.404941	0.00527	0.132387					
8	C	-0.718064	-1.250075	0.067701					
9	C	-1.491644	-2.463425	0.138817					
10	C	-2.863931	-2.466404	0.266958					
11	C	-2.846511	2.487585	0.264145					
12	C	-1.474282	2.474617	0.135651					
13	C	-0.709306	1.255717	0.06601					
14	C	0.718167	1.250655	-0.067949					
15	C	1.405041	-0.004689	-0.132643					
16	C	0.709401	-1.255136	-0.066285					
17	C	2.826501	-0.009778	-0.266696					
18	C	3.572786	-1.236433	-0.335008					
19	C	2.846602	-2.487012	-0.264455					
20	C	1.474375	-2.47404	-0.135957					
21	C	1.491751	2.464001	-0.139008					
22	C	2.864046	2.466976	-0.267088					
23	C	3.58166	1.211354	-0.336427					
24	N	4.935089	1.188748	-0.463006					
25	C	5.522525	-0.018294	-0.524172					
26	N	4.925997	-1.22207	-0.464353					
27	I	-3.934074	-4.288029	0.365064					
28	I	3.903866	-4.31605	-0.361095					
29	I	3.934203	4.288602	-0.365053					
30	I	-3.903784	4.316621	0.360734					
31	C	7.045776	-0.034281	-0.66239					
32	F	7.503839	1.162548	-1.246066					
33	F	7.449674	-1.079386	-1.514806					
34	C	7.803602	-0.211985	0.698689					
35	F	7.68343	-1.543931	1.11431					
36	F	7.178687	0.591169	1.671319					
37	C	9.324501	0.157896	0.70253					
38	F	9.987987	-0.438007	-0.361639					
39	F	9.909995	-0.290551	1.881316					
40	F	9.513817	1.529037	0.631073					
41	C	-7.04567	0.034651	0.662399					
42	F	-7.449871	1.081328	1.512688					
43	F	-7.503157	-1.161196	1.248639					
44	C	-7.803807	0.209228	-0.698862					
45	F	-7.179921	-0.596943	-1.669587					
46	F	-7.682571	1.540052	-1.117985					
47	C	-9.325028	-0.159298	-0.701303					
48	F	-9.910269	0.286052	-1.881405					
49	F	-9.987883	0.440394	0.361103					
50	F	-9.51552	-1.530056	-0.625623					

Figure J.8.: Calculated optimized molecular structure for TAPP-I, cartesian coordinates (DFT level: B3LYP/LANL2DZ).

J. Calculated Optimized Structures

TCNQ (B3LYP/6-311G)				
#	Sym	X	Y	Z
1	C	-0.678042	-1.23848	0.000018
2	C	0.678042	-1.23848	0
3	C	1.431463	-0.000001	-0.00001
4	C	0.678042	1.238479	0
5	C	-0.678042	1.238479	0.000018
6	C	-1.431463	0	0.000031
7	C	2.820872	0	-0.000026
8	C	-2.820873	0	0.000051
9	C	-3.569687	-1.212373	0.000002
10	C	-3.569686	1.212372	0.000002
11	C	3.569686	1.212372	-0.000009
12	C	3.569687	-1.212373	-0.000009
13	N	4.173243	-2.213236	0.000004
14	N	4.173241	2.213238	0.000004
15	N	-4.173239	2.213239	-0.000036
16	N	-4.173243	-2.213237	-0.000035
17	H	-1.21752	-2.174745	0.000024
18	H	1.21752	-2.174745	-0.000008
19	H	1.21752	2.174744	-0.000007
20	H	-1.21752	2.174744	0.000025

Figure J.9.: Calculated optimized molecular structure for TCNQ, cartesian coordinates (DFT level: B3LYP/6-311G).

F2TCNQ (B3LYP/6-311G(d,p))

#	Sym	X	Y	Z
1	C	1.196089	0.743691	0
2	C	0.008573	1.383035	0
3	C	-1.266863	0.695694	0
4	C	-1.196089	-0.743691	0
5	C	-0.008573	-1.383035	0
6	C	1.266863	-0.695694	0
7	C	2.488245	-1.348376	0
8	C	-2.488245	1.348376	0
9	C	3.700035	-0.596187	0
10	C	2.670073	-2.760393	0
11	C	-3.700035	0.596187	0
12	C	-2.670073	2.760393	0
13	F	-0.008573	2.718364	0
14	F	0.008573	-2.718364	0
15	N	4.679061	0.018762	0
16	N	2.903391	-3.892617	0
17	N	-4.679061	-0.018762	0
18	N	-2.903391	3.892617	0
19	H	2.106937	1.32859	0
20	H	-2.106937	-1.32859	0

Figure J.10.: Calculated optimized molecular structure for F₂TCNQ, cartesian coordinates (DFT level: B3LYP/6-311G(d,p)).

J. Calculated Optimized Structures

F4TCNQ (B3LYP/6-311G)

#	Sym	X	Y	Z
1	C	-0.676642	1.207146	-0.000004
2	C	0.676629	1.207154	-0.000002
3	C	1.472061	-0.000023	-0.000003
4	C	0.676642	-1.20721	-0.000003
5	C	-0.67663	-1.207218	-0.000005
6	C	-1.472061	-0.000038	-0.000001
7	C	2.859495	0.000002	-0.000003
8	C	-2.859495	-0.000012	0.000005
9	C	-3.64788	1.189842	0.000004
10	C	-3.647969	-1.189808	0.000006
11	C	3.647957	-1.189801	0.000004
12	C	3.647891	1.189848	0.000002
13	N	4.36495	2.111655	0.000006
14	N	4.365114	-2.111532	0.000001
15	N	-4.365154	-2.111516	0.000008
16	N	-4.364909	2.111672	0.000004
17	F	1.325051	-2.42251	-0.000004
18	F	-1.325022	-2.422527	-0.000009
19	F	-1.325063	2.422441	-0.000006
20	F	1.325033	2.422457	-0.000001

Figure J.11.: Calculated optimized molecular structure for F₄TCNQ, cartesian coordinates (DFT level: B3LYP/6-311G).

TTF (B3LYP/6-311G)

#	Sym	X	Y	Z
1	S	0	1.545334	1.681366
2	S	0	-1.545334	1.681366
3	S	0	-1.545334	-1.681366
4	S	0	1.545334	-1.681366
5	C	0	0	0.666969
6	C	0	0	-0.666969
7	C	0	0.664105	3.27877
8	C	0	-0.664105	3.27877
9	C	0	-0.664105	-3.27877
10	C	0	0.664105	-3.27877
11	H	0	1.292389	4.154238
12	H	0	-1.292389	4.154238
13	H	0	-1.292389	-4.154238
14	H	0	1.292389	-4.154238

Figure J.12.: Calculated optimized molecular structure for TTF, cartesian coordinates (DFT level: B3LYP/6-311G).

J. Calculated Optimized Structures

Bibliography

- [1] John Bardeen and Walter Hauser Brattain. The transistor, a semiconductor triode. *Physical Review*, 74(2):230, 1948.
- [2] William Shockley. A unipolar "field-effect" transistor. *Proceedings of the IRE*, 40(11):1365–1376, 1952.
- [3] SR Hofstein and FP Heiman. The silicon insulated-gate field-effect transistor. *Proceedings of the IEEE*, 51(9):1190–1202, 1963.
- [4] Probir K Bondyopadhyay. Moore's law governs the silicon revolution. *Proceedings of the IEEE*, 86(1):78–81, 1998.
- [5] Hagen Klauk, Ute Zschieschang, Jens Pflaum, and Marcus Halik. Ultralow-power organic complementary circuits. *nature*, 445(7129):745, 2007.
- [6] Howard E Katz and Jia Huang. Thin-film organic electronic devices. *Annual Review of Materials Research*, 39:71–92, 2009.
- [7] K Walzer, B Maennig, M Pfeiffer, and K Leo. Highly efficient organic devices based on electrically doped transport layers. *Chemical reviews*, 107(4):1233–1271, 2007.
- [8] Martin Kaltenbrunner, Matthew S White, Eric D Glowacki, Tsuyoshi Sekitani, Takao Someya, Niyazi Serdar Sariciftci, and Siegfried Bauer. Ultrathin and lightweight organic solar cells with high flexibility. *Nature communications*, 3:770, 2012.
- [9] Tsuyoshi Sekitani, Yoshiaki Noguchi, Kenji Hata, Takanori Fukushima, Takuzo Aida, and Takao Someya. A rubberlike stretchable active matrix using elastic conductors. *Science*, 321(5895):1468–1472, 2008.
- [10] Tsuyoshi Sekitani, Ute Zschieschang, Hagen Klauk, and Takao Someya. Flexible organic transistors and circuits with extreme bending stability. *Nature materials*, 9(12):1015, 2010.

Bibliography

- [11] Felice Torrisi, Tawfique Hasan, Weiping Wu, Zhipei Sun, Antonio Lombardo, Tero S Kulmala, Gen-Wen Hsieh, Sungjune Jung, Francesco Bonaccorso, Philip J Paul, et al. Inkjet-printed graphene electronics. *ACS nano*, 6(4):2992–3006, 2012.
- [12] Patrick Görrn, Michelle Sander, Jens Meyer, Michael Kröger, Eike Becker, H-H Johannes, Wolfgang Kowalsky, and Thomas Riedl. Towards see-through displays: fully transparent thin-film transistors driving transparent organic light-emitting diodes. *Advanced Materials*, 18(6):738–741, 2006.
- [13] Malte C Gather, Anne Koehnen, Aurelie Falcou, Heinrich Becker, and Klaus Meerholz. Solution-processed full-color polymer organic light-emitting diode displays fabricated by direct photolithography. *Advanced Functional Materials*, 17(2):191–200, 2007.
- [14] Lisong Zhou, Alfred Wanga, Sheng-Chu Wu, Jie Sun, Sungkyu Park, and Thomas N Jackson. All-organic active matrix flexible display. *Applied Physics Letters*, 88(8):083502, 2006.
- [15] M Riede, Tress Mueller, W Tress, R Schueppel, and K Leo. Small-molecule solar cells—status and perspectives. *Nanotechnology*, 19(42):424001, 2008.
- [16] Frank Würthner and Klaus Meerholz. Systems chemistry approach in organic photovoltaics. *Chemistry-A European Journal*, 16(31):9366–9373, 2010.
- [17] Serap Günes, Helmut Neugebauer, and Niyazi Serdar Sariciftci. Conjugated polymer-based organic solar cells. *Chemical reviews*, 107(4):1324–1338, 2007.
- [18] Ching W Tang and Steven A VanSlyke. Organic electroluminescent diodes. *Applied physics letters*, 51(12):913–915, 1987.
- [19] Sebastian Reineke, Frank Lindner, Gregor Schwartz, Nico Seidler, Karsten Walzer, Björn Lüssem, and Karl Leo. White organic light-emitting diodes with fluorescent tube efficiency. *Nature*, 459(7244):234, 2009.

- [20] JH Burroughes, DDC Bradley, AR Brown, RN Marks, K Mackay, RH Friend, PL Burns, and AB Holmes. Light-emitting diodes based on conjugated polymers. *nature*, 347(6293):539, 1990.
- [21] Henning Sirringhaus, Nir Tessler, and Richard H Friend. Integrated optoelectronic devices based on conjugated polymers. *Science*, 280(5370):1741–1744, 1998.
- [22] Jaesang Lee, Hsiao-Fan Chen, Thilini Batagoda, Caleb Coburn, Peter I Djurovich, Mark E Thompson, and Stephen R Forrest. Deep blue phosphorescent organic light-emitting diodes with very high brightness and efficiency. *Nature materials*, 15(1):92, 2016.
- [23] Stephen R Forrest. The path to ubiquitous and low-cost organic electronic appliances on plastic. *Nature*, 428(6986):911, 2004.
- [24] Sybille Allard, Michael Forster, Benjamin Souharce, Heiko Thiem, and Ullrich Scherf. Organische Halbleiter für aus Lösung prozessierbare Feldeffekttransistoren. *Angewandte Chemie*, 120(22):4138–4167, 2008.
- [25] Ute Zschieschang, Tatsuya Yamamoto, Kazuo Takimiya, Hirokazu Kuwabara, Masaaki Ikeda, Tsuyoshi Sekitani, Takao Someya, and Hagen Klauk. Organic electronics on banknotes. *Advanced Materials*, 23(5):654–658, 2011.
- [26] AN Sokolov and BC Tee. K; bettinger, cj; tok, jb h; bao, z. *Chemical and Engineering Approaches to Enable Organic Field-Effect Transistors for Electronic Skin Applications. Acc. Chem. Res*, 45:361–371, 2012.
- [27] Luisa Torsi, Maria Magliulo, Kyriaki Manoli, and Gerardo Palazzo. Organic field-effect transistor sensors: a tutorial review. *Chemical Society Reviews*, 42(22):8612–8628, 2013.
- [28] Sven Möller, Craig Perlov, Warren Jackson, Carl Taussig, and Stephen R Forrest. A polymer/semiconductor write-once read-many-times memory. *Nature*, 426(6963):166, 2003.
- [29] Klaus Müllen and Ullrich Scherf. *Organic light emitting devices: synthesis, properties and applications*. John Wiley & Sons, 2006.

Bibliography

- [30] Bernard Geffroy, Philippe Le Roy, and Christophe Prat. Organic light-emitting diode (OLED) technology: materials, devices and display technologies. *Polymer International*, 55(6):572–582, 2006.
- [31] Jin-Seong Park, Heeyeop Chae, Ho Kyoong Chung, and Sang In Lee. Thin film encapsulation for flexible AM-OLED: a review. *Semiconductor Science and Technology*, 26(3):034001, 2011.
- [32] Marcus Halik, Hagen Klauk, Ute Zschieschang, Günter Schmid, Sergei Ponomarenko, Stephan Kirchmeyer, and Werner Weber. Relationship between molecular structure and electrical performance of oligothiophene organic thin film transistors. *Advanced Materials*, 15(11):917–922, 2003.
- [33] Norbert Koch, Nobuo Ueno, and Andrew Thye Shen Wee. *The Molecule-Metal Interface*. John Wiley & Sons, 2013.
- [34] Norbert Koch. Organic electronic devices and their functional interfaces. *ChemPhysChem*, 8(10):1438–1455, 2007.
- [35] Hisao Ishii, Kiyoshi Sugiyama, Eisuke Ito, and Kazuhiko Seki. Energy level alignment and interfacial electronic structures at organic/metal and organic/organic interfaces. *Advanced materials*, 11(8):605–625, 1999.
- [36] Slawomir Braun, William R Salaneck, and Mats Fahlman. Energy-level alignment at organic/metal and organic/organic interfaces. *Advanced materials*, 21(14-15):1450–1472, 2009.
- [37] Martin Oehzelt, Norbert Koch, and Georg Heimel. Organic semiconductor density of states controls the energy level alignment at electrode interfaces. *Nature communications*, 5:4174, 2014.
- [38] Roman Forker, Marco Gruenewald, and Torsten Fritz. Optical differential reflectance spectroscopy on thin molecular films. *Annual Reports Section "C" (Physical Chemistry)*, 108:34–68, 2012.
- [39] Jana Zaumseil and Henning Sirringhaus. Electron and ambipolar transport in organic field-effect transistors. *Chemical reviews*, 107(4):1296–1323, 2007.
- [40] Freek JM Hoeben, Pascal Jonkheijm, EW Meijer, and Albertus PHJ Schenning. About supramolecular assemblies of π -conjugated systems. *Chemical Reviews*, 105(4):1491–1546, 2005.

- [41] Marina M Safont-Sempere, Gustavo Fernández, and Frank Würthner. Self-sorting phenomena in complex supramolecular systems. *Chemical reviews*, 111(9):5784–5814, 2011.
- [42] S Bommel, N Kleppmann, C Weber, H Spranger, P Schäfer, J Novak, SV Roth, F Schreiber, SHL Klapp, and S Kowarik. Unravelling the multilayer growth of the fullerene C60 in real time. *Nature communications*, 5:5388, 2014.
- [43] Maria Benedetta Casu. Growth, structure, and electronic properties in organic thin films deposited on metal surfaces investigated by low energy electron microscopy and photoelectron emission microscopy. *Journal of Electron Spectroscopy and Related Phenomena*, 204:39–48, 2015.
- [44] FS Tautz. Structure and bonding of large aromatic molecules on noble metal surfaces: The example of PTCDA. *Progress in Surface*, 82(9):479–520, 2007.
- [45] Björn Lüssem, Chang-Min Keum, Daniel Kasemann, Ben Naab, Zhenan Bao, and Karl Leo. Doped organic transistors. *Chemical reviews*, 116(22):13714–13751, 2016.
- [46] Yong Xu, Oliver T Hofmann, Raphael Schlesinger, Stefanie Winkler, Johannes Frisch, Jens Niederhausen, Antje Vollmer, Sylke Blumstengel, Fritz Henneberger, Norbert Koch, et al. Space-charge transfer in hybrid inorganic-organic systems. *Physical review letters*, 111(22):226802, 2013.
- [47] Norbert Koch, Alexander Gerlach, Steffen Duhm, Hendrik Glowatzki, Georg Heimel, Antje Vollmer, Yoichi Sakamoto, Toshiyasu Suzuki, Jörg Zegenhagen, Jürgen P Rabe, et al. Adsorption-induced intramolecular dipole: Correlating molecular conformation and interface electronic structure. *Journal of the American Chemical Society*, 130(23):7300–7304, 2008.
- [48] AM De Jong and JW Niemantsverdriet. Thermal desorption analysis: Comparative test of ten commonly applied procedures. *Surface Science*, 233(3):355–365, 1990.
- [49] David A King. Thermal desorption from metal surfaces: A review. *Surface Science*, 47(1):384–402, 1975.

Bibliography

- [50] Alejandro L Briseno, Joanna Aizenberg, Yong-Jin Han, Rebecca A Penkala, Hyunsik Moon, Andrew J Lovinger, Christian Kloc, and Zhenan Bao. Patterned growth of large oriented organic semiconductor single crystals on self-assembled monolayer templates. *Journal of the American Chemical Society*, 127(35):12164–12165, 2005.
- [51] Charles Michael Drain, Fotis Nifiatis, Alexander Vasenko, and James D Batteas. Porphyrin tessellation by design: Metal-mediated self-assembly of large arrays and tapes. *Angewandte Chemie International Edition*, 37(17):2344–2347, 1998.
- [52] John E Anthony. Höhere acene: Vielseitige organische halbleiter. *Angewandte Chemie*, 120(3):460–492, 2008.
- [53] Manfred Matena, Meike Stöhr, Till Riehm, Jonas Björk, Susanne Martens, Matthew S Dyer, Mats Persson, Jorge Lobo-Checa, Kathrin Müller, Mihaela Enache, et al. Aggregation and contingent metal/surface reactivity of 1, 3, 8, 10-tetraazaperopyrene (TAPP) on Cu (111). *Chemistry-A European Journal*, 16(7):2079–2091, 2010.
- [54] Lena Hahn, Friedrich Maaß, Tim Bleith, Ute Zschieschang, Hubert Wadepohl, Hagen Klauk, Petra Tegeder, and Lutz H Gade. Core halogenation as a construction principle in tuning the material properties of tetraazaperopyrenes. *Chemistry-A European Journal*, 2015.
- [55] Friedrich Maass, Arnulf Stein, Bernd Kohl, Lena Hahn, Lutz H Gade, Michael Mastalerz, and Petra Tegeder. Substrate-directed growth of n-heteropolycyclic molecules on a metal surface. *The Journal of Physical Chemistry C*, 120(5):2866–2873, 2016.
- [56] M Eremtchenko, D Bauer, JA Schaefer, and FS Tautz. Structure, bonding, and growth at a metal–organic interface in the weak chemisorption regime: Perylene–Ag (111). *Journal of materials research*, 19(7):2028–2039, 2004.
- [57] FS Tautz, S Sloboshanin, V Shklover, R Scholz, M Sokolowski, JA Schaefer, and E Umbach. Substrate influence on the ordering of organic submonolayers: a comparative study of PTCDA on Ag (110) and Ag (111) using HREELS. *Applied Surface Science*, 166(1-4):363–369, 2000.

- [58] P Navarro, FC Bocquet, I Deperasinska, G Pirug, FS Tautz, and M Orrit. Electron energy loss of terrylene deposited on Au(111): Vibrational and electronic spectroscopy. *The Journal of Physical Chemistry C*, 119(1):277–283, 2014.
- [59] Christopher Bronner, Stephan Stremlau, Marie Gille, Felix Brauße, Anton Haase, Stefan Hecht, and Petra Tegeder. Aligning the band gap of graphene nanoribbons by monomer doping. *Angewandte Chemie International Edition*, 52(16):4422–4425, 2013.
- [60] Cornelius Gahl, Daniel Brete, Felix Leyssner, Matthias Koch, Erik R McNellis, Johannes Mielke, Robert Carley, Leonhard Grill, Karsten Reuter, Petra Tegeder, et al. Coverage- and temperature-controlled isomerization of an imine derivative on Au(111). *Journal of the American Chemical Society*, 135(11):4273–4281, 2013.
- [61] Stephan Stremlau, Friedrich Maass, and Petra Tegeder. Adsorption and switching properties of nitrospiropyran on Bi(114). *Journal of Physics: Condensed Matter*, 29(31):314004, 2017.
- [62] Marten Piantek, Gunnar Schulze, Matthias Koch, Katharina J Franke, Felix Leyssner, Alex Krüger, Cristina Navío, Jorge Miguel, Matthias Bernien, Martin Wolf, et al. Reversing the thermal stability of a molecular switch on a gold surface: ring-opening reaction of nitrospiropyran. *Journal of the American Chemical Society*, 131(35):12729–12735, 2009.
- [63] Harald Ibach and Douglas L Mills. *Electron energy loss spectroscopy and surface vibrations*. Academic Press, New York, 1982.
- [64] Xiaowei Zhan, Antonio Facchetti, Stephen Barlow, Tobin J Marks, Mark A Ratner, Michael R Wasielewski, and Seth R Marder. Rylene and related diimides for organic electronics. *Advanced Materials*, 23(2):268–284, 2011.
- [65] Michael JD Bosdet, Warren E Piers, Ted S Sorensen, and Masood Parvez. 10a-aza-10b-borapyrenes: Heterocyclic analogues of pyrene with internalized BN moieties. *Angewandte Chemie International Edition*, 46(26):4940–4943, 2007.

Bibliography

- [66] Masayoshi Takase, Volker Enkelmann, Daniel Sebastiani, Martin Baumgarten, and Klaus Müllen. Annularly fused hexapyrrolohexaazacoronenes: an extended π system with multiple interior nitrogen atoms displays stable oxidation states. *Angewandte Chemie*, 119(29):5620–5623, 2007.
- [67] R Thomas Weitz, Konstantin Amsharov, Ute Zschieschang, Esther Barrera Villas, Dipak K Goswami, Marko Burghard, Helmut Dosch, Martin Jansen, Klaus Kern, and Hagen Klauk. Organic n-channel transistors based on core-cyanated perylene carboxylic diimide derivatives. *Journal of the American Chemical Society*, 130(14):4637–4645, 2008.
- [68] Frank Würthner and Matthias Stolte. Naphthalene and perylene diimides for organic transistors. *Chemical communications*, 47(18):5109–5115, 2011.
- [69] Christopher J Tonzola, Maksudul M Alam, Werner Kaminsky, and Samson A Jenekhe. New n-type organic semiconductors: synthesis, single crystal structures, cyclic voltammetry, photophysics, electron transport, and electroluminescence of a series of diphenylanthrazolines. *Journal of the American Chemical Society*, 125(44):13548–13558, 2003.
- [70] Sonia Alibert-Fouet, Isabelle Seguy, Jean-François Bobo, Pierre Destruel, and Harald Bock. Liquid-crystalline and electron-deficient coronene oligocarboxylic esters and imides by twofold benzogenic diels–alder reactions on perylenes. *Chemistry-A European Journal*, 13(6):1746–1753, 2007.
- [71] Ute Zschieschang, Konstantin Amsharov, R Thomas Weitz, Martin Jansen, and Hagen Klauk. Low-voltage organic n-channel thin-film transistors based on a core-cyanated perylene tetracarboxylic diimide derivative. *Synthetic Metals*, 159(21-22):2362–2364, 2009.
- [72] Zhenan Bao, Andrew J Lovinger, and Janelle Brown. New air-stable n-channel organic thin film transistors. *Journal of the American Chemical Society*, 120(1):207–208, 1998.
- [73] Arnulf Stein, Friedrich Maaß, and Petra Tegeder. Triisopropylsilylethynyl-pentacene on Au (111): Adsorption prop-

- erties, electronic structure, and singlet fission dynamics. *The Journal of Physical Chemistry C*, 121(33):18075–18083, 2017.
- [74] Mario Rocca. Low-energy EELS investigation of surface electronic excitations on metals. *Surface Science Reports*, 22(1-2):1–71, 1995.
- [75] William L Barnes, Alain Dereux, and Thomas W Ebbesen. Surface plasmon subwavelength optics. *nature*, 424(6950):824, 2003.
- [76] Bogdan Diaconescu, Karsten Pohl, Luca Vattuone, Letizia Savio, Philip Hofmann, Vyacheslav M Silkin, Jose M Pitarke, Eugene V Chulkov, Pedro M Echenique, Daniel Farias, et al. Low-energy acoustic plasmons at metal surfaces. *Nature*, 448(7149):57, 2007.
- [77] JM Pitarke, VU Nazarov, VM Silkin, EV Chulkov, E Zaremba, and PM Echenique. Theory of acoustic surface plasmons. *Physical Review B*, 70(20):205403, 2004.
- [78] Sung Jin Park and Richard E Palmer. Acoustic plasmon on the Au (111) surface. *Physical review letters*, 105(1):016801, 2010.
- [79] L Vattuone, M Smerieri, Thomas Langer, Christoph Tegenkamp, Herbert Pfnür, VM Silkin, Evgueni V Chulkov, Pedro Miguel Echenique, and M Rocca. Correlated motion of electrons on the Au (111) surface: anomalous acoustic surface-plasmon dispersion and single-particle excitations. *Physical review letters*, 110(12):127405, 2013.
- [80] Jan Pischel, Emanuel Welsch, Olaf Skibbe, and Annemarie Pucci. Acoustic surface plasmon on Cu (111) as an excitation in the mid-infrared range. *The Journal of Physical Chemistry C*, 117(51):26964–26968, 2013.
- [81] Karsten Pohl, B Diaconescu, G Vercelli, L Vattuone, VM Silkin, EV Chulkov, PM Echenique, and M Rocca. Acoustic surface plasmon on Cu (111). *Europhysics Letters*, 90(5):57006, 2010.
- [82] E Salomon, J-M Layet, and T Angot. Collective mode in a well-ordered organic monolayer. *Physical Review B*, 85(12):125420, 2012.
- [83] FS Tautz, M Eremtchenko, JA Schaefer, M Sokolowski, V Shklover, K Glöckler, and E Umbach. A comparison of the chemisorption behaviour of PTCDA on different Ag surfaces. *Surface Science*, 502:176–184, 2002.

Bibliography

- [84] FS Tautz, M Eremtchenko, JA Schaefer, M Sokolowski, V Shklover, and E Umbach. Strong electron-phonon coupling at a metal/organic interface: PTCDA/Ag (111). *Physical Review B*, 65(12):125405, 2002.
- [85] PA Redhead. Thermal desorption of gases. *Vacuum*, 12(4):203–211, 1962.
- [86] K Christmann. *Introduction to surface physical chemistry*. Steinkopff Verlag, Darmstadt, 1991.
- [87] Harald Ibach. *Physics of surfaces and interfaces*, volume 12. Springer, 2006.
- [88] Kurt K Kolasinski and Kurt W Kolasinski. *Surface science: foundations of catalysis and nanoscience*. John Wiley & Sons, 2012.
- [89] H Pfnür, P Feulner, HA Engelhardt, and D Menzel. An example of "fast" desorption: anomalously high pre-exponentials for CO desorption from ru (001). *Chemical Physics Letters*, 59(3):481–486, 1978.
- [90] Clarence G Goymour and David A King. Chemisorption of carbon monoxide on tungsten. part 2.—lateral interaction model for desorption kinetics. *Journal of the Chemical Society, Faraday Transactions 1: Physical Chemistry in Condensed Phases*, 69:749–760, 1973.
- [91] A Cassuto and David A King. Rate expressions for adsorption and desorption kinetics with precursor states and lateral interactions. *Surface Science*, 102(2-3):388–404, 1981.
- [92] EG Seebauer, ACF Kong, and LD Schmidt. The coverage dependence of the pre-exponential factor for desorption. *Surface Science*, 193(3):417–436, 1988.
- [93] Michael Schulze, Christopher Bronner, and Petra Tegeder. Adsorption energetics of azobenzenes on noble metal surfaces. *Journal of Physics: Condensed Matter*, 26(35):355004, 2014.
- [94] B Meng and WH Weinberg. Monte carlo simulations of temperature programmed desorption spectra. *The Journal of chemical physics*, 100(7):5280–5289, 1994.

- [95] DLS Nieskens, AP Van Bavel, and JW Niemantsverdriet. The analysis of temperature programmed desorption experiments of systems with lateral interactions; implications of the compensation effect. *Surface Science*, 546(2):159–169, 2003.
- [96] Keith JKJ Laidler. *Chemical kinetics*. Number 544.4 LAI. 1987.
- [97] E Habenschaden and J Küppers. Evaluation of flash desorption spectra. *Surface Science Letters*, 138(1):L147–L150, 1984.
- [98] JW Niemantsverdriet, P Dolle, K Markert, and K Wandelt. Thermal desorption of strained monoatomic Ag and Au layers from Ru (001). *Journal of Vacuum Science & Technology A: Vacuum, Surfaces, and Films*, 5(4):875–878, 1987.
- [99] Gerhard Ertl and Jürgen Küppers. *Low energy electrons and surface chemistry*. VCH Verlagsgesellschaft. Distribution, USA and Canada, VCH Publishers, 1985.
- [100] J. Pischel. *Über die schwingungsspektroskopische Untersuchung von Anregungen im mittleren und fernen Infrarot an Oberflächen metallischer Einkristalle*. PhD thesis, Universität Heidelberg, 2014.
- [101] F. Leyssner. *Analysis of Functional Organic Molecules at Noble Metal Surfaces by means of Vibrational Spectroscopies*. PhD thesis, Freie Universität Berlin, 2011.
- [102] M Pl Seah and WA Dench. Quantitative electron spectroscopy of surfaces: A standard data base for electron inelastic mean free paths in solids. *Surface and interface analysis*, 1(1):2–11, 1979.
- [103] Harald Ibach. *Electron energy loss spectrometers: the technology of high performance*, volume 63. Springer, 1991.
- [104] Hans Lüth. *Solid surfaces, interfaces and thin films*, volume 4. Springer, 2001.
- [105] RE Palmer and PJ Rous. Resonances in electron scattering by molecules on surfaces. *Reviews of modern physics*, 64(2):383, 1992.
- [106] George J Schulz. Resonances in electron impact on diatomic molecules. *Reviews of Modern Physics*, 45(3):423, 1973.

Bibliography

- [107] Harald Ibach and Hans Lüth. *Festkörperphysik: Einführung in die Grundlagen*. Springer-Verlag, 2009.
- [108] Frank Jensen. *Introduction to computational chemistry*. John Wiley & Sons, 2017.
- [109] Pierre Hohenberg and Walter Kohn. Inhomogeneous electron gas. *Physical review*, 136(3B):B864, 1964.
- [110] Max Born and Robert Oppenheimer. Zur Quantentheorie der Molekeln. *Annalen der Physik*, 389(20):457–484, 1927.
- [111] Llewellyn H Thomas. The calculation of atomic fields. 23(5):542–548, 1927.
- [112] Enrico Fermi. Eine statistische Methode zur Bestimmung einiger Eigenschaften des Atoms und ihre Anwendung auf die Theorie des periodischen Systems der Elemente. *Zeitschrift für Physik*, 48(1-2):73–79, 1928.
- [113] Felix Bloch. Über die Quantenmechanik der Elektronen in Kristallgittern. *Zeitschrift für physik*, 52(7-8):555–600, 1929.
- [114] Paul AM Dirac. Note on exchange phenomena in the thomas atom. 26(3):376–385, 1930.
- [115] Walter Kohn and Lu Jeu Sham. Self-consistent equations including exchange and correlation effects. *Physical review*, 140(4A):A1133, 1965.
- [116] PJ Stephens, FJ Devlin, CFN Chabalowski, and Michael J Frisch. Ab initio calculation of vibrational absorption and circular dichroism spectra using density functional force fields. *The Journal of Physical Chemistry*, 98(45):11623–11627, 1994.
- [117] Axel D Becke. Density-functional thermochemistry. III. the role of exact exchange. *The Journal of chemical physics*, 98(7):5648–5652, 1993.
- [118] Chengteh Lee, Weitao Yang, and Robert G Parr. Development of the colle-salvetti correlation-energy formula into a functional of the electron density. *Physical review B*, 37(2):785, 1988.
- [119] RBJS Krishnan, J Stephen Binkley, Rolf Seeger, and John A Pople. Self-consistent molecular orbital methods. XX. a basis set for correlated wave functions. *The Journal of Chemical Physics*, 72(1):650–654, 1980.

- [120] M. J. Frisch, G. W. Trucks, H. B. Schlegel, G. E. Scuseria, M. A. Robb, J. R. Cheeseman, G. Scalmani, V. Barone, B. Mennucci, G. A. Petersson, H. Nakatsuji, M. Caricato, X. Li, H. P. Hratchian, A. F. Izmaylov, J. Bloino, G. Zheng, J. L. Sonnenberg, M. Hada, M. Ehara, K. Toyota, R. Fukuda, J. Hasegawa, M. Ishida, T. Nakajima, Y. Honda, O. Kitao, H. Nakai, T. Vreven, J. A. Montgomery, J. E. Peralta, F. Ogliaro, M. Bearpark, J. J. Heyd, E. Brothers, K. N. Kudin, V. N. Staroverov, R. Kobayashi, J. Normand, K. Raghavachari, A. Rendell, J. C. Burant, S. S. Iyengar, J. Tomasi, M. Cossi, N. Rega, J. M. Millam, M. Klene, J. E. Knox, J. B. Cross, V. Bakken, C. Adamo, J. Jaramillo, R. Gomperts, R. E. Stratmann, O. Yazyev, A. J. Austin, R. Cammi, C. Pomelli, J. W. Ochterski, R. L. Martin, K. Morokuma, V. G. Zakrzewski, G. A. Voth, P. Salvador, J. J. Dannenberg, S. Dapprich, A. D. Daniels, Farkas, J. B. Foresman, J. V. Ortiz, J. Cioslowski, and D. J. Fox. Gaussian 09, Revision B.01, 2009.
- [121] M. Suenaga. Facio 19.1.4, 2016.
- [122] S. Stremlau. *High Resolution Vibrational Spectroscopy of Functional Organic Molecules at Surfaces*. PhD thesis, Freie Universitaet Berlin, 2015.
- [123] M Eremtchenko, R Temirov, D Bauer, JA Schaefer, and FS Tautz. Formation of molecular order on a disordered interface layer: Pentacene/Ag (111). *Physical Review B*, 72(11):115430, 2005.
- [124] Holly Walen, Da-Jiang Liu, Junepyo Oh, Hyunseob Lim, James W Evans, Yousoo Kim, and Patricia A Thiel. Self-organization of S adatoms on Au (111):v $3r30^\circ$ rows at low coverage. *The Journal of chemical physics*, 143(1):014704, 2015.
- [125] Zhao-Xiong Xie, Zhi-Feng Huang, and Xin Xu. Influence of reconstruction on the structure of self-assembled normal-alkane monolayers on Au (111) surfaces. *Physical Chemistry Chemical Physics*, 4(8):1486–1489, 2002.
- [126] Yun Wang, Noel S Hush, and Jeffrey R Reimers. Simulation of the Au (111)-(22 \times 3) surface reconstruction. *Physical Review B*, 75(23):233416, 2007.

Bibliography

- [127] RG Musket, W McLean, C A Colmenares, DM Makowiecki, and WJ Siekhaus. Preparation of atomically clean surfaces of selected elements: A review. *Applications of Surface Science*, 10(2):143–207, 1982.
- [128] Przemysław Kwolek, Marek Oszajca, and Konrad Szaciłowski. Catecholate and 2, 3-acenediolate complexes of d0 ions as prospective materials for molecular electronics and spintronics. *Coordination Chemistry Reviews*, 256(15-16):1706–1731, 2012.
- [129] Jörg Zegenhagen. Surface structure determination with X-ray standing waves. *Surface Science Reports*, 18(7-8):202–271, 1993.
- [130] DP Woodruff. Normal incidence X-ray standing wave determination of adsorbate structures. *Progress in Surface Science*, 57(1):1–60, 1998.
- [131] Wei Liu, Friedrich Maaß, Martin Willenbockel, Christopher Bronner, Michael Schulze, Serguei Soubatch, F Stefan Tautz, Petra Tegeder, and Alexandre Tkatchenko. Quantitative prediction of molecular adsorption: structure and binding of benzene on coinage metals. *Physical review letters*, 115(3):036104, 2015.
- [132] Wei Liu, Alexandre Tkatchenko, and Matthias Scheffler. Modeling adsorption and reactions of organic molecules at metal surfaces. *Accounts of chemical research*, 47(11):3369–3377, 2014.
- [133] Wei Liu, Victor G Ruiz, Guo-Xu Zhang, Biswajit Santra, Xinguo Ren, Matthias Scheffler, and Alexandre Tkatchenko. Structure and energetics of benzene adsorbed on transition-metal surfaces: Density-functional theory with van der Waals interactions including collective substrate response. *New Journal of Physics*, 15(5):053046, 2013.
- [134] Wei Liu, Javier Carrasco, Biswajit Santra, Angelos Michaelides, Matthias Scheffler, and Alexandre Tkatchenko. Benzene adsorbed on metals: Concerted effect of covalency and van der Waals bonding. *Physical Review B*, 86(24):245405, 2012.
- [135] Victor G Ruiz, Wei Liu, Egbert Zojer, Matthias Scheffler, and Alexandre Tkatchenko. Density-functional theory with screened van der Waals interactions for the modeling of hybrid inorganic-organic systems. *Physical review letters*, 108(14):146103, 2012.

- [136] Ingo Salzmann and Georg Heimel. Toward a comprehensive understanding of molecular doping organic semiconductors. *Journal of Electron Spectroscopy and Related Phenomena*, 204:208–222, 2015.
- [137] Emad F Aziz, Antje Vollmer, Stefan Eisebitt, Wolfgang Eberhardt, Patrick Pingel, Dieter Neher, and Norbert Koch. Localized charge transfer in a molecularly doped conducting polymer. *Advanced Materials*, 19(20):3257–3260, 2007.
- [138] Oliver T Hofmann, Patrick Rinke, Matthias Scheffler, and Georg Heimel. Integer versus fractional charge transfer at metal (/insulator)/organic interfaces: Cu (/NaCl)/TCNE. *ACS nano*, 9(5):5391–5404, 2015.
- [139] Thomas J Rockety, Minchul Yang, and Hai-Lung Dai. Adsorption energies, inter-adsorbate interactions, and the two binding sites within monolayer benzene on Ag(111). *The Journal of Physical Chemistry B*, 110(40):19973–19978, 2006.
- [140] Patrick Han and Paul S Weiss. Electronic substrate-mediated interactions. *Surface Science Reports*, 67(2):19–81, 2012.
- [141] Nicoleta Nicoara, Elisa Román, José M Gómez-Rodríguez, José A Martín-Gago, and Javier Méndez. Scanning tunneling and photoemission spectroscopies at the PTCDA/Au (111) interface. *Organic electronics*, 7(5):287–294, 2006.
- [142] I Chizhov, A Kahn, and G Scoles. Initial growth of 3, 4, 9, 10-perylenetetracarboxylic-dianhydride (PTCDA) on Au (111): a scanning tunneling microscopy study. *Journal of crystal growth*, 208(1):449–458, 2000.
- [143] Christian Weiss, Christian Wagner, Ruslan Temirov, and F Stefan Tautz. Direct imaging of intermolecular bonds in scanning tunneling microscopy. *Journal of the American Chemical Society*, 132(34):11864–11865, 2010.
- [144] CB France, PG Schroeder, JC Forsythe, and BA Parkinson. Scanning tunneling microscopy study of the coverage-dependent structures of pentacene on Au (111). *Langmuir*, 19(4):1274–1281, 2003.

Bibliography

- [145] PE Burrows and SR Forrest. Electroluminescence from trap-limited current transport in vacuum deposited organic light emitting devices. *Applied Physics Letters*, 64(17):2285–2287, 1994.
- [146] I Fernandez-Torrente, Serge Monturet, KJ Franke, J Fraxedas, Nicolas Lorente, and JI Pascual. Long-range repulsive interaction between molecules on a metal surface induced by charge transfer. *Physical review letters*, 99(17):176103, 2007.
- [147] S. U. Nanayakkara. *Ph.D. Thesis*. PhD thesis, The Pennsylvania State University, 2006.
- [148] J Friedel. Metallic alloys. *Il Nuovo Cimento (1955-1965)*, 7(2):287–311, 1958.
- [149] MF Crommie, CP Lutz, and DM Eigler. Imaging standing waves in a two-dimensional electron gas. *Nature*, 363(6429):524, 1993.
- [150] Y Hasegawa and Ph Avouris. Direct observation of standing wave formation at surface steps using scanning tunneling spectroscopy. *Physical Review Letters*, 71(7):1071, 1993.
- [151] Werner Reckien, Melanie Eggers, and Thomas Bredow. Theoretical study of the adsorption of benzene on coinage metals. *Beilstein journal of organic chemistry*, 10:1775, 2014.
- [152] Katrin Tonigold and Axel Groß. Adsorption of small aromatic molecules on the (111) surfaces of noble metals: A density functional theory study with semiempirical corrections for dispersion effects. *The Journal of chemical physics*, 132(22):224701, 2010.
- [153] Patrick Han, Brent A Mantoosh, E Charles H Sykes, Zachary J Donhauser, and Paul S Weiss. Benzene on Au(111) at 4 K: Monolayer growth and tip-induced molecular cascades. *Journal of the American Chemical Society*, 126(34):10787–10793, 2004.
- [154] S Lukas, S Vollmer, G Witte, and Ch Wöll. Adsorption of acenes on flat and vicinal Cu (111) surfaces: Step induced formation of lateral order. *The Journal of Chemical Physics*, 114(22):10123–10130, 2001.

- [155] SJ Stranick, MM Kamna, and PS Weiss. Interactions and dynamics of benzene on Cu {111} at low temperature. *Surface Science*, 338(1-3):41–59, 1995.
- [156] X-L Zhou, ME Castro, and JM White. Interactions of uv photons and low energy electrons with chemisorbed benzene on Ag(111). *Surface Science*, 238(1-3):215–225, 1990.
- [157] László Óvári, Ying Luo, Felix Leyssner, Rainer Haag, Martin Wolf, and Petra Tegeder. Adsorption and switching properties of a *n*-benzylideneaniline based molecular switch on a Au(111) surface. *The Journal of chemical physics*, 133(4):044707, 2010.
- [158] P Tegeder, S Hagen, F Leyssner, MV Peters, S Hecht, T Klamroth, P Saalfrank, and M Wolf. Electronic structure of the molecular switch tetra-*tert*-butyl-azobenzene adsorbed on Ag(111). *Applied Physics A*, 88(3):465–472, 2007.
- [159] Sebastian Hagen, Felix Leyssner, Dhananjay Nandi, Martin Wolf, and Petra Tegeder. Reversible switching of tetra-*tert*-butyl-azobenzene on a Au(111) surface induced by light and thermal activation. *Chemical physics letters*, 444(1-3):85–90, 2007.
- [160] Trent L Silbaugh and Charles T Campbell. Energies of formation reactions measured for adsorbates on late transition metal surfaces. *The Journal of Physical Chemistry C*, 120(44):25161–25172, 2016.
- [161] A Bondi. Van der Waals volumes and radii. *The Journal of physical chemistry*, 68(3):441–451, 1964.
- [162] Giuseppe Mercurio, Reinhard J Maurer, Wei Liu, Sebastian Hagen, Felix Leyssner, Petra Tegeder, J Meyer, Alexandre Tkatchenko, S Soubatch, K Reuter, et al. Quantification of finite-temperature effects on adsorption geometries of π -conjugated molecules: Azobenzene/Ag (111). *Physical Review B*, 88(3):035421, 2013.
- [163] T Vondrak and X-Y Zhu. Two-photon photoemission study of heterogeneous electron transfer: C₆F₆ on Cu (111). *The Journal of Physical Chemistry B*, 103(17):3449–3456, 1999.

Bibliography

- [164] Erik R McNellis, Christopher Bronner, Jörg Meyer, Martin Weinelt, Petra Tegeder, and Karsten Reuter. Azobenzene versus 3, 3, 5, 5-tetra-tert-butyl-azobenzene (TBA) at Au (111): characterizing the role of spacer groups. *Physical Chemistry Chemical Physics*, 12(24):6404–6412, 2010.
- [165] Denis Syomin, Jooho Kim, Bruce E Koel, and G Barney Ellison. Identification of adsorbed phenyl (C₆H₅) groups on metal surfaces: Electron-induced dissociation of benzene on Au(111). *The Journal of Physical Chemistry B*, 105(35):8387–8394, 2001.
- [166] Ming Xi, Michael X Yang, Sam K Jo, Brian E Bent, and Paul Stevens. Benzene adsorption on Cu (111): Formation of a stable bilayer. *The Journal of chemical physics*, 101(10):9122–9131, 1994.
- [167] J Heyd. J. heyd, ge scuseria, and m. ernzerhof, j. chem. phys. 124, 219906 (2006). *J. Chem. Phys.*, 124:219906, 2006.
- [168] Jochen Heyd, Gustavo E Scuseria, and Matthias Ernzerhof. Hybrid functionals based on a screened Coulomb potential. *The Journal of chemical physics*, 118(18):8207–8215, 2003.
- [169] John P Perdew, Kieron Burke, and Matthias Ernzerhof. Generalized gradient approximation made simple. *Physical review letters*, 77(18):3865, 1996.
- [170] Alexandre Tkatchenko, Robert A DiStasio Jr, Roberto Car, and Matthias Scheffler. Accurate and efficient method for many-body van der Waals interactions. *Physical review letters*, 108(23):236402, 2012.
- [171] Alberto Ambrosetti, Anthony M Reilly, Robert A DiStasio Jr, and Alexandre Tkatchenko. Long-range correlation energy calculated from coupled atomic response functions. *The Journal of chemical physics*, 140(18):18A508, 2014.
- [172] CD Lindstrom, M Muntwiler, and X-Y Zhu. Electron dynamics at polyacene/Au(111) interfaces. *The Journal of Physical Chemistry B*, 111(24):6913–6920, 2007.
- [173] K Tamada, J Nagasawa, F Nakanishi, K Abe, T Ishida, M Hara, and Wolfgang Knoll. Structure and growth of hexyl azobenzene thiol SAMs on Au(111). *Langmuir*, 14(12):3264–3271, 1998.

- [174] Jonas Björk, Manfred Matena, Matthew S Dyer, Mihaela Enache, Jorge Lobo-Checa, Lutz H Gade, Thomas A Jung, Meike Stöhr, and Mats Persson. STM fingerprint of molecule–adatom interactions in a self-assembled metal–organic surface coordination network on Cu(111). *Physical Chemistry Chemical Physics*, 12(31):8815–8821, 2010.
- [175] Alexandre Tkatchenko. personal communication.
- [176] Marco Gruenewald, Kristin Wachter, Matthias Meissner, Michael Kozlik, Roman Forker, and Torsten Fritz. Optical and electronic interaction at metal–organic and organic–organic interfaces of ultra-thin layers of PTCDA and SnPc on noble metal surfaces. *Organic Electronics*, 14(9):2177–2183, 2013.
- [177] Tobias Breuer, Michael Klues, and Gregor Witte. Characterization of orientational order in π -conjugated molecular thin films by NEXAFS. *Journal of Electron Spectroscopy and Related Phenomena*, 204:102–115, 2015.
- [178] Peng Chen, Guizhong Yang, Tianxi Liu, Tingcheng Li, Min Wang, and Wei Huang. Optimization of opto-electronic property and device efficiency of polyfluorenes by tuning structure and morphology. *Polymer international*, 55(5):473–490, 2006.
- [179] Roland Fitzner, Elena Mena-Osteritz, Amaresh Mishra, Gisela Schulz, Egon Reinold, Matthias Weil, Christian Körner, Hannah Ziehlke, Chris Elschner, Karl Leo, et al. Correlation of π -conjugated oligomer structure with film morphology and organic solar cell performance. *Journal of the American Chemical Society*, 134(27):11064–11067, 2012.
- [180] Amaresh Mishra, Markus KR Fischer, and Peter Bäuerle. Metal-free organic dyes for dye-sensitized solar cells: From structure: Property relationships to design rules. *Angewandte Chemie International Edition*, 48(14):2474–2499, 2009.
- [181] Yuhan Zhang, Jingsi Qiao, Si Gao, Fengrui Hu, Daowei He, Bing Wu, Ziyi Yang, Bingchen Xu, Yun Li, Yi Shi, et al. Probing carrier transport and structure-property relationship of highly ordered organic semiconductors at the two-dimensional limit. *Physical review letters*, 116(1):016602, 2016.

Bibliography

- [182] Till Riehm, Gabriele De Paoli, Asgeir E Konradsson, Luisa De Cola, Hubert Wadepohl, and Lutz H Gade. Tetraazaperopyrenes: a new class of multifunctional chromophores. *Chemistry-A European Journal*, 13(26):7317–7329, 2007.
- [183] Makoto Tadokoro, Syuma Yasuzuka, Masaharu Nakamura, Takumi Shinoda, Toshinori Tatenuma, Minoru Mitsumi, Yoshiki Ozawa, Koshiro Toriumi, Harukazu Yoshino, Daisuke Shiomi, et al. A high-conductivity crystal containing a copper (I) coordination polymer bridged by the organic acceptor TANC. *Angewandte Chemie*, 118(31):5268–5271, 2006.
- [184] Katherine Hutchison, Gordana Srdanov, Robin Hicks, Huinan Yu, Fred Wudl, Thomas Strassner, Maja Nendel, and KN Houk. Tetraphenylhexaazaanthracene: A case for dominance of cyanine ion stabilization overwhelming 16π antiaromaticity. *Journal of the American Chemical Society*, 120(12):2989–2990, 1998.
- [185] Michael Winkler and KN Houk. Nitrogen-rich oligoacenes: candidates for n-channel organic semiconductors. *Journal of the American Chemical Society*, 129(6):1805–1815, 2007.
- [186] Qian Miao, Thuc-Quyen Nguyen, Takao Someya, Graciela B Blanchet, and Colin Nuckolls. Synthesis, assembly, and thin film transistors of dihydrodiazapentacene: an isostructural motif for pentacene. *Journal of the American Chemical Society*, 125(34):10284–10287, 2003.
- [187] Ming L Tang and Zhenan Bao. Halogenated materials as organic semiconductors. *Chemistry of Materials*, 23(3):446–455, 2010.
- [188] Joo H Kang and X-Y Zhu. Pi-stacked pentacene thin films grown on Au (111). *Applied physics letters*, 82(19):3248–3250, 2003.
- [189] E Clar and W Schmidt. Correlations between photoelectron and ultraviolet absorption spectra of polycyclic hydrocarbons: the terylene and peropyrene series. *Tetrahedron*, 34(21):3219–3224, 1978.
- [190] John Venable. *Introduction to surface and thin film processes*. Cambridge University Press, 2000.
- [191] Alberto Pimpinelli and Jacques Villain. *Physics of crystal growth*, volume 19. Cambridge university press Cambridge, 1998.

- [192] Kenjiro Oura, VG Lifshits, AA Saranin, AV Zotov, and M Katayama. *Surface science: an introduction*. Springer Science & Business Media, 2013.
- [193] E A Silinsh. *Organic Molecular Crystals*. Springer Verlag, Berlin, 1980.
- [194] CD Dimitrakopoulos, S Purushothaman, J Kyminis, A Callegari, and JM Shaw. Low-voltage organic transistors on plastic comprising high-dielectric constant gate insulators. *Science*, 283(5403):822–824, 1999.
- [195] John E Anthony, James S Brooks, David L Eaton, and Sean R Parkin. Functionalized pentacene: improved electronic properties from control of solid-state order. *Journal of the American Chemical Society*, 123(38):9482–9483, 2001.
- [196] Millicent B. Smith and Josef Michl. Singlet fission. *Chemical Reviews*, 110(11):6891–6936, 2010.
- [197] Millicent B Smith and Josef Michl. Recent advances in singlet fission. *Annual review of physical chemistry*, 64:361–386, 2013.
- [198] N Monahan and X-Y Zhu. Charge transfer-mediated singlet fission. *Annual review of physical chemistry*, 66:601–618, 2015.
- [199] S Singh, WJ Jones, W Siebrand, BP Stoicheff, and WG Schneider. Laser generation of excitons and fluorescence in anthracene crystals. *The Journal of Chemical Physics*, 42(1):330–342, 1965.
- [200] William Shockley and Hans J Queisser. Detailed balance limit of efficiency of p-n junction solar cells. *Journal of applied physics*, 32(3):510–519, 1961.
- [201] Kalishankar Bhattacharyya and Ayan Datta. Polymorphism controlled singlet fission in tips-anthracene: role of stacking orientation. *The Journal of Physical Chemistry C*, 121(3):1412–1420, 2017.
- [202] John Anthony. personal communication.
- [203] P Swiderek, M-J Fraser, M Michaud, and L Sanche. Electron-energy-loss spectroscopy of the low-lying triplet states of styrene. *The Journal of chemical physics*, 100(1):70–77, 1994.

Bibliography

- [204] Petra Swiderek, M Michaud, G Hohlneicher, and L Sanche. Electron energy loss spectroscopy of solid naphthalene and acenaphthene: search for the low-lying triplet states. *Chemical physics letters*, 175(6):667–673, 1990.
- [205] Andrea Gnoli, Hande Ustunel, Daniele Toffoli, Liyang Yu, Daniele Catone, Stefano Turchini, Silvano Lizzit, Natalie Stingelin, and Rosanna Larciprete. Bis (triisopropylsilylethynyl) pentacene/Au(111) interface: Coupling, molecular orientation, and thermal stability. *The Journal of Physical Chemistry C*, 118(39):22522–22532, 2014.
- [206] Stefan CB Mannsfeld, Ming Lee Tang, and Zhenan Bao. Thin film structure of triisopropylsilylethynyl-functionalized pentacene and tetraceno [2, 3-b] thiophene from grazing incidence X-ray diffraction. *Advanced Materials*, 23(1):127–131, 2011.
- [207] V Shklover, FS Tautz, R Scholz, S Sloboshanin, M Sokolowski, JA Schaefer, and E Umbach. Differences in vibronic and electronic excitations of PTCDA on Ag (111) and Ag (110). *Surface Science*, 454:60–66, 2000.
- [208] Brian J Walker, Andrew J Musser, David Beljonne, and Richard H Friend. Singlet exciton fission in solution. *Nature chemistry*, 5(12):1019, 2013.
- [209] Brigitte Wex, O Ala’a, Antoine Vanvooren, Ute Zschieschang, Hagen Klauk, Jeanette A Krause, Jérôme Cornil, and Bilal R Kaafarani. Crystalline TQPP as p-type semiconductor: X-ray crystallographic investigation, OTFT device, and computational analysis of transport properties. *Journal of Molecular Structure*, 1093:144–149, 2015.
- [210] Bernd Kohl, Mercedes V Bohnwagner, Frank Rominger, Hubert Wade-pohl, Andreas Dreuw, and Michael Mastalerz. Attractive dispersion interactions versus steric repulsion of tert-butyl groups in the crystal packing of a D3h-symmetric tris (quinoxalinophenanthrophenazine). *Chemistry-A European Journal*, 22(2):646–655, 2016.
- [211] Bernd Kohl, Frank Rominger, and Michael Mastalerz. Crystal structures of a molecule designed not to pack tightly. *Chemistry-A European Journal*, 21(48):17308–17313, 2015.

- [212] E Clar. Untersuchungen über die Feinstruktur des Peropyrens und seiner Benzologen nach dem Anellierungsverfahren (Aromatische Kohlenwasserstoffe, XL. Mittel.). *Berichte der deutschen chemischen Gesellschaft (A and B Series)*, 76(5):458–466, 1943.
- [213] Till Riehm, Gabriele De Paoli, Asgeir E Konradsson, Luisa De Cola, Hubert Wadepohl, and Lutz H Gade. Tetraazaperopyrenes: a new class of multifunctional chromophores. *Chemistry-A European Journal*, 13(26):7317–7329, 2007.
- [214] Susanne C Martens, Ute Zschieschang, Hubert Wadepohl, Hagen Klauk, and Lutz H Gade. Tetrachlorinated tetraazaperopyrenes (TAPPs): Highly fluorescent dyes and semiconductors for air-stable organic n-channel transistors and complementary circuits. *Chemistry-A European Journal*, 18(12):3498–3509, 2012.
- [215] Sonja Geib, Ute Zschieschang, Marcel Gsänger, Matthias Stolte, Frank Würthner, Hubert Wadepohl, Hagen Klauk, and Lutz H Gade. Core-brominated tetraazaperopyrenes as n-channel semiconductors for organic complementary circuits on flexible substrates. *Advanced Functional Materials*, 23(31):3866–3874, 2013.
- [216] Manfred Matena, Meike Stöhr, Till Riehm, Jonas Björk, Susanne Martens, Matthew S Dyer, Mats Persson, Jorge Lobo-Checa, Kathrin Müller, Mihaela Enache, et al. Aggregation and contingent metal/surface reactivity of 1, 3, 8, 10-tetraazaperopyrene (TAPP) on Cu (111). *Chemistry-A European Journal*, 16(7):2079–2091, 2010.
- [217] F. Maass. *Untersuchung des Adsorptionsverhaltens und der elektronischen Eigenschaften organischer Halbleitermaterialien auf der Au(111)-Oberfläche*. PhD thesis, Universität Heidelberg, 2014.
- [218] Lena Hahn, Friedrich Maaß, Tim Bleith, Ute Zschieschang, Hubert Wadepohl, Hagen Klauk, Petra Tegeder, and Lutz H Gade. Core halogenation as a construction principle in tuning the material properties of tetraazaperopyrenes. *Chemistry-A European Journal*, 21(49):17691–17700, 2015.
- [219] Erwan Varene, Yan Pennec, and Petra Tegeder. Assembly and electronic

Bibliography

- structure of octithiophene on Au (111). *Chemical Physics Letters*, 515(1-3):141–145, 2011.
- [220] Erwan Varene, Lea Bogner, Stephan Meyer, Yan Pennek, and Petra Tegeder. Coverage-dependent adsorption geometry of octithiophene on Au (111). *Physical Chemistry Chemical Physics*, 14(2):691–696, 2012.
- [221] Bernd Kohl, Mercedes V. Bohnwagner, Frank Rominger, Hubert Wade-pohl, Andreas Dreuw, and Michael Mastalerz. Attractive dispersion interactions versus steric repulsion of tert-butyl groups in the crystal packing of D_{3h}-symmetric tris(quinoxalinophenanthrophenazine). *Chemistry-A European Journal*, 2015.
- [222] Sahar Sharifzadeh, Cathy Y Wong, Hao Wu, Benjamin L Cotts, Leor Kronik, Naomi S Ginsberg, and Jeffrey B Neaton. Relating the physical structure and optoelectronic function of crystalline TIPS-pentacene. *Advanced Functional Materials*, 25(13):2038–2046, 2015.
- [223] Erich Hückel. Quantentheoretische Beiträge zum Benzolproblem. *Zeitschrift für Physik*, 70(3-4):204–286, 1931.
- [224] Shuwen Zeng, Dominique Baillargeat, Ho-Pui Ho, and Ken-Tye Yong. Nanomaterials enhanced surface plasmon resonance for biological and chemical sensing applications. *Chemical Society Reviews*, 43(10):3426–3452, 2014.
- [225] Ekmel Ozbay. Plasmonics: merging photonics and electronics at nanoscale dimensions. *Science*, 311(5758):189–193, 2006.
- [226] Xiangang Luo and Teruya Ishihara. Surface plasmon resonant interference nanolithography technique. *Applied Physics Letters*, 84(23):4780–4782, 2004.
- [227] S Wedge, JAE Wasey, William L Barnes, and I Sage. Coupled surface plasmon-polariton mediated photoluminescence from a top-emitting organic light-emitting structure. *Applied Physics Letters*, 85(2):182–184, 2004.
- [228] Alan J Bennett. Influence of the electron charge distribution on surface-plasmon dispersion. *Physical Review B*, 1(1):203, 1970.

- [229] T Kloos and H Raether. The dispersion of surface plasmons of Al and Mg. *Physics Letters A*, 44(3):157–158, 1973.
- [230] Sung Jin Park and Richard E Palmer. Plasmon dispersion of the Au (111) surface with and without self-assembled monolayers. *Physical review letters*, 102(21):216805, 2009.
- [231] K-D Tsuei, EW Plummer, A Liebsch, K Kempa, and P Bakshi. Multipole plasmon modes at a metal surface. *Physical review letters*, 64(1):44, 1990.
- [232] Peter J Feibelman and KD Tsuei. Negative surface-plasmon dispersion coefficient: A physically illustrative, exact formula. *Physical Review B*, 41(12):8519, 1990.
- [233] Ku-Ding Tsuei, E Ward Plummer, and Peter J Feibelman. Surface-plasmon dispersion in simple metals. *Physical review letters*, 63(20):2256, 1989.
- [234] P Amsalem, L Giovanelli, JM Themlin, and T Angot. Electronic and vibrational properties at the ZnPc/Ag (110) interface. *Physical Review B*, 79(23):235426, 2009.
- [235] Heinz Raether. Surface excitations. In *Excitation of Plasmons and Interband Transitions by Electrons*, pages 116–171. Springer, 1980.
- [236] Heinz Raether. Surface plasmons on gratings. In *Surface plasmons on smooth and rough surfaces and on gratings*, pages 91–116. Springer, 1988.
- [237] Christof Kunz. Messung charakteristischer Energieverluste von Elektronen an leichtoxydierbaren Metallen im Ultrahochvakuum. *Zeitschrift für Physik*, 196(4):311–331, 1966.
- [238] EV Chulkov, AG Borisov, JP Gauyacq, D Sánchez-Portal, VM Silkin, VP Zhukov, and PM Echenique. Electronic excitations in metals and at metal surfaces. *Chemical Reviews*, 106(10):4160–4206, 2006.
- [239] Paul Drude. Zur Elektronentheorie der Metalle. *Annalen der Physik*, 306(3):566–613, 1900.
- [240] David Pines and David Bohm. A collective description of electron interactions: II. collective vs individual particle aspects of the interactions. *Physical Review*, 85(2):338, 1952.

Bibliography

- [241] U Stroth. Plasmaphysik: Phänomene, Grundlagen, Anwendungen. *Vieweg + Teubner Verlag, Wiesbaden*, 2011.
- [242] RH Ritchie. Plasma losses by fast electrons in thin films. *Physical Review*, 106(5):874, 1957.
- [243] SJ Allen Jr, DC Tsui, and RA Logan. Observation of the two-dimensional plasmon in silicon inversion layers. *Physical Review Letters*, 38(17):980, 1977.
- [244] Yu Liu, Roy F Willis, KV Emtsev, and Th Seyller. Plasmon dispersion and damping in electrically isolated two-dimensional charge sheets. *Physical Review B*, 78(20):201403, 2008.
- [245] Yu Liu. *Plasmon dispersion in two-dimensional charge-sheets*. The Pennsylvania State University, 2009.
- [246] Tadaaki Nagao, Torsten Hildebrandt, Martin Henzler, and Shuji Hasegawa. Dispersion and damping of a two-dimensional plasmon in a metallic surface-state band. *Physical review letters*, 86(25):5747, 2001.
- [247] S Das Sarma and EH Hwang. Dynamical response of a one-dimensional quantum-wire electron system. *Physical Review B*, 54(3):1936, 1996.
- [248] VM Silkin, A García-Lekue, JM Pitarke, EV Chulkov, E Zaremba, and PM Echenique. Novel low-energy collective excitation at metal surfaces. *Europhysics Letters*, 66(2):260, 2004.
- [249] NH March and MP Tosi. Collective effects in condensed conducting phases including low-dimensional systems. *Advances in Physics*, 44(4):299–386, 1995.
- [250] J Ruvalds. Plasmons and high-temperature superconductivity in alloys of copper oxides. *Physical Review B*, 35(16):8869, 1987.
- [251] A Bill, H Morawitz, and VZ Kresin. Dynamical screening and superconducting state in intercalated layered metalochloronitrides. *Physical Review B*, 66(10):100501, 2002.
- [252] David Pines. Electron interaction in solids. *Canadian Journal of Physics*, 34(12A):1379–1394, 1956.

- [253] VM Silkin, JM Pitarke, EV Chulkov, and PM Echenique. Acoustic surface plasmons in the noble metals Cu, Ag, and Au. *Physical Review B*, 72(11):115435, 2005.
- [254] Hans Lüth. Surface and interface physics: Its definition and importance. In *Solid Surfaces, Interfaces and Thin Films*, pages 1–28. Springer, 2015.
- [255] AV Chaplik. Possible crystallization of charge carriers in low-density inversion layers. *Soviet Journal of Experimental and Theoretical Physics*, 35:395, 1972.
- [256] Branko Gumhalter. Transient interactions and coherent motion of optically excited electron–hole pairs in the image potential states at metal surfaces. *Surface Science*, 518(1-2):81–103, 2002.
- [257] S Das Sarma and A Madhukar. Collective modes of spatially separated, two-component, two-dimensional plasma in solids. *Physical Review B*, 23(2):805, 1981.
- [258] Feng Duan and Jin Guojun. *Introduction To Condensed Matter Physics: Volume 1*. World Scientific Publishing Company, 2005.
- [259] Gustav Bihlmayer, O Rader, and R Winkler. Focus on the rashba effect. *New journal of physics*, 17(5):050202, 2015.
- [260] F Reinert, G Nicolay, S Schmidt, D Ehm, and S Hüfner. Direct measurements of the L-gap surface states on the (111) face of noble metals by photoelectron spectroscopy. *Physical Review B*, 63(11):115415, 2001.
- [261] Jun Yan, Karsten W Jacobsen, and Kristian S Thygesen. Conventional and acoustic surface plasmons on noble metal surfaces: a time-dependent density functional theory study. *Physical Review B*, 86(24):241404, 2012.
- [262] JM Pitarke, VM Silkin, EV Chulkov, and PM Echenique. Theory of surface plasmons and surface-plasmon polaritons. *Reports on progress in physics*, 70(1):1, 2006.
- [263] Ph Hofmann, KC Rose, V Fernandez, AM Bradshaw, and W Richter. Study of surface states on Cu (110) using optical reflectance anisotropy. *Physical review letters*, 75(10):2039, 1995.

Bibliography

- [264] V Shklover, FS Tautz, R Scholz, S Sloboshanin, M Sokolowski, JA Schaefer, and E Umbach. Differences in vibronic and electronic excitations of PTCDA on Ag (111) and Ag (110). *Surface Science*, 454:60–66, 2000.
- [265] Kaname Kanai, Kouki Akaike, Kiichirou Koyasu, Kentaro Sakai, Toshio Nishi, Yasunori Kamizuru, Tatsuhiko Nishi, Yukio Ouchi, and Kazuhiko Seki. Determination of electron affinity of electron accepting molecules. *Applied Physics A*, 95(1):309–313, 2009.
- [266] David Gerbert, Friedrich Maaß, and Petra Tegeder. Extended space charge region and unoccupied molecular band formation in epitaxial tetrafluorotetracyanoquinodimethane films. *The Journal of Physical Chemistry C*, 121(29):15696–15701, 2017.
- [267] Marisa N Faraggi, Nan Jiang, Nora Gonzalez-Lakunza, Alexander Langner, Sebastian Stepanow, Klaus Kern, and Andres Arnau. Bonding and charge transfer in metal–organic coordination networks on Au (111) with strong acceptor molecules. *The Journal of Physical Chemistry C*, 116(46):24558–24565, 2012.
- [268] Christian Wäckerlin, Cristian Iacovita, Dorota Chylarecka, Petra Fesser, Thomas A Jung, and Nirmalya Ballav. Assembly of 2D ionic layers by reaction of alkali halides with the organic electrophile 7, 7, 8, 8-tetracyano-p-quinodimethane (TCNQ). *Chemical Communications*, 47(32):9146–9148, 2011.
- [269] Steven K Wells, Jerzy Giergiel, Terry A Land, John M Lindquist, and John C Hemminger. Beam-induced modifications of TCNQ multilayers. *Surface Science*, 257(1-3):129–145, 1991.
- [270] MM Kamna, TM Graham, JC Love, and PS Weiss. Strong electronic perturbation of the Cu {111} surface by 7, 7, 8, 8-tetracyanoquinodimethane. *Surface Science*, 419(1):12–23, 1998.
- [271] Changwon Park, Geoffrey A Rojas, Seokmin Jeon, Simon J Kelly, Sean C Smith, Bobby G Sumpter, Mina Yoon, and Petro Maksymovych. Weak competing interactions control assembly of strongly bonded TCNQ ionic acceptor molecules on silver surfaces. *Physical Review B*, 90(12):125432, 2014.

- [272] David Gerbert and Petra Tegeder. Molecular ion formation by photoinduced electron transfer at the tetracyanoquinodimethane/Au (111) interface. *The journal of physical chemistry letters*, 8(19):4685–4690, 2017.
- [273] Alexander W Hains, Ziqi Liang, Michael A Woodhouse, and Brian A Gregg. Molecular semiconductors in organic photovoltaic cells. *Chemical reviews*, 110(11):6689–6735, 2010.
- [274] Koji Shibata, Hiroshi Wada, Ken Ishikawa, Hideo Takezoe, and Takehiko Mori. (tetrathiafulvalene)(tetracyanoquinodimethane) as a low-contact-resistance electrode for organic transistors. *Applied physics letters*, 90(19):193509, 2007.
- [275] Etienne Menard, Vitaly Podzorov, S-H Hur, Anshu Gaur, Michael E Gershenson, and John A Rogers. High-performance n-and p-type single-crystal organic transistors with free-space gate dielectrics. *Advanced materials*, 16(23-24):2097–2101, 2004.
- [276] Hiroyuki Yamane and Nobuhiro Kosugi. High hole-mobility molecular layer made from strong electron acceptor molecules with metal adatoms. *The journal of physical chemistry letters*, 8(21):5366–5371, 2017.
- [277] Lin Ma, Peng Hu, Hui Jiang, Christian Kloc, Handong Sun, Cesare Soci, Alexander A Voityuk, Maria E Michel-Beyerle, and Gagik G Gurzadyan. Single photon triggered dianion formation in TCNQ and F4TCNQ crystals. *Scientific reports*, 6:28510, 2016.
- [278] K-D Tsuei, EW Plummer, A Liebsch, E Pehlke, K Kempa, and P Bakshi. The normal modes at the surface of simple metals. *Surface Science*, 247(2-3):302–326, 1991.
- [279] T Angot and G Gewinner. Identification of plasmon modes in two-dimensional er silicide epitaxially grown on Si(111). *Journal of electron spectroscopy and related phenomena*, 104(1-3):173–184, 1999.
- [280] Ansgar Liebsch. *Electronic excitations at metal surfaces*. Springer Science & Business Media, 2013.

Bibliography

- [281] Jiong Lu and Kian Ping Loh. High resolution electron energy loss spectroscopy study of zinc phthalocyanine and tetrafluoro tetracyanoquinodimethane on Au (111). *Chemical Physics Letters*, 468(1-3):28–31, 2009.
- [282] T Hasegawa, S Kagoshima, T Mochida, S Sugiura, and Y Iwasa. Electronic states and anti-ferromagnetic order in mixed-stack charge-transfer compound (BEDT-TTF)(F₂TCNQ). *Solid state communications*, 103(8):489–493, 1997.
- [283] Yosei Shibata, Jun'ya Tsutsumi, Satoshi Matsuoka, Koji Matsubara, Yuji Yoshida, Masayuki Chikamatsu, and Tatsuo Hasegawa. Uniaxially oriented polycrystalline thin films and air-stable n-type transistors based on donor-acceptor semiconductor (diC₈BTBT)(F_nTCNQ)[n= 0, 2, 4]. *Applied Physics Letters*, 106(14):42_1, 2015.
- [284] Debraj Choudhury, Barun Das, DD Sarma, and CNR Rao. XPS evidence for molecular charge-transfer doping of graphene. *Chemical Physics Letters*, 497(1-3):66–69, 2010.
- [285] M Leufgen, O Rost, C Gould, G Schmidt, J Geurts, LW Molenkamp, NS Oxtoby, M Mas-Torrent, N Crivillers, J Veciana, et al. High-mobility tetrathiafulvalene organic field-effect transistors from solution processing. *Organic Electronics*, 9(6):1101–1106, 2008.
- [286] THOMAS J Kistenmacher, TERRY E Phillips, and DWAIN O Cowan. The crystal structure of the 1: 1 radical cation–radical anion salt of 2, 2'-bis-1, 3-dithiole (TTF) and 7, 7, 8, 8-tetracyanoquinodimethane (TCNQ). *Acta Crystallographica Section B: Structural Crystallography and Crystal Chemistry*, 30(3):763–768, 1974.
- [287] Jerry B Torrance. The difference between metallic and insulating salts of tetracyanoquinodimethone (TCNQ): how to design an organic metal. *Accounts of chemical research*, 12(3):79–86, 1979.
- [288] AN Aleshin, JY Lee, SW Chu, JS Kim, and YW Park. Mobility studies of field-effect transistor structures based on anthracene single crystals. *Applied physics letters*, 84(26):5383–5385, 2004.

- [289] Aline Hepp, Holger Heil, Wieland Weise, Marcus Ahles, Roland Schmechel, and Heinz von Seggern. Light-emitting field-effect transistor based on a tetracene thin film. *Physical review letters*, 91(15):157406, 2003.
- [290] Choongik Kim, Antonio Facchetti, and Tobin J Marks. Polymer gate dielectric surface viscoelasticity modulates pentacene transistor performance. *Science*, 318(5847):76–80, 2007.
- [291] Kostya S Novoselov, Andre K Geim, Sergei V Morozov, DA Jiang, Y. Zhang, Sergey V Dubonos, Irina V Grigorieva, and Alexandr A Firsov. Electric field effect in atomically thin carbon films. *Science*, 306(5696):666–669, 2004.
- [292] Antonio Politano and Gennaro Chiarello. Plasmon modes in graphene: status and prospect. *Nanoscale*, 6(19):10927–10940, 2014.
- [293] H Pfnür, C Tegenkamp, and L Vattuone. Plasmons in one and two dimensions. *arXiv preprint arXiv:1701.05049*, 2017.
- [294] Yu Liu and Roy F Willis. Plasmon-phonon strongly coupled mode in epitaxial graphene. *Physical Review B*, 81(8):081406, 2010.
- [295] SY Shin, ND Kim, JG Kim, KS Kim, DY Noh, Kwang S Kim, and JW Chung. Control of the π plasmon in a single layer graphene by charge doping. *Applied Physics Letters*, 99(8):082110, 2011.
- [296] Hugen Yan, Tony Low, Wenjuan Zhu, Yanqing Wu, Marcus Freitag, Xuesong Li, Francisco Guinea, Phaedon Avouris, and Fengnian Xia. Damping pathways of mid-infrared plasmons in graphene nanostructures. *Nature Photonics*, 7(5):394, 2013.
- [297] Roy F Willis. *Vibrational spectroscopy of adsorbates*, volume 15. Springer Science & Business Media, 2012.
- [298] F Moresco, M Rocca, T Hildebrandt, and M Henzler. Plasmon confinement in ultrathin continuous Ag films. *Physical review letters*, 83(11):2238, 1999.
- [299] C Tegenkamp, H Pfnür, T Langer, J Baringhaus, and HW Schumacher. Plasmon electron–hole resonance in epitaxial graphene. *Journal of Physics: Condensed Matter*, 23(1):012001, 2010.

Bibliography

- [300] Alberto Modelli, Laura Mussoni, and Daniele Fabbri. Electron affinities of polycyclic aromatic hydrocarbons by means of B3LYP/6-31+ G* calculations. *The Journal of Physical Chemistry A*, 110(20):6482–6486, 2006.
- [301] Ugo Fano. Sullo spettro di assorbimento dei gas nobili presso il limite dello spettro d'arco. *Il Nuovo Cimento (1924-1942)*, 12(3):154–161, 1935.
- [302] Ugo Fano. Effects of configuration interaction on intensities and phase shifts. *Physical Review*, 124(6):1866, 1961.
- [303] Boris M. Smirnov. *Physics of Atoms and Ions*. Springer-Verlag New York, 2013.
- [304] Kilian Peter Heeg, C Ott, D Schumacher, H-C Wille, R Röhlberger, Thomas Pfeifer, and Jörg Evers. Interferometric phase detection at x-ray energies via Fano resonance control. *Physical review letters*, 114(20):207401, 2015.
- [305] Jian Ye, Fangfang Wen, Heidar Sobhani, J Britt Lassiter, Pol Van Dorpe, Peter Nordlander, and Naomi J Halas. Plasmonic nanoclusters: near field properties of the Fano resonance interrogated with SERS. *Nano letters*, 12(3):1660–1667, 2012.
- [306] Andrey E Miroshnichenko, Sergej Flach, and Yuri S Kivshar. Fano resonances in nanoscale structures. *Reviews of Modern Physics*, 82(3):2257, 2010.
- [307] Boris Luk'yanchuk, Nikolay I Zheludev, Stefan A Maier, Naomi J Halas, Peter Nordlander, Harald Giessen, and Chong Tow Chong. The Fano resonance in plasmonic nanostructures and metamaterials. *Nature materials*, 9(9):707, 2010.
- [308] AM Martínez-Argüello, M Martínez-Mares, M Cobián-Suárez, G Báez, and RA Méndez-Sánchez. A new Fano resonance in measurement processes. *Europhysics Letters*, 110(5):54003, 2015.
- [309] Yong S Joe, Arkady M Satanin, and Chang Sub Kim. Classical analogy of Fano resonances. *Physica Scripta*, 74(2):259, 2006.

- [310] BNJ Persson and M Persson. Vibrational lifetime for CO adsorbed on Cu(100). *Solid State Communications*, 36(2):175–179, 1980.
- [311] BNJ Persson. Vibrational energy relaxation at surfaces: O₂ chemisorbed on Pt (111). *Chemical physics letters*, 139(5):457–462, 1987.
- [312] A Peremans, Y Caudano, PA Thiry, P Dumas, WQ Zhang, A Le Rille, and A Tadjeddine. Electronic tuning of dynamical charge transfer at an interface: K doping of C₆₀/Ag (111). *Physical review letters*, 78(15):2999, 1997.
- [313] Friedrich Maaß, Yingda Jiang, Wei Liu, Alexandre Tkatchenko, and Petra Tegeder. Binding energies of benzene on coinage metal surfaces: Equal stability on different metals. *The Journal of chemical physics*, 148(21):214703, 2018.
- [314] Jeffrey P Merrick, Damian Moran, and Leo Radom. An evaluation of harmonic vibrational frequency scale factors. *The Journal of Physical Chemistry A*, 111(45):11683–11700, 2007.
- [315] M. Willenbockel. *A Study on the Interplay of Molecule-Molecule and Molecule-Substrate Interactions at Metal-Organic Interfaces*. PhD thesis, RWTH Aachen, 2014.
- [316] R. Raval, S. F. Parker, M. E. Pemble, P. Hollins, J. Pritchard, and M. A. Chesters. FT-RAIRS, EELS and LEED studies of the adsorption of carbon monoxide on Cu(111). *Surface Science*, 203(3):353–377, 1988.
- [317] C. M. Mate and G. A. Somorjai. Carbon monoxide induced ordering of benzene on Pt(111) and Rh(111) crystal surfaces. *Surface Science*, 160(2):542–560, 1985.
- [318] M. A. Van Hove, R F Lin, and G a Somorjai. Surface structure of coadsorbed benzene and carbon monoxide on the rhodium(III) single crystal analyzed with low energy electron diffraction intensities. *Journal of the American Chemical Society*, 108(10):2532–2537, 1986.

Bibliography

List of Publications

Publications Related to this Thesis

Binding energies of benzene on coinage metal surfaces: Equal stability on different metals

Friedrich Maass, Yingda Jiang, Wei Liu, Alexandre Tkatchenko, and Petra Tegeder

J. Chem. Phys. **148**, 214703 (2018)

TIPS-Pentacene on Au(111): Adsorption Properties, Electronic Structure and Singlet-Fission Dynamics

Arnulf Stein, Friedrich Maass, and Petra Tegeder

J. Phys. Chem. C **121**, 18075 (2017)

Substrate-Directed Growth of N-Heteropolycyclic Molecules on a Metal Surface

Friedrich Maass, Arnulf Stein, Bernd Kohl, Lena Hahn, Lutz H. Gade, Michael Mastalerz, and Petra Tegeder

J. Phys. Chem. C **120**, 2866 (2016)

Core Halogenation as a Construction Principle in Tuning the Material Properties of Tetraazaperopyrenes

Lena Hahn, Friedrich Maass, Tim Bleith, Ute Zschieschang, Hubert Wadepohl, Hagen Klauk, Petra Tegeder, and Lutz H. Gade

Chem. Eur. J. **21**, 17691 (2015)

Quantitative Prediction of Molecular Adsorption: Structure and Binding of Benzene on Coinage Metals

Wei Liu, Friedrich Maass, Martin Willenbockel, Christopher Bronner, Michael Schulze, Serguei Soubatch, F. Stefan Tautz, Petra Tegeder, and Alexandre Tkatchenko

Bibliography

Phys. Rev. Lett. **115**, 036104 (2015)

Publications Not Related to this Thesis

Electronic structure changes during the on-surface synthesis of nitrogen-doped chevron-shaped graphene nanoribbons

Friedrich Maass, Manuel Utecht, Stephan Stremlau, Marie Gille, Jutta Schwarz, Stefan Hecht, Tillmann Klamroth, and Petra Tegeder

Phys. Rev. B **96**, 045434 (2017)

Extended Space Charge Region and Unoccupied Molecular Band Formation in Epitaxial Tetrafluorotetracyanoquinodimethane Films

David Gerbert, Friedrich Maass, and Petra Tegeder

J. Phys. Chem. C **121**, 15696 (2017)

Adsorption and switching properties of nitrospiropyran on Bi(114)

Stephan Stremlau, Friedrich Maass, and Petra Tegeder

J. Phys.: Condens. Matter **29**, 314004 (2017)

Publications In Preparation or Under Review

Binding energies of acenes on Au(111): The interplay of vertical attraction and lateral repulsion

Friedrich Maass, Yingda Jiang, Wei Liu, Alexandre Tkatchenko, and Petra Tegeder

in preparation

Collective Excitations at the Metal/Organic Interface - A Universal Trend

Friedrich Maass, and Petra Tegeder

in preparation

Prices and Awards

Heidelberg (2017) Dr.-Sophie-Bernthsen Award
Faculty of Chemistry and Earth Sciences
Ruprecht-Karls-Universität Heidelberg

Acknowledgments

First I want to thank Petra Tegeder for supervising my thesis work, for her continuous support, for both, guiding through countless ideas for collaborations and interesting experiments and giving the freedom and time to follow own thoughts and solutions, and particularly for giving the opportunity to visit the group of Xiaoyang Zhu (Columbia University, New York, USA), the Donostia International Physics Center (San Sebastian), and to attend a beam time at BESSY II (Berlin) as well as to participate at numerous conferences and meetings. Additionally, I would like to thank Annemarie Pucci for being the second advisor of my thesis and for fruitful discussions regarding collective excitations at metal surfaces.

A very special thank goes to the numerous collaborators I was allowed to work with during this work and without whom most of the work would have been simply not possible. Alexandre Tkatchenko and Wei Liu (Fritz-Haber Institut Berlin, Université du Luxembourg, Nanjing University of Science and Technology) who did all the theoretical work regarding binding energies. Lena Hahn and Lutz H. Gade, Bernd Kohl and Michael Mastalerz, Fabian Paulus and Uwe Bunz (all Universität Heidelberg) for the supply with materials and ideas regarding the tetraazaperopyrenes, quinoxalinophenanthrophenazines, and aza-substituted TIPS-pentacene, respectively. And Vjatcheslav Silkin (Donostia International Physics Center, San Sebastian, Spain) for the fruitful and ongoing discussions about plasmonic excitations at adsorbate-covered metal surfaces.

I also want to thank the people from Stefan Tautz's group (Forschungszentrum Jülich), especially Sergey Soubatch, and the group of Georg Koller (Universität Graz, Österreich) for interesting days and nights at the BESSY II synchrotron in Berlin and the group of Xiaoyang Zhu (Columbia University, New York, USA) for giving inspiring insight into their research during my visit.

For the help with the experiments and doing lots of measurements mentionable independent I want to thank my interns and bachelor students Antonia Becker, Felix Berger, Christian Diercks, Michael Gast, Sebastian Grieger, Deb-

orah Hartmann, Christoph Hendrich, Thomas Josephy, Jens Neus, Dominik Pastötter, Julian Türck, and Philippe Wagner.

For the pleasant time in the lab, the office, and during group excursions, I want to thank my co-workers Christopher Bronner, David Gerbert, Marc Hänsel, Vipilan Sivanesan, Michael Schulze, Arnulf Stein, and Stephan Strem-lau.

Stephan Strem-lau deserves additional gratitude as he advised me to the HREELS experiment in detail and shared all his knowledge generously. Arnulf Stein and Max Vogtland did their master theses under my supervision and helped me with their ideas and experimental efforts. A further thank goes to Mohsen Ajdari for continuing the HREEL experiments in our group.

For their support during my studies and the work on this thesis, I want to give a special thank to my parents and my family. Finally, I thank Smilla, Emil and Kendra for giving me joy and fun, the necessary diversion from work, motivation and everything else.

Thank you!

**Eidesstattliche Versicherung gemäß § 8 der Promotionsordnung
der Naturwissenschaftlich-Mathematischen Gesamtfakultät
der Universität Heidelberg**

1. Bei der eingereichten Dissertation zu dem Thema

handelt es sich um meine eigenständig erbrachte Leistung.

2. Ich habe nur die angegebenen Quellen und Hilfsmittel benutzt und mich keiner unzulässigen Hilfe Dritter bedient. Insbesondere habe ich wörtlich oder sinngemäß aus anderen Werken übernommene Inhalte als solche kenntlich gemacht.

3. Die Arbeit oder Teile davon habe ich wie folgt/bislang nicht¹⁾ an einer Hochschule des In- oder Auslands als Bestandteil einer Prüfungs- oder Qualifikationsleistung vorgelegt.

Titel der Arbeit: _____

Hochschule und Jahr: _____

Art der Prüfungs- oder Qualifikationsleistung: _____

4. Die Richtigkeit der vorstehenden Erklärungen bestätige ich.

5. Die Bedeutung der eidesstattlichen Versicherung und die strafrechtlichen Folgen einer unrichtigen oder unvollständigen eidesstattlichen Versicherung sind mir bekannt.

Ich versichere an Eides statt, dass ich nach bestem Wissen die reine Wahrheit erklärt und nichts verschwiegen habe.

Ort und Datum

Unterschrift

¹⁾ Nicht Zutreffendes streichen. Bei Bejahung sind anzugeben: der Titel der andernorts vorgelegten Arbeit, die Hochschule, das Jahr der Vorlage und die Art der Prüfungs- oder Qualifikationsleistung.

12/2012